UNIVERSITY OF CALIFORNIA,
IRVINE

Phonon Imaging of Nanostructure Interfaces by Electron Microscopy

DISSERTATION

submitted in partial satisfaction of the requirements
for the degree of

DOCTOR OF PHILOSOPHY

in Physics

by

Chaitanya Avinash Gadre

Dissertation Committee:
Professor Xiaoqing Pan, Chair
Professor Ruqian Wu
Professor Wilson Ho

2023

DEDICATION

To

Prabhu Baa

My wife Soumya

My family

TABLE OF CONTENTS

LIST OF FIGURES

ACKNOWLEDGEMENTS

Firstly, I would like to thank my adviser, Prof Xiaoqing Pan, for his instrumental effort in bringing world-class electron microscopy to UCI and our group. I had the privilege to use the best tools and conduct first-rate science under his tutelage. Throughout my PhD career I was challenged to perform above what I thought I was capable of. His extremely ambitious standards for experimental process and data presentation pushed me to exceed my own standards. In his research group, I had the tools and mentorship that propelled me to achieve my dream of publishing a Nature paper, an achievement which will be a sense of pride for me for the rest of my life. I would also like to express my deep gratitude to Prof. Ruqian Wu and Prof. Gang Chen for vital collaboration and expert support in my academic endeavors. I would also like to thank Prof. Ruqian Wu and Prof. Wilson Ho for serving on my PhD committee.

Next, I would like to thank Xingxu Yan, who is arguably the most vital piece in my success as a PhD student. I would like to specifically thank him for his utmost patience in mentoring me. He has transformed me from a naïve and lost student to an extremely adept researcher capable of planning, leading, and executing high impact works. The research and organizational skills he drilled into me have stayed with me for the entirety of my PhD career and will propel me to even higher heights in the next stages of my professional career.

I would also like to thank my dear friends and colleagues in Pan Research Group for their companionship and support; I could not have asked for a more friendly and supportive group. I thank the first post-doctoral researchers in our group at UCI, Dr. Mingjie Xu, Dr. Linze Li, Prof. Yi Zhang, and Prof. Sheng Dai for being strong pillars of knowledge and excellence and shining examples of what a top-tier researcher should be. I express my gratitude to all my peers I have met and bonded with during my time as a PhD student. The times I spent with Christopher Addiego and Thomas Blum during group meetings discussing science, ranting about our experimental woes, and just chatting about our lives, have been some of the most cherishable memories I have created. Chatting with Huaixun Huyan and Peter Tieu late at night made it all the more bearable.

I want to especially thank Tom Lee for being a faithful friend throughout our time together. The countless hours of discussions we had, the many dinners we had to celebrate our progress, and joint experimental sessions we suffered through are some of my best memories.

I also want to thank my mentees for dealing with someone as stubborn as me. I have been constantly impressed with the rate of growth Tom Lee, Xiaowang Wang, Han-Hsuan, and Yifeng Huang have shown. I have been able to plan and execute exciting projects with them and I firmly believe they will make their mark in the academic world.

I am sincerely grateful to highly skilled and knowledgeable staff members at the Irvine Materials Research Institute, Dr. Toshihiro Aoki, Dr. Jian-Guo Zheng, Dr. Li Xing for their guidance and training. It was their vital mentorship that accelerated my learning in electron

microscopy. Specifically, I would like to thank Dr. Toshihiro Aoki for his instrumental role in maintaining the Nion microscope with Xingxu Yan and I and for being a friendly face I could just have a casual conversation with. I feel he is the most vital piece for the smooth functioning of IMRI and all its microscopes.

I also want to extend my gratitude to the staff at Nion including Tracy Lovejoy and Petr for setting up crucial EELS drives on our system and other support, Chris Meyer for his massive help in developing an auto acquisition script for our Nion microscope, Ondrej Krivanek and Niklas Delby, and other vital staff for setting up vital settings.

Significant portions of this text are reprinted from "Nanoscale imaging of phonon dynamics by electron microscopy" Nature 606.7913 (2022): 292-297. Portions of the work presented here were performed and supervised by the co-authors listed on these articles: Xingxu Yan, Qichen Song, Jie Li, Lei Gu, Huaixun Huyan, Toshihiro Aoki, Sheng-Wei Lee, Gang Chen, Ruqian Wu & Xiaoqing Pan. I would also like to thank Springer Nature Ltd. for their permission to reproduce my previously published works in this dissertation.

I would like to acknowledge funding provided by US Department of Energy, Office of Basic Energy Sciences, Division of Materials Sciences and Engineering under Award DESC0014430, the US National Science Foundation (NSF) under grant numbers DMR-1506535, DMR-2034738, and the National Science Foundation (NSF) Materials Research Science and Engineering Center (MRSEC) program through the UC Irvine Center for Complex and Active Materials (DMR-2011967). Electron microscopy experiments and sample preparation were performed at the Irvine Materials Research Institute supported in part by the National Science Foundation through the Materials Research Science and Engineering Center program (DMR-2011967).

Finally, I want to thank Prabhu baa, my wife Soumya, and my family. They formed an indestructible foundation upon which I was able to establish my success.

VITA

Chaitanya Avinash Gadre

EDUCATION

Doctor of Philosophy in Physics **2023**
University of California, Irvine *Irvine, CA*

Master of Science in Physics **2023**
University of California, Irvine *Irvine, CA*

Bachelor of Science in Physics **2015**
University of California, Santa Barbara *Goleta, CA*

RESEARCH EXPERIENCE

Graduate Research Assistant 2018–2023
University of California, Irvine *Irvine, CA*

TEACHING EXPERIENCE

Teaching Assistant **2015–2018**
University of California, Irvine *Irvine, CA*

REFEREED JOURNAL PUBLICATIONS

Atomic-scale origin of the low grain-boundary resistance in perovskite solid electrolyte Li0.375Sr0.4375Ta0.75Zr0.25O3. **2023**
T. Lee, J. Qi, and **C. Gadre**, et. al. *Nature Communications* 14.1 (2023): 1940.

Nanoscale Phonon Dynamics in the Electron Microscope **2022**
C. Gadre and X. Yan, et. al. *Nature* 606.7913 292-297.

Curvature-Induced One-Dimensional Phonon Polaritons at Edges of Folded Boron Nitride Sheets **2022**
X. Yan, **et. al.** *Nano Letters* 22 (23), 9319-9326

Experimental observation of localized interfacial phonon modes **2021**
Z. Cheng, **et al**. *Nature Communications* 12.1 1-10.

Single-defect phonons imaged by electron microscopy **2021**
X. Yan, **et al**. *Nature* 589.7840 65-69.

Direct observation of polarization-induced two-dimensional electron/hole gases at ferroelectric-insulator interface **2021**
H. Huyan, **et. al.** *npj Quantum Materials* 6 (1), 88

Investigating the Degradation of Nb2O5 Thin Films Across 10,000 Lithiation/Delithiation Cycles **2021**
I. Andoni, **et. al.** *ACS Applied Energy Materials* 4 (7), 6542-6552

Anomalous Linear Layer-Dependent Blue Shift of Ultraviolet-Range Interband Transition in Two-Dimensional MoS2 **2019**
X. Yan, **et. al.** *The Journal of Physical Chemistry C* 124 (2), 1609-1616

Unexpected strong thermally induced phonon energy shift for mapping local temperature. **2019**
X. Yan, **et al**. *Nano Letters* 19.10 7494-7502.

Observation of strong polarization enhancement in ferroelectric tunnel junctions **2019**
L. Li, **et al**. *Nano letters* 19.10 6812-681*8.

Control of domain structures in multiferroic thin films through defect engineering **2018**
Advanced Materials 30 (38), 1802737
L. Li, **et. al.** *Advanced Materials* 30 (38), 1802737

REFERRED CONFERENCE PUBLICATIONS

Nanoscale Interface Phonon Dynamics Imaged by Electron Microscopy **Mar 2022**
APS March Meeting

Polarization-Induced Anisotropic Phonons at Ferroelectric-Insulator Interfaces **Aug 2021**
Microscopy and Microanalysis

Phonon Reflections from Nanostructure Interfaces Imaged by Momentum-Averaged and Resolved Vibrational EELS **Aug 2021**
Microscopy and Microanalysis

Nanoscale Vibrational Mapping of Single SiGe Quantum Dots in the Electron Microscope **Mar 2021**
APS March Meeting

Nanoscale Phonon Mapping of Single SiGe Quantum Dots by Vibrational EELS **Aug 2020**
Microscopy and Microanalysis

Mapping the Nanoscale Redshift of Optical Phonon Modes in a Strained Quantum Dot System **Aug 2019**
Microscopy and Microanalysis

Investigation of Surface and Bulk Vibrational modes in SiC polytypes using spatially resolved monochromated EELS **Aug 2018**
Microscopy and Microanalysis

ABSTRACT OF THE DISSERTATION

Phonon Imaging of Nanostructure Interfaces by Electron Microscopy

By

Chaitanya Avinash Gadre

Doctor of Philosophy in Physics

University of California, Irvine, 2023

Professor Xiaoqing Pan, Chair

Thermal properties in nanostructured materials are dominated by atomic scale and nanoscale inhomogeneities in crystal lattices. However, tools for studying nanoscale thermal properties have relied on theoretical frameworks and optical measurements of defect aggregates. Vibrational spectroscopy in a transmission electron microscope offers unprecedented access into nanoscale phonon physics. We have studied a SiGe quantum dot (QD) superlattice which is a strong candidate for high temperature thermoelectrics. These dome shaped, SiGe alloy QDs are bounded by a sharp and gradual interface due to its nonuniform alloy distribution. With a 6mev (~50 cm^{-1}) energy resolution via a monochromated beam, we map Si optical phonons in a single SiGe QD. We find a composition-induced strain in the alloy matrix in the QD nanostructure that manifests as a redshift in the phonon energy that is exactly consistent with the nonuniform composition distribution. More notably, we find an accumulation of non-equilibrium phonons below the

sharp interface. To investigate the dynamics of this further, I developed a new technique called differential momentum mapping (DPM) that allows for the mapping of propagating phonon modes. With this, we mapped phonon group velocity vectors showing unequivocally a drastically larger reflection of phonons from the sharp interface than the gradual one. For the first time, dynamical thermal processes at the nanoscale have been imaged.

This vibrational EELS capability is then applied to a ferroelectric-insulator system: $BiFeO_3/TbScO_3$ (BFO/TSO). Our goal for this study was to identify relationships between the phonon structure and ferroelectricity in BFO. Ferroelectric domain walls (DW) and the emergence of free charge gases at the interface offered us an excellent opportunity to also investigate nanoscale electron-phonon dynamics. We discovered that DW-localized shear strain due to alternating polarization, causes phonons to propagate anisotropically by utilizing the DPM technique developed in the previous work. Furthermore, the free charge gasses at the interface also break phonon symmetry but due to accumulated net charge rather than structural distortions. This work provides a nanoscale angle-resolved picture for the decrease in cross-DW and cross-interface thermal conductivity. Uncovering this physics is fundamental to the well-informed fabrication of ferroelectric-based materials and proper design of ferroelectric memories.

To enable trustable data analysis of EELS data, a data workflow stack has been developed with the following key aspects in mind: accuracy, efficiency, transparency, and useability. With the advent of advanced detectors and electron spectroscopy techniques, demand for intelligent, high throughput, processing has sky-rocketed, but the lack of programming and data analysis expertise has been a high barrier to entry. The developed

modules serve to mitigate this problem by taking advantage of relatively low-level APIs that interface with data and provide scientific analysis tools and wrapping them in high level modules designed for user-specific workflows. An example workflow for vibrational EELS includes aligning of the zero-loss peak (ZLP), background subtracting the vibrational signal, using PCA to reconstruct the data in a lower dimensional representation, fitting prominent peaks, and finally visualizing the data in the form of line plots or contour maps. This framework also includes tools for analyzing the fine structure of core-loss edges, bandgap measurements, and a general set of tools including deconvolution, clustering, and filtering. Because entire blocks in the workflow are condensed into single lines of code, these high-level modules can aid non-coders to process their data using innovative data analysis techniques.

Chapter 1

Introduction

1.1 Phonons and Thermal Transport

Phonons are the quantized vibrations of the atomic lattice in a solid. They are responsible for the structural and thermal properties of a material and play a crucial role in heat transport. The study of phonons is essential for understanding the thermal conductivity of a material, which determines how efficiently heat is conducted through it. Phonons also play a critical role in determining a material's mechanical and electronic properties. The phonon spectrum determines the strength of the bonds between atoms in a solid, which describes the energy and momentum of the different phonon modes in a material. Additionally, phonons can couple to electronic excitations, leading to phenomena such as electron-phonon interaction, which can significantly impact the electronic properties of a material. Understanding phonons are essential for designing and improving technologies that rely on heat management, such as electronic devices. It also provides insight into materials' mechanical and electronic properties, which can be helpful in various scientific and engineering applications. Additionally, studying phonons can help to understand the fundamental properties of solids and the behavior of heat in solids.

As a result, it becomes necessary to put forth a detailed mathematical treatment of lattice dynamics in three dimensions. The equations of motion for a solid describe the motion of atoms in the lattice in response to external forces. These equations are derived from the laws of classical mechanics and take the form of a set of coupled second-order differential equations. The equations of motion are typically written in terms of the displacement vector of each atom in the lattice. These vectors describe the deviation of the atom's position from its equilibrium position.

The dynamical matrix is a key concept in the study of phonons and is closely related to the equations of motion. It is a matrix that describes the interatomic force constants in a solid, which are the forces that govern the motion of atoms in the lattice. The dynamical matrix can be derived from the equations of motion and is closely related to the Hessian matrix, which describes the second derivatives of the system's potential energy with respect to the atomic coordinates. The eigenvalues and eigenvectors of the dynamical matrix correspond to the solid's phonon frequencies and phonon modes. The phonon frequencies are the frequencies at which the lattice vibrations occur, while the phonon modes describe the spatial distribution of the atomic displacements for each frequency. The phonon frequencies are related to the thermal properties of the solid and can be used to calculate thermal conductivity.

The dynamical matrix can also be used to calculate the electron-phonon interaction, which plays an essential role in determining the electronic properties of a material. This is done by calculating the electron-phonon matrix elements, which describe the coupling between electronic and phononic excitations. In summary, the equations of motion and the dynamical

matrix are closely related concepts essential for understanding phonons' behavior in solids. The equations of motion describe the motion of atoms in the lattice in response to external forces, while the dynamical matrix describes the interatomic force constants that govern this motion. The eigenvalues and eigenvectors of the dynamical matrix correspond to the phonon frequencies and phonon modes of the solid, respectively, and can be used to calculate a material's thermal, mechanical, and electronic properties.

We first start by defining a crystal as a periodic arrangement of unit cells in 3 dimensions. With an arbitrary unit cell chosen as the origin, we define index of other unit cells as:

$$\boldsymbol{a} = (a_1, a_2, a_3) \tag{1.1}$$

Where a_n refers to the nth unit cell from the origin. The origin of the ath unit cell is then:

$$\boldsymbol{r}_a = a_1\boldsymbol{a}_1 + a_2\boldsymbol{a}_2 + a_3\boldsymbol{a}_3 \tag{1.2}$$

Relative to the origin a $= (0, 0, 0)$. Each unit cell then has n atoms which we will label $k = 1, 2, 3, \ldots, n$. The atoms will be placed at positions $\mathbf{r}_k$ relative to the origin of a given unit cell $\mathbf{r}_k$. Each atom will then have a position

$$\boldsymbol{r}_{k,a} = \boldsymbol{r}_a + \boldsymbol{r}_k \tag{1.3}$$

relative to the origin of the unit cells. $\mathbf{r}_{k,a}$ defines the equilibrium position. The subscripts k and a refer to the kth atom and a^{th} unit cell. From here we define displacements from equilibrium due to thermal motion as

$$\boldsymbol{u}_{k,a} = (u_{k,a,x}, u_{k,a,y}, u_{k,a,z}) \tag{1.4}$$

Where the subscripts x, y, and z refer to the conventional cartesian directions. Then, the full position of the atoms relative to the origin defined earlier is given by

$$\boldsymbol{R}_{k,a} = \boldsymbol{r}_a + \boldsymbol{r}_k + \boldsymbol{u}_{k,a} \tag{1.5}$$

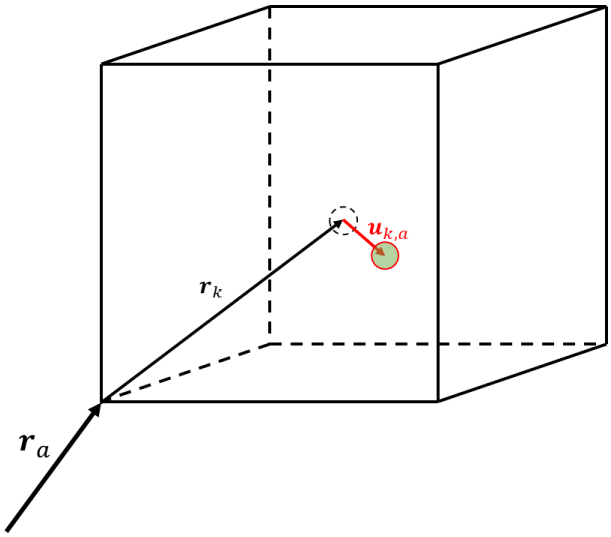

Figure 1.1 Schematic of coordinate system for defining atomic position. First, the position of the unit cell is defined with respect to some arbitrary, globally defined origin. Then, the equilibrium position of atom k is defined locally within the unit cell. The equilibrium position of atom k is given by the dashed circle. Lastly, thermal motion is accounted for by defining a displacement $u_{k,a}$ representing the displacement of the atom from its equilibrium position. The complete definition of atomic position is given by $\mathbf{r}_a+\mathbf{r}_k+\mathbf{u}_{k,a}$.

Now that the atomic positions are defined, we write our equation of motion:

$$\boldsymbol{F}_{\alpha}^{ka} = M_k \frac{\partial^2 \boldsymbol{u}_{k',a,\alpha'}}{\partial t^2} = \sum_{k',a',\alpha'} \boldsymbol{\Phi}_{\alpha,\alpha'}^{ka,k'a'} \boldsymbol{u}_{k',a,\alpha'} \tag{1.6}$$

Where M is the mass of the kth atom and $\boldsymbol{\Phi}_{\alpha,\alpha'}^{k,k'}$ is the matrix of force constants. We must first define the matrix of force constants in terms of the system energy. To that end, we first write the total energy of the system about structural equilibrium as a series expansion:

$$E = E_0 + \frac{\partial E}{\partial u}u + \frac{1}{2!}\frac{\partial^2 E}{\partial u^2}u^2 + \frac{1}{3!}\frac{\partial^3 E}{\partial u^3}u^3 + \cdots \tag{1.7}$$

At equilibrium, the forces

$$\boldsymbol{F}_{k,\alpha} = -\frac{\partial E}{\partial \boldsymbol{u}} \tag{1.8}$$

Are all 0 so the 1st term in Eq. 1.7 vanishes. The 0th term in Eq. 1.7 represents the energy of the system at equilibrium which we can define to be 0. In the harmonic approximation, higher order terms are neglected giving us

$$E_{harmonic} = \frac{1}{2}\sum_{kk',aa'} \boldsymbol{u}_{ka}^{T} \cdot \Phi \cdot \boldsymbol{u}_{k'a'} = \frac{1}{2}\sum_{kk',aa'}\sum_{\alpha\alpha'} \boldsymbol{u}_{k,a,\alpha}\boldsymbol{\Phi}_{\alpha,\alpha'}^{k,k'}\,\boldsymbol{u}_{k',a,\alpha'} \tag{1.9}$$

Where $\boldsymbol{u}_{\alpha,k,a}$ is the displacement of atom k in unit cell a along Cartesian direction α. Then the matrix of force constants is given by

$$\boldsymbol{\Phi}_{\alpha,\alpha'}^{k,k'}(a) = \frac{\partial \boldsymbol{F}_{u_{k,a,\alpha,}}}{\partial \boldsymbol{u}_{k',a,\alpha'}} = \frac{\partial^2 E}{\partial \boldsymbol{u}_{k,a,\alpha}\partial \boldsymbol{u}_{k',a',\alpha'}} \tag{1.10}$$

Like the commonly discussed 1D case, we can write an ansatz for a plane wave solution in 3D as follows:

$$\boldsymbol{u}_{\alpha,k} = \boldsymbol{\varepsilon}_{k,q,\nu} e^{i(\boldsymbol{q}\cdot\boldsymbol{R}_{k,a}-\omega t)} \tag{1.11}$$

Here, $\boldsymbol{q}$ and ω are phonon wavevector and frequency also referred to as phonon momentum and energy, respectively and $\boldsymbol{\nu}$ is mode label. Inserting Eq. 1.11 into Eq. 1.6 gives us

$$\boldsymbol{F}_{k,a} = -M_k\omega^2\boldsymbol{\varepsilon}_{k,\boldsymbol{q},\nu}e^{i(\boldsymbol{q}\cdot\boldsymbol{R}_{k,a}-\omega t)} = -\sum_{k',a',\alpha'} \boldsymbol{\Phi}_{\alpha,\alpha'}^{k,k'}\boldsymbol{\varepsilon}_{k',\boldsymbol{q},\nu}e^{i(\boldsymbol{q}\cdot\boldsymbol{R}_{k',a'}-\omega t)} \tag{1.12}$$

which simplifies to

$$M_k\omega^2\boldsymbol{\varepsilon}_{k,\boldsymbol{q},\nu} = \sum_{k',a',\alpha'} \boldsymbol{\Phi}_{\alpha,\alpha'}^{k,k'}\boldsymbol{\varepsilon}_{k'\boldsymbol{q},\nu}e^{i(\boldsymbol{q}\cdot\boldsymbol{R}_{k',a'}-\boldsymbol{R}_{k,a})} \tag{1.13}$$

We then make a change in variables and define the column vector of atomic displacements $\boldsymbol{e}(\boldsymbol{q},\nu)$ that will make the expression more compact:

$$\boldsymbol{e}(\boldsymbol{q},\nu) = \frac{1}{\sqrt{M_k}}\boldsymbol{\varepsilon}_{k,\boldsymbol{q},\nu} \tag{1.14}$$

where k = 1, 2, 3…n for each cartesian direction α. Eq. 1.13 then becomes

$$\omega^2\boldsymbol{e}(\boldsymbol{q},\nu) = \left[\frac{1}{\sqrt{M_k M_{k'}}}\sum_{aa'}\boldsymbol{\Phi}_{\alpha,\alpha'}^{k,k'}e^{i(\boldsymbol{q}\cdot\boldsymbol{R}_{k',a'}-\boldsymbol{R}_{k,a})}\right]\cdot\boldsymbol{e}(\boldsymbol{q},\nu) \tag{1.15}$$

$$\omega^2\boldsymbol{e}(\boldsymbol{q},\nu) = \boldsymbol{D}_{\alpha,\alpha'}^{k,k'}(\boldsymbol{q})\cdot\boldsymbol{e}(\boldsymbol{q},\nu) \tag{1.16}$$

where the dynamical matrix is a 3N × 3N matrix where N is the number of atoms in the system and is defined as

$$\boldsymbol{D}_{\alpha,\alpha'}^{k,k'}(\boldsymbol{q}) = \frac{1}{\sqrt{M_k M_{k'}}}\sum_{aa'}\boldsymbol{\Phi}_{\alpha,\alpha'}^{k,k'}e^{i\boldsymbol{q}\cdot(\boldsymbol{R}_{k',a'}-\boldsymbol{R}_{k,a})} \tag{1.17}$$

To obtain phonon dispersion relations $\omega(q)$, one need only solve the Eigenvalue problem presented below:

$$\left|\boldsymbol{D}_{\alpha,\alpha'}^{k,k'}(\boldsymbol{q}) - \boldsymbol{\omega}^2(\boldsymbol{q})\right| = \boldsymbol{0} \tag{1.18}$$

$$\boldsymbol{DOS}(\boldsymbol{\omega}) = \frac{\boldsymbol{q}^2}{\boldsymbol{2\pi^2}}\left(\frac{\mathbf{d}\boldsymbol{\omega}(\boldsymbol{q})}{\mathbf{d}\boldsymbol{q}}\right)^{-\boldsymbol{1}} \tag{1.19}$$

Solving this Eigenvalue problem will return phonon dispersion relations for any arbitrary crystal structure, even ones with non-trivial periodicity and boundary conditions. The density of states, which describes the number of states per energy, can then be obtained by Eq. 1.19. The true difficulty lies in obtaining a sufficiently accurate potential and computational complexity. Given a potential, one can then obtain inter-atomic force constants to compute the dynamical matrix and finally the phonon dispersion relations.

The phonon density of states (DOS) is a fundamental concept that describes the distribution of phonon frequencies in a material. The DOS is directly related to thermal transport in the material, as phonons are the primary heat carriers in semiconductors and insulators. Specifically, the thermal conductivity of a material is proportional to the phonon mean free path and the group velocity, which are both determined by the phonon DOS. A high phonon DOS at a certain frequency means there are many phonons in that frequency range, which can result in strong phonon-phonon scattering and a shorter mean free path. On the other hand, a low phonon DOS at a certain frequency means there are fewer phonons in that frequency range, resulting in weaker phonon-phonon scattering and a longer mean free path. Therefore, understanding the phonon DOS is crucial for predicting and optimizing the thermal transport properties of materials, which has important implications for a wide range of applications, from thermoelectric materials to thermal management in electronics.

The contribution of phonon DOS to the material thermal conductivity will briefly be developed in the following discussion. The purpose of this is not to provide an in-depth mathematical treatment as was done for the phonon DOS, but to develop a qualitative intuition on how phonon properties determine material thermal transport, and therefore thermal conductivity.

The concept of thermal transport and conductivity arises when the system is lifted from its equilibrium state, meaning that temperature is not uniform throughout the region. In thermal equilibrium, the phonon modes $\boldsymbol{k}$ and $-\boldsymbol{k}$ are occupied equally, resulting in zero heat current. However, when a temperature gradient is applied, the occupation of states k and -k

is no longer equivalent. The heat current density $\boldsymbol{j}_Q$ can then be determined by adding up the contributions from all phonon modes:

$$\boldsymbol{j}_Q(\boldsymbol{r},T) = \sum_{\nu} \int \mathrm{DOS}(\boldsymbol{q},\nu,r)\, E(\boldsymbol{q},\nu,\boldsymbol{r})\, f(\boldsymbol{q},\nu,\boldsymbol{r},T)\, v_g(\boldsymbol{q},\nu,\boldsymbol{r},T)\; d^3\boldsymbol{q} \tag{1.19}$$

Here $\mathrm{DOS}(\boldsymbol{q},\nu,\boldsymbol{r})$ is the phonon DOS, $E(\boldsymbol{q},\nu,\boldsymbol{r})$ is the phonon energy at momentum $\boldsymbol{q}$ and branch ν and position $\boldsymbol{r}$; v_g is the phonon group velocity which is the gradient of the phonon energy with respect to momentum, and $f(\boldsymbol{q},\boldsymbol{r},\nu,\mathrm{T})$ is the occupation of a phonon at momentum $\boldsymbol{q}$, real-space position $\boldsymbol{r}$, and branch ν. Simply put, the heat current per unit area $\boldsymbol{j}_Q$, is a function of what kind of phonons states are available $\mathrm{DOS}(\boldsymbol{q},\nu,\boldsymbol{r})$, how many of them are occupied $f(\boldsymbol{q},\boldsymbol{r},\nu,T)$**,** the energy of those phonon $E(\boldsymbol{q},\nu,\boldsymbol{r})$, and the speed at which the phonons travel $\boldsymbol{v}_g$.

The group velocity is explicitly defined as follows:

$$\boldsymbol{v}_g(q,\nu) = \frac{\boldsymbol{\nabla} E(\boldsymbol{q},\nu)}{\hbar} \tag{1.21}$$

Here $E(\boldsymbol{q},\nu,\boldsymbol{r})$ more general represents the curves of the phonon dispersion obtained from the dynamical matrix (Eq. 1.18). The last term in Eq. 1.19 is known as the phonon occupation and deals with how many phonons in a particular branch are occupying a given space at a given temperature and is given by:

$$f(\boldsymbol{q},\boldsymbol{r},\nu,T) = \frac{1}{e^{\frac{E(\boldsymbol{q},\nu)}{kT}} - 1} \tag{1.22}$$

In this expression $\boldsymbol{k}$ is the Boltzmann constant and T is the temperature in Kelvin. $E(\boldsymbol{q},\nu,\boldsymbol{r})$ is present in each term of Eq. 1.19 signifying how central the phonon dispersion and consequently, the phonon DOS is to thermal transport. Essentially, nearly all phonon

information is contained in $E(\boldsymbol{q}, \nu, \boldsymbol{r})$. Qualitatively, the heat current density or heat flux $\boldsymbol{j}_Q$, describes how much energy is transported by phonons per unit area per second.

In an isotropic medium and assuming perfect harmonicity, the more phonons you have available, the greater the ability to transport that heat. Additionally, the faster the phonons travel, the quicker heat energy will be transported. However, this isotropic and harmonic assumption breaks down due to phonon scattering. In physical systems, the effective nuclear potential that phonons "see" is anharmonic and the degree of anharmonicity determines, in part, the scattering frequency of phonons in materials[1]. This causes phonons to scatter with themselves or with defects in the material that, in some cases, can significantly modify the thermal conductivity. Conversely, in the harmonic approximation, phonons move through each other and do not scatter. These effects arise at the nanoscale and cannot be rigorously treated by trivial ensembles or averages over isotropic and equilibrium states.

The Boltzmann transport equation (BTE) has been effectively used for handling phonon scattering events including, phonon-phonon, electron-phonon, phonon-defect, and other scattering events[2]. Using the BTE without the presence of external forces, one can model the phonon occupancy including scattering effects:

$$\frac{\partial f}{\partial t} + \boldsymbol{v} \cdot \boldsymbol{\nabla} f = \left(\frac{\partial f}{\partial t}\right)_{\text{coll}} \tag{1.23}$$

The collision term can take on many terms depending on the different types of scattering events that occur. The case of phonon scattering due to material interfaces is treated in detail in appendix A.

In the Boltzmann Transport Equation (BTE), the term that directly accounts for scattering events is the collision term, often denoted as $\left(\frac{\partial f}{\partial t}\right)_{\text{coll}}$.This term represents the rate of change of the distribution function due to collisions, or in the context of phonons, scattering events. When there are increased scattering events, such as due to an increase in defects or other scattering sources, the value of the collision term increases. This is because each scattering event can change the state of a phonon, altering its momentum and energy, and thus changing the distribution function.

The effect on the phonon occupation number, *f*, depends on the nature of the scattering events. Scattering can cause phonons to move from one state to another, changing the occupation numbers of those states. If scattering events are primarily moving phonons from higher-energy states to lower-energy states (down-scattering), the occupation numbers of the higher-energy states will decrease, and those of the lower-energy states will increase. Conversely, if scattering events are primarily moving phonons from lower-energy states to higher-energy states (up-scattering), the opposite will occur. In a steady state, the total rate at which phonons scatter into a given state will balance the total rate at which they scatter out of that state. This balance determines the steady-state occupation number for each state.

In general, increased scattering tends to disrupt phonon transport, leading to a decrease in thermal conductivity. This is because the phonons are more likely to scatter before they can transport energy a significant distance. However, the specific effect on the phonon occupation numbers will depend on the details of the scattering processes and the energy distribution of the phonons. There are several other forms approximations to the isotropic, harmonic case and are too extensive for the scope of this thesis and so will not be discussed.

1.2 Thermoelectricity and phonon engineering

With more than half of the energy produced by human activity being heat, it is imperative that it is recycled back into a usable form, electricity for example, to power humanity's increasing energy demands. One answer to this problem is a class of nanostructured materials called thermoelectrics: material systems that utilize the Peltier effect to convert heat into electricity.

Thermoelectricity is not a new concept; it was discovered by Thomas Seebeck as far back as 1820, a century before the world wars. Since then, there have been several billions of dollars poured into researching how to engineer a material system with a high figure of merit, zT. This unitless quantity is a measure of the efficiency of heat conversion to electricity and is a function of both how well a material conducts electricity and prohibits the transfer of heat across its volume.

Studies of thermoelectrics endeavor to design materials that either impede thermal transport or promote the flow of charges both of which are difficult to achieve simultaneously. One strategy is to impede the flow of heat while maintaining the flow of electrons. The physics behind thermal optimization is especially complex and is trickier than our intuition about how heat flows and is transferred from object to object. At the macroscopic scale, we know that heat travels from hot to cold and depending on what kind of material it is, with varying rates of heat transfer. The microscopic physics of thermal transport is a lot more involved when we consider heat transfer from a group of atoms to the next or even.

In semiconductor crystals, thermal energy is predominantly carried by lattice vibrations or phonons. The energies or frequencies of these periodic atomic displacement waves are strongly dependent on the material's atomic species, and bonding properties. In infinite crystals with no inhomogeneities, the propagation of phonons is unhindered. In this bulk regime, the transport of thermal energy can be accurately described by the Fourier conduction law[3,4]. However, this law becomes increasingly inaccurate in describing nanoscale thermal transport in the presence of defects that break crystal lattice periodicity. Not only is this the case in almost all naturally occurring compounds but also in material systems that are integrated into micro- or even nanoscale devices. The control of phonon propagation and thermal conductivity of materials by nanoscale structural engineering is exceedingly important for many technological developments such as thermoelectrics, phononic devices and power electronics.

The last few decades have seen renewed interest with the development of advanced engineering schemes and tools of investigation. Scientists have employed complex strategies involving the engineering of atomic-scale interfaces, nanostructures, and even alloying two different materials together. These nano disruptions of the periodic lattice scatter phonons thereby impeding the transport of heat.

An ideal thermoelectric impedes the propagation of phonons and facilitates the flow of electrons. As a result, it has been a central issue to reduce the lattice thermal conductivity of thermoelectric materials for the enhancement of their figure of merit (ZT)[5–9]. Although many single phase/crystal materials already possess high ZT values due to the relatively high carrier mobility, their thermoelectric performance can be further enhanced by reducing

thermal conductivity[10–12]. Numerous strategies have been employed to reduce the thermal conductivity or phonon transport of a given material by introducing material intermixing[13], nanostructures[5,6,8,12], and interfaces[2,6].

Through these mechanisms, short, medium, and long wavelength phonons are scattered, respectively. The SiGe QD superlattice (QDSL) structure is one such system that efficiently reduces thermal conductivity by 20 times by implementing all three phonon scattering mechanisms[14]. SiGe QDSLs consist of alternating layers of Si and Ge with embedded SiGe quantum dots. The periodic breaking of structural and chemical periodicity in this material promotes low thermal conductivity which is highly desirable for thermoelectrics.

The thermal properties of QDSLs are intimately related to the propagation of phonons. In SiGe QDSLs, the quantum dots and their interfaces act as scatterers that impede the propagation of phonons, leading to a significant reduction in the lattice thermal conductivity. Furthermore, the reduction in the lattice thermal conductivity of QDSLs can be enhanced by tailoring the size and spacing of the quantum dots. The size of the quantum dots determines which wavelengths of phonons are more strongly scattering while the spacing between the SL layers determines the extent of phonon scattering, with smaller spacings leading to more efficient scattering[6].

For heterogeneous interfaces, like the interface between Si and SiGe QDs, phonon scattering occurs primarily due to a mismatch of phonon states on either side of the interface. That is to say, not all phonons in Si can travel unaffected to the SiGe side as not all the modes have a corresponding energy and momentum state in SiGe. This is most easily seen when examining the phonon DOS. Fig. 1.2 how modes in SiGe have greater dispersion due to it being an alloy.

Although the densities of states in Si and Ge have significantly less overlap than those of Si and SiGe, and therefore should impede phonon propagation more, they have other disadvantages which makes them less-deal for thermoelectric applications. For example, the lattice mismatch between Si and Ge is great enough to prohibit the growth of high-layer superlattices due to the occurrence of structural dislocations. These dislocations can significantly impede electron mobility and are detrimental to thermoelectric performance.

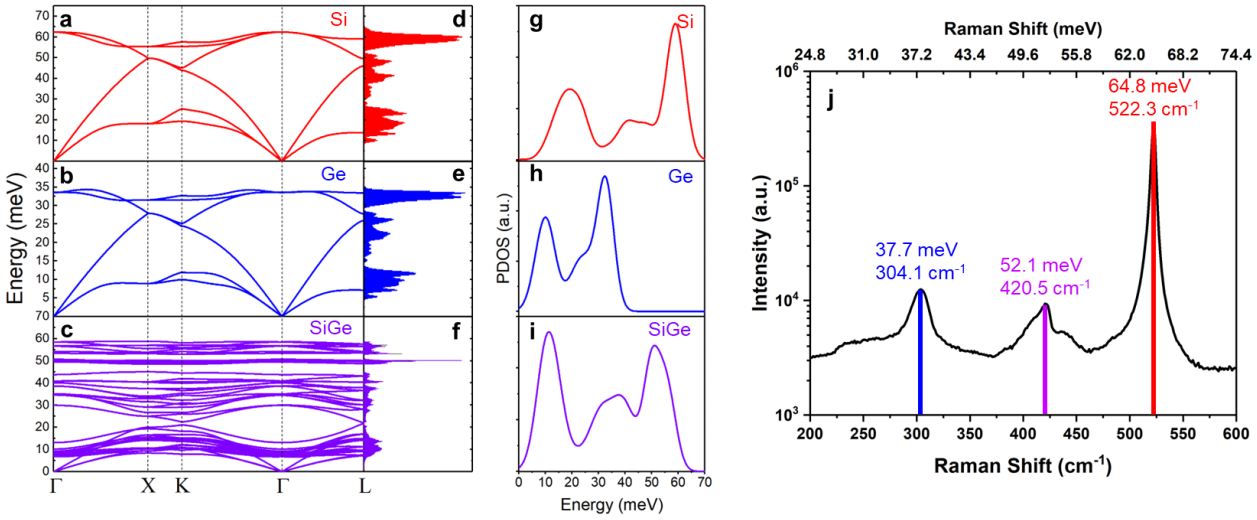

Figure 1.2 Phonon dispersions in Si, Ge, and SiGe and Raman Spectrum of SiGe a-c, Phonon dispersion relations of bulk Si, Ge, and $Si_{0.5}Ge_{0.5}$, respectively. **d-f**, Phonon density of states of bulk Si, Ge, and $Si_{0.5}Ge_{0.5}$, respectively. **g-i**, d-e after convolution with a gaussian of width 7meV. **j**, Log spectra from SiGe QD superlattice sample grown on silicon. The spectrum shows 3 distinct peaks at 37.7, 52.1, and 64.8 meV arising from Ge, SiGe, and Si optical modes, respectively.

1.3 $BiFeO_3$-$TbScO_3$: A multiferroic, perovskite-oxide heterostructure

Ferroelectric materials exhibit a permanent dielectric polarization that can be switched by an external electric field. At the atomic level, the polarization is a consequence of the separation of the positive and negative charge centers in the unit cell[15]. Like ferromagnets,

ferroelectrics exhibit order at the microscopic level, in which the electric dipoles within the material are aligned in a specific direction; these local regions of uniform polarization are known as ferroelectric domains[16]. This alignment of dipoles in domains gives rise to the ability of ferroelectrics to store electrical charge of generate an electric field. The polarization of ferroelectric domains can be switched between different stable configurations with the application of an external field and is foundational to the research efforts in ferroelectric materials. This property makes them highly attractive for a variety of applications including data storage, sensors, and actuators. For example, the nanoscale size of ferroelectric domains and the speed of polarization switch make them ideal for low power non-volatile memory[17]. Research in this area drives progress for designing more functional ferroelectrics with enhanced properties.

Perovskite oxide ferroelectrics are a unique class of materials that have several advantages over other ferroelectric materials such as high dielectric constant[18], which is a measure of the material's ability to store electrical charge. Additionally, perovskite oxide ferroelectrics also have a high Curie temperature making them more stable and less susceptible to degradation at high temperatures. Perovskite oxide ferroelectrics grown as thin films provide additional properties that emerge due to unique film-substrate interactions at the heterostructure interface. For example, at ferroelectric-insulator interfaces, free charge accumulates to compensate for the increase in electrostatic potential[19]. Although this provides an additional avenue of device control, this area of research is still quite sparse and lacks nanoscale understanding.

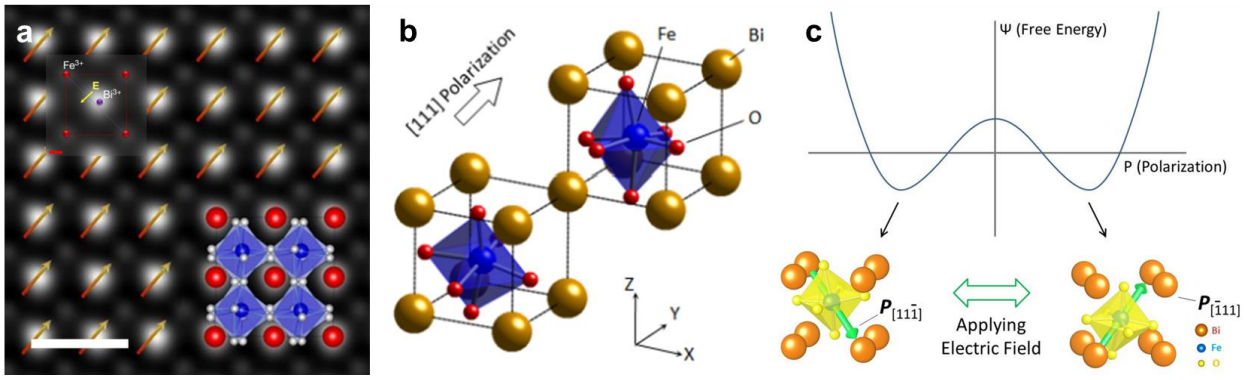

Figure 1.3 Properties of multiferroic BFO a, HAADF image overlaid with an annotated view of a single unit cell and a 2×2 structure showing a detailed view of the canted oxygen octahedral. The overlay in the top left shows the direction of the electric field which is along the displacement of the Fe atom and is opposite to the polarization direction. **b**, Unit cell structure with polarization direction labeled. In BFO, polarization is along body diagonal i.e., along [111] directions. **c**, Free energy curve showing two alternate ground states for BFO. Upon application of an external electric field, the dipoles will switch to orient themselves along the electric field. Scale bar denotes 5 Å. Figure is adapted from Nelson, Christopher T., et al. Nano letters 11.2 (2011): 828-834 with permission.

Among perovskite oxide ferroelectrics, $BiFeO_3$ (BFO) is a displacement-type ferroelectric that has been known and studied for many years. It was first synthesized in the 1960s, and since then, it has been the subject of numerous research studies due to its interesting and useful properties, such as ferroelectricity, multiferroicity, and a high-temperature piezoelectric response. BFO is a perovskite-type oxide material with a rhombohedral crystal structure consisting of alternating layers of bismuth and iron ions, with oxygen ions located at the vertices of the crystal lattice (Fig. 1.3a). In the rhombohedral structure, the bismuth and iron ions are arranged in a hexagonal pattern, with the oxygen ions forming a three-dimensional network around them.

In epitaxially grown BFO films, the misfit strain between the film and the substrate determines its structure. BFO grown on insulating $TbScO_3$ (TSO) adopts a rhombohedral unit cell which also can be considered a pseudo-cubic structure. In this phase, polarization points

along any of the [111] body diagonal directions (Fig. 1.3b). More specifically, the polarization is caused by a rotation of the oxygen octahedron about [111] and displacement of the Fe atom along the unit cell [111] body diagonal. The free energy surface of BFO reveals two alternate ground states. Upon application of an external electric field, the dipoles will switch to orient themselves along the electric field (Fig. 1.3c).

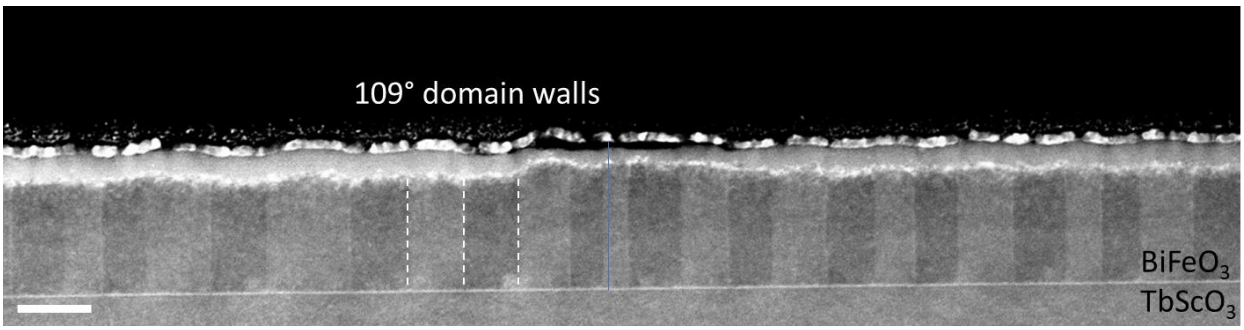

Figure 1.4 Off-axis bright-field (BF) image showing domain contrast. By displacing the scattered central electron beam and allowing the BF detector to collect off-axis electrons, we can form a STEM image that shows domain contrast. This is not unlike using a high contrast aperture to select $(10\bar{1})$ diffraction spots in a TEM to reveal domain contrast. Scale bar denotes 50 nm.

Fig. 1.4 shows a BFO thin film grown on an insulating TSO substrate. This results in alternating domain contrast punctuated by 109° DWs. The 109° refers to the angle that subtends the 3D polarization directions on either side of the DW. This image is taken using a bright field detector but with the aperture shifted off-axis such that the domain contrast be maximized. More details on techniques will be discussed in the following chapters.

At the BFO-TSO interface, the specific way the polarization terminates creates positive or negative bound charges in domains where the polarization is pointing upward or downward, respectively. To compensate, a 2D electron or hole gas (2DE/HG) accumulates at the interface[19] occupying about 1-2nm above the BFO-TSO interface (Fig. 1.5). The emergence

of free charge gas has only recently been discovered, and although, atomic resolution imaging is standard, understanding the emergent physics behind change distributions and their interaction with the perovskite oxide lattice, is still a challenging task[19,20]. As lattice structure is intimately related to both phonons and the formation of the free charge carriers, it becomes necessary to study the interplay between phonons and these carriers.

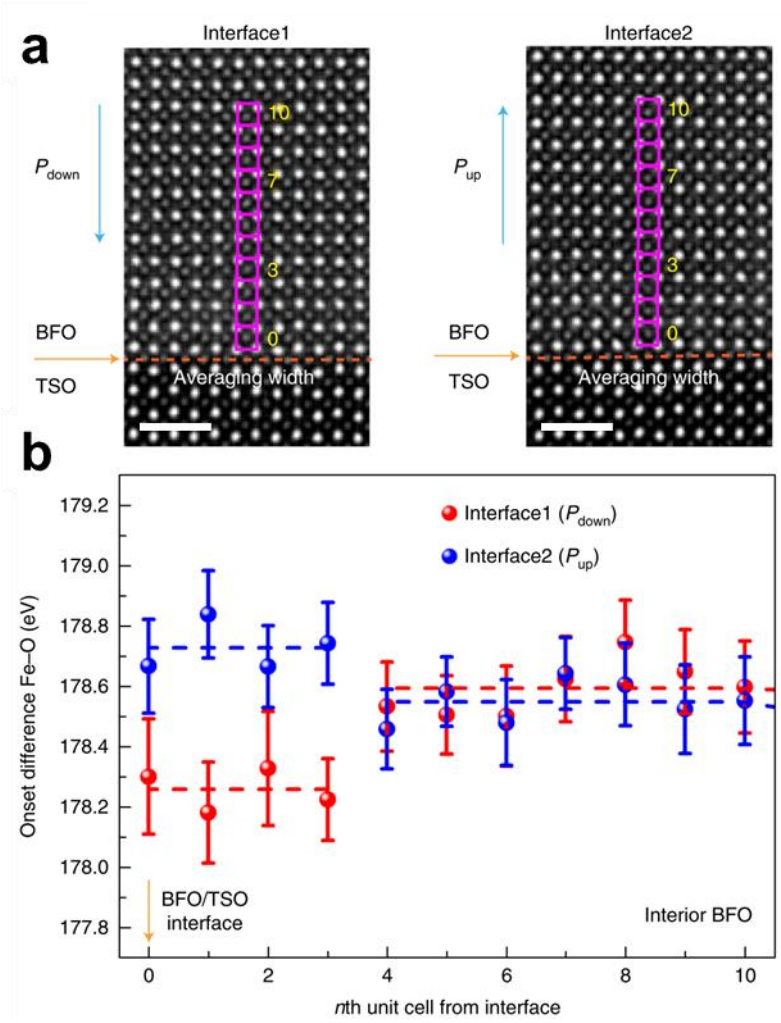

Figure 1.5 Presence of interfacial free charge discovered by probing Fe valence state. a, HAADF-STEM images obtained at the BFO/TSO interface with down and up polarizations. Scale bars denote 1 nm. **b**, Using high-loss STEM-EELS, the valence state of Fe was probed indirectly by measuring the Fe L-edge and O K-edge onset energy delta. Lower and higher delta indicate lower and higher Fe valence. A lower Fe valence signifies an accumulation of electrons while a higher Fe valence denotes the accumulation of holes. Figure is adapted from Zhang, Yi, et al. Nature nanotechnology 13.12 (2018): 1132-1136 with permission.

In general, the study of phonons in the context of ferroelectricity is needed to understand the interplay of lattice and polarization[15]. More interestingly, studying phonon properties at the two-dimensional electron gas (2DEG) and two-dimensional hole gas (2DHG) regions is an untapped field and is crucial for both fundamental scientific understanding and practical applications. In the unique environments of 2DEG and 2DHG, there can be strong coupling between phonons and charge carriers, leading to phenomena such as polaron formation and potentially influencing superconductivity.

Understanding these phonon properties can provide insights into the behavior of these two-dimensional systems and contribute to our knowledge of quantum physics, solid-state physics, and materials science. From a practical standpoint, these regions have potential applications in various electronic devices, such as transistors, sensors, and quantum computing devices[19,20]. Knowledge of phonon behavior can aid in the design and optimization of these devices, as phonons can affect device performance through mechanisms like scattering of charge carriers. Furthermore, if we can manipulate phonon properties through means like strain or electric fields, we may be able to achieve desired material properties or enhance device performance. Thus, the study of phonon properties in 2DEG and 2DHG regions is a critical aspect of modern materials science research.

Chapter 2

Methods

2.1 Scanning Transmission Electron Microscopy (STEM) and spectroscopy

Transmission electron microscopy (TEM) is an indispensable technique for materials characterization that allows us to gaze into the world of atoms. The TEM grants us access to scales that are fundamentally impossible for light-based microscopy techniques to achieve by utilizing electrons instead of light. Accelerated electrons that are focused to form a parallel beam by electromagnetic lenses are scattered by the material and collected by a detector on the other side. In contrast, a scanning TEM (STEM) utilizes a convergent, atom-wide probe of electrons that scans across the sample to generate images. If the sample is not too thick, most electrons travel through the material and reach the detector. Analysis of how electrons have been scattered by the material and how much energy they have lost is the entire endeavor of transmission electron microscopy.

STEM microscopy offers several advantages over traditional TEM. For one, it provides higher resolution and better contrast due to the use of a focused beam that can be controlled with high precision. STEM imaging can be used to study a wide range of materials, including metals, semiconductors, ceramics, and biological samples. It is particularly useful for

studying materials with complex structures or compositions, such as alloys or nanomaterials, because it can reveal details about their atomic structure and properties. The diverse distribution of post-specimen electron scattering can be analyzed spectroscopically to reveal chemical composition, electronic structure, and vibrational information at atomic scales. A combination of STEM microscopy and spectroscopy allows researchers to study materials at a resolution of less than one nanometer, providing unprecedented insight into the behavior and properties of nanoscale materials and structures. It has applications in a wide range of fields, including materials science, nanotechnology, biology, and electronics.

To perform STEM microscopy, a thin sample of the material of interest is prepared using a process called thinning, which can be done by various methods like ion milling or mechanical polishing. The sample is then loaded into the STEM instrument, which is a vacuum chamber that houses the electron source, detectors, and various lenses that focus the electron beam. The electron source generates a beam of high-energy electrons that are focused into a thin beam using electromagnetic lenses. As the beam passes through the sample, it interacts with the atoms, causing some of the electrons to scatter in different directions (Fig. 2.1a). A detector on the opposite side of the sample collects the transmitted electrons that have passed through the sample without being scattered. These electrons are converted into an electrical signal that is used to create an image. Likewise, scattered electrons can be dispersed using a magnetic spectrometer to analyze their kinetic energy distributions to reveal information about specific excitations in the material system.

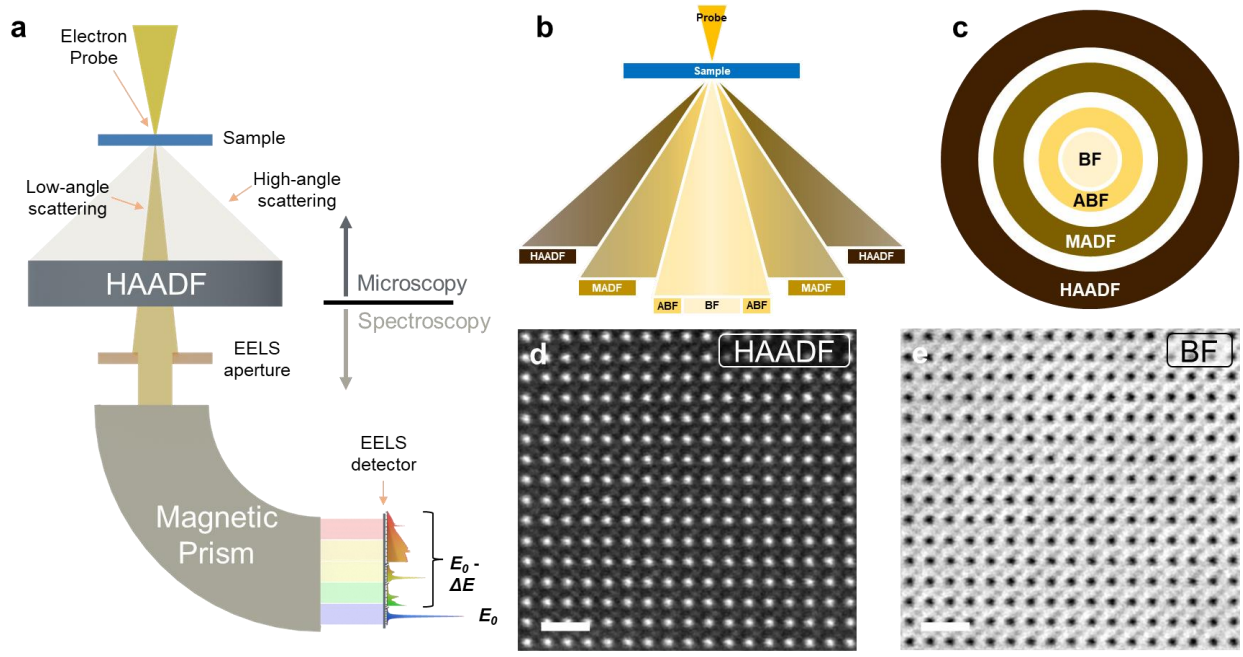

Figure 2.1 Schematic diagrams illustrating types of STEM imaging. a, Schematic of the STEM-EELS experimental setup. An electron beam is focused to form an atom-wide probe on the sample. Electrons are then elastically and inelastically scattered by the sample. High-angle scattered electrons are recorded by the high-angle annular dark field (HAADF) detector. The lower-angle scattered electrons enter the spectrometer after passing through an aperture and are then dispersed based on energy. Elastically scattered electrons form the ZLP, while inelastic electrons contribute to specific excitations in the sample. **b**, Fast electrons scattered by the sample are collected by a series of monolithic annular detectors. **c**, The arrangement of the monolithic annular detectors from a top-down view. **d**, Examples of HAADF and **e**, bright field (BF) images after low pass filtering. The scale bars are 1 nm.

STEM imaging utilizes a series of annular detectors to collect electrons scattered at various angles (Fig. 2.1b). The annular imaging detectors are usually kept at different heights in the STEM column depending on the specific alignment of the instrument. The imaging detectors form concentric rings with each capturing electrons of different scattering angles. The central detector, the bright field (BF) detector, collects weakly scattered electrons. These are electrons that scatter to very low angles or don't scatter at all and primary make up the direct, post-scattered electron beam. Annular BF detectors typically collect the outer angles of the direct beam. Images generated by both BF detectors are sensitive to phase contrast

similar to parallel-beam TEM images but are more interpretable and resistant to thickness gradients and probe focus. Both BF detectors are useful in imaging both heavy and light elements[21,22]. Electrons scattered to higher angles are collected by annular dark field (ADF) detectors. Of these, the medium angle DF (MADF) captures electrons where elastic scattering is still significant. As a result, MADF imaging is sensitive to the variations in electron diffraction. This property allows MADF imaging to be ideal for revealing defects in the sample that would normally be difficult to locate. High-angle annular DF (HAADF) detectors record electrons scattered to angles roughly 3 times the semi-angle of the direct beam. HAADF imaging is sensitive to the atomic number of atoms. That is to say, the intensity of HAADF images is proportional to the square of the atomic number. This property is very useful for imaging materials with complex compositions and is usually the imaging method of choice for high resolution STEM images. Since STEM imaging detectors are placed in an annular configuration, simultaneous imaging of both DF and BF can be performed.

STEM imaging efficiently captures information encoded in the scattering angle of the electrons scattered from the sample. It does not, however, contain any information regarding how much energy was lost by the scattered electron. This valuable information can be recovered by retracting the BF detector and letting the electrons pass through a magnetic prism. The magnetic prism disperses the scattered electrons energetically after which they land on a detector. This is known as electron energy loss spectroscopy (EELS). The magnetic prism sacrifices the scattered angle information for revealing the energy losses of the scattered electrons. The main advantage of spectroscopy in the STEM lies in its ability to combine the atomic resolution imaging capabilities afforded by an atom-wide probe and a

HAADF detector to correlate spectroscopic and real-space information. EELS will be discussed in great detail in section 2.2.

2.1.1. Specimen preparation using focused ion beams

Using electrons to probe materials instead of photons imposes specific criteria on how the specimen can be prepared. Typical TEM specimens are less than 100nm thick and are prepared such that the cross section of the bulk crystal or thin film is visible in the final specimen. Two common methods for preparing crystalline TEM samples involve either mechanically griding down a bulk material using diamond lapping film or by using focused ion beams to extract a cross-sectional lamella from the surface of a bulk or thin film material.

A thin and clean sample is vital to obtaining high quality, interpretable data. Thicker samples cause fewer electrons to make it to the detectors resulting in noisy images and spectra while samples plagued with contaminants and artifacts make precise interpretation of data problematic. Ideal sample thickness depends predominantly on kinetic energy of the beam electrons i.e., acceleration voltage the STEM is operating at. For 60kV electrons and for lighter materials like Si, a sample thickness of 30-70nm is ideal. Although the thinner the sample the better the image quality, it is generally preferrable to have enough thickness for spectroscopic purposes. In this work, Si-based samples studied were between 30-50nm in thickness while perovskite samples with heavier elements were around 20-35nm thick. This thickness allows for acceptable image quality while obtaining appreciable counts in energy loss spectra. Although the ideal thickness for obtaining optimal signal-to-noise spectra is

closer to 20-30nm for Si and 10-20nm for perovskites, it is extremely difficult to prepare samples of that thickness using focused ion beams.

I have found that, for the purposes of vibrational EELS, using focused ion beams (FIB) to prepare lamellas is superior to preparation by mechanical polishing. While mechanical polishing can produce thinner samples, they are inherently wedge shaped with typically high thickness gradients of 0.2-0.3. This thickness gradient makes the interpretation of feature-specific changes in phonon intensity, difficult to isolate and characterize. Sample preparation by FIB however is known to produce highly uniform samples with thickness gradients in the range of 0.02-0.05 with acceptable thickness for imaging and spectroscopic purposes. With the focus of vibrational EELS in mind, I will only discuss sample preparation by FIB.

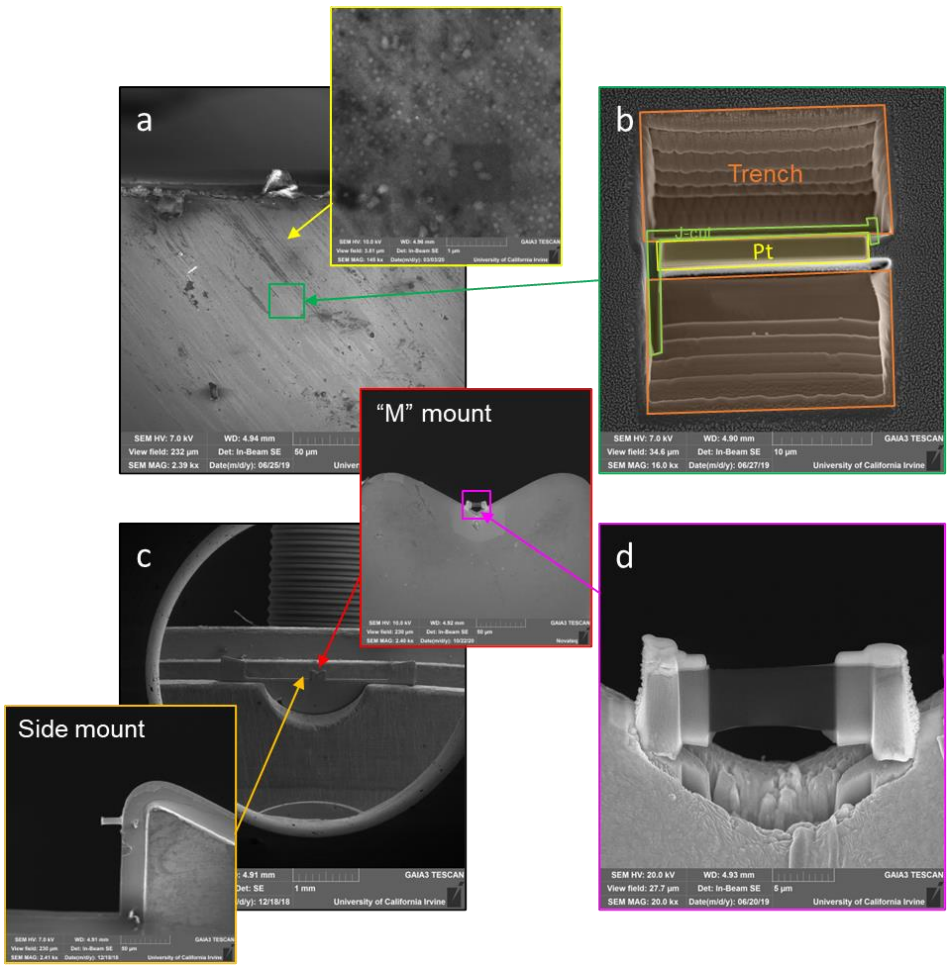

Figure 2.2 TEM sample preparation using focused ion beams. a. SEM image of bulk sample surface. Yellow inset shows a high magnification SEM image of SiGe quantum dots. **b**, Lamella preparation. First, the sample is protected by Pt deposition. The bulk sample surface is then milled away by a high current of Ga ions. When the lamella is less than 1nm thick, a "J"-cut is performed at a 55° angle to the surface of the bulk sample. **c**, FIB grid. Orange and red insets show side-mounted and "M"-mounted lamella, respectively. **d**, lamella thinned to electron transparency after multiple iterations of low kV ion milling.

Preparation of TEM samples by focused ion beams involves a combination of bombarding the surface of the bulk sample with Ga ions to create a thin cross-sectional lamella. Visual descriptions of the preparation are provided in Fig. 2.2. The studies in this dissertation utilized a Tescan Gaia SEM/FIB system to prepare FIB samples. FIB sample preparation involves first sputter coating the surface of the bulk sample with a protective coating of

either Pt or Ir. Then, in an SEM/FIB system, Pt is deposited using an electron beam followed by Pt deposition by an ion beam. In all, these three layers of deposition protect the surface of the material from Ga ions while the material around is milled. The cross-sectional lamella is trenched out from the bulk sample by Ga ions at 30kV and a current of 19na. Since the purpose of this step is to rapidly mill away material, a high current is required even if it comes at the cost of resolution. The lamella is further thinned at lower and lower currents until it is no more than 1 nm thick. Traditionally 2nm is the requirement but additional thinning at this step and higher current saves time during subsequent thinning. A "J"-cut is performed to release the thinned lamella from all sides except one. The omni probe approaches the free end of the lamella and is welded on using Pt. The fixed end of the lamella is then cut leaving the lamella to be only attached to the omni probe.

The sample is then moved using the omni probe and is Pt welded onto the grid. This can either be done on the side of the FIB grid or on the "M" and is ready for final thinning. In my experience, mounting the lamella on the "M" has significant advantages over the side mount like preventing sample bending and robust contacts. However, there is a possibility of Cu redeposition onto the lamella surface during the final thinning stage but can be cleaned by low energy milling in a nano mill. During final thinning, the lamella is rotated by $\pm 2°$ and is milled on either side by successive low voltage and current settings. The result of a successful procedure is shown in Figure 2.2.d. Thinning samples beyond 20nm requires a highly precise system and tuning of ion optics. Additionally, amorphization due to ion damage starts to become prominent. For high quality and thin samples, the Pt should be nearly milled off and the image contrast in the electron transparent area of the lamella should be dark and uniform. One should also clean the sample surface in a nanomill using 700-300eV Ar ions

preferably at liquid nitrogen temperatures. This rids the lamella surface of any ion damage and surface amorphization as well as Cu redeposition from the FIB grid.

Thin film specimens are generally prepared such that the film cross-section will be visible in the final specimen. Both the conventional method involving mechanical polishing followed by low energy ion milling and FIB preparation can produce high quality specimens with their own advantages. In the mechanical polishing process, a section of the thin film (approximately 5 mm square) is first glued to a piece of sacrificial silicon and then polished into a wedge with a shallow angle such that the silicon is slowly polished away using successively smoother lapping films until the specimen is as thin as possible while avoiding any cracking. Then the specimen is transferred to a low energy Ar ion milling system, Gatan PIPS II, and thinned to electron transparency [53]. In the FIB preparation process, a small section of the thin film (approximately 20 μm width x 2 μm height x 10 μm deep) is cut out of the surface of the film and mounted to a copper grid using the FIB. The grid is then rotated such that the thin film is facing the ion beam head-on and the 2 μm height is milled away until the sample is electron transparent [54].

Mechanically polished samples generally have the advantage of resulting in a large cross-section of the film being electron transparent, and thus accessible for imaging. The thickness along the beam direction can vary from less than 5 nm at the center of the ion milled region to over 100 nm at the edges. Since the sample is prepared as a wedge, the thinnest regions will always appear closer to the film surface. The large initial size of the mechanically polished specimen and broad thickness variability means that a wide variety of microscopic structures are present in the specimen. This makes it difficult to tell what these structures

are prior to completing the sample as there is little microscopic control over exactly which region the sample is cut from. In contrast, FIB specimens can be made with uniform thickness along the beam direction and the SEM/FIB can be used to select specific features/regions to include in the sample. However, it is difficult to make a FIB specimen less than 20 nm thick without the ion beam causing considerable damage, precluding their use for a variety of advanced S/TEM techniques that require very thin samples. In the imaging of electronic properties, many techniques require specimens to be 5-10 nm thick along the beam direction. Therefore, all specimens used in this work were prepared by mechanical polishing and low energy ion-milling.

2.1.2 Electron scattering

In a scanning transmission electron microscope (STEM), a beam of electrons is focused to a small probe size and scanned over a sample, allowing for high-resolution imaging and analysis of the sample's structure and composition. The fast electrons interact with the material and can lose energy and change direction. In a crystalline material, post-specimen scattering electrons generate an electron diffraction pattern that provides a wealth of information about the structure of the material. At the diffraction plane, annular detectors are placed to capture electrons at various angles. This is one of the main ways that imaging information is gathered in STEM. Understanding how electrons are distributed in the diffraction, or scattering plane is central to using them to understand material properties. This section focuses on post-specimen scattering of electrons and how their momentum and kinetic energy are changed upon interaction with the material.

It is most straightforward to first classify types of electrons scattering in terms of energy exchange between the fast electrons and the material. Fast electrons in the electron beam can either pass through the material having lost no energy or having lost some energy i.e., elastic scattering or inelastic scattering, respectively. Electrons elastically scatter in a material when they interact with atoms and lose no energy. Although there is no energy exchange between the fast electron and the material, fast electrons may still undergo a change in momentum. In crystalline materials, this is usually referred to as Bragg scattering and is responsible for the bright, localized spots in electron diffraction. Inelastic scattering, on the other hand, occurs when the electrons in the beam transfer a portion of their energy to the material's atoms, resulting in the electrons being scattered away from the beam axis. This type of scattering can be used to gather information about the sample's chemical composition and bonding using EELS. Both cases are governed by the conservation of energy and momentum.

$$W = \gamma m_0 c^2 \tag{2.1}$$

$$\boldsymbol{p} = \gamma m_0 \boldsymbol{v} = \hbar \boldsymbol{k}_0 \tag{2.2}$$

Together, eq. 2.1 and 2.2 gives the total relativistic energy as a function of relativistic momentum:

$$W^2 = (m_0 c^2)^2 + (\boldsymbol{p}c)^2 = (m_0 c^2)^2 + (\hbar \boldsymbol{k}_0 c)^2 \tag{2.3}$$

Using conversation of energy, we have:

$$W - E = W_1 = \sqrt{(m_0 c^2)^2 + (\hbar \boldsymbol{k}_1 c)^2} \tag{2.4}$$

Where W_1 and k_1 are the total energy and wavenumber of the scattered electron. E represents the energy loss of the scattered electron. Expanding Eq. 2.4 using Eq. 2.3 results in an expression that describes the change in momentum of the scattered electron as a function of its energy loss:

$$\boldsymbol{k_1}^2 = \boldsymbol{k_0}^2 - \frac{2\gamma m_0 E}{\hbar^2} + \frac{E^2}{(\hbar c)^2} = \boldsymbol{k_0}^2 \left[1 + \left(\frac{E}{\boldsymbol{p}\, c}\right)^2 \left(1 - \frac{2W}{E}\right)\right] \tag{2.5}$$

It should be noted that this relationship is independent of the scattering angle θ as well as the scattered momentum q. In order to form a relationship that involves the scattering angle, the scattering geometry must be considered (Fig. 2.3). Momentum conservation gives us:

$$\boldsymbol{q} = \boldsymbol{k_0} - \boldsymbol{k_1} \tag{2.6}$$

The scattering geometry from Fig. 2.3 relates momentum transfer q to angle of deflection θ:

$$\boldsymbol{q}^2 = \boldsymbol{k_0}^2 + \boldsymbol{k_1}^2 - 2\boldsymbol{k_0}\boldsymbol{k_1}\cos\theta \tag{2.7}$$

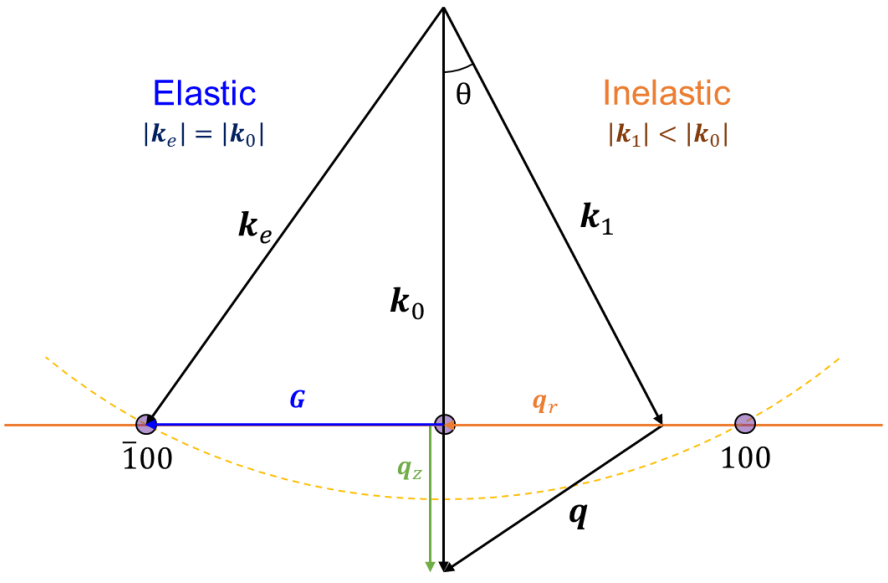

Figure 2.3 Kinematical scattering geometry. Inelastic scattering is depicted with momentum k_1 of the scattered electron. Momentum transfer occurs in the in-plane (q_r) and out-of-plane (q_z). Elastic scattering is illustrated with momentum k_e of the scattered electron. Here, q_r is

the reciprocal lattice vector G for the in-plane momentum transfer. The yellow dashed curve represents the Ewald sphere which defines the different values of q and θ possible for a given value of k_1. The purple markers indicate Bragg peaks which are locations of Brillouin zone (BZ) zone centers.

Although Fig. 2.3 suggests that energy loss always involves a finite scattering angle, this is not necessarily the case. Setting θ to 0 in Eq. 2.7 and simplifying, gives us the expression for the minimum momentum transfer q_{min} which lies in the out-of-plane direction:

$$\boldsymbol{q}_z = \boldsymbol{q}_{min} = \boldsymbol{k}_0 - \boldsymbol{k}_1 \tag{2.8}$$

All vectors in Eq. 2.8 lie in the out-of-plane direction and as such, Eq. 2.7 also holds for their respective magnitudes. Solving for q_z gives us a relationship between the minimum momentum transfer and then energy loss of the electron:

$$\boldsymbol{q}_{min} = \boldsymbol{k}_0 \left[1 - \sqrt{1 + \left(\frac{E}{\boldsymbol{p}\, c}\right)^2 \left(1 - \frac{2W}{E}\right)} \right] \tag{2.9}$$

Since E" W, we can use binomial expansion to obtain an approximation for Eq. 2.8. Ignoring quadratic and higher powers of E, we have:

$$\boldsymbol{q}_{min} = \boldsymbol{k}_0 \left(\frac{E}{\gamma m \boldsymbol{v}^2}\right) = \boldsymbol{k}_0 \theta_E \tag{2.10}$$

Where θ_E is called the characteristic scattering angle. For 60 keV electrons, an energy loss ranging from 0.1-1000 eV gives a range of 8.6×10^{-7} to 8.6×10^{-3} for typical energy losses. The small energy and momentum transfers justify the use of the approximations above. In the same vein, we can write Eq. 2.5 in its approximated form:

$$\boldsymbol{k}_1 \approx \boldsymbol{k}_0 (1 - \theta_E) \approx \boldsymbol{k}_0 \tag{2.11}$$

Inserting Eq. 2.5 and Eq. 2.11 into Eq. 2.7 gives us an approximated expression for momentum transfer $\boldsymbol{q}$:

$$\boldsymbol{q}^2 \approx {\boldsymbol{k}_0}^2 + {\boldsymbol{k}_0}^2(1-\theta_E)^2 - 2{\boldsymbol{k}_0}^2(1-\theta_E)\left(1-\frac{\theta^2}{2}\right) \tag{2.12}$$

Here we will only retain up to the second order in θ to get:

$$\boldsymbol{q}^2 \approx {\boldsymbol{k}_0}^2(\theta^2 + {\theta_E}^2) \tag{2.13}$$

Although several approximations have been used to obtain Eq. 2.12, the approximation only underestimates the exact value of $\boldsymbol{q}$ by 0.4%! Again, the extremely small momentum and energy exchanges that occur in typical scattering events allow us to make these approximations. The in-plane ($\boldsymbol{q}_r$) and out-of-plane ($\boldsymbol{q}_z$) momentum are also obtained with the same approximations:

$$\boldsymbol{q}_r \approx \boldsymbol{k}_1\theta \approx \boldsymbol{k}_0(1-\theta_E)\theta \approx \boldsymbol{k}_0\theta \tag{2.14}$$

$$\boldsymbol{q}_z \approx \boldsymbol{q}_{min} + \boldsymbol{k}_0(1-\theta_E)\frac{\theta^2}{2} \approx \boldsymbol{q}_{min} \approx \boldsymbol{k}_0\theta_E \tag{2.15}$$

The elastic case is easily derived from the equations for inelastic scattering. With E=0 and $\mathbf{k}_0=\mathbf{k}_1$, Eq. 2.7 becomes:

$$\boldsymbol{q} = 2\boldsymbol{k}_0 \sin\frac{\theta}{2} \tag{2.16}$$

We can derive the Bragg law by considering the scattering geometry of an off-axis Bragg spot (Fig. 2.3) with $\mathbf{q}_z \approx 0$, $G=2\pi/d$, and $\mathbf{k}_0 = 2\pi/\lambda$:

$$\lambda = 2d \sin\Phi \tag{2.17}$$

G is the reciprocal lattice vector, d is the lattice spacing, λ is the wavelength of the fast electron, and Φ is the semi-angle. Rigorously speaking, $\boldsymbol{q}_z$ is small but not 0, even in elastic scattering. As a result, the Bragg equation is an approximation that assumes that fast electrons are plane waves.

When an electron diffracts from a crystal lattice, it interacts with the periodic potential of the crystal and its momentum changes according to Bragg's law. The momentum transfer can be decomposed into components perpendicular (out-of-plane) and parallel (in-plane) to the crystal lattice planes. For an off-axis Bragg spot, the momentum transfer of the electron has both in-plane and out-of-plane components. The in-plane component is responsible for the diffraction of the electron and determines the position of the Bragg spot on the diffraction pattern. The out-of-plane component, on the other hand, does not contribute to the diffraction and is usually referred to as the rocking curve. The rocking curve describes the variation in the intensity of the Bragg spot as a function of the angle of incidence of the electron beam with respect to the crystal lattice planes. The width of the rocking curve depends on the crystal imperfections such as defects, strain, and thickness variations. In a perfect crystal, the rocking curve would be infinitely narrow, meaning that all the electrons would be diffracted into a single Bragg spot. However, in a real crystal, the rocking curve is broadened due to the imperfections, which leads to the spread of the diffraction pattern in the out-of-plane direction.

Until now the properties of the scattering were not considered. In general, scattering is probabilistic and dependent on not only the incident angle and momentum of the fast electron but also on the electrical potential of the scatter. This information is encoded in the

differential scattering cross-section which describes probabilities of scattering. The effort to compare calculation with experiment necessitates the inclusion of the effects of the scattering media. However, only a brief discussion of specific formalisms will be given, and tedious algebra and calculus will be omitted. For a more complete derivation of subsequent formulas, the reader is directed to Ref.[23]. First, we derive the scattering cross-section of elastic scattering from an atom. For a scattering nucleus, the scattering cross-section is given by:

$$\frac{\mathrm{d}\sigma}{\mathrm{d}\Omega} = \frac{4\gamma^2 Z^2}{{a_0}^2 q^4} \tag{2.18}$$

Where $\mathrm{d}\sigma/\mathrm{d}\boldsymbol{\Omega}$ is the differential scattering cross-section, a_0 is the Bohr radius, and Z is atomic number. The rest of the variables are the same as defined previously. Although simple, it does not consider complex properties of the atom such as how the valence electron density screens the nuclear potential. This can be done by the inclusion of a screening potential such as a Wentzel or Yukawa model[23] that describes the effects of the potential as a function of distance r to its center:

$$\Phi(\boldsymbol{r}) = \frac{Ze}{4\pi\varepsilon_0 r} e^{-\frac{\boldsymbol{r}}{r_0}} \tag{2.19}$$

This leads to a differential scattering cross section that has an angular distribution:

$$\frac{\mathrm{d}\sigma}{\mathrm{d}\Omega} = \frac{4\gamma^2}{{a_0}^2}\left(\frac{Z}{\boldsymbol{q}^2 + {\boldsymbol{r}_0}^{-2}}\right) \approx \frac{4\gamma^2 Z^2}{{a_0}^2 {\boldsymbol{k}_0}^4}\left(\frac{1}{\left(\theta^2 + {\theta_0}^2\right)^2}\right) \tag{2.20}$$

Here, θ_0 is a characteristic angle of elastic scattering. The angular dependence mimics the form of Eq. 2.13 scaled by the scattering factor from the coulomb potential. Eq. 2.20 suggests that the probability of scattering is higher for heavier atoms which is intuitive since one

would expect stronger fields to change the trajectory of the fast electron. In contrast, faster electrons are scattered less, presumably since they spend less time in the field. Eq. 2.20's θ^{-4} dependence on angle suggests that scattering probability is peaked for electrons that do not get deflected and falls off rapidly for higher angles.

For inelastic scattering, a more detailed theory than basic angular and wavevector dependence will be covered. Bethe's theory describes the interaction between a high-energy electron and a target atom or molecule. The theory considers the energy loss of the electron as it collides with the target and transfers energy to its atomic or molecular constituents.

Bethe's theory of inelastic electron scattering has been widely used in experimental studies of materials, such as in electron energy loss spectroscopy (EELS) and scanning transmission electron microscopy (STEM). The theory has helped to elucidate the electronic and structural properties of materials at the atomic and molecular scale, and it continues to be a valuable tool for researchers in condensed matter physics and materials science[24].

Bethe's theory provides a way to calculate the cross section for inelastic electron scattering, which is a measure of the probability that an electron will scatter inelastically off a target. The cross section depends on the energy of the incident electron, the properties of the target, and the details of the scattering process.

For core-shell losses, the behavior of each atomic electron is specified in terms of transitions. The core electron begins in its initial state ψ_0 and is excited to a subsequent state ψ_n by the fast electron. Using the born approximation, the differential scattering cross section for core-shell losses is given by:

$$\frac{d\sigma}{d\Omega} = \left(\frac{m_0}{2\pi\hbar^2}\right)\frac{\boldsymbol{k}_1}{\boldsymbol{k}_0}\left|\int V(\boldsymbol{r})\,\psi_0\psi_n{}^* e^{i\boldsymbol{q}\cdot\boldsymbol{r}} d\tau\right| \tag{2.21}$$

For inelastic scattering, knowledge of the various states in the media are necessary in order to figure out what the fast electron is giving energy to. A potential that encompasses coulombic forces of the nucleus as well as repulsive effects from each atomic electron is given by:

$$V(\boldsymbol{r}) = \frac{e^2}{4\pi\varepsilon_0}\left(\frac{Z}{\boldsymbol{r}} - \sum_{j=1}^{Z}\frac{1}{|\boldsymbol{r}-\boldsymbol{r}_j|}\right) \tag{2.22}$$

Here r_j is the location of the jth electron. Inserting Eq. 2.22 into Eq. 2.21 gives:

$$\frac{\mathrm{d}\sigma_n}{\mathrm{d}\Omega} = \frac{4\gamma^2 R}{E_n q^2}\frac{\boldsymbol{k}_1}{\boldsymbol{k}_0} f_n(\boldsymbol{q}) \tag{2.23}$$

Where f_n represents the generalized oscillator strength (GOS) of the target atom for the transition with an associated energy change E_n. It is related to the inelastic form factor ε_n:

$$f_n(\boldsymbol{q}) = \frac{E_n}{R}\frac{|\varepsilon_n(\boldsymbol{q})|^2}{(\boldsymbol{q}\,a_0)^2} = \frac{E_n}{R}\frac{1}{(\boldsymbol{q}\,a_0)^2}\left|\langle\psi_n|\sum_j e^{i\boldsymbol{q}\cdot\boldsymbol{r}}|\psi_0\rangle\right|^2 \tag{2.24}$$

Here, R is the Rydberg energy, R=13.6 eV. For small defections of the scattered electron, f_n reduces to the dipole oscillator strength which describes atomic response to optical stimuli. Eq. 2.23 can be generalized to ionization transitions to a continuum of states:

$$\frac{d^2\sigma_n}{d\Omega dE} = \frac{4\gamma^2 R}{Eq^2}\frac{\boldsymbol{k}_1}{\boldsymbol{k}_0}\frac{d}{dE} f_n(\boldsymbol{q},E) = \frac{4\gamma^2 R}{E\boldsymbol{k}_0{}^2}\left(\frac{1}{\theta^2+\theta_E{}^2}\right)\frac{df}{dE} \tag{2.25}$$

Eq. 2.25's angular dependence goes as θ^{-2} compared to θ^{-4} for elastic scattering suggesting that inelastic scattering has a broader angular distribution and is more probable than elastic scattering at higher angles.

The discussion thus far has been adequate for building intuition about energy loss, momentum transfer, and scattering angle using relatively simple but instructive models and approximations. As a result, these models do not capture the intricate physics of continuous media or its correlated effects. Additionally, each type of excitation has its own scattering cross-section which requires a separate set of assertions. For example, vibrational excitations depend on how the phonons are distributed in terms of wavelength and frequency. This, combined with the periodicity and general local structure of the material, determines the shape of the vibrational energy loss spectrum. The inelastic cross-section for phonon excitations in a periodic lattice is given in the next chapter. The next section of this chapter discusses methods involving how these excitations are measured.

2.2 Electron Energy Loss Spectroscopy

As discussed in the previous section, fast electrons undergo elastic and inelastic scattering upon interacting with the sample. By measuring how much energy the electrons have lost to the material, we can obtain information about specific excitations in the material system. This is the entire endeavor of electron energy loss spectroscopy (EELS).

EELS is a powerful analytical tool that analyzes the energy loss of electrons as they pass through a thin sample and interact with the atoms in the material. The energy loss can be a result of the transfer of kinetic energy from the electron beam to the inner-shell electrons, electron gases, electronic transitions, ionization, and vibrations of the atoms in the material. about the chemical composition and bonding states of the material, as well as information about the valence band and conduction band energy states, the density of states, and the

energy gaps between bands. When combined with the spatial resolution of STEM, EELS can provide broadband spectroscopic information at the nano and even atomic scales giving it several advantages over other conventional spectroscopic techniques such as Raman, IR, neutron, UV, and X-ray spectroscopies to name a few. As a result, it is widely used in materials science, physics, chemistry, and biology to study a variety of materials, including metals, ceramics, polymers, and biological samples.

Originally, EELS was developed as a technique for analyzing energy losses of electrons that have been reflected from material surfaces at glancing incidences known as high resolution EELS (HREELS). This scattering geometry usually involves the scattering of low primary energy electrons (0.1-10 keV) from a bulk sample's surface where the interaction is limited to a few atomic layers after which they enter a spectrometer to be energetically dispersed[25,26]. The kinetic energy of these primary electrons is much lower than those used in intersecting geometries due to their lack of penetration depth. Although this results in a poor spatial resolution of tens of nanometers, an energy resolution of 1-2 meV has been achieved enabling the direct detection of surface phonons.

In transmission EELS, as in the TEM or STEM, primary electrons are incident perpendicular to a thin sample ($<$100 nm) with a much higher kinetic energy ($>$30eV) allowing them to transmit through the sample with negligible reflection and absorption. A portion of these transmitted electrons subsequently enter a spectrometer which disperses them energetically before they are collected by a detector. In a parallel-beam configuration as in the TEM, energy-filtered TEM (EFTEM) images can be formed by using electrons of a specific energy bin to generate real-space images[27]. In a convergent-beam configuration as in the

STEM, a sub-angstrom sized electron probe is scanned across a defined region resulting in pixel-by-pixel acquisition, wherein an entire EEL spectrum is recorded at each probe position along with a simultaneous HAADF image.

2.2.1 EELS Spectrometer

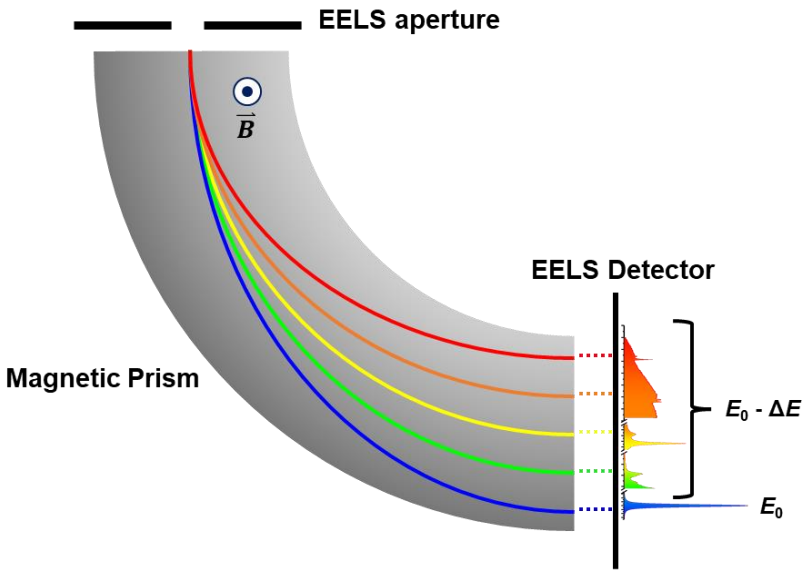

Fig. 2.4. Energy dispersion in an EELS spectrometer. The lower-angle scattered electrons enter the spectrometer with a typical collection semi-angle of $\beta = 25$ mrad and are dispersed based on kinetic energy by a strong magnetic field perpendicular to the scattered electron path. Elastically scattering electrons form the ZLP while inelastically scattered electrons represent energy losses from inner-shell electrons, electron gases, electronic transitions, ionization, and vibrations of the atoms in the material. Electrons that have undergone no energy loss (blue) are deflected the least by the magnetic field while electrons that have undergone high energy loss (red) are deflected the most.

Before the electron beam is incident on the material, their kinetic energy distribution lies tightly around the high tension (HT) value, or acceleration voltage value. This energy spread is due to the energy distribution of electrons ejected by cold field emission. For non-monochromated systems, this is about 0.5% of the acceleration voltage or about 300 meV.

In the nion microscope, monochromation produces an even tighter energy distribution with only a 0.01% spread or 6meV. After scattering, electron energy loss to the material creates a diverse distribution of kinetic energies which are dispersed by a powerful magnetic field (Fig. 2.4). The magnetic field causes electrons to undergo a curved trajectory of which the radius is a function of the velocity:

$$R = \frac{\gamma m_e}{e\,B} v \tag{2.1}$$

The radius R is a monotonic function of the electron velocity v and its linear relationship is scaled by the relativistic factor $\gamma = 1/(1-v^2/c^2)^{1/2}$, the electron mass m_e, electron charge e, and magnetic field strength B. Since typical energy losses observed are between 0 and 2000eV, about 0-3% of the primary energy, a strong magnetic field is required to appreciably disperse the electrons by their velocities. This presents an easily digestible but oversimplified view of electron deflecting in an EELS spectrometer. A more accurate picture, however, is fairly complex and involves consideration of focusing mechanisms and lens aberrations. In order to understand the nature of the focusing and its relation to energy dispersion and resolution, a proper first order treatment is given in the following paragraphs.

Fundamentally, a magnetic prism spectrometer bends, disperses, and focuses fast electrons. Of these, focusing is of prime importance as the attainable energy resolution depends on the width of the exit beam at the dispersion plane. First-order theory is used to predict object and image distances, image magnifications, and dispersive power, while second- or higher-order analysis is needed to describe image aberration and distortion, and other properties such as the dispersion-plane tilt[23]. The simplistic view presented in Fig. 2.4. assumes a

constant, uniform magnetic field that exists only in the spectrometer. That is to say, only the dispersive aspect of the spectrometer is portrayed. However, even if the field is assumed to be constant in time and uniform in space, there still exist fringing fields at the edges of the spectrometer that cause non-negligible effects on the trajectory of electrons. Fig. 2.4 also does not consider the angular distribution of electrons entering the prism. Realistically in a STEM, there are a series of lenses that converge, diverge and in general manipulate the trajectory in all three spatial dimensions. Even first order effects must take these factors into account to obtain transformations to the electron beam.

Due to the complex nature of the electron path in this setup, approximations have to be employed to make the problem tractable. If the magnetic field is assumed to be constant up to the polepiece edges, the trajectory of electrons is simplified by employing the sharp cutoff fringing field (SCOFF) approximation. It is mainly useful for the first-order analysis of focusing in a magnetic prism spectrometer; therefore, it may not fully capture higher-order EELS aberrations. The EFF model allows for a more accurate prediction of spectrometer focusing by specifying the z-dependence of field strength adjacent to the magnet boundaries with one or more coefficients, but it is still a first-order model, so it cannot fully describe higher order EELS aberrations without additional analysis. The discussion of higher order spectrometer aberrations is beyond the scope of this dissertation due to its complexity. The reader is instead directed to Ref. [23]. In the next paragraph, first order transformations of the electron trajectory in the spectrometer path will be covered as they are the dominant factors in creation of the electron image, or spectrum, at the detector plane.

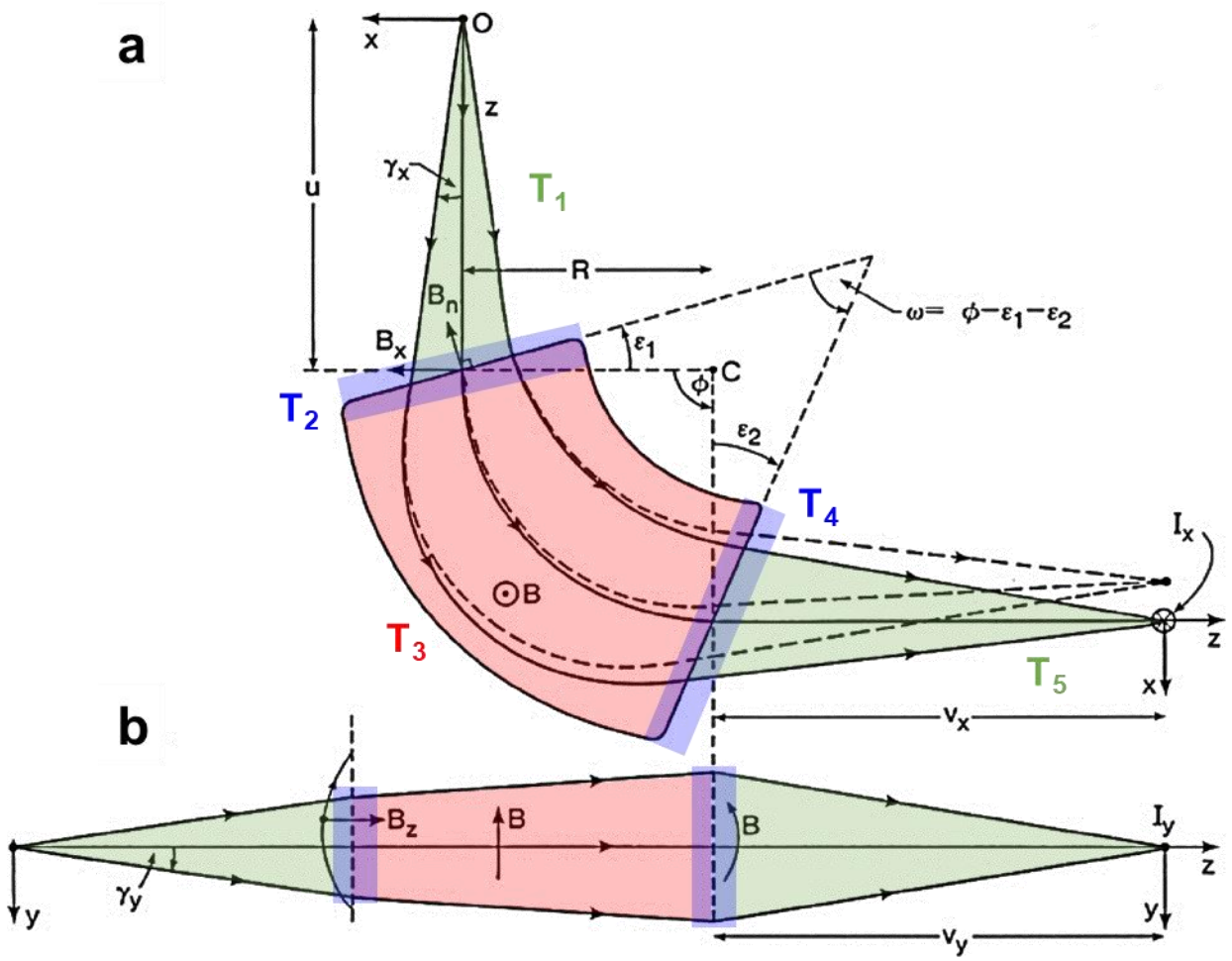

Fig. 2.5. Focusing and dispersive properties of a magnetic prism. a, Radial focusing in the x–z plane (the first principal section). The coordinate system rotates with the electron beam, so the x-axis always represents the radial direction and the z-axis is the direction of motion of the central zero-loss trajectory (the optic axis). **b**, Axial focusing in the *y*–*z* plane (a flattened version of the second principal section). The trajectories of electrons that have lost energy are indicated by dashed lines and the normal component B_n of the fringing field is shown for the case $y > 0$. Figure is adapted from Electron Energy-Loss Spectroscopy in the Electron Microscope by R. F. Egerton with permission.

Fig. 2.5. presents a more accurate picture of the bending, dispersing, and focusing actions of the spectrometer system. The entire electron trajectory can be separated into 5 sections including field-free, fringe field, and spectrometer regions. It is instructive to look at components of the electron trajectory at each region separately to understand what

transformations are occurring and how they relate to bending, dispersing, and focusing actions. Electrons start at a singular point **O** with a range of angular distributions.

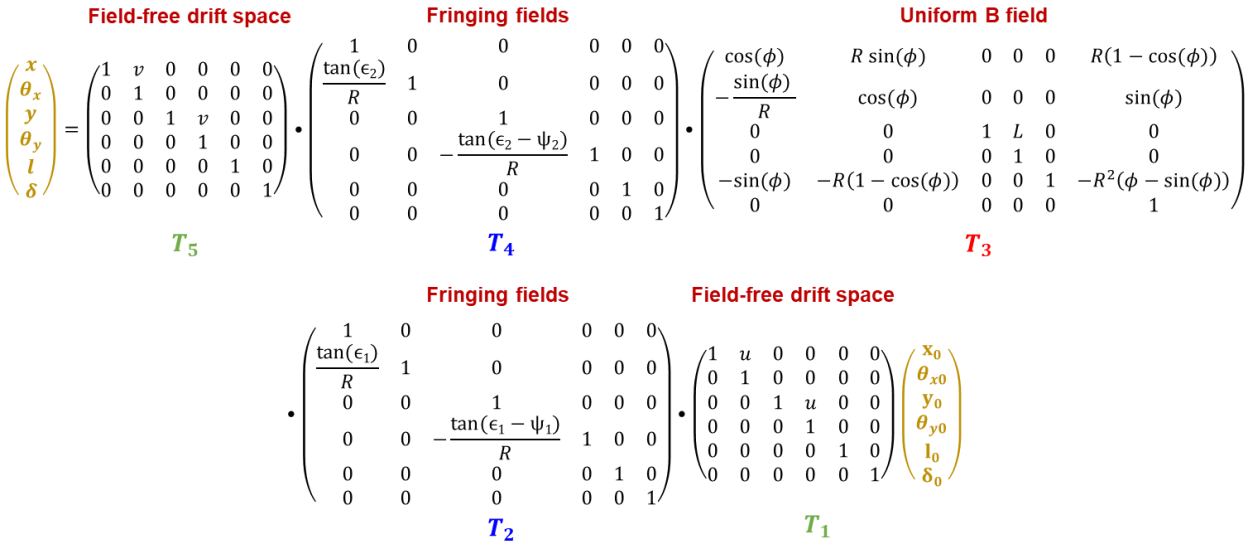

Fig. 2.6. First order transfer matrices of electron trajectory through an EELS spectrometer setup. 6×6 matrices describing transformations of electron linear and angular positions as well as total travel distance and fraction momentum deviation. Under first order approximations, the electron encounters 5 distinct regions on its way to the imagining plane. The electrons encounter a field-free drift space from the pole-piece to spectrometer entrance, then fringing fields at the spectrometer entrance, then a constant, uniform B field in the spectrometer, fringing fields again at the spectrometer exit, and finally a field-free drift space from the spectrometer exit to the imaging plane. The column vectors in green represent the final and initial states of the fast electron. By multiplying all the matrices together, one obtains the fully transformed trajectories of fast electrons through an EELS spectrometer setup.

They first travel through a field-free drift space, denoted in green labeled as T_1 in Fig. 2.5, where the only change to their trajectory is due to their initial angular distribution.

$$\begin{pmatrix} x_0 + u\,\theta_{x0} \\ \theta_{x0} \\ y_0 + u\,\theta_{y0} \\ \theta_{y0} \\ l_0 \\ \delta_0 \end{pmatrix} \tag{2.2}$$

Only the linear position variables are modified based on how the electron velocities are pointing at point **O**. If we assume no convergence like in Fig. 2.4, the field-free region does not change electron positions as expected.

At the entrance edge of the spectrometer, electrons encounter fringing fields that are non-negligible in magnetic and extend slightly outside of the spectrometer. This $\boldsymbol{B}$ field has components in all three dimensions: an out of the page component denoted as $\boldsymbol{B_n}$, a component pointing radially away from point **C** labeled as $\boldsymbol{B_x}$, and finally a component parallel to the electron trajectory denoted as $\boldsymbol{B_z}$. The first-order effect of this field only affects the angular component of the electrons' trajectory while their distance from the optic axis and path length unchanged:

$$\begin{pmatrix} x_0 \\ x_0 \dfrac{tan(\epsilon_1)}{R} + \theta_{x0} \\ \text{y0} \\ -y_0 \dfrac{tan(\epsilon_1 - \psi_1)}{R} + \theta_{y0} \\ l_0 \\ \delta_0 \end{pmatrix} \tag{2.3}$$

The electrons encounter a focusing action of the fringing fields at the tilted edge of the spectrometer. This can be seen from how the linear positions remain unchanged while only the angular trajectories are affected where ε_1 refers to the tilt of the entrance face of the spectrometer. These factors are calculated using the SCOFF approximation producing a

focusing of equal magnitude but opposite sign. The y-z plane focusing is modified using the EFF approximation with a correction ψ_1 for the y component of the angular trajectory:

$$\psi_1 = \frac{g}{R}\frac{K_1\left(1+\sin^2(\epsilon_1)\right)}{\cos(\epsilon_1)} \tag{2.4}$$

Where K_1 is:

$$K_1 = \int_{-\infty}^{\infty} \frac{B_y(z')(B - B_y(z'))}{gB^2} dz' \tag{2.5}$$

The shape parameter K_1 accounts for the effect of fringing fields as a function of the pole-piece gap g. Depending on how large the polepiece gap and the strength of the fringing field, a second parameter K_2 may be needed to accurate describe their effect on the electron trajectory. The SCOFF approximation amounts to K_1=0.

The constant and uniform magnetic field in the spectrometer amounts to a dipole field and bends electrons differently according to how far they are from the optic axis. For brevity let us assume Φ=0 making the spectrometer a sector magnet. Then the transformed coordinates become:

$$\begin{pmatrix} R\delta_0 + R\theta_{x0} \\ -\frac{x_0}{R} + \delta_0 \\ y_0 + L\theta_{y0} \\ \theta_{y0} \\ l_0 - x_0 - \left(-1+\frac{\pi}{2}\right)R^2\delta_0 - R\theta_{x0} \\ \delta_0 \end{pmatrix} \tag{2.6}$$

This focusing action occurs only in the x-z plane leaving the angular y-component unchanged as expected. This can be seen in the transformed parameters where the angular trajectory in the y-z plane is unchanged. In the x-z plane, the electrons disperse based on the dispersive

power of the spectrometer and their path radius which is a function of electron velocity. The path length of an electron that has lost energy will be less than that of a zero-energy-loss electron l_0 as expected. This path length is a function of how far the energy-loss electron is from the optic axis (path of the zero-energy-loss electrons), its path radius, angular trajectory, and dispersive power of the spectrometer. Although this parameter is not needed for calculating dispersive properties of the spectrometer, it is useful for electron time-of-flight measurements as a function of energy loss.

The first-order trajectory of the electron beam is obtained upon multiplying the 5 matrices in Fig. 2.6 together:

$$T_5 \bullet T_4 \bullet T_3 \bullet T_2 \bullet T_1 = \begin{pmatrix} R_{11} & R_{12} & 0 & 0 & 0 & R_{16} \\ R_{21} & R_{22} & 0 & 0 & 0 & R_{26} \\ 0 & 0 & R_{33} & R_{34} & 0 & 0 \\ 0 & 0 & R_{43} & R_{44} & 0 & 0 \\ R_{51} & R_{52} & 0 & 0 & 1 & R_{56} \\ 0 & 0 & 0 & 0 & 0 & 1 \end{pmatrix} \tag{2.7}$$

Several of these components are relevant to the way the final EEL spectrum appears on the detector. At the x-z focusing plane, $R_{12}=0$ represents optimal energy resolution. In general, spectrometers are not double-focusing and so focus in the y-z plane is not zero. That is to say, R_{34} represents the length of the line focus in the y-direction is not necessarily equal to 0. The energy dispersion of the spectrometer setup is related to R_{16} by

$$D = \frac{\partial x}{\partial E} = \frac{R_{16}}{2\gamma T} = \left(\frac{R}{2\gamma T}\right) \frac{\sin\Phi - (1-\cos\Phi)(\tan\epsilon_1 + {}^{R}/_{u})}{\sin\Phi\left[1 - \tan\epsilon_2\left(\tan\epsilon_1 + {}^{R}/_{u}\right)\right] - \cos\Phi\left(\tan\epsilon_1 + \tan\epsilon_2 + {}^{R}/_{u}\right)} \tag{2.8}$$

These three terms in the R matrix of Eq. 2.7 represent the most relevant parameters for one acquiring EELS and require careful consideration of first-order effects. Determining optimal focusing and energy resolution can be done by considering the shape of the beam at the

detector plane. Proper first order focusing is achieved when the width of the beam along the energy axis is brought to a minimum. Under a double-focusing condition where $\varepsilon_1 = \varepsilon_2$, the beam width also approaches a minimum in the y direction resulting in a point-like or circle-like beam shape on the detector. However, in most cases, the spectrometer is not double focusing and so the beam appears as a thin vertical line on the detector where the horizontal and vertical directions are the energy dispersed and undispersed directions.

First-order F_x and F_y aberrations are dominant factors in energy resolution and generally worsen on a shorter timescale than higher order aberrations. As a result, these aberrations are routinely tuned in an effort to focus the beam to a single vertical line on the detector. This is especially true for monochromated experiments where energy resolution is of paramount importance.

2.2.2 EEL Spectrum

An electron that becomes part of the energy loss spectrum begins its 20-nanosecond journey at the gun tip. From there its trajectory is bent by several magnetic fields until it reaches a thin TEM specimen. If it makes it through, chances are it didn't even notice there was something in the way. If it instead bounces off something inside the specimen, it likely finds itself to be slowed and pushed slightly from its initial trajectory. Once again, it encounters several magnetic fields that redirect its course slightly until finally it finds itself captured by a pixel of a charge coupled device. Essentially, the journey of the electron through the column of a STEM involves being slowed and slightly redirected. However, we can obtain a wealth of information from the specimen solely based on how much slower the electrons got having

passed through the thin material. The process of how electrons of various speeds are organized and dispersed was covered in the previous section. In this section, the focus will be on understanding what different ranges of energy losses reveal about the physics in the material.

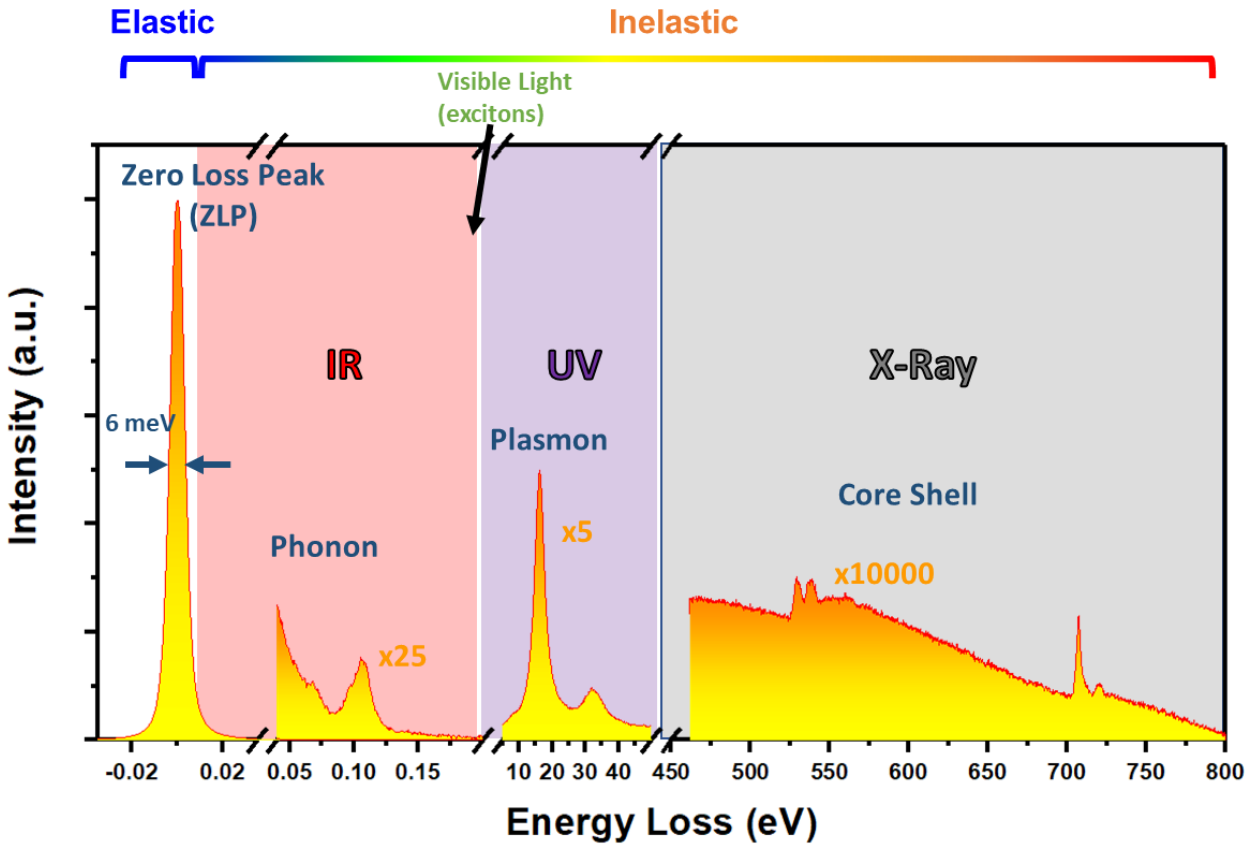

Fig. 2.7. Electron energy loss spectrum. Energy-loss spectrum covering a broad range of energy losses from a few meV to hundreds of eV. Monochromation of the primary electron energy results in an ultra-thin ZLP and uncovers phonon losses clearly. This spectrum shows ZLP at the far left at 0 energy loss, phonon losses in the infrared (IR) range from a few meV to several tens of meV, plasmon peaks above 10 meV in the ultraviolet (UV) range, and finally core shell losses ranging from several tens of meV to several hundreds of meV in the X-ray range. For heavier elements, core shell losses can extend to tens of thousands of eV.

Fig. 2.7 illustrates a monochromated EEL spectrum stitched together by combing spectra of various energy ranges. Essentially, the width of the energy range the detector is able to cover

depends on the dispersive power of the spectrometer i.e., how many eV's per pixel. Each distinct range of energies in an EEL spectrum corresponds with specific physical processes that occur in the material system as a result of its interaction with the electron beam. The goal of this section is to provide a brief introduction and description of these physical processes and what they can tell us about the material system. The order of discussion will begin with the most conventional EELS techniques starting at the high-loss energy range and ending with the monochromator-enabled state-of-the-art vibrational EELS in the ultra-low-loss range.

The most conspicuous and intense feature of an EEL spectrum of thin materials is the zero-loss peak (ZLP). This tall peak represents, as the name suggests, electrons that have passed through the sample without slowing down. However, even if electrons have not slowed down, they may still be deflected from their initial trajectory as described earlier in the chapter. In an unmonochromated system, the ZLP represents the energy distribution of a cold field which has a width ranging from 250-330 meV depending on the tip material, extraction voltage, and sharpness. This energy width is obtained from the full-width at half maximum (FWHM) and is the generally accepted figure of merit for defining the energy resolution of the spectra as well as the system in general. With this energy resolution, an unmonochromated ZLP contains phonon as well as narrow bandgap excitonic excitations and as a result, does not strictly represent zero-energy-loss electrons. In a monochromated system like the UltraSTEM HERMES from Nion, the optimal ZLP width, or energy resolution, for 60keV electrons is around 5-6 meV in width. Depending on the material system being studied, phonon losses should be well resolved and separated from the ZLP. Although, rigorously speaking, even a ZLP of such a narrow width will still generally contain low-

energy acoustic modes for which the energy transfer is less than the energy resolution. In general, ZLPs will contain more elastically scattered electrons than those scattered from phonons.

Energy losses from the ZLP center to 300 meV contain vibrational losses. In crystals, these vibrations are called phonons and represent the normal modes of atomic displacements in a periodic lattice. Vibrational signals appear as peak-like intensities in the EEL spectrum. These peaks, however, do not correspond to specific phonons but are rather a collection of phonons occupying a similar energy width. For crystals with a few-atom basis and light elements, phonon signals can be separated into individual modes or at least group of modes with comparable properties[28]. In multi-atom-basis crystals, the dispersion curve and DOS is a lot less interpretable and phonons often cannot be separated by their specific character. In biological and molecular materials where there is no periodic lattice, vibrations are the result of dipole motions of light elements such as C. The vibrational spectra are more easily interpretable as most bonds occupy a unique space in energy and as such, can be directly labeled[29,30]. In general, resolving, acquiring, and analyzing phonon signals is far more involved than other excitations. Low currents due to monochromation require high exposure to acquire appreciable detail. Additionally, phonon excitations' proximity to the ZLP imposes unique data analysis challenges to interpreting the signals and drawing reliable conclusions. Detailed discussion of strategies for acquiring and analyzing high quality spectra of interpreting vibrational information is given in chapter 6. A detailed mathematical treatment of how these vibrations arise in a periodic lattice was given in chapter 1. How vibrational signals appear in the EEL spectrum is a function of the scattering cross section. A detailed

mathematical treatment of EELS response to vibrations is given in chapter 3, the next chapter.

In the visible and UV light range of about 1-12 eV, you will find the bandgap onsets of several semiconducting and insulating materials. Semiconductors with heavy doping will be on the lower end of this range and may even enter the visible light regime while strongly insulating materials will have their bandgap onset towards the higher end of UC range. In semiconductors, the bandgap onset represents the shortest energy delta between the valence band and conduction band. This feature manifests as either a gradual or abrupt increase. Indirect bandgaps which involve energy and momentum transfer to the excited electron typically manifest as a gradually increasing intensity in the EEL spectrum often characterized by the linear law[31]. Direct bandgap transitions manifest as more abrupt edges often characterized by the square-root law[31]. In general, any electronic transition from an occupied band to an unoccupied band will generate an exciton. This quasiparticle is a bound state consisting of an electron and the hole it created. This bosonic quasiparticle can arise from an electronic transition between any occupied band to any unoccupied band. The bandgap exciton is a special case where the transition takes place between the highest valence band and the lowest conduction band making it the lowest energy transition in the system. Transitions from any other combination of occupied and unoccupied bands will result in intensities above the bandgap onset with intensities sometimes extended well into the plasmon range[32]. Mapping excitons at the nanoscale informs local electronic properties; understanding which is crucial for efficient and versatile nanoelectronics.

The most obvious peak in the 5-50 meV range of the EEL spectrum belongs to the plasmon excitations. Fast electrons that have created these bosons have lost energy in order to generate oscillations of the valence charge density around the probe. These excitations typically lie in the UV to extreme UV range but can exist in the visible light or even IR ranges due to their sensitivity to size effects. Plasmon peaks appear as nearly Lorentzian peaks whose intensity is seconded only by the ZLP. This is because the scattering cross-section for electrons generating plasmons is much higher than other excitations captured in EELS. In other words, the distance between scattering events where a plasmon has been generated, is shorter than distances for other types of inelastic scattering. A direct consequence of this is the occurrence of plural plasmon scattering in thick specimens which manifests as multiple plasmon peaks at multiples of the plasmon energy. The intensity of the plasmon peaks and how many of them are visible is often an indication of how thick the TEM specimen is. For thin specimens, the occurrence of the second order plasmon is suppressed while the 3rd is nearly absent. Due to the high scattering cross section of the electron-plasmon excitation, a single fast electron may often excite a plasmon in addition to other inelastic excitations. For example, in the core-loss regime, a fast electron that has undergone a core-shell excitation may also excite a plasmon. This manifests as a broadening of the ionization edges making it more difficult to accurately determine the energy and intensity of the features. Plural plasmon scattering can also introduce thickness related artifacts making interpretation of the fine structure of these core-edges, difficult. The plasmon-loss' intimate relationship with the thickness of the material can produce often spurious fine-structure results that are more strongly correlated with the thickness gradient of the material than with the electronic structure. As the sample thickness increases, the intensity of the ZLP

drops and that of the plural scattering increases. This relationship can be exploited to map the thickness of the material.

Assuming independent scattering events, the probability that an electron scatters n times is

$$P_n = \frac{I_n}{I_t} = \left(\frac{1}{n!}\right)\left(\frac{t}{\lambda}\right)^n e^{-\frac{t}{\lambda}} \tag{2.9}$$

I_n represents intensity where n-fold scattering has occurred, I_t represents the total integrated intensity, λ is the average distance between fast electron-plasmon scattering events or the mean free path (MFP), and t is the thickness of the TEM specimen[23]. Setting n=0, we get I_0 which represents the intensity where no scattering has occurred, i.e., the ZLP. The ratio of the ZLP and total intensities is then used to obtain the thickness of the material:

$$\frac{t}{\lambda} = \ln\left(\frac{I_0}{I_t}\right) \tag{2.10}$$

The MFP λ depends on several factors including kinetic energy of the fast electrons, EELS collection aperture semi-angle, the angular distribution of the scattered intensity, and then atomic density of the specimen. Further discussion of obtaining λ is given in Ref.[23].

In the X-ray range of the EEL spectrum, we have inner-shell excitations. The acquisition and analysis of these excitations typifies the most well-known capability of EELS: mapping of the elemental distributions in materials. This information is found in the high-energy-loss region of the spectrum or the X-ray regime. In standard core-loss EELS, this region generally spans about 100-2000 eV with losses towards the lower end of the range coming from core-shells of light atoms or narrow transitions of heavier atoms. Features in this energy range begin as rapidly rising intensities at approximately the electron transition energies and are usually 10^4-10^6 times less intense than the ZLP (Fig. 2.7. and Ref.[33]). These edges represent electron

transitions from core states to vacuum states or transitions between occupied and unoccupied orbitals in the atom. These transitions have specific energy deltas that are unique and can serve as identifiers of atomic species. As a result, features in this energy range can be used to probe a material's elemental composition. When combined with an aberration-corrected STEM, core-loss EELS offers the unprecedented ability to map elemental distributions of individual atoms[34].

In the core-loss region of Fig. 2.7, the oxygen K edge is depicted with an edge onset at 532 eV and iron L edge with an edge onset at 712 eV. K edges correspond to 1s orbital binding energies while L edges correspond to binding energies of the second electron shell in an atom and is occupied by the 2s and 2p orbitals.

2.2.3 Monochromation

The energy spread of electrons ejected from source material in the gun is the main factor that determines the energy resolution of the STEM-EELS system. The typical distribution of kinetic energies of electrons extracted from a cold field emission gun (FEG) with a tungsten electron source is about 0.27-0.35 eV[35–37]. This energy spread depends on the quality of the tip material and its sharpness among other factors. In contrast, electrons ejected by thermionic or Schottky emission tend to have an energy distribution of around 0.5-0.8 eV[38–40]. The ZLP obtained by placing the electron probe in the vacuum is a direct way to visualize the energy spread of the electron gun.

As most energy losses are far beyond the 0.27-0.35 eV energy width of the ZLP, monochromation is not necessary to resolve those features. The ability to resolve features whose energy spacing is on the order of the energy resolution also demands higher resolution. For example, higher energy resolution may be needed for resolving detail in the ELNES and the EXELFS portions of core-loss spectra. For resolving low losses on the order of this energy spread, a sufficient energy resolution is needed such that these features are not overwhelmed and buried by the ZLP or its tail. Another highly relevant parameter when determining the resolvability of low loss excitations is the ZLP width at 1/1000-max or at 1/10000-max[37,41,42]. A comparison of this parameter, which roughly represents the extent of the ZLP tail, with the expected intensity of low-loss features is helpful in determining EELS' sensitivity to those excitations and whether it will obscure them completely. As a result, the ability to tighten the energy distribution is highly desirable for resolving finer features and low energy excitations such as narrow-bandgap excitons and phonons.

Monochromators are devices that seek to decrease the energy spread of the electrons by collimating an energy-dispersed distribution of electrons and can achieve energy spreads of sub-10 meV beams[43]. This enables the accurate detection of narrow bandgap and vibrational excitations. Fig. 2.8a shows the typical trajectory of fast electrons in a Nion HERMES with the gun on the bottom and the EELS spectrometer at the top.

The operating principle of monochromators is quite similar to that of EELS spectrometers. Typical monochromation involves first dispersing the electron beam energetically and employing an energy selecting slit to collimate the energy distribution (Fig. 2.8b). This requires the beam to be magnified at the slit plane so that high energy resolutions can be

achieved. This was achieved by the development of an alpha-type monochromator which essentially consisted of 3 spectrometers arranged in a dispersing-undispersing configuration. Quadrupoles before the slit magnified the spectrum by 100x at the slit[44]. This monochromator design coupled with the Nion Iris spectrometer[45] has now enabled energy resolutions down to 4.2 meV[46] and 2.98 meV[47] for 30 keV and 20 keV electrons, respectively.

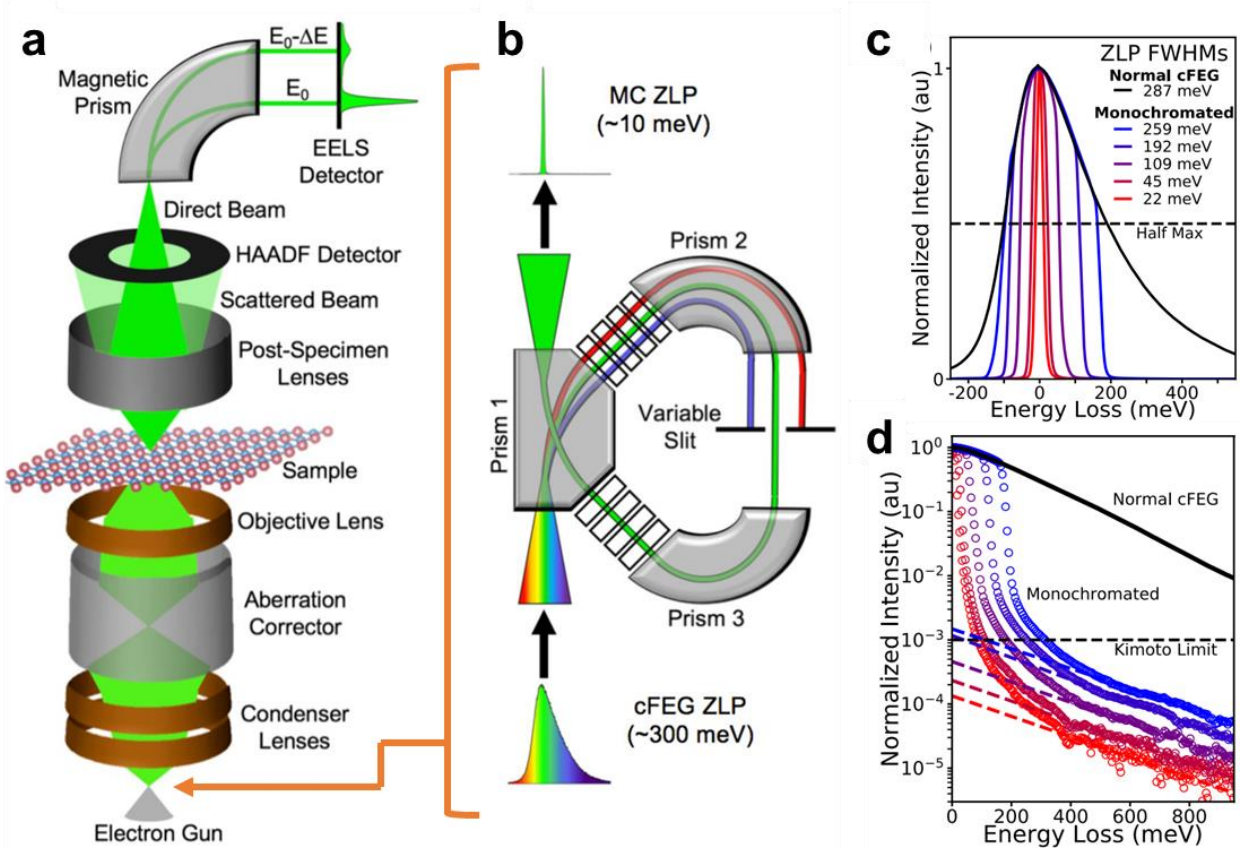

Figure 2.8. Effect of monochromation on electron energy distribution. **a**, Schematic of electron energy-loss spectroscopy (EELS) experiment in a scanning transmission electron microscope (STEM). **b**, Schematic of monochromation of electron beam (occurring between the electron gun and the condenser lenses). **c**, ZLPs of a non-monochromated cFEG gun (black), and the same gun at various levels of monochromation (increasing from blue to red), showing increased energy resolution and reduced ZLP tails. **d**, Log plots for the ZLPs shown in (a), demonstrating that the intensity of the ZLP tail is reduced by several orders of magnitude by monochromation. The dashed line marks where the intensity of ZLP tail falls below 10−3 (also known as the Kimoto limit), indicating that the background is small enough for effective EELS analysis. Dashed lines are power-law fits to the ZLP tails at higher energies. Figure is adapted from J. A. Hachtel, et al. Scientific Reports 8.1 (2018): 5637.

Fig. 2.8c shows various levels of monochromation from 287 meV for the unmonochromated beam to 22 meV. It is evident that once the monochromating slit is inserted, the energy distribution is sharply cut. This has the intended effect of improving the energy resolution, or FWHM, as a linear function of the slit size but also sharply eliminates the ZLP tail. The tail of an unmonochromated ZLP still maintains about 1% of its maximum even at an energy loss of 1 eV. The background is a concern since studies have demonstrated that EELS signals are challenging to detect until the intensity of the zero-loss peak (ZLP) tail has decreased to less than 0.1% of its maximum value (known as the Kimoto limit[42]). The sharp truncation of the tail means that energy losses that were previously overwhelmed the by the ZLP tail can now be reliably imaged. Fig. 2.8d is useful as a guide for determining what level of monochromation is needed such that low-loss features lie above the Kimoto limit. Monochromation even to a slightly better energy resolution than the unmonochromated beam still has the added advantage of abruptly decaying tails while maintaining majority of the total counts. Lower energy excitations such as phonons rely on monochromation for improving the ZLP FWHM as well as minimizing the tail since they occupy the 10-300 meV range in the EEL spectrum.

Ultrahigh energy monochromation has enabled the detection of vibrations of a diverse set of materials ranging from semiconductors and insulators, to organic solids. Since the first landmark paper demonstrating sub-10 meV resolution vibrational spectroscopy in the electron microscope, several seminal papers have emerged from imaging vibrational fingerprints of biological structures[29], mapping shape-induced phonon polariton modes of a single nanocube[48], identifying site-specific isotopic labels in L-alanine[30], imaging single-

defect phonons[49], and mapping phonon dispersions[50–52]. These works and several others will be discussed in greater detail in the next chapter.

Chapter 3

Vibrational EELS

3.1 Phonon excitations by fast electrons

Phonon excitations by fast electrons is a phenomenon that occurs when high-energy electrons scatter off atoms in a solid, causing them to vibrate generating phonons. Since phonons play a crucial role in determining the thermal and mechanical properties of materials, the ability to probe them, especially at atomic scales, becomes necessary for progress in nanoscale materials engineering. As discussed in the previous chapter, phonon excitations are generated the same way as other excitations in the material system. That is to say, a fast electron impinges on the atomic lattice and deposits some of its energy. A small amount of energy, on the order of tens to a few hundreds of meV, goes into generating acoustic phonons and optical phonons.

Phonon excitations by fast electrons are studied by using a variety of techniques such as electron energy loss spectroscopy (EELS). This has been done using HREELS for decades but only recently has this technique been enabled at the nanoscale[43] and atomic resolutions[53,54]. These techniques allow for the measurement of the phonon vibrational spectrum and can provide valuable information on the crystal structure, bonding, and electronic properties of a material and culminates into a powerful tool for solid state physics research. The main

advancement that has facilitated this development is the integration of a high-dispersion monochromator which energetically stretches the beam so that it can be properly collimated. This chapter is dedicated to the discussion of various state-of-the-art vibrational EELS (vibEELS) techniques including high spatial resolution imaging of vibrational modes to momentum-resolved imaging of phonon dispersions. In the first section, a strong theoretical framework is necessary for the accurate interpretation of vibEELS results is presented. This theoretical model is best known as the double-differential scattering cross-section of vibEELS. It should be noted that this is a quantum mechanical description that does not consider optical effects that result in aloof modes. This is briefly discussed theoretically in the next section.

We begin by denoting the quantum state of the fast electron and the slab before the scattering by $|n_0 k_0\rangle$ and after the scattering by $|n_1 k_1\rangle$. Before and after scattering, the fast electron and the slab do not interact and the quantum state can be expressed as a product state,

$$|n_i \boldsymbol{k}_i\rangle = |n_i\rangle|\boldsymbol{k}_i\rangle \tag{3.1}$$

Then we denote H_{int}, the interaction Hamiltonian between the fast electron and the slab, given by the Coulomb interaction of fast electron and electrons in the slab,

$$H_{\text{int}}(\boldsymbol{r}) = \frac{e^2}{4\pi\varepsilon_0}\int d\boldsymbol{r}' \frac{\rho_{\text{tot}}(\boldsymbol{r}')}{|\boldsymbol{r}-\boldsymbol{r}'|} \tag{3.2}$$

where $\boldsymbol{r}$ is the position of fast electron, $\boldsymbol{r}'$ is the coordinate inside the slab and $\rho_{\text{tot}}(\boldsymbol{r}')$ is the total charge density of electrons and nuclei in the slab.

The transition rate between the initial state and final state is given by Fermi's Golden rule,

$$w(|n_0\boldsymbol{k}_0\rangle \to |n_1\boldsymbol{k}_1\rangle) = \frac{2\pi}{\hbar}|\langle n_0\boldsymbol{k}_0|H_{\text{int}}|n_1\boldsymbol{k}_1\rangle|^2\delta\left(E_{n_0} + E_0 - E_{n_1} - E_1\right) \tag{3.3}$$

$$= \frac{2\pi}{\hbar}|\langle n_0|H_{\text{int}}|n_1\rangle|^2\delta\left(E_{n_0} + E_0 - E_{n_1} - E_1\right)$$

According to Sturm[55], the double differential cross section for EELS is,

$$\frac{d^2\sigma}{d\Omega dE_1} = \frac{m^2e^2}{4\pi^2\hbar^4q^4\varepsilon_0^2}\frac{k_1}{k_0}\frac{1}{N}\sum_{n_0,n_1}P_{n_0}\left|\langle n_0|\int e^{-i\boldsymbol{q}\cdot\boldsymbol{r}'}\rho_{\text{tot}}(r')dr'\,|n_1\rangle\right|^2\delta\left(E_{n_0} + E_0 - E_{n_1} - E_1\right) \tag{3.4}$$

where $N$is the number of unit cells in the solid, the transferred momentum $\boldsymbol{q} = \boldsymbol{k}_0 - \boldsymbol{k}_1$ and differential energy $dE_1 = \frac{\hbar^2\boldsymbol{k}_1}{m}d\boldsymbol{k}_1$.

According to Van Hove[56], P_{n_0} is the statistical weight of the initial state $|n_0\rangle$ (usually the Boltmann factor divided by the sum of states). Thus, P_{n_0} is given by,

$$P_{n_0} = \frac{\langle n_0|e^{-\beta H_{\text{slab}}}|n_1\rangle}{Z} = \frac{e^{-\beta E_{n_0}}}{Z} \tag{3.5}$$

where $\beta = \frac{1}{k_BT}$, $E_{n_0}$is the energy of state $|n_0\rangle$ and $Z$is the partition function. The Hamiltonian for the slab after second quantization is,

$$H_{\text{slab}}(r) = \sum_i E_iC_i^\dagger C_i + \sum_\alpha \hbar\omega_\alpha b_\alpha^\dagger b_\alpha + H_{e-e} + H_{e-ph} + H_{ph-ph} \tag{3.6}$$

Here, $C_i^\dagger$ and C_i are creation and annihilation operators for electron state i. $b_\alpha^\dagger$ and b_α are creation and annihilation operators for phonon state α. Typically, the energy loss from the fast electron ranges from meV to keV. We are interested in the inelastic process of generating phonons around several tens of meV. The electronic state of slab is only weakly perturbed by existence of phonons since the electron energy is on the order of eV. In addition, the

electron-phonon interaction in the slab is negligible since it barely affects phonon dynamics due to low carrier concentration. The electron-electron interaction is weak in semiconductors and can be ignored. For metals and materials with high carrier concentration this term is non-negligible. At room temperature, the phonon-phonon interaction is not strong and the phonon states can be treated as independent quasi-particles. Thus, we approximate the Hamiltonian by,

$$H_{\text{slab}}(\boldsymbol{r}) \approx E_e + \sum_{\alpha} \hbar\omega_\alpha b_\alpha^\dagger b_\alpha \tag{3.7}$$

where $\alpha = \boldsymbol{q}v$ is the phonon state with momentum $\boldsymbol{q}$ and phonon branch index v.

The quantum state of the slab is,

$$|n_0\rangle = |E_e, f_{\boldsymbol{q}_1 v_1}, f_{\boldsymbol{q}_2 v_2}, f_{\boldsymbol{q}_3 v_3}, \dots\rangle = |E_e\rangle \left|f_{\boldsymbol{q}_1 v_1}\right\rangle \left|f_{\boldsymbol{q}_2 v_2}\right\rangle \dots \left|f_{\boldsymbol{q}_{N_D} v_{N_D}}\right\rangle \tag{3.8}$$

where f_α refers to quantum state (Fock state) for phonon state α and $N_D = 3N_{atom}$ is the total number of degree of freedoms.

Partition function

The canonical ensemble partition function for the slab is,

$$\begin{aligned} Z &= e^{-\beta E_e} \sum_{\{f_\alpha\}} e^{-\beta \sum_\alpha f_\alpha \hbar\omega_\alpha} \\ &= e^{-\beta E_e} \prod_\alpha \sum_{f_\alpha=0}^{\infty} e^{-\beta \sum_\alpha f_\alpha \hbar\omega_\alpha} \\ &= e^{-\beta E_e} \prod_\alpha \frac{1}{1-e^{-\beta\hbar\omega_\alpha}} \end{aligned} \tag{3.9}$$

As a result, we obtain the expression for probability of finding the slab at initial state $|n_0\rangle$,

$$\begin{aligned} P_{n_0} &= \frac{e^{-\beta E_e} e^{-\beta \sum_\alpha f_\alpha \hbar\omega_\alpha}}{Z} \\ &= \prod_\alpha \frac{e^{-\beta f_\alpha \hbar\omega_\alpha}}{1-e^{-\beta\hbar\omega_\alpha}} \end{aligned} \tag{3.10}$$

Electron density

Denote electron density in Eq. 3.4 by,

$$\begin{aligned} \rho(\boldsymbol{q},t) &= \int e^{-iq\cdot r'} \rho_{\text{tot}}(\boldsymbol{r}')dr' \\ &= \sum_{\tau i} e^{-iq\cdot R_{\tau i}} \int e^{-i\boldsymbol{q}\cdot(\boldsymbol{r}'-\boldsymbol{R}_{\tau i})} d\boldsymbol{r}' \\ &= \sum_{\tau i} e^{-i\boldsymbol{q}\cdot\boldsymbol{R}_{\tau i}} F_i(\boldsymbol{q}) \end{aligned} \tag{3.11}$$

where τ is the index of unit cell and i is the atom index in a unit cell. The atom position can be expressed by,

$$\boldsymbol{R}_{\tau i} = \boldsymbol{R}_{0,\tau i} + \boldsymbol{u}_{\tau i} \tag{3.12}$$

where $\boldsymbol{R}_{0,\tau i}$ is the atom at equilibrium and $\boldsymbol{u}_{\tau i}$ is the atomic displacement from equilibrium position. Since the atomic displacements are typically small compared with phonon wavelength, we can write the electron density using Taylor's expansion to the first order,

$$\rho(\boldsymbol{q},t)=\left[\sum_{\tau i}F_i(\boldsymbol{q})e^{-i\boldsymbol{q}\cdot\boldsymbol{R}_{0,\tau i}}(1-\boldsymbol{q}\cdot\boldsymbol{u}_{\tau i})\right]+O(|\boldsymbol{q}\cdot\boldsymbol{u}_{\tau i}|^2) \tag{3.13}$$

Displacement operator

The displacement operator writes,

$$\boldsymbol{u}_{\tau i}=\sum_{\boldsymbol{q}\nu}\boldsymbol{e}_i(\boldsymbol{q},\nu)\left(\frac{\hbar}{2NM_i\omega_{\boldsymbol{q}\nu}}\right)^{1/2}\left(b^{\dagger}_{\boldsymbol{q}\nu}e^{i\omega_{\boldsymbol{q}\nu}t}+b_{\boldsymbol{q}\nu}e^{-i\omega_{\boldsymbol{q}\nu}t}\right)e^{i\boldsymbol{q}\cdot\boldsymbol{R}_{0,\tau i}} \tag{3.14}$$

where $\boldsymbol{q}\nu$ represents the momentum and branch index of a phonon state and $e_{\boldsymbol{q}\nu}$ is the phonon polarization vector. The term in Eq. 3.4 can be expressed by,

$$\begin{aligned}
&\langle n_0|\sum_{\tau i}F_i(\boldsymbol{q})e^{-i\boldsymbol{q}\cdot\boldsymbol{R}_{0,\tau i}}\boldsymbol{q}\cdot\boldsymbol{u}_{\tau i}\,|n_1\rangle \\
&\qquad=\langle n_0|\sum_{\tau i}F_i(\boldsymbol{q})e^{-i\boldsymbol{q}\cdot\boldsymbol{R}_{0,\tau i}}\boldsymbol{q} \\
&\qquad\cdot\sum_{\boldsymbol{q}'\nu}\boldsymbol{e}_i(\boldsymbol{q}',\nu)\left(\frac{\hbar}{2NM_i\omega_{\boldsymbol{q}'\nu}}\right)^{\frac{1}{2}}\left(b^{\dagger}_{\boldsymbol{q}'\nu}e^{i\omega_{\boldsymbol{q}'\nu}t}+b_{\boldsymbol{q}'\nu}e^{-i\omega_{\boldsymbol{q}'\nu}t}\right)e^{i\boldsymbol{q}'\cdot\boldsymbol{R}_{0,\tau i}}\,|n_1\rangle \\
&=\langle n_0|N\sum_{i\nu}F_i(\boldsymbol{q})\boldsymbol{q}\cdot\boldsymbol{e}_i(\boldsymbol{q},\nu)\left(\frac{\hbar}{2NM_i\omega_{\boldsymbol{q}\nu}}\right)^{\frac{1}{2}}\left(b^{\dagger}_{\boldsymbol{q}\nu}e^{i\omega_{\boldsymbol{q}\nu}t}+b_{\boldsymbol{q}\nu}e^{-i\omega_{\boldsymbol{q}\nu}t}\right)|n_1\rangle \\
&=\langle n_0|\sum_{i}F_i(\boldsymbol{q})\boldsymbol{q}\cdot\boldsymbol{e}_i(\boldsymbol{q},\nu)\left(\frac{N\hbar}{2M_i\omega_{\boldsymbol{q}\nu}}\right)^{\frac{1}{2}}\left(\sqrt{f_{\boldsymbol{q}\nu}+1}e^{i\omega_{\boldsymbol{q}\nu}t}+\sqrt{f_{\boldsymbol{q}\nu}}e^{-i\omega_{\boldsymbol{q}\nu}t}\right)|n_0\rangle
\end{aligned} \tag{3.15}$$

As a result, we have,

$$|\langle n_0|\rho(\boldsymbol{q},t)|n_1\rangle|^2=\frac{N\hbar}{2\omega_{\boldsymbol{q}\nu}}\left|\sum_{\tau i}F_i(\boldsymbol{q})e^{-i\boldsymbol{q}\cdot\boldsymbol{R}_{0,\tau i}}-\sum_{i}F_i(\boldsymbol{q})\boldsymbol{q}\cdot\boldsymbol{e}_i(\boldsymbol{q},\nu)\left(\frac{1}{M_i}\right)^{\frac{1}{2}}\left(\sqrt{f_{\boldsymbol{q}\nu}+1}+\sqrt{f_{\boldsymbol{q}\nu}}\right)\right|^2 \tag{3.16}$$

The first term inside the norm can be dropped since it corresponds to elastic scattering. The latter term can be further decomposed to Stokes process and anti-Stokes process. For Stokes process, we have the scattering cross section,

$$\begin{aligned}\frac{d^2\sigma}{d\Omega dE_1} &= \frac{m^2e^2}{4\pi^2\hbar^3q^4\varepsilon_0^2}\frac{\boldsymbol{k}_1}{\boldsymbol{k}_0}\sum_{n_0}P_{n_0}\frac{f_{\boldsymbol{q}\nu}+1}{2\omega_{\boldsymbol{q}\nu}}\left|\sum_i F_i(\boldsymbol{q})\boldsymbol{q}\cdot\boldsymbol{e}_i(\boldsymbol{q},\nu)\left(\frac{1}{M_i}\right)^{\frac{1}{2}}\right|^2\delta(\omega_1-\omega_0-\omega_{\boldsymbol{q}\nu}) \\ &= \frac{m^2e^2}{4\pi^2\hbar^3q^4\varepsilon_0^2}\frac{\boldsymbol{k}_1}{\boldsymbol{k}_0}\sum_{n_0}P_{n_0}\frac{f_{\boldsymbol{q}\nu}+1}{2\omega_{\boldsymbol{q}\nu}}\left|\sum_i F_i(\boldsymbol{q})\boldsymbol{q}\cdot\boldsymbol{e}_i(\boldsymbol{q},\nu)\left(\frac{1}{M_i}\right)^{\frac{1}{2}}\right|^2\delta(\omega_1-\omega_0-\omega_{\boldsymbol{q}\nu})\end{aligned} \tag{3.17}$$

In particular, the summation of a function $A(\boldsymbol{q}\nu)$ of phonon state $\boldsymbol{q}\nu$ over all possible initial $|n_0\rangle = \left|f_{\boldsymbol{q}\nu}\right\rangle\left|f_{\boldsymbol{q}'\nu'}\right\rangle \ldots \left|f_{\boldsymbol{q}_{N_D}\nu_{N_D}}\right\rangle$ states in the slab is,

$$\begin{aligned}\sum_{n_0}P_{n_0}A(\boldsymbol{q}\nu) &= A(\boldsymbol{q}\nu)\sum_{f_{\boldsymbol{q}\nu}}\sum_{\{f_\alpha,\alpha\neq\boldsymbol{q}\nu\}}P_{n_0} \\ &= A(\boldsymbol{q}\nu)\sum_{f_{\boldsymbol{q}\nu}}e^{-\beta f_{\boldsymbol{q}\nu}\hbar\omega_{\boldsymbol{q}\nu}}\left(\sum_{\{f_\alpha,\alpha\neq\boldsymbol{q}\nu\}}e^{-\beta\sum_\alpha f_\alpha\hbar\omega_\alpha}\right)\prod_\alpha\left(1-e^{-\beta\hbar\omega_\alpha}\right) \\ &= A(\boldsymbol{q}\nu)\sum_{f_{\boldsymbol{q}\nu}}e^{-\beta f_{\boldsymbol{q}\nu}\hbar\omega_{\boldsymbol{q}\nu}}\left(1-e^{-\beta\hbar\omega_{\boldsymbol{q}\nu}}\right)\end{aligned} \tag{3.18}$$

We assume the function $F_i(\boldsymbol{q})$, polarization vector $\boldsymbol{e}_i(\boldsymbol{q},\nu)$ and frequency $\omega_{\boldsymbol{q}\nu}$ are temperature independent. Then, only $f_{\boldsymbol{q}\nu}$ is temperature dependent. Therefore, we have,

$$\begin{aligned}&\sum_{n_0}P_{n_0}\frac{f_{\boldsymbol{q}\nu}+1}{2\omega_{\boldsymbol{q}\nu}}\left|\sum_i F_i(\boldsymbol{q})\boldsymbol{q}\cdot\boldsymbol{e}_i(\boldsymbol{q},\nu)\left(\frac{1}{M_i}\right)^{\frac{1}{2}}\right|^2\delta(E_1-E_0-\omega_{\boldsymbol{q}\nu}) \\ &= \sum_{\boldsymbol{q}\nu}\frac{1}{2\omega_{\boldsymbol{q}\nu}}\left|\sum_i F_i(\boldsymbol{q})\boldsymbol{q}\cdot\boldsymbol{e}_i(\boldsymbol{q},\nu)\left(\frac{1}{M_i}\right)^{\frac{1}{2}}\right|^2\delta(E_1-E_0-\omega_{\boldsymbol{q}\nu})\sum_{f_{\boldsymbol{q}\nu}}e^{-\beta f_{\boldsymbol{q}\nu}\hbar\omega_{\boldsymbol{q}\nu}}(f_{\boldsymbol{q}\nu}+1)\left(1-e^{-\beta\hbar\omega_{\boldsymbol{q}\nu}}\right) \\ &= \sum_{\boldsymbol{q}\nu}\frac{f_{BE,\boldsymbol{q}\nu}+1}{2\omega_{\boldsymbol{q}\nu}}\left|\sum_i F_i(\boldsymbol{q})\boldsymbol{q}\cdot\boldsymbol{e}_i(\boldsymbol{q},\nu)\left(\frac{1}{M_i}\right)^{\frac{1}{2}}\right|^2\delta(E_1-E_0-\omega_{\boldsymbol{q}\nu})\end{aligned} \tag{3.19}$$

The function $f_{BE,\boldsymbol{q}\nu}$ is identified as Bose-Einstein distribution function. It can be solved from Boltzmann transport equation for non-equilibrium systems.

The final expression in Eq. 3.19 describes the differential probability of exciting mode $\omega_{\boldsymbol{q}\nu}$ as a function of various physical and experimental parameters. The first term is concerned with the population of phonons at a given temperature, momentum, phonon branch. Normally the n is put in place of f and is used to represent the equilibrium phonon population. In this case of Eq. 3.19, f denotes the total phonon population accounting for the equilibrium and non-equilibrium populations. This value is scaled by twice the frequency of the phonon. The central term in bars represents the specific interaction of the fast electron with the charge density of the atom. This charge density is not constant and varies in space and time. It is also related to the specific direction and magnitude of the atomic displacements. The dot product between the momentum of the fast electron q and the eigen displacement e selects atomic displacements whose direction is parallel or anti-parallel with the momentum of the scattered fast electron. This has profound consequences on mode selectivity by vibEELS. For example, at high symmetry points within the first Brillouin zone (FBZ), transverse modes will always have the displacements of their constituting atoms perpendicular to the direction of the fast electron momentum transfer. This largely means that transverse modes should not be detected within the FBZ due to this selection rule. The last term in this expression represents probability of a specific phonon mode $\omega_{\boldsymbol{q}\nu}$. When we convert the summation into a continuous integral with respect to momentum, we must account for the fact that different momenta hold different number of states. This results in the phonon density of states. This term is responsible for largely providing the shape of the vibEELS signal. The first and second term serve to scale and slightly modify this shape. In the next few sections, this physics is applied to different novel vibEELS techniques that leverages various advantages of the STEM's capabilities.

3.2 Aloof beam vibrational EELS

While most vibrational spectroscopies involve direct interaction between the probe and the material, aloof-beam vibrational EELS is a technique that involves fields that can couple to dipole moments in the material over long ranges. This means that the electron beam can be placed out-side the sample, in vacuum, and still experience energy losses from phonon excitations in the material. These excitation modes are aloof modes. In a periodic lattice, these aloof modes become polariton modes which are modes that couple with light. Most quasiparticles in polar materials can be coupled with light in this fashion to create a polariton. Phonons, excitons, and plasmons are a few examples where their surface modes couple with light of the appropriate energy to general a polariton. Only these light-coupled excitations can be detected while the electron beam is far from the sample. Due to the long-range nature of the dipole-scattering interaction, atomic and nanoscale information cannot be easily captured.

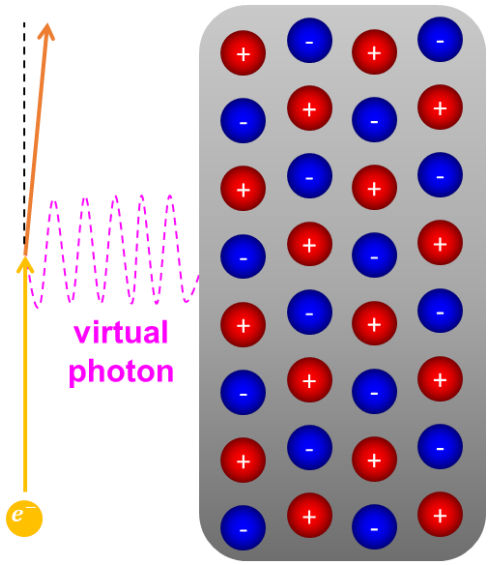

Figure 3.1 Dipole scattering from Aloof-beam vibrational EELS. A simple schematic showing illustrating a virtual photon from the electron beam exciting polaritonic vibration. The

electron beam loses energy to a virtual IR photon. The field of the IR photon causes oscillations in the polar lattice. The net effect results in only the surface charges being sensitive to the electric field. These surface oscillations are known as surface phonon-polaritons (SPhP). In some 2D Van-der-Waals materials such as boron nitride (BN), these are known as hyperbolic phonon polaritons (HPhP).

Using dipole theory, we can formulate the angle dependence of dipole scattering:

$$\frac{dI}{d\Omega} \propto \frac{1}{\theta^2 + {\theta_E}^2} \tag{3.20}$$

Which has the same form as Eq. 2.25. This suggests that the scattering by dipoles is restricted to low angles. We can get an idea for consequences of this in real space by applying the uncertainty principle. If dipole scattering is concentrated at low angles, its momentum precision is high. This translates to low real-space precision. This suggests that the dipole field that induces this scattering has long-range effects. To understand that energy-specific form of this scattering we need to consider the detailed material response to the excitation as a function of energy.

A more complete way of understanding this excitation is by examining the -classical dielectric function (DF) of a polar crystal. This function contains all the information on how a material system responds in the presence of an external electric field. For a simple polar crystal such as SiC, the frequency-dependent DF has this simplified form:

$$\epsilon(\omega) = \frac{-\mathrm{i}\Gamma_{\mathrm{LO}}\omega - \omega^2 + {\omega_{\mathrm{LO}}}^2}{-\mathrm{i}\Gamma_{\mathrm{TO}}\omega - \omega^2 + {\omega_{\mathrm{TO}}}^2} \tag{3.21}$$

The material DF contains information about how optical excitations in the IR range react with light. It is a function of transverse optical (TO) and longitudinal optical (LO) mode energies as acoustic modes do not couple with light. Next, we want to see how electrons bring

about these excitations in a polar material. Here, I present the EELS scattering cross section which describes how electrons interact with the material to excite these modes[57]:

$$\frac{\mathrm{d}^2P(\omega,b)}{\mathrm{d}\omega\mathrm{d}z} = \frac{e^2}{2\pi^2\varepsilon_0\hbar v^2} \times K_0\left(\frac{2\omega b}{v\gamma}\right) \times \mathrm{Im}\left(-\frac{2}{1+\varepsilon_1(\omega)}\right) \tag{3.22}$$

Here, ε_0 is the zero-frequency dielectric constant, b is the impact parameter which represents the distance of the beam from the material, ω is the vibration frequency, v is the electron velocity in the material, $\varepsilon_1(\omega)$ is the DF, and γ is the Lorentz factor. It is informative to isolate key features of this expression into coefficient, decay, and dielectric terms. The coefficient does not affect the behavior of the interaction but rather only scales it. The term with a K_0 represents a 0th order Bessel function of the second kind. This roughly translates into an exponential-like decay behavior which describes how the probability of exciting a SPhP decays roughly exponentially with distance from the material. Finally, we have the imaginary part of the reciprocal of the DF which gives the energy of excitation.

The exponential decay behavior of the aloof-loss in vibEELS presents us with interesting consequences. The fact that the dipole vibrations can be detected far away from the sample means that these modes are non-local matching with our expectations using Eq. 3.20. Fig. 3.2 shows the delocalization as a function of energy loss.

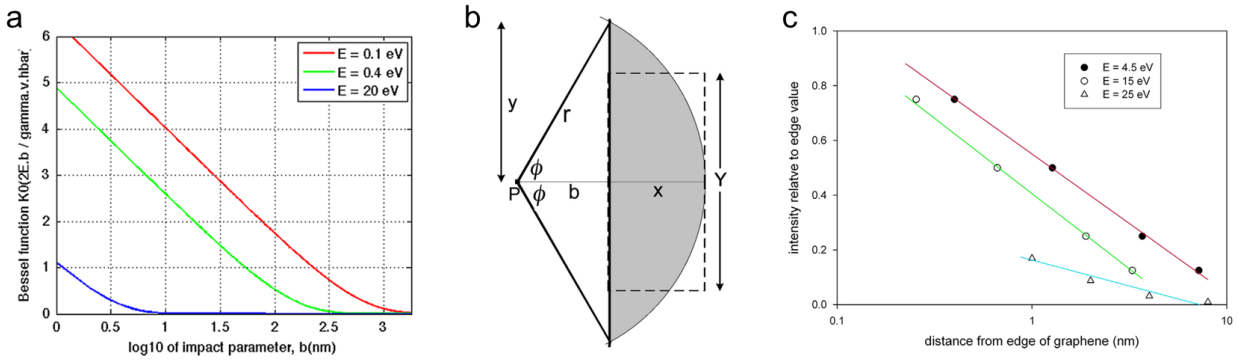

Figure 3.2. Probe-material distance relationships as a function of excitation energy. a, Bessel function term of Eq. 3.22 plotted as a function of $\log_{10}(b)$, showing how the intensity of inelastic scattering at three energy losses (0.1 eV, 0.4 eV and 20 eV) varies with the impact parameter b of an aloof probe of 60 keV electrons. **b**, Geometry for an aloof beam at point P, relative to the edge of the material (vertical y-axis). Dashed lines outline an area equal to the shaded area that represents regions of specimen that lie within a distance r (b+x) of the probe. **c**, Energy-loss intensity at three values of energy loss E, measured by Zhou et al.[58] with an aloof probe of 60 keV electrons (diameter about 0.1 nm) held at various distances from the edge of a monolayer graphene sheet. The horizontal impact-parameter scale is logarithmic. Figure is adapted from Egerton, R. F. Ultramicroscopy 159 (2015): 95-100 with permission.

Fig. 3.2 depicts the variation of Eq. (3.22) with respect to the impact parameter b on a logarithmic scale. The plot includes two different energies, $E = 0.1$ eV and 0.4 eV, which define the range of most vibEELS peaks, and a typical valence-electron loss energy of $E = 20$ eV. By comparing the curves for the different energies, the plot demonstrates that the vibEELS signal persists over a much larger range of impact parameters than the valence-loss signal, which is consistent with experimental observations.

Fig. 3.2 shows that the b-dependence of valence-electron (plasmon) scattering also follows a nearly logarithmic behavior, which has been experimentally observed and is shown in Fig. 3.2.3c. The data in Fig. 3.2c were obtained using an aloof STEM probe[58], and the plot is presented with a logarithmic distance scale. This experimental evidence confirms the assumptions that we will use to calculate damage rates and spatial resolution in aloof-mode spectroscopy.

These properties of polaritonic modes, especially phonon-polaritons, can be used for a variety of purposes ranging from probing beam sensitive materials to the spatial modulation of surface phonon modes in crystal lattices. Since the sample experiences no electron dose

under this configuration, knock-on damage is eliminated and radiolysis is minimized as the valence-loss excitations are significantly suppressed, abating the radiation damage. This is highly beneficial for beam-sensitive crystals and biological materials. Additionally, this technique enables the mapping of shape effects in the material which inform nanoscale engineering of light transport mechanisms.

In 2016 Rez et al.[29] demonstrated that by using aloof-mode vibEELS, radiolysis can be minimized resulting in damage-free vibrational measurements of biological materials. Biological materials are generally not as robust as crystals and as a result, suffer from electron beam damage. They show that the electron beam can be placed tens of nanometers away from the sample edge while still obtaining accurate spectra. Additionally, they have demonstrated group-specific vibrational characteristics.

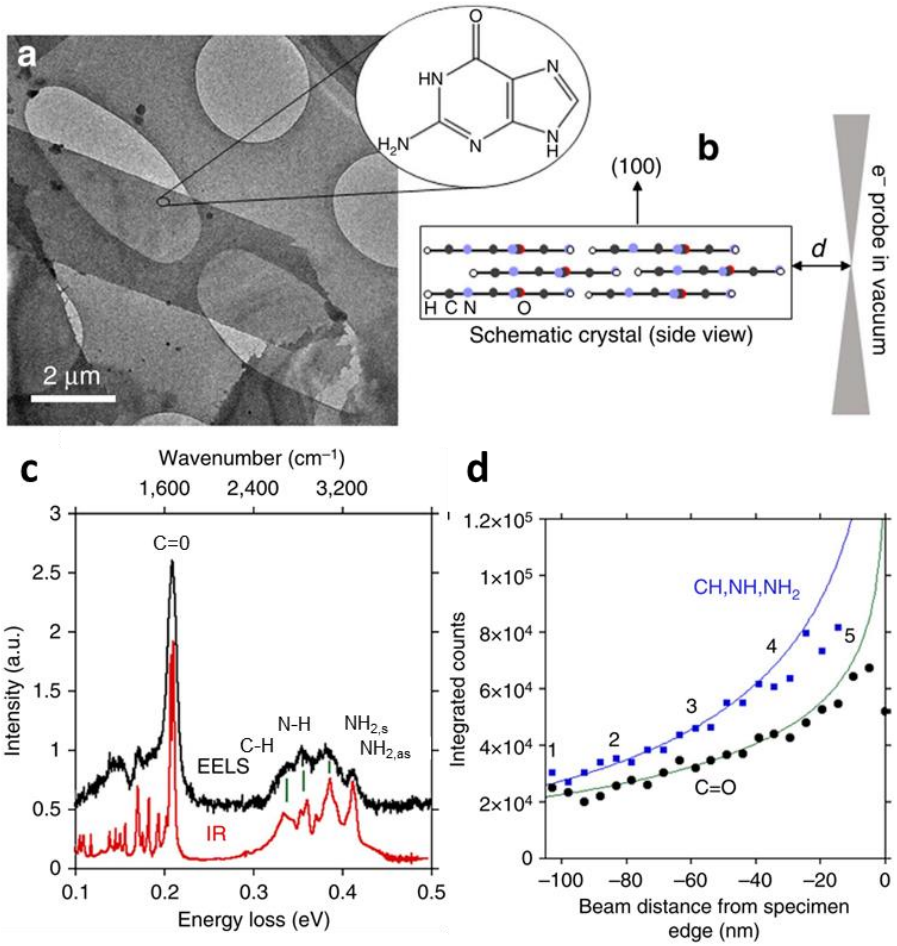

Figure 3.3 Position of the electron beam with respect to the guanine crystal and vibEELS spectra. a, Low-magnification 'top-view' image of guanine crystals laying on holey carbon film. (a, inset) one schematic guanine molecule. **b**, Side schematic of molecules arranged in layers parallel to specimen surface to form the crystal. The electron probe a distance d outside the crystal in the vacuum. **c**, An EEL spectrum at the infrared region, collected when the electron probe is d=30 nm from the edge of the crystal, compared with an ex-situ FTIR spectrum. Peaks corresponding to C=O, NH, CH, NH_2 symmetric and NH_2 antisymmetric stretches can be seen in the EEL spectrum. **d**, Variation of total intensity of the C=O peak (circles) and the combination of CH, and NH and NH_2 peaks (squares) from the EELS signal as the probe approaches the sample compared with the theoretical variation derived from classical dielectric theory given as equation (2) (solid lines). Figure adapted from Rez, Peter, et al. Nature communications 7.1 (2016): 10945 with permission.

With the electron beam placed outside the sample, or in a non-intersecting geometry (Figs. 3.3a,b), spectra can still be recorded with substantial detail (Fig. 3.3c). This technique is also

able to resolve spatial characteristics of each type of vibration. Fig. 3.3d shows that the C=0 dipole vibration has a slower decaying tail than the modes at higher energies. This is consistent with Fig. 3.2 in that lower energy modes have a larger delocalization. The technique opens up the possibility of non-destructively probing vibrational fingerprints of organic molecules with much higher spatial resolution than optical methods.

For crystalline materials, aloof modes correspond to polaritonic modes in materials with strong dipole moments. These modes can be exploited to study shape related vibrational effects. Lagos et al.[48] distinguished the polaritonic modes from bulk modes in a MgO nanocube and demonstrated that different polaritonic modes are sensitive to the edges and corners of the nanocube. Fig. 3.4c shows representative spectra in intersecting and aloof beam geometries. It can be seen that in the intersecting geometry, both aloof and bulk modes can be detected while in the aloof geometry, only the phonon polariton signals exist. The phonon polariton modes reveal sensitivity to shape geometries of the nanocube (Fig. 3.4d). The bulk modes are characterized as such since they only exist when the electron beam is impinging on the material directly (Fig. 3.4e). This work has demonstrated the selectivity of highly localized bulk modes and delocalized surface modes and lays the groundwork for probing surface and bulk confined phonon modes in other materials.

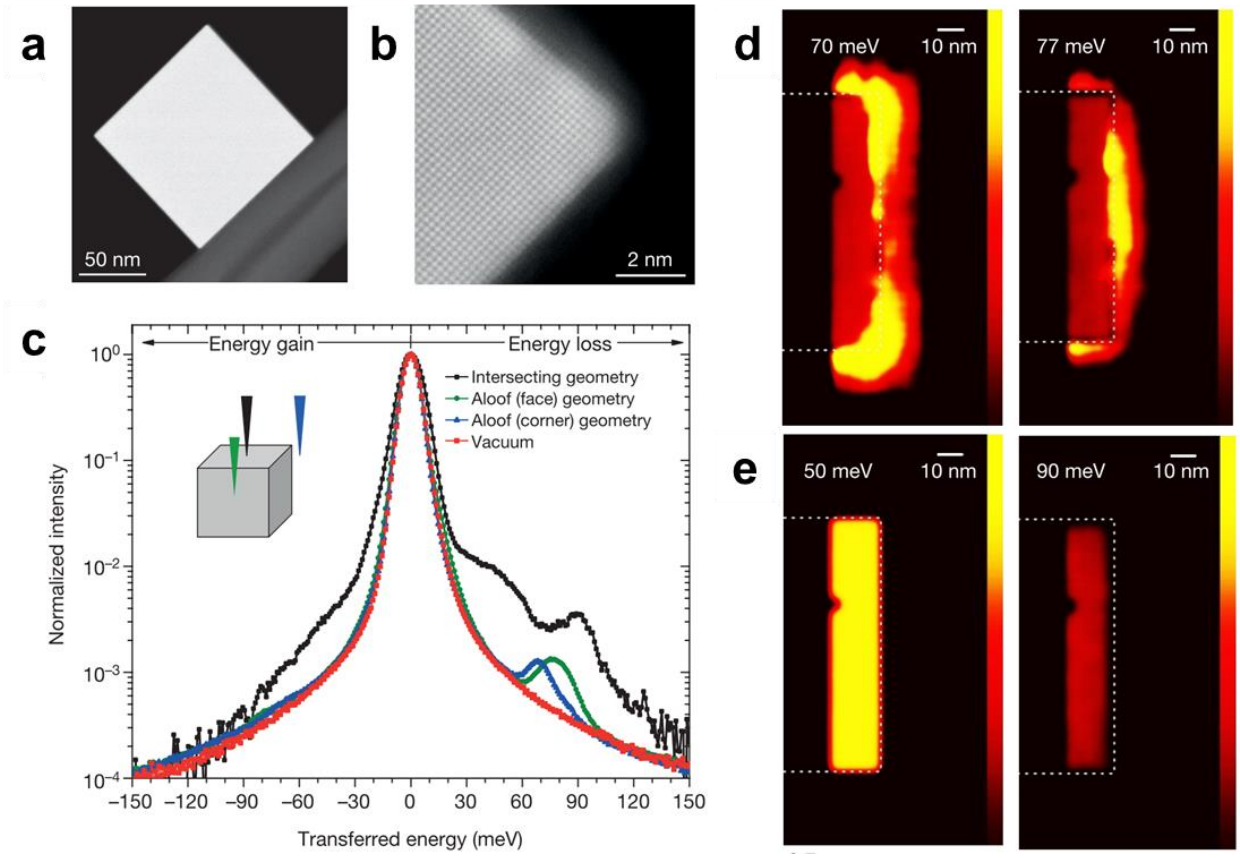

Figure 3.4 STEM Imaging and EELS mapping of MgO cubes. a, ADF image of a suspended 150-nm MgO cube. **b**, High-resolution ADF image of a cube oriented along the [001] direction. The cube faces are defined by the (100) atomic planes; the corners and edges are round. A coating layer of about 1–2 nm in thickness is also present. **c**, Typical normalized spectra acquired with the electron beam located in various positions (see inset): green, aloof geometry (beam located near a face); blue, aloof geometry (beam located near a corner); black, intersecting geometry. The spectrum in red is the ZLP spectra acquired in the vacuum. Curves were normalized so that the resonance peak maxima approximate a fractional scattering probability. Regions with positive and negative values of transferred energies are labelled energy loss and energy gain, respectively. **d**, Experimental two-dimensional EELS scattering maps showing the spatial distribution of the corner (left, 70 meV) and face (right, 77 meV) modes. **e**, Experimental two-dimensional EELS maps of two bulk phonon excitations (left, 50 meV; right, 90 meV). The bulk modes have been reduced by a factor of about two to emphasize the visualization of the surface modes. The color scale in d,e indicates the scattering intensity in arbitrary units. In (d) and (e), the dotted white box outlines the cube. Figure adapted from Lagos, Maureen J., et al. Nature 543.7646 (2017): 529-532 with permission.

3.3 Spatial and momentum resolution in STEM-EELS

In scanning transmission electron microscopy (STEM), spatial and momentum resolution are two crucial parameters that determine the quality of the images obtained. Spatial resolution refers to the ability to distinguish between two closely spaced objects, while momentum resolution relates to the ability to distinguish between electrons with slightly different momenta. The spatial resolution in STEM microscopy is determined by a range of factors such as the electron beam size, aberration correction, and the detector resolution. The momentum resolution is mainly influenced by the energy spread of the electrons in the beam and the chromatic aberration of the microscope. In order to achieve high spatial and momentum resolution, a combination of sophisticated electron optical design, advanced image processing algorithms, and optimized experimental conditions is necessary. Ultimately, the resolution achieved in STEM microscopy is limited by physical constraints, such as the interaction between the electrons and the sample.

Most conventional techniques in STEM-EELS take advantage of large convergence semi-angles to probe features at high spatial resolutions. As the trademark advantage of STEM, high resolution EELS imaging provides significant advantages over competing techniques. These techniques utilize large convergence semi-angles to focus the probe down to sub-angstrom sizes, or in the case of vibrational EELS, down to atomic width. A direct consequence of this is the loss in momentum resolution in the diffraction pattern. In most cases, momentum resolution is not necessary and spatial resolution is highly desired. For example, high spatial resolution is prioritized when probing elemental compositional variation on the angstrom scale or more fundamentally, for atomic resolution imaging. The

information gained from the use of such a condition does not offer any information on how the electrons have scattered and the dynamics of processes in the material.

Flexible electron optics in the Nion UltraSTEM, and most high-end STEM-EELS systems, allow for variable convergence angle of the electron probe. Changing the angle at which electrons impinge upon the sample determines both the size of the probe and the momentum resolution of the scattered electrons. Upon lowering the convergence semi-angle, the beam broadens in real-space and becomes more parallel. A direct consequence of this is that now the diffraction spots are separated from each other when previously only a singular large disk was visible. Resolving the Brillouin zone (BZ) structure affords us the ability to select specific points in momentum space for study. With the recovery of momentum resolution, the real-space resolution suffers and atomically resolved contrast is lost. Depending on how parallel the beam is made (low convergence semi-angle), the broader the real-space probe will be. Deflection of the post-specimen scattered electrons using post-specimen magnetic lenses then allows us to select which region of diffraction space to include into the EELS spectrometer.

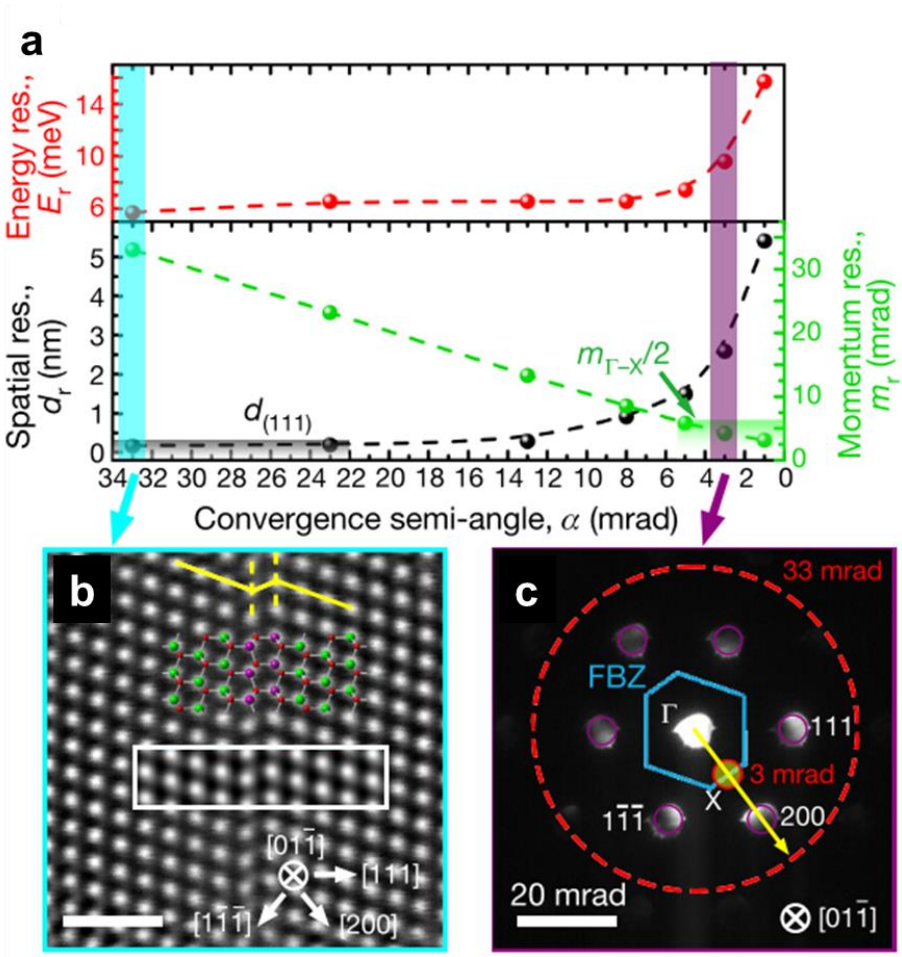

Figure 3.5 Spatial, momentum, and energy resolutions as a function of convergence semi-angle in SiC. a, The impact of probe convergence semi-angle (α) on the energy (E_r), spatial (d_r) and momentum (m_r) resolution. The grey shaded area shows the optimal range for resolving stacking-fault structures in SiC, while the green shaded area is ideal for fully separating the Γ and X points in the FBZ. **b**, Atomic resolution annular dark-field (ADF) STEM image of a cross-sectional SiC specimen with a single stacking fault projected along the [011] direction, with α = 33 mrad (4.3 $Å^{-1}$) indicated by the cyan bar in b. Scale bar is 1 nm. The atomic structure and a simulated STEM image (white box) are both superimposed on the STEM image. **c**, Diffraction pattern of SiC along the [011] direction with α = 3 mrad (0.39 $Å^{-1}$) as marked by the purple bar in (a). The large red dashed circle and the small red circle correspond to convergence semi-angles of 33 mrad and 3 mrad, respectively. Figure is adapted from Yan, Xingxu, et al. Nature 589.7840 (2021): 65-69.

Yan et al. developed a strategy for utilizing both the high spatial and momentum resolution capabilities of STEM-EELS for studying atomic scale structures. Here, we demonstrate the clear relationship between spatial (d_r), momentum (m_r), and energy (E_r) resolutions and

their dependence on the probe convergence semi-angle (α) (Fig. 3.5a). Figure 3.5b displays a single edge-on stacking fault in 3C-phase SiC projected along the [011] zone axis, with convergence semi-angle $\alpha = 33$ mrad forming an electron probe with a size of about 0.14 nm. The resultant annular dark-field (ADF) STEM image is consistent with the defect atomic structure and with the simulated image demonstrating high spatial resolution. Since d_r is inversely proportional to α, there is a smallest α below which the feature of interest cannot be resolved. This is highly dependent on the real-space size of the feature. For example, to spatially resolve a stacking fault in SiC, α should be greater than 22 mrad.

In this study we aimed to investigate the effects of the stacking fault on acoustic modes. In reciprocal, or momentum space, acoustic phonon modes reach their highest energy (and become easiest to detect) at the edge of the BZ. This necessitates a momentum resolved condition such the FBZ edge can be selected. In the diffraction pattern obtained with $\alpha = 3$ mrad ($0.39\ \text{Å}^{-1}$) in Fig. 3.5c, the X point, which lies at the edge of the FBZ, is well suited to acquiring an angle-resolved vibrational signal. Because the momentum resolution is improved as α decreases, α should be smaller than 5.5 mrad ($0.71\ \text{Å}^{-1}$, half the reciprocal distance between Γ and X) to fully separate the Γ and X points (Fig. 3.5c). Therefore, we developed a combined method to take advantage of both wide and narrow aperture settings for a systematic study of vibrational signals of an isolated crystal defect. Fig. 3.6 shows the results of using the angle (momentum)-resolved condition taken at the X point. A clear deviation in the TA mode can be seen at the site of the stacking fault which would normally be hard to detect in the momentum-averaged, or high spatial resolution condition. This study establishes a strategy that takes advantage of both spatial and momentum resolutions for a systematic study of vibrational signals of an isolated crystal defect.

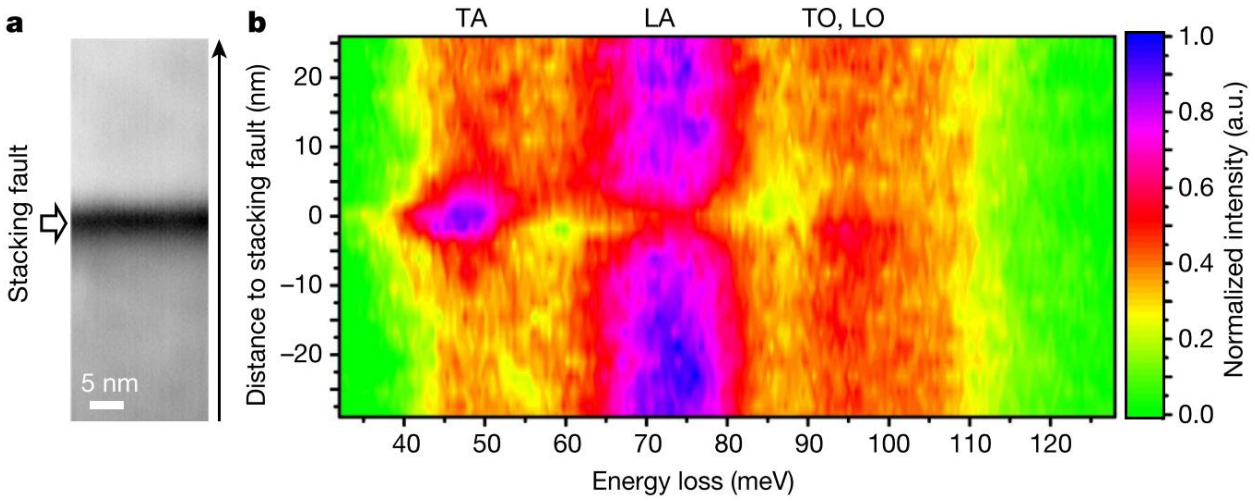

Figure 3.6 Spatial distribution of individual phonon modes under the angle-resolved condition. a, ADF STEM image with a convergence semi-angle of 3 mrad. **b**, Line profile of the angle-resolved vibrational spectra at the X point of the FBZ across the stacking fault in the direction denoted by the black arrow in a. Color scale shows the signal intensity normalized by its maximum. This figure has been adapted from Yan, Xingxu, et al. Nature 589.7840 (2021): 65-69.

3.4 High spatial resolution vibrational EELS

The mapping of high spatial resolution vibrational modes is achieved by measuring the bulk phonon modes of a crystal. This set of techniques take full advantage of the high spatial resolution of the STEM. High spatial resolution mapping of phonons is important for the study of nanomaterials, where the phonon properties can be significantly different from those of bulk materials. For example, phonons resulting from crystal defects and interfaces, which are nanoscale, can only be studied with a high-resolution technique. In addition, high spatial resolution mapping of phonons can provide valuable information on the local variations in the crystal structure and bonding in a material. By mapping the spatial distribution of specific phonon modes, researchers can gain insight into the local variations in the bond strength and coordination of atoms in a material. Overall, high spatial resolution

mapping of phonons is a valuable tool for the study of materials at the nanoscale and can provide valuable insights into the structure and properties of a wide range of materials, including semiconductors, metals, ceramics, and biological materials.

In this section high resolution vibEELS is accomplished with proportionally small electron probe. STEM imaging resolution is directly linked to the probe size but this is not necessarily the case for vibEELS. In the case of non-polar materials such as pure materials like Si or C based systems, or strongly covalent materials like SiGe, the probe size strictly determines the spatial resolution of vibEELS. However, the vast majority of materials are polar and strongly interact with light to generate polaritonic modes. As discussed in the previous section, surface phonon polariton modes are non-local and can be detected up to several tens or even hundreds of nanometers from the source. This section aims to cover techniques that can handle both situations. First, non-polar materials techniques will be discussed followed by strategies to exclude polaritonic modes and isolate high spatial resolution phonon modes.

3.4.1 On-axis, bright field vibrational EELS

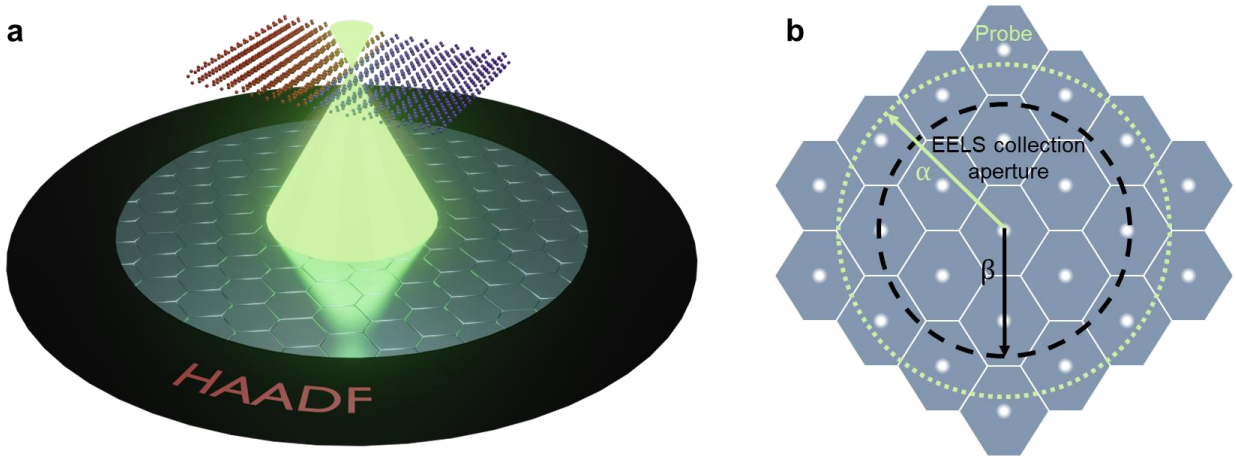

Figure 3.7 Momentum-averaged, on-axis vibrational EELS beam-detector geometry. a, Schematic of momentum averaged beam scattering geometry. A 33 mrad probe covers multiple BZ's of Si and results in a momentum-averaged scattering geometry. **b**, top-down view of probe convergence semi-angle and EELS collection aperture semi-angle. $\alpha = 33$ mrad and $\beta = 25$ mrad.

In order to achieve a small probe size in the STEM, the convergence semi-angle needs to be maximized. With aberration correction, a 1.5 Å, high-current probe at 60keV can be achieved in the Nion UltraSTEM 200 at a convergence semi-angle of 33 mrad (Fig. 3.7a). Under this configuration, the direct beam encompasses several BZs in reciprocal space. As a result, momentum resolution is completely lost and all bulk vibrational spectra become momentum-averaged spectra. This amounts to including all modes selected by Eq. 3.19, within the FBZ. Essentially momentum resolution is being sacrificed for high spatial resolution and is a direct consequence of the uncertainty principle. In other words, phonons are detected with high real-space precision, while obtaining no information about their individual momenta.

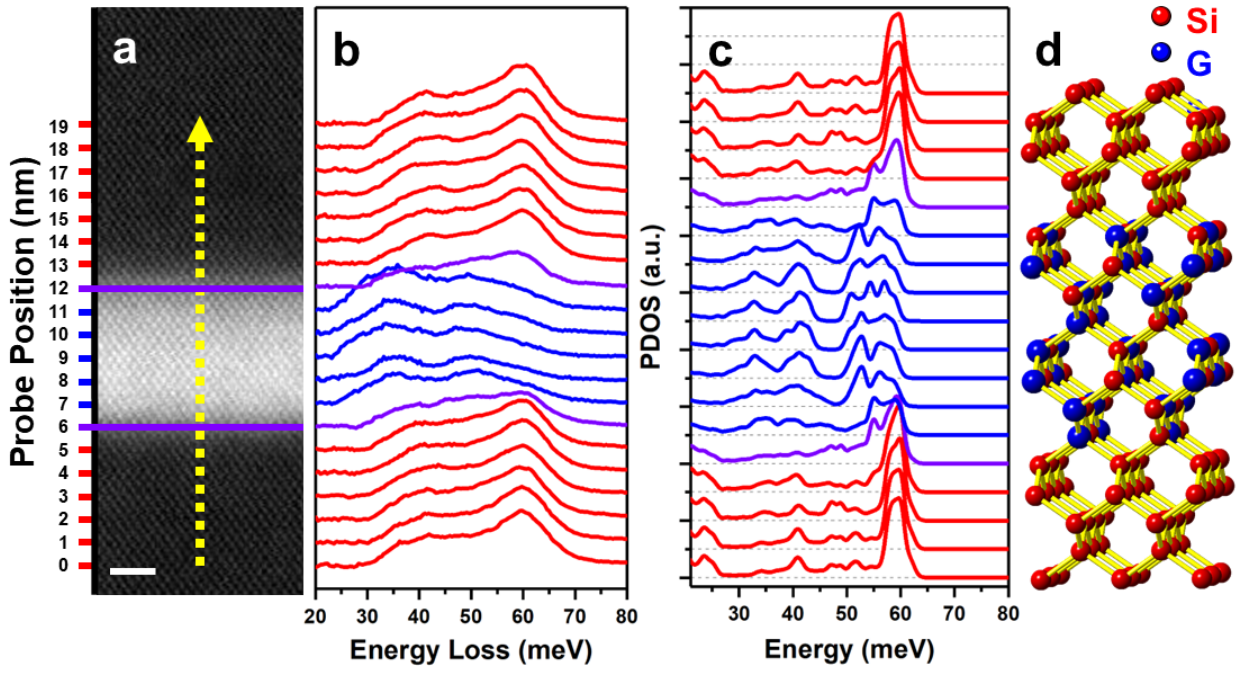

Figure 3.8 Line scan across QD. a, HAADF image of the region consisting of top and bottom interfaces of a single QD. The yellow arrow notes the direction of the line scan and the purple lines mark the QD interfaces. Scale bar denotes 2 nm. **b**, Stacked background subtracted spectra with red, blue, and purple curves representing phonon signals in interlayer Si, SiGe QD, and interface signals. Stacked positions correspond to the probe positions labeled in **a**. **c**, stacked calculated phonon density of states and **d**, associated atomic structure of abrupt Si-SiGe interface.

To outline this high spatial resolution, consider Fig. 3.8 which shows a phonon linescan from Si to SiGe and back to Si (Fig. 3.8a). Since SiGe is strongly covalent, the electron beam responds very weakly to its dipole moment such that the long-range effects are negligible. This is demonstrated in the abrupt change in the phonon signal shape from Si to SiGe. In pure Si we have pure Si modes while in SiGe the signal shape changes to accommodate Ge-Ge and Si-Ge vibrations. The mode shape in the experimental data Fig. 3.8b changes as abruptly as the DFT result for phonon DOS in Fig. 3.8c indicating a signal with atomic-scale spatial resolution. This most directly demonstrates high spatial resolution at the nanoscale and illustrates a clear advantage over optical methods like Raman spectroscopy with its ~1 μm spatial resolution.

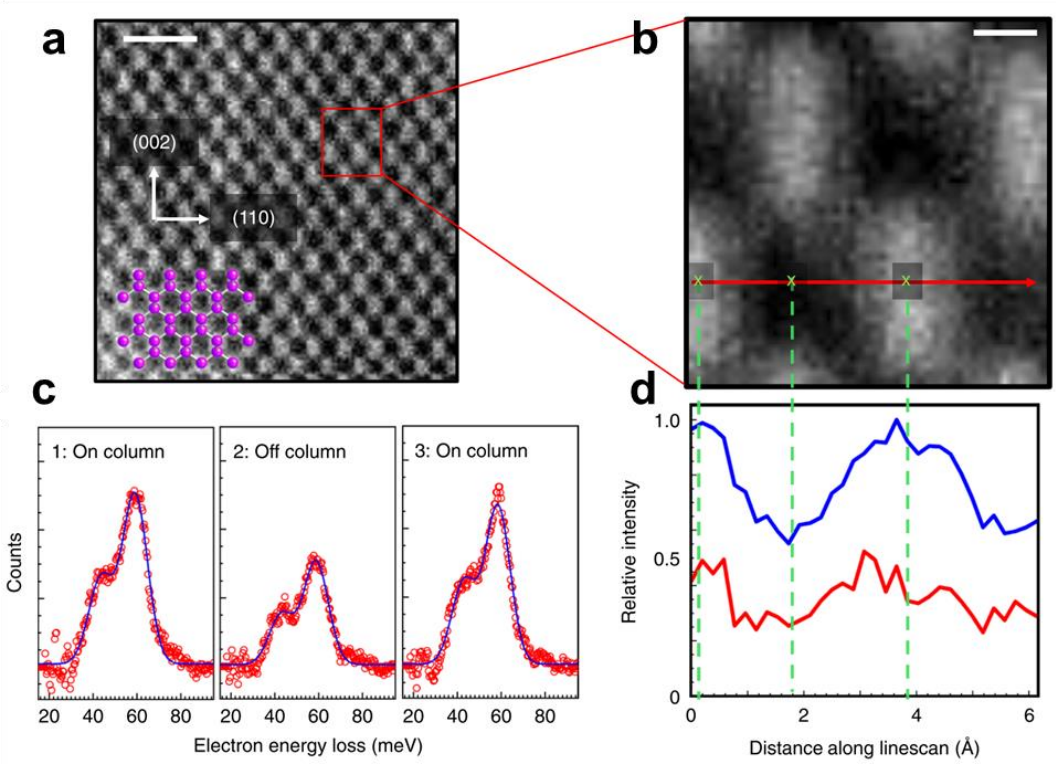

Fig. 3.9. Atomic resolution line scan of phonons in Si. a, Atomic resolution annular dark field (ADF) image with electron beam monochromation of ~10 meV from Si in [1̄10] projection with light contrast corresponding to Si dumbbell column pairs. Scale bar denotes 1 nm. A model of Si in the [1̄10] projection overlaid on the ADF image shows the position of atomic columns that form dumbbells. **b**, Magnified image of area indicated by red box in (a). The arrow indicates position and direction of EELS linescan acquisition. Scale bar denotes 1 Å. **c**, Individual spectra from different positions along linescan shown by the green x-symbols in (b). The red circles are experimental data points, and the blue line is the result of the Gaussian fit. **d**, The variation in intensity for higher (blue) and lower (red) energy phonons over the lines can indicated in (b). The profiles are spatially aligned with the ADF image in (b), as indicated by dashed green guidelines. An increase in phonon intensity can be observed around the dumbbell columns. Figure is adapted from Venkatraman, Kartik, et al. Nature Physics 15.12 (2019): 1237-1241 with permission.

As mentioned earlier, the presence of dipole modes limits the spatial resolution of vibEELS but Venkatraman et al.[59] showed that in elemental materials like Si, only high-spatial resolution modes remain, and their changes can be tracked on the atomic scale. Elemental materials like Si allow for the use of a conventional STEM-EELS beam-detector geometry to

obtain atomically resolved mapping of phonons. This can be described as an on-axis bright field beam-detector geometry which is used for nearly all conventional EELS experiments. Fig. 3.9 shows that as the probe is moved from on-column to an off-column configuration, the intensity of the background-subtracted phonon signal decreases. This is an abrupt change on the order of angstroms and is the trademark of atomically resolved features. Mapping the two modes, low energy mode at around 40 meV and higher energy mode at around 60 meV shows a clear periodic trend as the probe is scanned across a series of atomic columns. Their behavior is largely similar and suggests that the intensity of the phonon signal is directly related to real-space features. This is likely due to the probe feeling the effect charge density of the atom and the closer it is to the nucleus, the much more strongly it feels the unscreened nuclear charge. This would explain why the phonon signal is stronger on the atomic columns than off.

The situation becomes more complex when two different materials are compared. In Fig. 3.10 we have an interface between Si and SiGe. Unlike in pure Si where the phonon modes consist of only vibrating Si atoms, the SiGe alloy lattice includes phonons that have a Ge contribution as well, giving the material a more complex phonon DOS. Similar to Venkatraman et al.[59], the entire vibrational signal shows oscillations that match the atomic contrast in the HAADF image. However, in SiGe, even when the maximum peak heights are normalized to 1, the Ge OM still shows a strong modulation (Fig. 3.10d,e). This means that phonons where Ge atoms participate in the vibration have a stronger sensitivity to atomic columns. This suggests that it is even easier to achieve atom resolution phonon mapping for heavier elements.

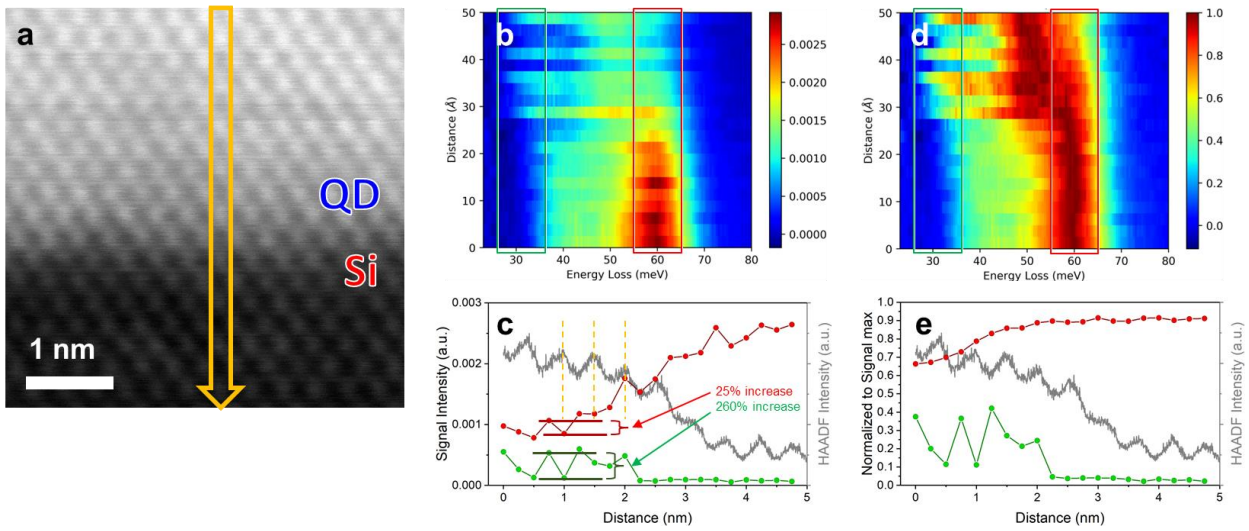

Figure 3.10. Phonon Mode Sensitives and Atomic Contrast. a, Atomic resolution HAADF image of a bottom QD interface. The downward yellow arrow indicates the direction of the phonon line scan. Solid lines mark the atomic positions in the HAADF image while the dashed line marks the Si-QD interface. **b**, Contour plot of line scan spectra normalized to the ZLP. Fringes are clearly seen and correlate with the atomic positions in the HAADF image in (a). **c**, Averaged Line profiles of P1 (26-36 meV), predominantly Ge-Ge vibrations, and Si OM vibrations (55-65 meV) from regions indicated in (b) overlaid with HAADF intensity from (a). **d**, Spectral contour plot normalized to the signal maximum. Fringes are only seen on the Ge optical mode while the intensity on the Si optical mode is uniform. **e**, Averaged Line profiles of P1 and Si OM vibrations normalized by signal maximum from regions indicated in (d) overlaid with HAADF intensity from (a).

3.4.2 Off-axis, dark field EELS

The off-axis, dark field EELS (DFEELS) configuration excludes dipole excitations from entering the entrance aperture. This is achieved by using flexible electron optics to tilt the post-specimen beam away from the beam axis (Fig. 3.11). The primary goal of this configuration, at least for vibrational EELS, is to avoid long-range signals like those of dipole excitations. Eq. 3.20 suggests that dipole excitations occur at very low scattering angles and generally obfuscate highly local vibrational signals due to their delocalized nature. To be clear, this is only an issue for polar materials with non-negligible dipole moments. Elemental

materials such as Si[28,59], C-based systems[51], and alloy materials whose constituting atoms share similar electronegativities, do not have dipole-coupled vibrations.

Dwyer et. Al.[60] first demonstrated that by moving the EELS entrance aperture away from the direct beam, one can exclude all dipole related vibrational signals. In their demonstration, they used a 6 mrad aperture center on the K-point of the boron nitride (BN) Brillouin zone (BZ). The configuration allows for higher spatial resolution vibrational signals than the traditional on-axis configuration as only local vibrational signals are included.

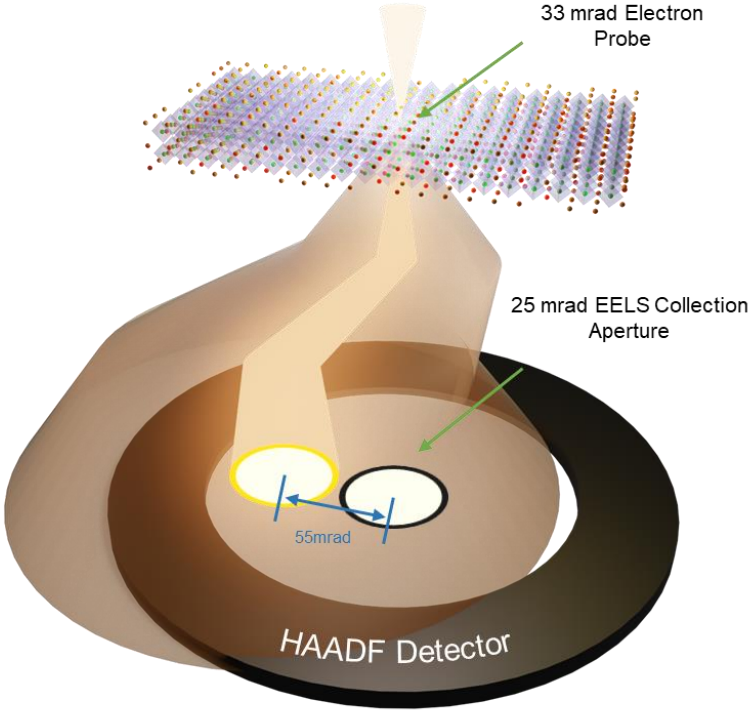

Figure 3.11 DF VibEELS beam-detector geometry illustrating a deflected post-specimen scattering beam and the collection of off-axis scattered electrons. The convergence semi-angle is 33 mrad and the direct beam is deflected by 55 mrad from the collection aperture center. Shifting the diffraction image by 55mrad off-axis ensures no intensity belonging to the central disk enters the EELS entrance aperture of 25 mrad.

Hage et. al. later utilized this concept with a high convergence angle probe and demonstrated atomic resolution mapping on BN[53]. The DFEELS signal reveals atomic contrast which matched closely with that of ADF imaging while the on-axis beam detector geometry vibrational mapping offered no atomic contrast (Fig. 3.12.c,d). More specifically, there is a clear intensity modulation in the signal on the atomic column versus off column (Fig 3.12a,b). They also demonstrate that their method can distinguish between distinct types of phonons, including longitudinal optical (LO) and transverse optical (TO) phonons.

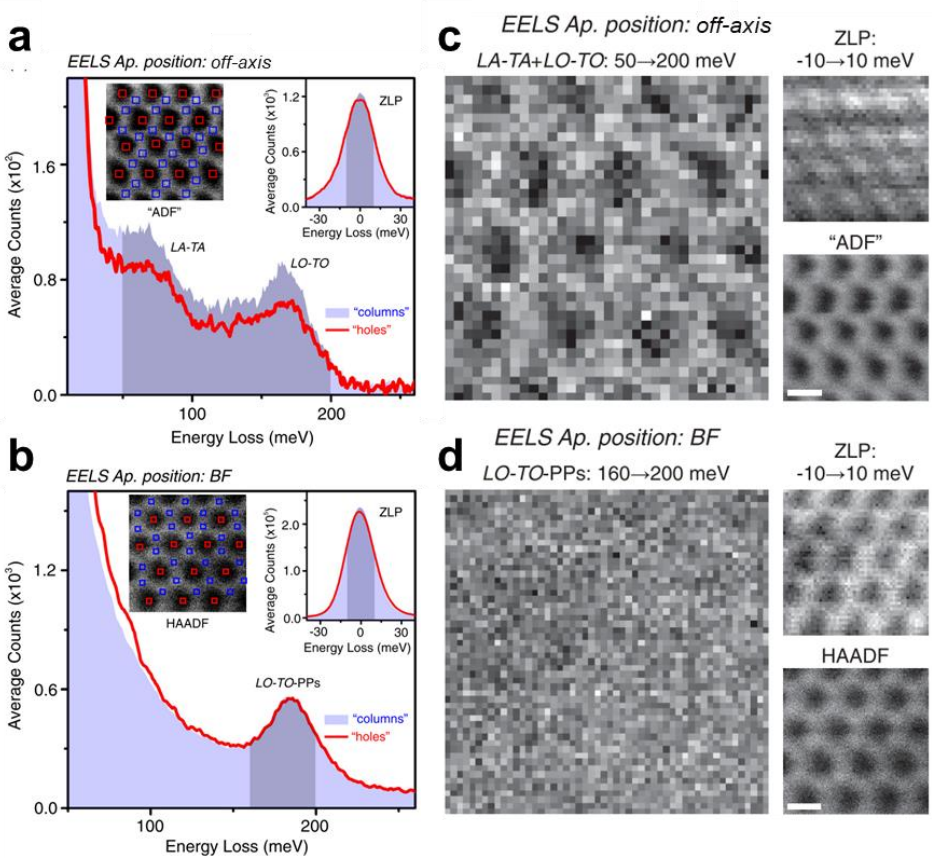

Fig. 3.12. Off-axis and on-axis spectra and mapping in BN a, Low-loss spectra for the off-axis detector averaged over probe positions on the atomic columns, labeled "columns" (blue squares on the inset on left) and in the holes between the columns (red squares), labeled "holes." The whole zero-loss peak is shown in the inset on the right. **b**, the same as (a) except that the detector is now in the BF position. Energy-loss ranges used for mapping are indicated in both (a) and (b) by shaded areas. **c**, EELS intensity maps formed by signal integration over the energy windows indicated in (a) (off-axis) and **d**, for the energy

windows indicated in (b) (on-axis). Scale bars: 2 Å. Figure adapted from Hage, F. S., et al. Physical review letters 122.1 (2019): 016103 with permission.

In their subsequent work they demonstrated the power of the DFEELS technique by probing the vibration of a single Si dopant atom in a graphene matrix[54]. On-axis vibrational EELS would show a delocalized signal from the dipolar Si-C bond. This delocalization would make it impossible to isolate single-atom vibrations. Hage et. al. demonstrated that the signal from the single Si atom decays rapidly with increasing distance from the dopant atom. There is a distinct appearance of low energy Si modes which do not exist in the graphene phonon DOS. This work discusses the importance of understanding atomic vibrations in materials, as these vibrations can have a significant impact on the material's properties. Prior methods to this typically required averaging over many atoms and would not provide information about individual atomic vibrations. This study lays the foundation for single-atom nanoscale engineering. As we move towards designing and manufacturing at the nanoscale, understanding the behavior of individual atoms becomes increasingly important. The properties of materials can change dramatically at the nanoscale, and these changes are often linked to the behavior of individual atoms.

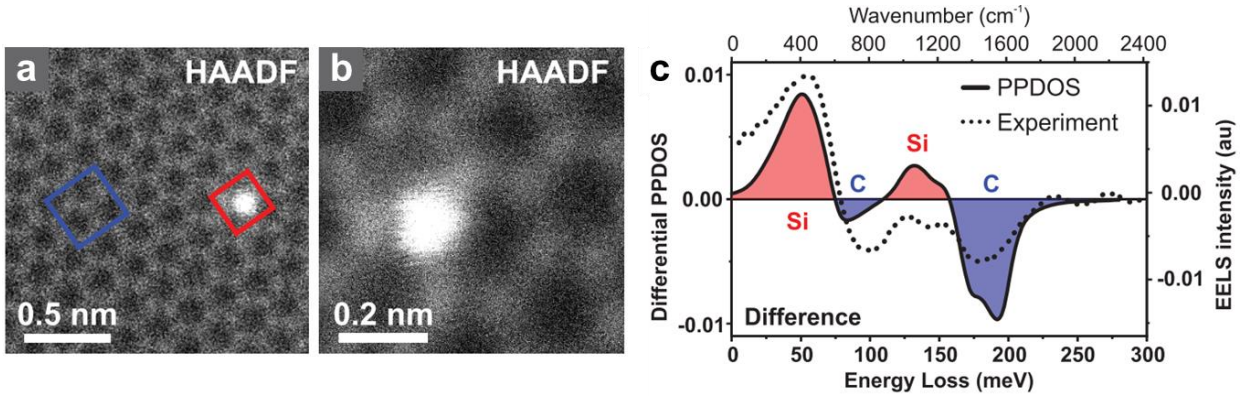

Figure 3.13 vibrational STEM-EEL spectrum of a Si impurity in graphene. a, HAADF overview of the experimental region. Red and blue boxes indicate the positions of the sub-scan regions from which the Si and C spectra, respectively, were acquired. **b**, HAADF close-up of the (bright) trivalent Si impurity. **c**, Comparison of the calculated differential PPDOS (broadened to match the experimental resolution) and the experimental difference spectrum. The blue and red shaded areas highlight energy ranges where the contributions of the Si impurity and its three nearest neighbors, or that of bulk graphene, are comparatively stronger. au, arbitrary units. Figure adapted from Hage, F. S., et al. Science 367.6482 (2020): 1124-1127. With permission.

3.5 Momentum resolved vibrational EELS

As discussed in section 3.3, flexible electron optics in the STEM also allow for the changing of the convergence semi-angle. Momentum resolution is achieved by decreasing the convergence semi-angle such that the Bragg disks no longer overlap (Fig. 3.14). Further decreasing the semi-angle will improve momentum resolution and worsen real-space resolution. Typical convergence semi-angles for momentum resolved experiments range from 1mrad to 6 mrad. Lattice parameters of common materials require a convergence angle of at least 6 mrad to be able to separate the Bragg disks clearly. By resolving individual BZ's one can select phonon signals of specific wavelength. For example, studying acoustic modes at the BZ edge ensures that they are at their highest value making them easier to study[49]. The following discussions attempt to encompass seminal papers that showcase the power of momentum resolved vibrational EELS and phonon dispersion mapping.

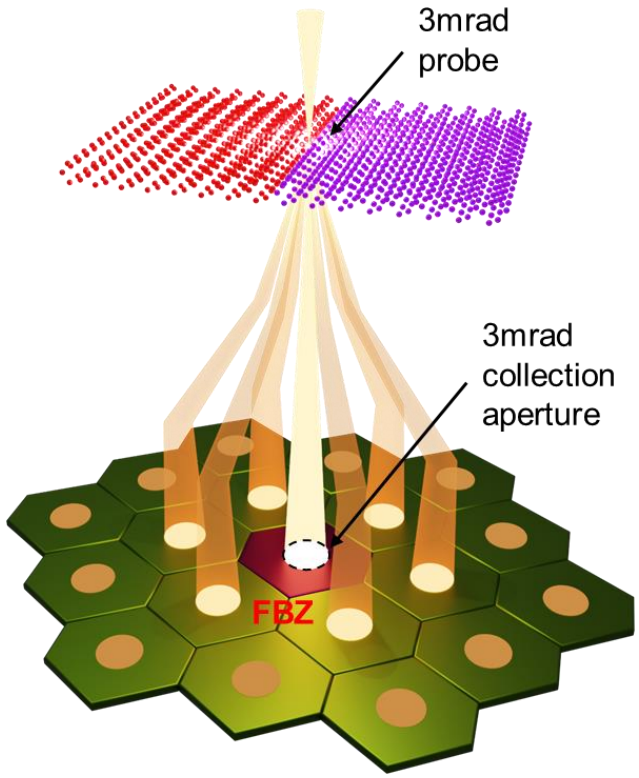

Figure 3.14 Schematic of momentum-resolved beam-detector geometry. The electron beam is focused into a 3 mrad convergence semi-angle probe. Post specimen deflectors tilt the scattered beam so that the off-axis signal enters the 3mrad EELS collection aperture. A 3mrad convergence semi-angle probe is about 1/3 the size of the FBZ in Si.

Phonon dispersion curves offer a wealth of information including wavelength-specific mode energies, phonon group velocities, phonon bandgap, and anisotropic propagation. Conventional methods capable of probing momentum transfer dependence or dispersion of phonons have been limited to bulk or surface level techniques such as inelastic neutron, x-ray, reflection EELS, or optical spectroscopies. None of these techniques are able to provide phonon dispersion information at the nanoscale[50]. In this work, Hage et. al. tilted the pre-specimen beam to shift the post-specimen diffraction pattern along specific points of interest in the diffraction plane (Fig. 3.15a). However, tilting the pre-specimen beam cause the fast electrons to impinge the sample at non-zero angles to the crystal zone axis which can

modulate phonon intensity and shift energies of phonon modes in unintended ways[59]. Spectra are then acquired at each point along a specific symmetry line and are processed to extract individual modes. These agree with simulated dispersion curves validating the accuracy and feasibility of the technique (Fig. 3.15e,f).

Senga et. al.[51] extended this technique by utilizing post-specimen tilting which does not suffer from the same issues as pre-specimen tilting (Fig. 3.15g). The authors shifted the diffraction patter in the plan of the EELS entrance aperture but using post-specimen lenses and collected spectra at specific points in reciprocal space. The spectra are acquired on BN and graphite and then joined together to form a continuous phonon dispersion curve which has high agreement with simulated ones (Fig. 3.15h,i). More interesting is perhaps their mapping of graphene nanostructures at $q = 3.5$ Å away from the central Γ point. Their results show that the high energy TO/LO modes do not respond strongly to defects and other inhomogeneities and essentially reflect the sample thickness. However, the lower energy acoustic modes are highly sensitive to defects and edges. With this they have demonstrated that optical and acoustic modes have distinct characteristics in nanostructures paving the way for mode-specific engineering of nanostructures.

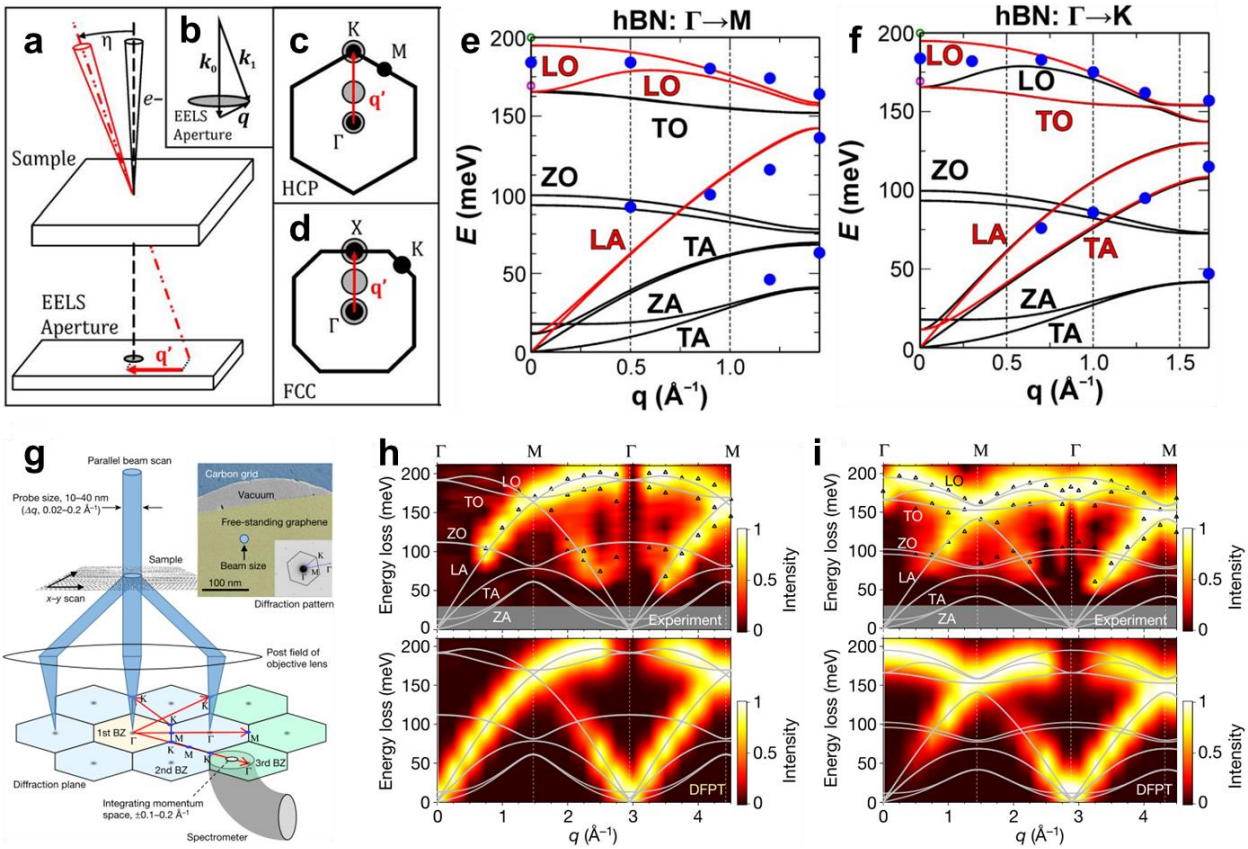

Figure 3.15 Momentum-resolved vibrational EELS by pre- and post-specimen tilting a, by tilting the incident beam by an angle η, the forward scattered beam is effectively displaced with respect to the spectrometer entrance aperture (in momentum space) by a distance and direction given by a wave vector q′. **b**, q as defined by the incident (k_0) and scattered (k_1) wave vectors, for q′→0. **c**, Sketch of the first Brillouin zone of a 2D-projected hexagonal close-packed (HCP) crystal and **d**, a 2D-projected face-centered cubic (FCC) crystal illustrating how effectively displacing the EELS entrance aperture (gray discs) by q′ with respect to the forward scattered beam results in EEL spectrum momentum selectivity. **e-f**, Simulated (full curves) and experimental (blue discs) hBN and cBN phonon dispersions. **g**, Schematic of the experimental set-up. Inset, a typical transmission electron microscopy (TEM) image of the sample and its diffraction pattern, showing a central spot. The EEL spectra are obtained from each spot along several lines, as shown in the lower part of the main panel, with the EELS aperture focused on the diffraction plane. The post field of the objective lens and other imaging lenses were used to form a magnified diffraction pattern. **h-i**, Color-coded intensity maps of graphite and hBN, shown with their respective simulated phonon dispersion curves (solid lines). Peak positions extracted from the measured spectra by line shape analysis are indicated by open triangles in the top panels. The grey regions show experimentally inaccessible energy regions where the peaks are difficult to discriminate from the quasi-elastic line. Panels (a-f) are adapted from Hage, Fredrik S., et al. Science Advances 4.6 (2018): eaar7495 with permission. Copyright 2018 AAAS. Panels (g-i) are adapted from Senga, Ryosuke, et al. Nature 573.7773 (2019): 247-250 with permission. Copyright 2019 Springer Nature.

A recent study took measuring nanoscale phonon dispersions to the next level by measuring them at an interface. Qi and Shi et. al. used a slot-type aperture to acquire phonon dispersion curves in parallel, meaning that shifting to each new k-point and acquiring spectra is not needed and one can acquire entire dispersion curves in one 2D acquisition (Fig. 3.16a). The authors used a cubic BN and diamond heterostructure with an atomically sharp interface to demonstrate what a phonon dispersion looks like at the interface of the two materials (Fig. 3.16a,b).

The measured dispersion showed distinct features for the cubic boron nitride, the interface, and the diamond. The difference between the interface spectra and the average of the two bulk spectra revealed new features at the interface. Interfacial localized modes were observed below 150 meV, where both acoustic and optical branches were recognizable. The acoustic branch had increasing energy from the Brillouin zone center to the boundary, which may aid thermal transport laterally along the interface due to their large group velocity (Fig. 3.16c).

In addition, there was a dispersion line with negative intensity at 150–160 meV, which corresponds to an isolated mode (Fig. 3.16d). The study concludes that the new vibrational modes measured at the interface are expected to substantially affect thermal transport across the interface. The interfacial modes scatter frequently with bulk modes on both sides and thus serve as an intermediate state of energy transfer. In contrast, isolated modes hardly correlate with any mode and give almost no contribution to the interfacial thermal conductance. They have reduced amplitudes at the interface and separate bulk modes in

space, making energy exchange between two materials much harder. Therefore, direct measurement of interfacial and isolated modes can provide useful information for the thermal transport properties for a given interface. This work provides a strong understanding of how dispersions are affected at a single interface and establishes a foundation for experimental understanding of thermal transport across them.

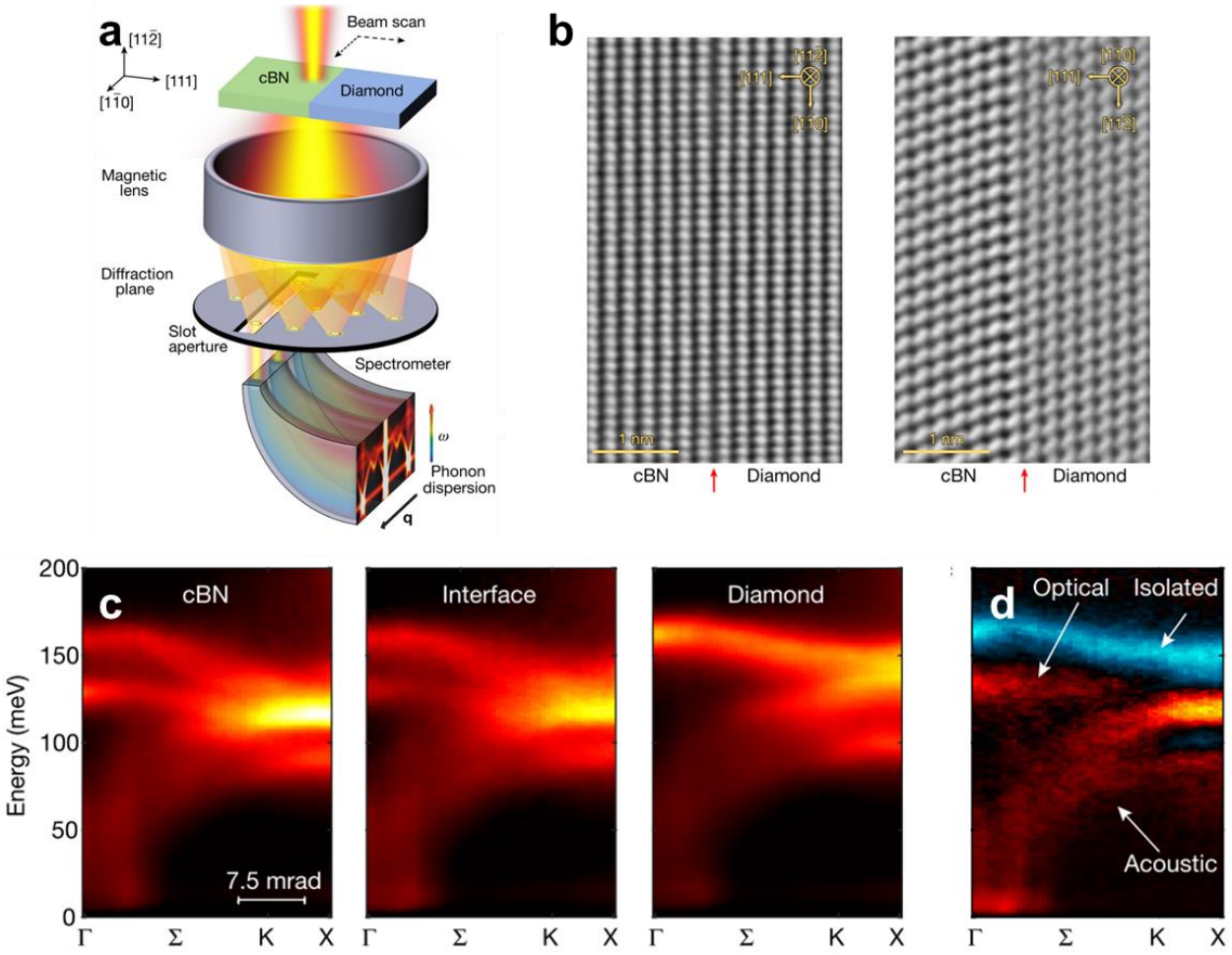

Fig. 3.16 Measuring phonon dispersion at an interface using momentum resolved vibrational EELS and a slot-type aperture a, A schematic of the experimental setup (4D EELS) used to acquire phonon dispersion curves. The slot aperture is placed parallel to the interface, producing dispersion diagrams along the high-symmetry line Γ–Σ–K–X. **b**, iDPC-STEM images of the coherent cBN/ diamond interface, viewed from the [112] zone axis and the [110] zone axis, respectively. The red arrows mark the interface. **c**, the measured phonon dispersion diagrams along the Γ–Σ–K–X line with the beam located in cBN (left), at the

interface (middle) and in diamond (right). Figure is adapted from Qi, Ruishi, et al. Nature 599.7885 (2021): 399-403 with permission.

Chapter 4

Nanoscale imaging of phonon dynamics by electron microscopy

4.1 Introduction

Our ability to engineer devices that span a few nanometers has outpaced our understanding of their detailed inner workings. Most notably, direct evidence of how nanostructures impede phonons has not been carefully studied. Light-based spectroscopies have been excellent for determining aggregate phenomena induced by these crystal inhomogeneities but fall short of telling us how individual nanostructures, for example, scatter phonons. This is because these atomic-scale features (on the order of a billionth of a meter) are much smaller than the wavelength of visible light (on the order of a millionth of a meter) rendering them invisible to these optical techniques. In short, the progress of nanoengineering has outpaced the advancements in microscopy and spectroscopy. Although theoretical models suffer no such drawback, they remain unverified by experiments that can peer into the nanoscale universe. As a result, a detailed experimental study of the atomic scale structure and how it effectively impedes vibrational waves was completely absent before this work.

Interfacial phonon scattering is a subject of intensive study and has been largely carried out via modeling and simulation, combined with experimental measurement of the effective

thermal conductivity of many layers[61–63], rather than direct imaging of phonons. Although it is understood that phonon reflection at an interface is responsible for thermal boundary resistance[64], there is no direct experimental observation of local phonon reflection. Raman spectroscopy has been used to study strain and compositional effects on phonons in SiGe superlattices[65,66], while time-domain thermoreflectance measurements have been conducted to investigate thermal conductivity via ballistic transport[67]. However, both techniques lack spatial and momentum resolutions needed to study phonon dynamics of individual nanostructures and interfaces. Therefore, an experimental technique that probes nanoscale vibrational properties with high spatial, momentum, and energy resolutions is vital for deepening the understanding of nanoscale phonon transport physics.

Electron microscopes have a tremendous advantage over traditional methods of investigation due to their ability to resolve atoms. However, until 2014, there was no method of probing well-resolved vibrational information at that scale[43]. Since then, vibrational spectroscopy in the electron microscope has become a powerful tool for studying the vibrational properties of crystal defects and other inhomogeneities. In this work, we have utilized this powerful capability and developed special techniques that will hasten the pace of thermoelectric research.

Recent advances in monochromated electron microscopy have enabled the spectroscopy of vibrational excitations at the nanometer[43] and even atomic[53,59] scales. So far, 2D mapping of surface and bulk excitations[48] and detection of single-atom[54] and defect[49] vibrational signals have been achieved. Although dipole scattering in polar materials such as BN[51,53,68], MgO[48], and SiC[43,69], under on-axis STEM-EELS geometry produces long-range and non-local

polariton modes reducing the atomic scale contrast in vibrational EELS signal mapping[70], dipole scattered signals are significantly suppressed and negligible in elemental and homopolar materials with weak dipoles such as Si[59] and SiGe, which only contain highly localized phonon scattering. Here, we report quantitative high spatial resolution mapping of phonons in SiGe QDs using an on-axis beam-detector geometry (Fig. 3.7).

4.2 Quantum dot morphology and phonons in Si and SiGe

In this work, we investigated a system of stacked silicon-germanium (SiGe) alloy quantum dots (QD) separated by silicon. This system employs all 3 phonon impedance strategies: disordered alloying of silicon and germanium within the QD, interfaces between the silicon-germanium QD and surrounding silicon, and the QD nanostructure itself. The alloying creates a highly compositionally disordered structure whereby silicon phonons cannot propagate efficiently.

The quantum dot sample was grown at 600 °C in an ultra-high vacuum chemical vapor deposition (UHV/CVD) system. For Ge and Si depositions, pure GeH_4 and SiH_4 gases were used as precursors, respectively. The Si wafers were first etched in a diluted HF solution to create a hydrogen-passivated surface prior to deposition. After the deposition of a 50-nm-thick buffer layer of Si, Ge layers were grown with 20 nm Si spacer layers in between each Ge quantum dot layer for the formation of self -assembled conventional QDs. For investigating thermal stability and tunability of the structural parameters, *in-situ* post deposition annealing was conducted at the growth temperature for 1 hour. The final product was a thin-film-like material of 40-period multifold QDs stacks with a thickness as high as

~1.2 μm. QD nanostructures spanned 70–90 nm across and were 6–8 nm thick. A comprehensive morphological characterization is presented in Fig. 4.1. The SiGe QDs have a diamond-like structure like that of Si and Ge with a random and disordered arrangement of Si and Ge atoms. More details of the growth process can be found in Ref.[71]. The cross-sectional TEM sample used in this study was prepared by focused ion beam milling while the planar-view TEM sample was prepared by mechanical polishing. The QD interfaces were normal to the (001) crystallographic plane while the zone axis was along the [110] crystallographic direction. Of all the QD's investigated several of them were elongated by up to 10-15% (Figs. 4.1g,h) in no particularly consistent direction. However, there are some quite symmetric SiGe QD's (Fig. 4.1i).

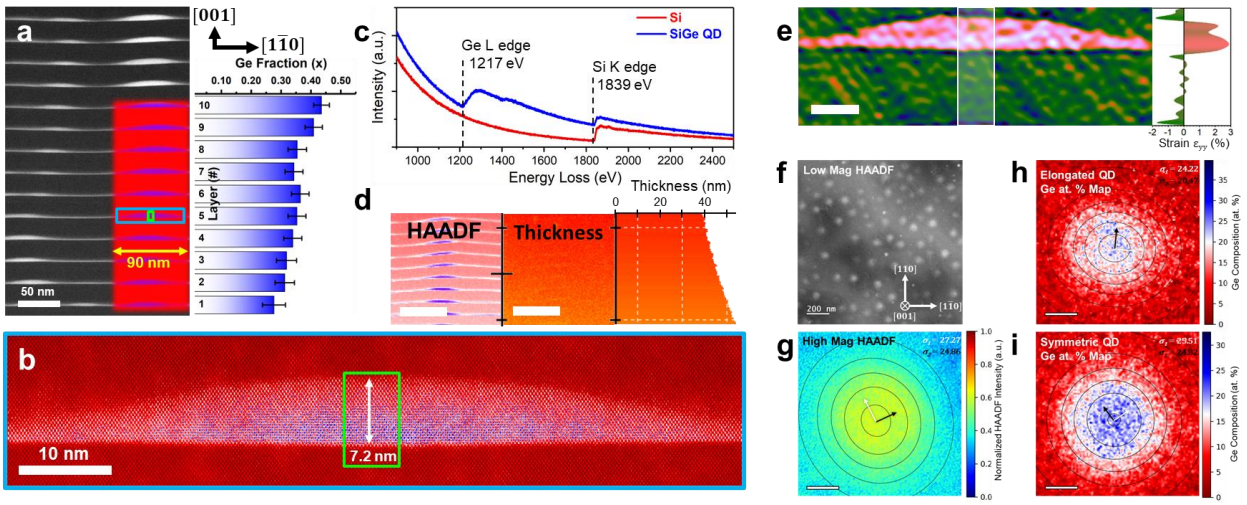

Figure 4.1 STEM characterization of quantum dot layers. a, Low-magnification STEM image of SiGe QD superlattice. Due to the Z-contrast property of HAADF imaging, the bright regions are SiGe, while the darker regions are interlayer Si. The crystal orientations are indicated as [001] for the growth direction and [110] for the lateral, planar direction. A HAADF image of the first 10 layers from the Si substrate is superimposed with an elemental EELS map. Red and blue indicate silicon and germanium concentration, respectively. The histogram plot to the right displays Ge composition fraction of the corresponding 10 layers. **b**, HAADF image of a single QD from the blue region in (a) showing dome-like structure and dislocation-free interfaces. The green box denotes the region in Fig. 4.2a. **c**, Core-loss EEL spectra of interlayer Si and SiGe QD. **d**, Low-magnification HAADF image with associated thickness mapping and horizontally averaged thickness profile. QDs studied in this work were chosen in the 40–50

nm thickness range. Scale bar is 100 nm. **e**, Strain mapping of QD in b and interlayer Si using geometrical phase analysis (GPA) with associated line profile of the horizontally integrated region marked by the white box. Reference strain of 0% was chosen to be that of interlayer Si. Scale bar is 10 nm. **f**, Low-magnification HAADF image of several planar-view QDs with the associated crystal directions. **g**, High magnification HAADF image of a single QD showing a slight elongation of 8.8%. **h**, **i**, High resolution EELS Ge composition maps showing 15.5% (h) and 2.68% (i) elongation, respectively. The variances in the lateral direction were obtained via 2D Gaussian fitting. The white and black arrows denote long and short axes, respectively. The scale bars in **g**–**i** are 20 nm.

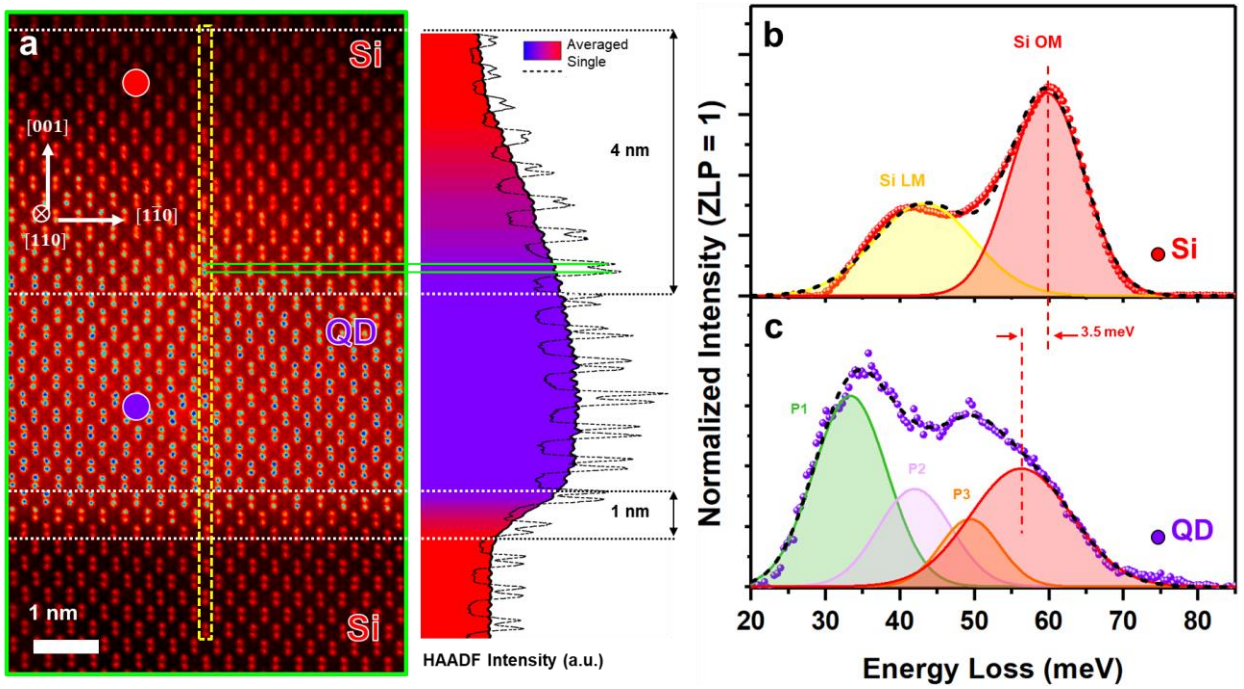

Figure 4.2 Atomic structure and vibrational spectra of SiGe QD and Si-SiGe interfaces. a, Atomic resolution high-angle annular dark field (HAADF) image containing both top and bottom QD interfaces from the region outlined in green in Fig. 4.1b. Line profile of a single array of atomic columns to the right is overlaid with a horizontally averaged profile of the entire image showing a gradual interface 4 nm wide and an abrupt one 1 nm wide for the top and bottom QD interfaces, respectively, estimated by the 10-90% criterion. [001] denotes the growth direction and is perpendicular to the interfaces, [1$\bar{1}$0] denotes a direction that is parallel to the interfaces, and [110] denotes the beam direction which points into the page. **b, c**, Background subtracted, pseudo-Voigt peak separated vibrational spectra of interlayer Si and SiGe QD from locations denoted by the red and blue dots in **a**, respectively. The low energy mode (LM) represents a combination of Si longitudinal acoustic (LA) and LO modes while optical mode (OM) represents a combination of Si TO and LO modes. Due to the complex band structure inside the QD, we label the first 3 peaks shown here as P1, P2, and P3 with the 4th peak labeled as Si OM.

Each QD has a dome-like interface at the top and a flat interface at the bottom (Fig. 4.1b) due to how the SiGe QD system was engineered. These results (Fig. 4.1) are similar to previous results supported by atomic force microscopy (AFM) and TEM characterizations[71,72]. Due to the Z-contrast property of high-angle annular dark field (HAADF) STEM imaging, the HAADF intensity can reflect the composition information of local regions. Utilizing this property, the widths of the top and bottom interfaces were measured to be about 4 nm and 1 nm, respectively (Fig. 4.2a). The dome-like interface at the top of the QD and flat interface at the bottom, closer to the substrate, are henceforth denoted as the gradual and abrupt interfaces, respectively. Elemental mapping results provide similar evidence of asymmetric Ge distribution inside the QDs as well and can be explained by Si diffusion from the top into the Ge layer during growth. Ge fractional composition, obtained by analyzing the core-loss EELS of Si K edge and Ge L edge (Fig. 4.1c), varies almost monotonically with increasing layer number in the first several layers (Fig. 4.1a) due to the growth conditions of the SiGe QD superlattice structure. Si undergoes thermal and strain activated diffusion into the SiGe QDs generating alloyed nanostructures[73]. As a result, SiGe QD layers closer to the substrate, which were grown first, experience higher amounts of Si diffusion than those that are farther away. The varying composition of these QDs offers an interesting opportunity utilizing high resolution vibrational electron microscopy to investigate alloying effects on local vibration within a single sample, which is not possible for macroscopic optical methods[66,74–76].

To study the compositional strain inside the QD, vibrational EEL spectra were acquired using an on-axis beam-detector geometry (Fig. 3.7). In the interlayer pure Si, two distinct Si-Si vibrational peaks are visible (Fig. 4.2b) after spectra processing (more information in the data analysis section). The peak located at 59.8 ± 0.2 meV belongs to Si transverse and

longitudinal optical (TO and LO) modes, denoted as OM, and another peak to the left which we classify as the low energy mode (LM) signal with an energy of 43.2 $\pm$ 0.4 meV (LA and optical phonon modes near zone edges). Inside the SiGe QD, the calculated phonon density of states (DOS) in the SiGe region in Fig. 4.3 suggests that there are 4 separable modes in the 20–80 meV range corresponding to the various combined vibrations of the Si and Ge atoms in the SiGe alloy QD (Fig. 4.2c). Of these, the Si OM energy is redshifted to a value of 56.3 $\pm$ 0.3 meV due to the surrounding Ge atoms which lead to a larger reduced mass.

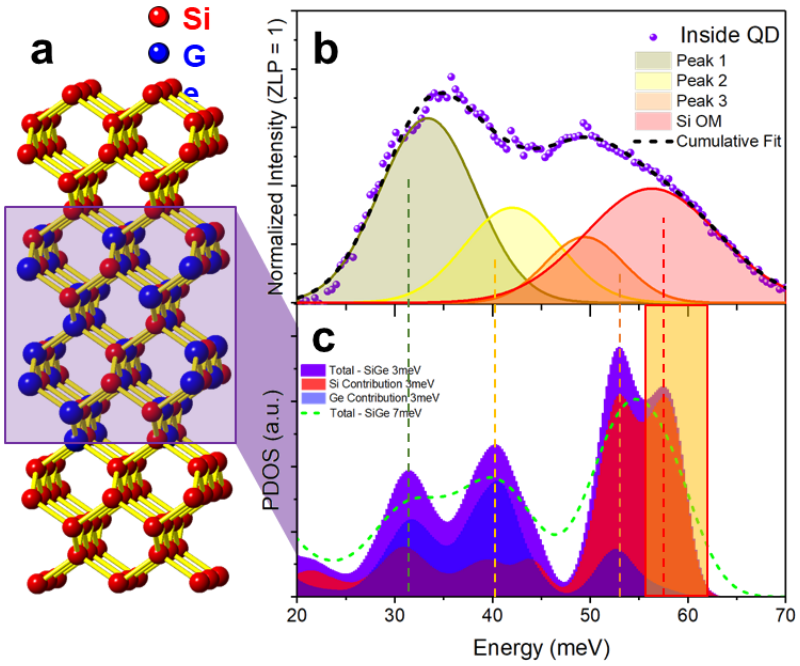

Figure 4.3 Convolved Density of states informing peak decomposition. a, Atomic structure of Si-SiGe abrupt interface. **b**, Background subtracted, pseudo-Voigt peak separated vibrational spectra of SiGe QD. **c**, 3meV-gaussian-convolved phonon DOS of the $Si_{0.5}Ge_{0.5}$ region in **a** and its projected 3meV-gaussian-convolved phonon DOS curves of Si and Ge. A 7meV-gaussian-convolved phonon DOS of the same region matching the experimental energy resolution is overlaid in green. The colored dashed lines show that positions of the prominent peaks in the phonon DOS match with the 4-peak decomposition of the experimental EELS data in **e**. The yellow box highlights the fact that the highest energy mode is almost entirely comprised of Si contribution to the modes in that energy region. The energy discrepancy between experimental data and theoretical model may arise from the different chemical composition and varied disordered structure.

There is a 5 meV discrepancy between Si OM energies from Raman (64.8 meV in Fig. 1.2j) and EELS (59.8 meV in Fig. 4.2b) in the pure Si region. This energy offset is accounted for by noting our experimental conditions (Fig. 3.7). Since 33 mrad and 25 mrad convergence and collection semi-angles were used, electrons scattered at angles beyond even the second Brillouin zone (BZ) are included; a similar EELS configuration was used by K. Venkatraman *et al.*[59] and can be considered a momentum averaged EELS acquisition geometry. While Raman spectroscopy only probes near-zero momentum phonons at the BZ center due to the low momentum of visible-light photons, vibrational EELS in our configuration probes phonons of all momenta thus producing the discrepancy between our results and those in Raman literature. The calculated phonon densities of states (Figs. 1.2g,i) match well with Figs. 4.2b,c while also correctly capturing the momentum averaged Si OM peak position.

Since silicon atoms are closer together than germanium atoms in their respective pure structures, the alloy stretches the silicon atoms a bit. Due to this strain, the optical modes are softened in the quantum dot due to the strain and alloying engineered within the nanostructure. Softened phonons have less energy which means that each phonon carries less heat, reducing thermal conductivity as a result. The softening of vibrations is behind one of the many mechanisms of how thermoelectrics impede the flow of heat.

4.3 Compositional energy shift of the Si optical mode

Vibrational EELS allows for the nanometer correlation of elemental and vibrational information (Figs. 4.4a, b). Both the composition and Si OM peak position maps were taken from the same QD. The 80 × 15 nm dimensions of the Si OM energy shift map covers nearly

the entire QD as well as surrounding interlayer Si and matches well with the QD shape confirming high spatial resolution. The Si OM energy shift is non-uniform inside the QD and has excellent tracking with the QD's Ge composition: Si OM energy shift is highest where the Ge content is highest (Fig. 4.4c) with a maximum red shift of 3.88 meV. The asymmetry that is reflected in the 2D composition map is observed in the energy shift map and consistent with the observation in Fig. 4.2a. Meanwhile, we see that that bottom interface of the QD is much more abrupt than dome interface at the top, consistent with the aforementioned diffusion mechanism of the superlattice structure. Although 1D nanoscale composition of SiGe structures have been obtained[77], we employ 2D spatial composition mapping and correlate it with the composition-induced vibrational energy shift.

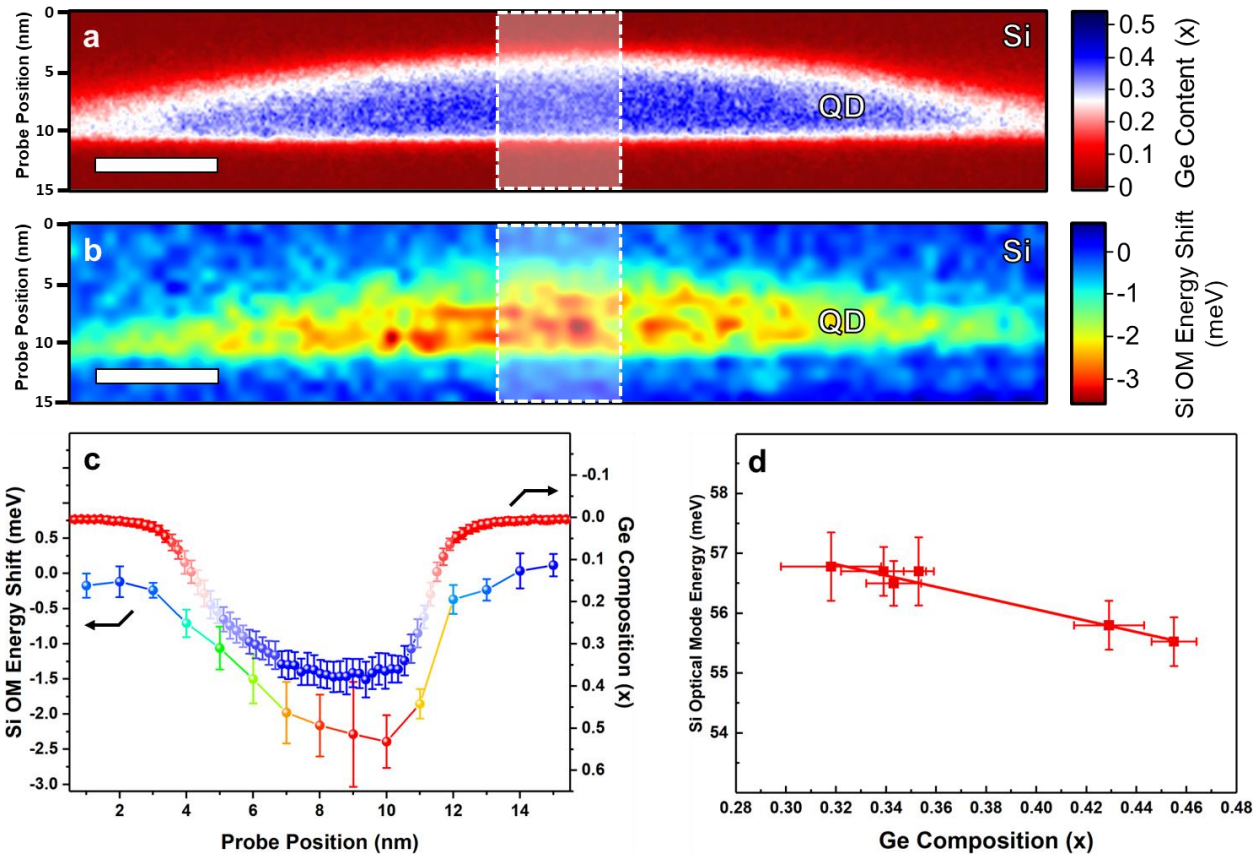

Figure 4.4 Spatial mapping of Ge concentration and Si OM energy shift in a single QD. a, Map of Ge composition acquired by core-loss EELS. The white contrast in the color map makes it easy to see relatively how far the interface extends around the QD. The red and blue colors indicate nearly 0 and 50 at. % Ge concentration, respectively. **b**, Two-dimensional spatial mapping of Si OM energy shift from a nominal value of 58.9 meV of a single QD. The blue and red color extremes denote standard and shifted energies, respectively. Scale bars in **a** and **b** are 10 nm. **c**, 10 horizontal-pixel-averaged 1D profiles of Ge composition (red-blue) and Si OM energy shift (colored) matching the color schemes of their respective maps. Energy shifts are obtained by subtracting 58.9 meV (average phonon energy in the surrounding Si) from all measured Si OM energy values. **d**, Peak positions of Si OM in several QDs as germanium concentration (x) in the center of the QD increases.

Furthermore, effects of varying composition across several QDs were investigated in a single sample effectively limiting the number of free variables in our experimental setup. Fig. 4.4d shows the energy shift trend of the Si OM as a function of the Ge composition (x) at the center of corresponding QD's. Our data expresses a linear trend with a slope of -9.3 $\pm$ 1.09 meV/x lying within accepted values in literature with values obtained by Raman spectroscopy ranging from -7.7 to -8.8 meV/x[66,74–76] and a y-intercept of 59.8 $\pm$ 0.4 meV matching well with the momentum averaged Si OM energy in pure Si.

4.4 Intensity enhancement of the Si optical mode

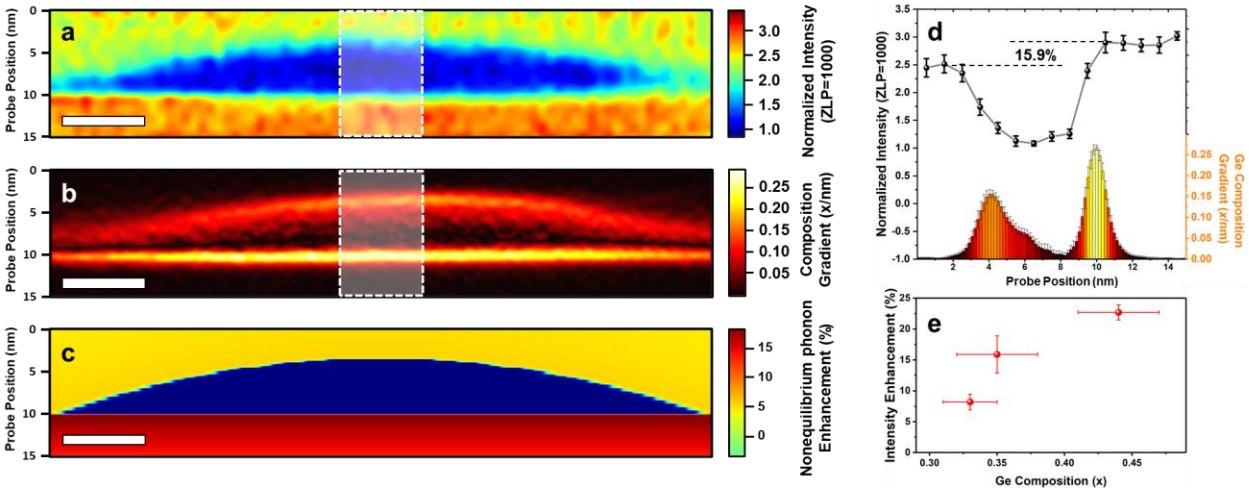

Fig. 4.5 Asymmetric spectral intensities of Si OM near the gradual and abrupt interfaces. a, Two-dimensional spatial map of Si OM intensity of a 35 at. % average Ge composition QD. The red and blue contrast extremes denote high and low relative mode intensities. **b**, Absolute value of the vertical gradient of the elemental map in Fig. 4.4a, emphasizing relative interface abruptness. The dashed arrows show the direction of the 1D profiles. **c**, Boltzmann transport simulated mapping of nonequilibrium phonon enhancement of Si OM with top interface $SR = 0$ and bottom interface $SR = 1$. Simulation was conducted only for the Si side and only normal incident phonons are considered. Phonons with oblique incidence do not contribute to the enhancement of EELS intensity. The red color in the map denotes a greater enhancement of non-equilibrium phonons. Scale bars in **a-c** are 10 nm. **d**, 10 horizontal-pixel-averaged 1D profiles of the maps in **a** and **b**. The 1D intensity line profile of **a** is plotted with the histogram profile of **b**. **e,** Plot of Si OM intensity enhancement as a function of maximal Ge composition in the QD.

Fig. 4.5a displays a 2D intensity mapping of the Si OM obtained from the same QD as in Fig. 4.4b. A striking feature is that the Si OM at the bottom interlayer Si has a 15.9% intensity enhancement relative to that at the top one, highlighted in Fig. 4.5d, despite there being no compositional variance in the interlayer Si as evidenced by Fig. 4.4a. We posit that the source of this enhancement arises from the distinct scattering dynamics due to the two differing interfaces: an abrupt bottom interface and a gradual top interface (Figs. 4.5c,d). The

momentum averaged scattering cross section is given by $\sigma = \int \sigma(\omega, \boldsymbol{q})\, d\boldsymbol{q}$[51] and the momentum-resolved Stokes scattering probability of fast electrons due to the lattice vibration near an interface has been derived.

To explain the experimental intensity enhancement, the local variations of equilibrium phonon population $n_{\boldsymbol{q},\nu}$, where $\boldsymbol{q}$ denotes the phonon momentum and ν denotes a certain phonon branch, and local density of states (LDOS) were considered individually. Since the beam-induced temperature rise is negligible (see more details in Appendix A), $n_{\boldsymbol{q},\nu}$ is constant in two Si regions near the abrupt and gradual interfaces. The computed LDOS showed no intensity enhancement likely due to the unchanged composition (Fig. A.1). Hence, the local non-equilibrium phonon occupation $f_{\boldsymbol{q}\nu}$ is determined to be a significant factor for producing the intensity enhancement below the abrupt interface in Fig. 4.5a (see more details in Appendix A). The nonequilibrium phonon occupation consists of two parts $f_{\boldsymbol{q},\nu} = f_{\boldsymbol{q},\nu,0} + g_{\boldsymbol{q},\nu}$, with $f_{\boldsymbol{q},\nu,0}$ being the equilibrium Bose-Einstein distribution ($n_{\boldsymbol{q},\nu}$) at room temperature and $g_{\boldsymbol{q}\nu}$ being the population deviation from equilibrium due to electron energy loss and interface reflections.

Near the interfaces, optical phonons in the Si side are reflected by the interface due to mode mismatch. Thus, the population deviation $g_{\boldsymbol{q},\nu}$ can be further decomposed into two parts as the phonons emanating from the electron beam g_0 and the specularly reflected phonons from interface. We use Boltzmann transport equation to solve for population deviation g and find that $g = g_0 + D\,S\,R \exp(-2b/\Lambda)$, where D is a prefactor, S and R are the specularity parameter and reflectance of the interface, respectively, b is the distance to interface, and Λ is the phonon mean free path (MFP). From atomistic Green's function calculation, we find minimal

difference in the reflectance for an abrupt interface and a gradual interface as a function of nanostructure curvature. Thus, we conclude that the difference in the nonequilibrium phonon population must be attributed to the difference in S of the abrupt interface and the gradual interface. Our BTE simulation shows that the EELS intensity enhancement is attributed to higher S of the abrupt interface than gradual interface. As the Ge content in the QD is increased, the composition change at the abrupt interface becomes more drastic leading to an intensity enhancement that exhibits a monotonic relationship with increasing Ge composition inside the QD, shown by Fig. 4.5e.

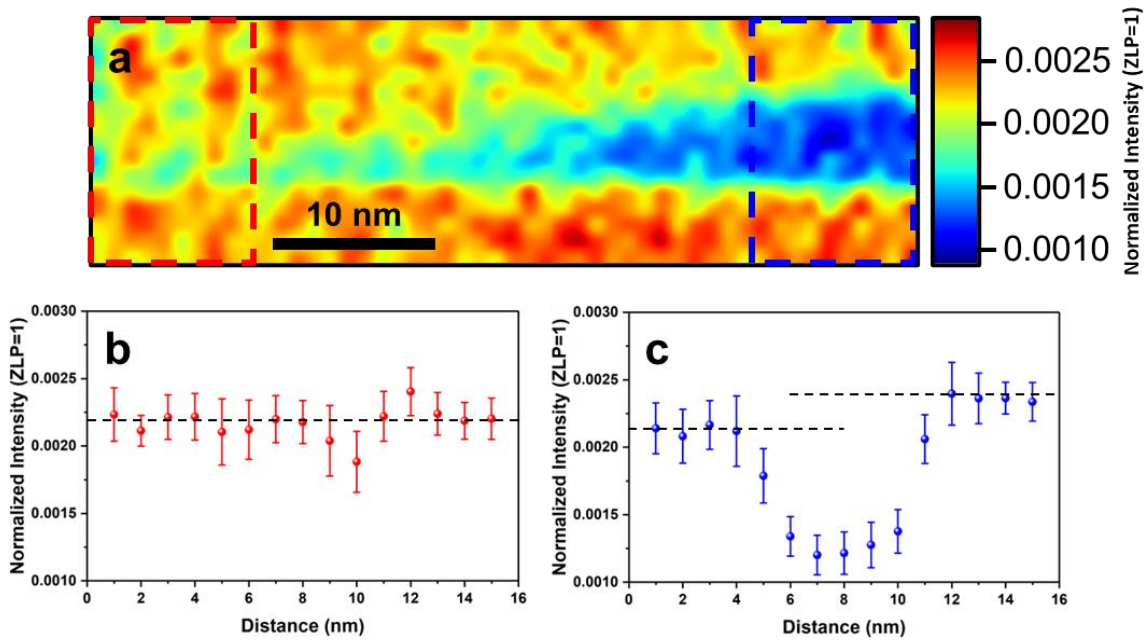

Figure 4.6. Phonon map of QD side. (**A**) Spatial mapping of Si phonon peak intensity of the side of a QD. (**B**) Integrated line profile of the left-hand side of the map (red) showing consistent intensity above and below the QD edge. (**C**) Integrated line profile of the right-hand side of the map (blue) showing an intensity discrepancy above and below the QD. The dashed lines in **A** and **C** show the intensity discrepancy in the middle QD region and consistent intensity in the side region.

We also see from Fig. 4.6 that the enhancement fades as phonons at the end of the QD are probed. Here the gradual and abrupt interfaces are less pronounced and nearly identical. The

thinner interface may have a smaller reflectance thus reducing the reflected phonon population equally on either side of the interface.

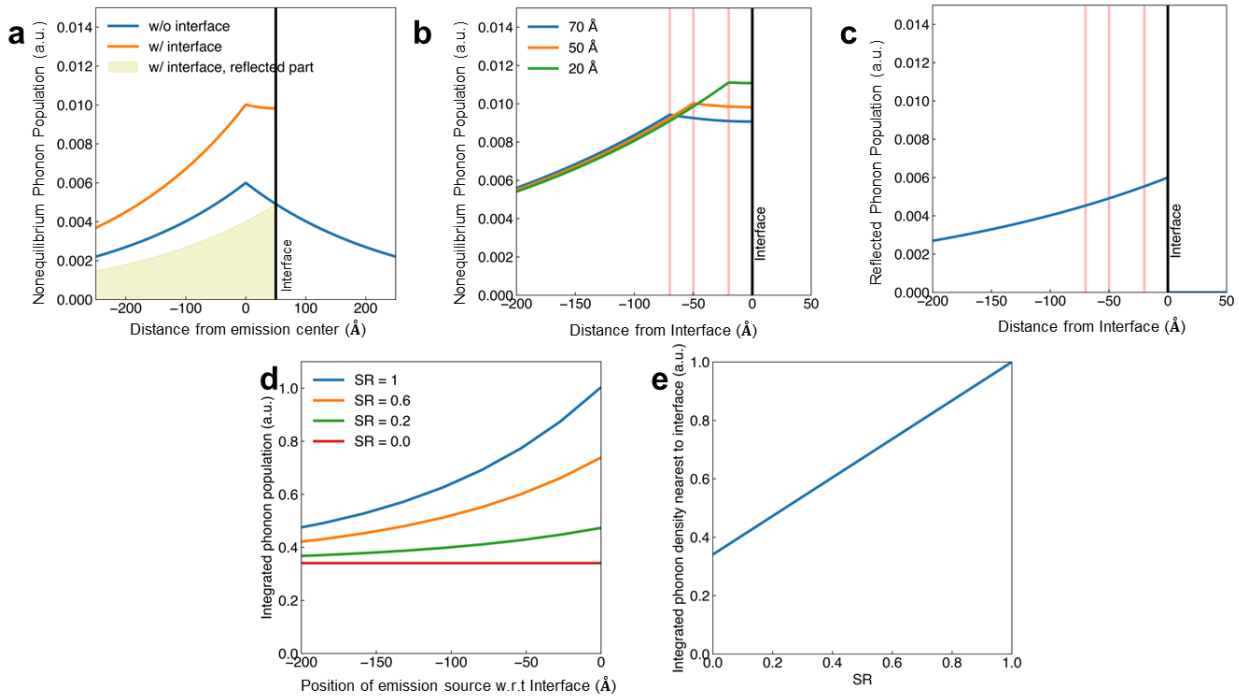

Figure 4.7 Effect of interface specularity on phonon decay. a, The total nonequilibrium phonon distribution function with and without the presence of an interface, and phonons that are reflected by the interface with flipped velocity direction. The blue curve describes the phonon distribution function when there is no interface. The light-yellow filled region describes the reflected phonons' contribution to phonon distribution, which only exist in the proximity of interface. The orange line is the phonon distribution when including the contribution of reflected phonons. The phonon emission source is placed at 0, black line indicates the location of interface. **b**, When moving the phonon emission source (marked by red bar), the phonon distribution function has a different profile. Three cases with different distances to the interface is plotted. The longer the distance from the interface, the lower the peak of the distribution, due to increasingly smaller contributions from reflected phonons. **c**, Plot of integrated area in red in plot **b** as a function of distance from the interface. The reflected phonon distribution has an exponential decay profile away from interface and changing the beam position will probe different amount of reflected nonequilibrium phonon. **d**, The integrated phonon population profile at various parameters of SR. **e**, The integrated phonon population at the position closest to the interface as a function of parameter SR. The integration is conducted within the radius of a.

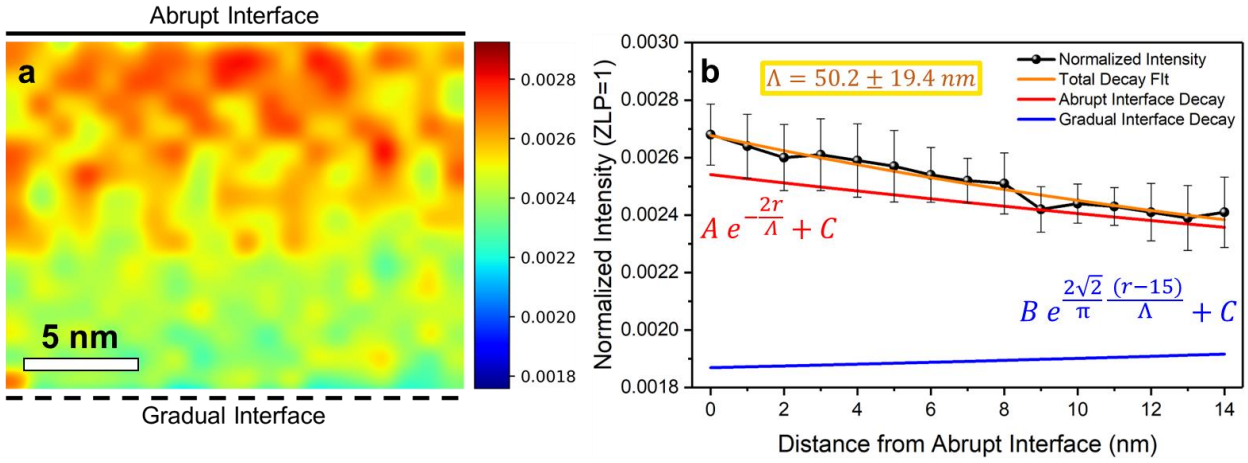

Figure 4.8 Interlayer Si Phonon map. a, A 20 x 15 nm map of Si phonon peak intensity in the interlayer Si region bounded by two QDs. **b**, Integrated 1D line profile of **a** with exponential decay fitting. Red and blue curves represent decay of phonon population as a function of distance from abrupt and gradual interfaces, respectively. The constants A and B represent the total phonon population at the edge of sharp and smooth interfaces, respectively. The constant C represents the equilibrium phonon population following the Bose-Einstein distribution. The orange curve is the sum of the red and blue curves. Parameters A and B were fit to the data and represent the reflection intensity in the immediate vicinity of the interface while C was taken to represent the equilibrium phonon population that the non-equilibrium population would eventually decay to. The measured value for Si OM MFP is 57.0±19.4 nm where the uncertainty of each point is considered factored into the total error.

Additionally, phonon reflection can be used to study phonon MFP (Figs. 4.7 and 4.8). The reflection-induced nonequilibrium phonon population g' decays as a function of distance from the interface with the decay length being the MFP of the Si OM (Fig. 4.7). A 20×15 nm mapping of the interlayer Si bounded by two QDs illustrates a gradual change in the Si OM intensity (Fig. 4.8). The top of the region is bounded by an abrupt interface while the bottom is bounded by a gradual interface. With the consideration that both interfaces have some degree of specularity, the data was fit with the sum of the two exponential decays arising from both the interfaces. With the fit, we obtained a MFP (Λ) value of 50.2 ±19.4 nm for the Si OM which is around an order of magnitude of accepted values being in the range of tens of

nanometers[78], demonstrating that MFP of phonons can be measured at nanometer resolution.

4.5 Differential phonon momentum (DPM)

Well-established momentum-resolved approaches can measure phonon dispersion curves along certain reciprocal directions and reveal the local spectral variation induced by exotic phonon modes. However, such approaches cannot identify the direction of phonon propagation, which is essential for understanding the heat transport in real devices. To obtain the propagation direction of specific phonons, we develop a DMP method by subtracting phonon states at opposite reciprocal locations. Although the state-of-the-art methods in momentum resolved vibrational EELS have had great success in measuring phonon dispersion curves[51], and studying nanoscale defect modes[49], they have not yet taken advantage of the momentum polarization selection that becomes available in this configuration.

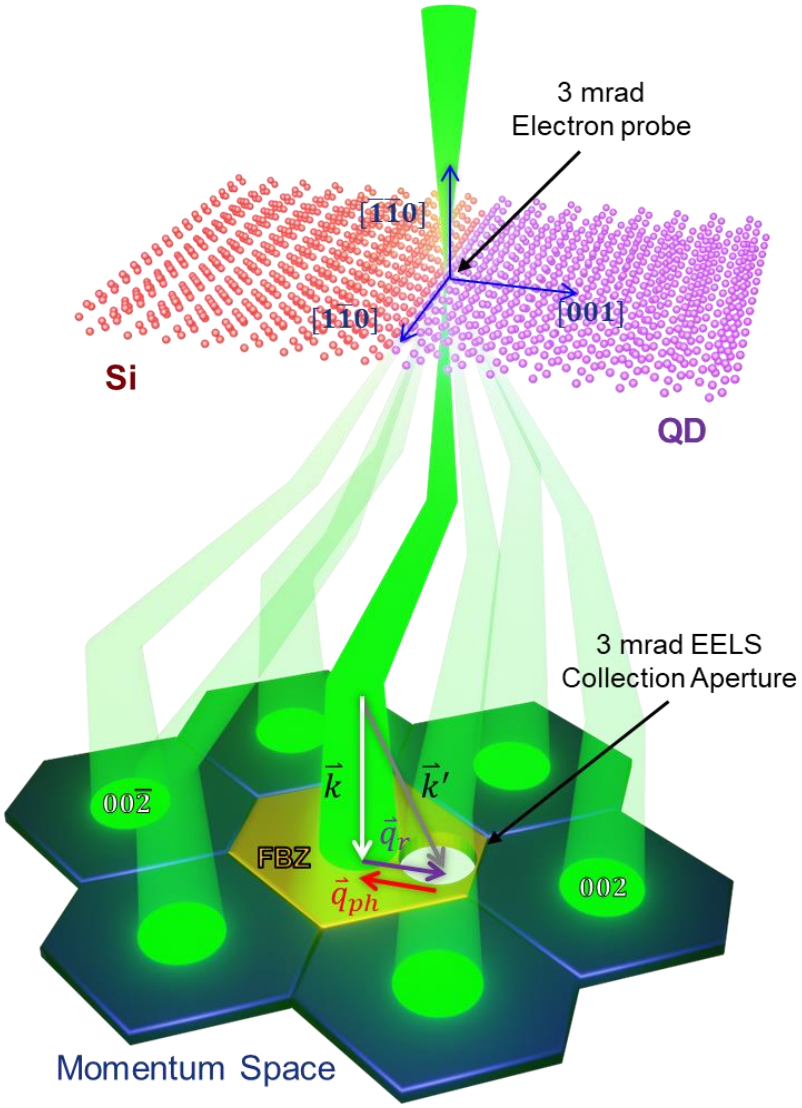

Figure 4.9. Experimental beam geometry for differential phonon momentum (DPM) mapping a, Schematic of the experimental beam geometry showing an off-axis position of the EELS aperture in the first Brillion Zone (FBZ) of Si, achieved via post specimen tilting of the scattered electron beam. The crystal axes are superimposed on the Si-QD crystal structure, and the momentum conservation vectors of the electron-phonon energy exchange process are superimposed on the momentum space portion of the diagram. Electron scattering wavevector diagram illustrates the fast electron-phonon momentum transfer. Under these momentum-resolved experimental conditions, $\boldsymbol{q} \approx \boldsymbol{q_r}$ meaning that momentum of generated phonons is predominantly in the in-plane direction (perpendicular to the interface) and has an opposite sign to the momentum change of the electron beam.

To recover directional and momentum information and elucidate phonon dynamics at the QD interfaces, a momentum-resolved beam-detector geometry was employed (Fig. 4.9) to obtain a differential phonon momentum (DPM) map. A convergence semi-angle of 3 mrad (momentum resolution of 0.5 $Å^{-1}$) was used here which was about 1/3 the size of the Si BZ as shown in Fig. 4.10a allowing for momentum resolution while the 33 mrad area encompasses even neighboring BZ's. Integrated spectral intensity in the 55–65 meV region (Si OM) in the red and blue regions represents Si OM phonons created by electrons deflected towards the 002 (Δ_+) and $00\bar{2}$ (Δ_-) regions in reciprocal space, respectively (Figs. 4.10b,c).

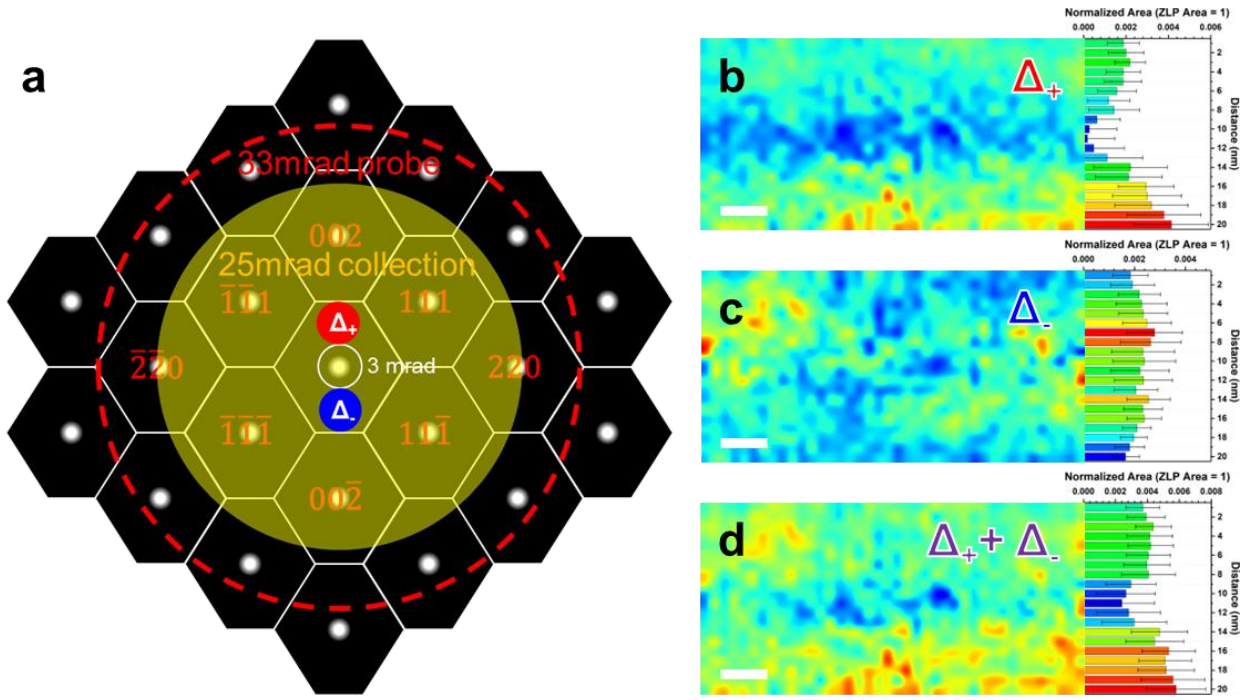

Figure 4.10 Momentum resolved experimental beam geometry. a, Reciprocal space schematic diagram of Si. White borders denote individual Brillion zones (BZ) with the BZ's near the center labeled. White spots at the center of each BZ depict areas of dominant elastically scattered electrons while the black background is dominated by inelastically scattered electrons. Various beam-detector geometries corresponding to momentum-averaged and momentum-resolved conditions are denoted by circles with their size in semi-angle labeled. Red and blue regions in the FBZ correspond to the areas where momentum

resolved differential data was obtained. **b-c**, Mapping of integrated background subtracted spectral intensity in the 55-65 meV region acquired from electrons deflected towards the 002 (Δ_+) and $00\bar{2}$ (Δ_-) crystal direction corresponding to the red and blue regions in (a) respectively. **d**, Combined spectral intensity of Si OM peaks from Δ_+ and Δ_-. Phonon momenta are taken to be in the opposite direction of electron deflection. Scale bars denote 5 nm.

A theoretical description of DPM imaging begins with the EELS scattering cross section, which considers the non-equilibrium phonons by replacing the equilibrium phonon occupation $n_{\boldsymbol{q},\nu}$ with the complete phonon population $f_{\boldsymbol{q},\nu} = n_{\boldsymbol{q},\nu} + g_{\boldsymbol{q},\nu}$, where $g_{\boldsymbol{q},\nu}$ denotes only the non-equilibrium contribution:

$$\frac{d^2\sigma\,(\boldsymbol{q},\omega)}{d\Omega\,d\omega} = \frac{4}{{a_0}^2}\frac{\hbar}{q^2}\sum_{\nu}\frac{f_{\boldsymbol{q},\nu}+1}{\omega_{\boldsymbol{q},\nu}}\left|\sum_i \frac{1}{\sqrt{M_i}}F_i(\boldsymbol{q})\;\boldsymbol{q}\cdot e_{\boldsymbol{q},\nu}e^{-iq\cdot\tau_i}\right|^2 \delta\big(\omega-\omega_{\boldsymbol{q},\nu}\big). \tag{1}$$

Here, a_0 is the Bohr radius, $\hbar$ is reduced Planck's constant, $\boldsymbol{q}$ is the momentum transfer, $\omega_{\boldsymbol{q},\nu}$ is the phonon frequency for momentum transfer $\boldsymbol{q}$ and phonon branch ν, M_i and $\boldsymbol{\tau}_i$ are the atomic mass and position, $F_i(\boldsymbol{q})$ is the component in the Fourier transform of the charge density associated with atom i, and $\boldsymbol{e}_{\boldsymbol{q},\nu}$ represents the eigenvector for atom i with mass M_i.

Then we perform integration over the energy of the Si OM and over the physical aperture size and location in momentum space. We replace ν with Si OM as well. We then get an expression for the EELS phonon intensity in the DMP spectra:

$$I_{\mathrm{DMP}} = -\frac{4\hbar}{{a_0}^2}\int_{\omega_{\mathrm{Si\,OM}}} d\omega\left(\int_{\Delta_+}-\int_{\Delta_-}\right)\frac{d\Omega}{q^2}\frac{f_{\boldsymbol{q},\mathrm{Si\,OM}}+1}{\omega_{\boldsymbol{q},\mathrm{Si\,OM}}}\left|\sum_i\frac{1}{\sqrt{M_i}}F_i(\boldsymbol{q})\;\boldsymbol{q}\cdot e_{q,\mathrm{Si\,OM}}e^{-iq\cdot\tau_i}\right|^2\delta\big(\omega-\omega_{q,\mathrm{Si\,OM}}\big). \tag{2}$$

The key aspect of this expression is the differential across the diametrically opposed aperture locations and the non-equilibrium phonon population. The specularity of interfaces creates an anisotropy in the non-equilibrium phonon population which provides the contrast in the DPM map.

When compared to the on-axis, momentum-averaged mapping in Fig. 4.5a, the intensity of the Si OM mode is higher in the QD for the Δ_- region than the interlayer Si despite a lower Si concentration suggesting that there is a stronger preference for phonons to have a downward momentum in the QD. The same intensity enhancement as seen in Fig. 4.5a is recovered when intensity from summing both Δ_+ and Δ_- regions (Fig. 4.6d).

4.6 Phonon reflection from a Si-SiGe interface

To recover directional and momentum information and elucidate phonon dynamics at the QD interfaces, a momentum-resolved beam-detector geometry was employed (Fig. 4.9) using a 3mrad convergence semi-angle[49,50] to obtain a differential phonon momentum (DPM) map. Mapping the difference and considering momentum conservation (the phonon momentum vector is opposite to that of the electron momentum change direction as shown in Fig. 4.11b), a DPM map in the vertical direction is generated and phonon momenta directions are experimentally imaged at the nanoscale for the first time.

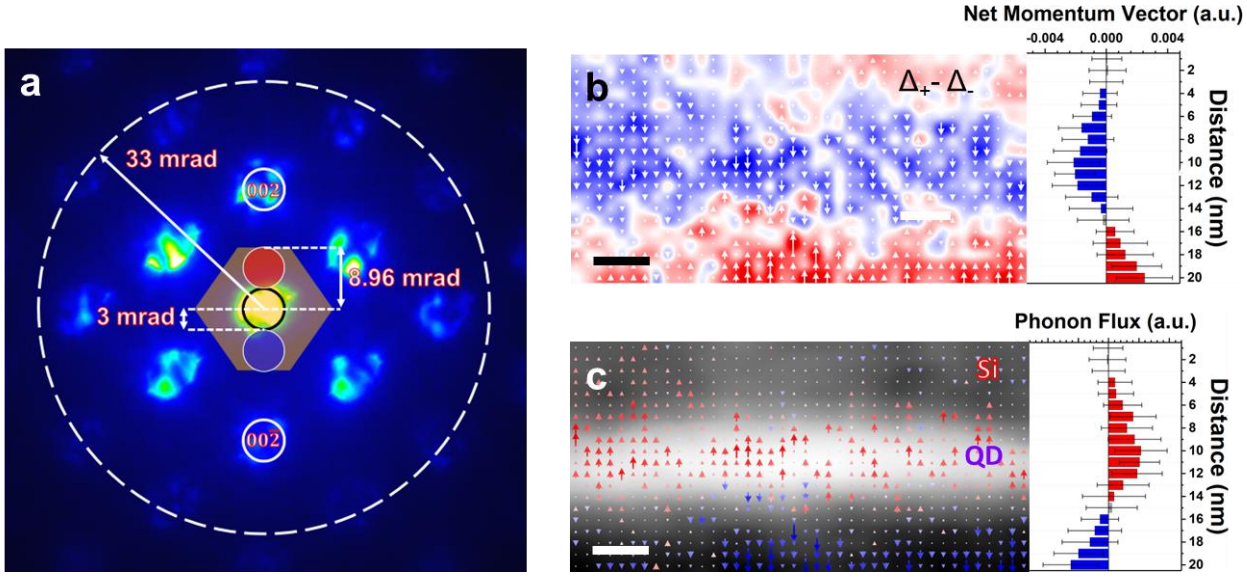

Figure 4.11. Momentum resolved DPM map of phonon momentum and flux normal to Gradual and Abrupt QD interfaces. a, 3 mrad convergence semi-angle convergent beam electron diffraction pattern where the 002 and $00\bar{2}$ spots are labeled. The orange hexagonal shape in the center denotes the FBZ of Si with the Γ–X distance labeled as 8.96 mrad. The red and blue circles near the center denote the EELS entrance aperture positions where off axis data was acquired. **b**, Mapping of net vertical momenta of Si optical phonons. **c**, Phonon flux vector map obtained from the product of group velocity and the quantity of phonons with a given momentum direction overlaid on a 3 mrad HAADF image. **b** and **c** are accompanied by their respective horizontally averaged line profiles. Scale bars denote 5 nm.

For an atomically ideal interface, phonon reflection at interfaces is considered to be specular where the momentum parallel to the interface $q_{//}$ is conserved due to the translational symmetry as seen. Conversely, for an atomically irregular interface, the atomic disorder breaks the transverse translational symmetry and consequently, phonon modes with different $q_{//}$ can also be coupled leading to a diffuse scattering process. The DPM map in Fig. 4.11d shows momentum vectors pointing towards the abrupt interface and given that optical phonons in Si have a group velocity in the opposite direction of their momentum from Γ–X (Fig. 1.2), Si optical phonons are then taken to be propagating away from the abrupt interface. The phonon flux, the product of group velocity and quantity of phonons with a given momentum shown in Fig. 4.11c, experimentally confirms this phenomenon and is consistent with the physics encapsulated by Figs. 4.5a,b. The more abrupt interface has a higher degree of specularity and therefore the generation of backward moving phonons are preferred while the more gradual interface at the top has much weaker directional preference due to its more gradual transition from Si to SiGe.

In this work, we found that the more abrupt the interface between the quantum dot and the surrounding silicon is, the more effectively the phonons are reflected. This is because Si phonons encounter a vibrational barrier as they approach the SiGe QD. There are less Si

atoms in the QD to occupy all the incoming phonons and so several of them will be reflected. Conversely, at the gradual interface, far fewer phonons are reflected, and Si phonons are transformed to SiGe phonons over the length of the interface. What this shows is that atomically sharp interfaces are much more effective at reflecting heat than atomically disordered interfaces.

Being able to map vibrations in nanostructured semiconductors is crucial in the fields of energy conversion, quantum computing, and nanotechnology. This work has demonstrated that using vibrational EELS can help investigate how interactions affect local vibrations. These results provide understanding of phonon physics at interfaces and shows how nanostructures and interfaces affect local vibrations. We have showcased experimental evidence of phonon processes through phonon reflection from interfaces at the nanoscale, showing how phonons interact with interface characteristics. To achieve high phonon impedance and lower thermal conductivity, it is best for nanostructures to have an abrupt change in structure. Additionally, using sub nanometer resolution combined with vibrational information allows us to access nanoscale thermodynamics beyond thermal transport, including heat capacity and entropy. This seminal study not only demonstrates the viability of vibrational spectroscopy in the electron microscope for the field of thermoelectrics, but also provides a physical foundation for their targeted engineering.

Chapter 5

Imaging anisotropic phonons in ferroelectrics by electron microscopy

5.1 Introduction

Atomically controlled interfaces of perovskite oxides offer a new dimension of control at the nanoscale. Specifically, ferroelectric-insulator interfaces have garnered significant interest for their ability to conduct charge in a highly localized region a few nanometers wide[19,20], making them highly attractive for field-effect transistor applications. Although the electronic properties of domain walls (DW) and charged interfaces have been investigated using other methods for their viability in operating electronics, thermal management is equally crucial and has not been investigated at the nanoscale. Interfacial thermal transport, a prominent component of device thermal management, has been investigated either theoretically[79] or using optical methods[80,81] but experimental study at the nanoscale is absent.

Interface thermal transport is studied using a variety of experimental and theoretical techniques. Theoretically, the thermal conductance of an interface can be calculated using a variety of approaches, including classical molecular dynamics simulations and ab initio calculations and are capable frameworks for broadly predicting thermal properties. Nevertheless, experimental study to elucidate vibrational dynamics at relevant scales is

crucial for validating theoretical models. Recently, it has been shown that applying uniaxial strain can modify interfacial thermal transport across ferroelectric-metal interfaces[80]. Additionally, studies have shown the ability to leverage DW tunability to modulate thermal conductivity[81]. However, these studies utilize methods that provide information about global phenomenon due to the lack of sufficient spatial resolution. To uncover local lattice dynamics, a technique that can probe vibrations, or phonons, at atomic scales is necessary.

Where optical methods lack the necessary spatial resolution to study individual interfaces, vibrational electron energy loss spectroscopy (vibEELS) emerges as a powerful tool for probing phonons at the nanoscale[43] and even atomic regimes[53]. Recently, vibEELS has been used to probe single defect modes such as point defects[54], stacking faults[49]. Furthermore, we have developed a technique that is able to map phonon reflections from interfaces[28] that we apply to this system. Armed with this technical capability, we demonstrate the detection of polarization-induced phonon modulation as well as the existence of anisotropic phonons at ferroelectric-insulator interfaces.

In BiFeO3 (BFO), a multiferroic material with a complex crystal structure, studying phonons can provide insights into the material's unique properties and behavior. For example, phonon measurements can be used to study the lattice dynamics and energy transport in BFO, which can help to understand the mechanisms underpinning its multiferroic behavior and its potential applications in device technologies such as sensors, actuators, and data storage. Phonon measurements can also be used to study the interaction between different types of excitations in BFO, such as magnons (excitations of the magnetic moments in the material) and phonons. This can provide insights into the underlying physical mechanisms

that govern the material's magneto-electric properties, which have potential applications in spintronic devices. This work focuses on studying phonons at the nanoscale for the sake of uncovering relationships between vibrations and polarization in perovskite-oxide ferroelectrics.

5.2 Phonon spectra of BFO and TSO

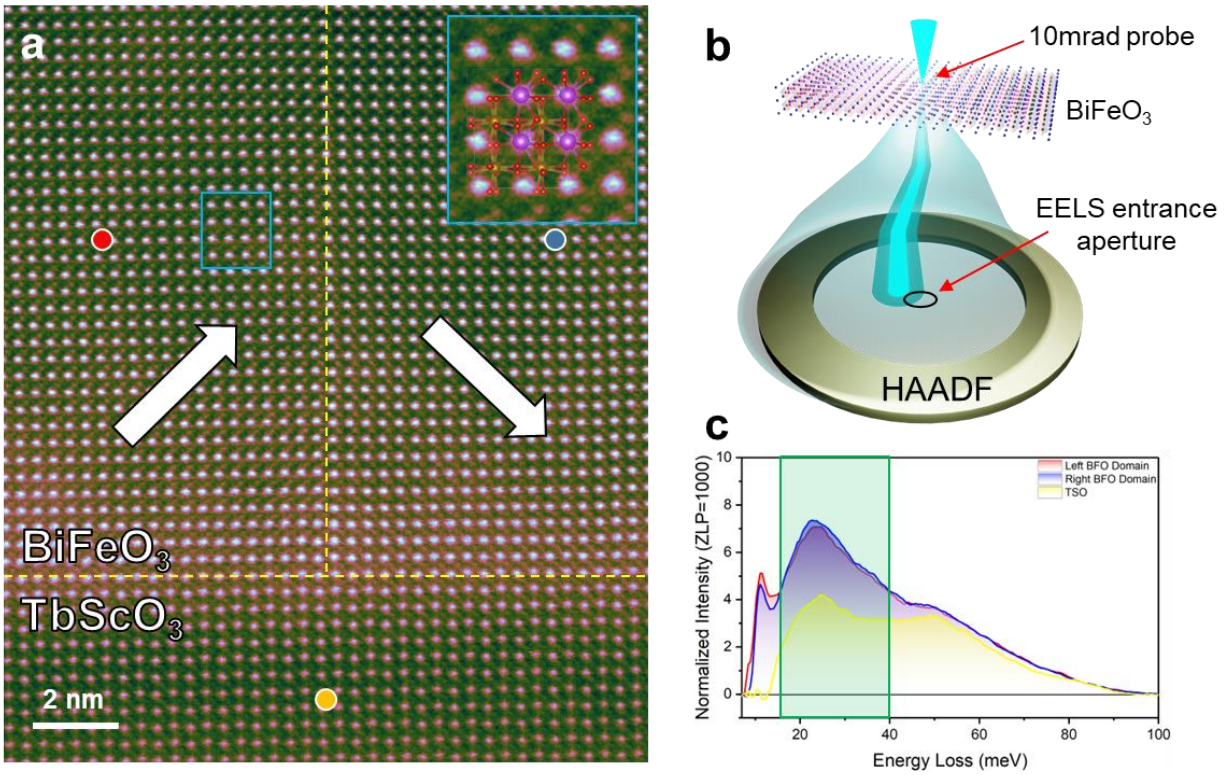

Figure 5.1 Vibrational spectra in thin film BFO and substrate TSO. a, HAADF image containing two domains and TSO substrate. The arrows indicate the direction of polarization. b, Dark Field Vibrational EELS (DF VibEELS) beam-detector geometry. While the central beam escapes the EELS collection aperture, the neighboring diffraction spots (denoted by the immediate darker outer cone) offer significant elastically scattered electrons that contribute to a strong ZLP. c, DF VibEELS spectra at the locations marked in (a). The spectra of the two domains have the most substantial departure in the 12-45 meV energy range, corresponding to strong Fe and O contributions to the total phonon signal. The region in green denotes the energy range of modes considered in subsequent analysis.

While the BFO unit cell retains its pseudo cubic structure, large scale polarization induces a shift of the cation as well as a tilt of the oxygen octahedra. Modulation of phonon properties by octahedral tilts has already been demonstrated[82] but changes due to cation displacement has yet to be investigated. As a result, it becomes necessary to characterize this structure change in terms of vibrational properties. Our system consists of a 100nm thick BFO film grown on $TbScO_3$ (TSO) producing large, 50-100 nm-wide domains (Fig 5.1a).

The differing polarizations on either side of the 109° DW induce a change in the signal intensity corresponding to specific vibrational modes. Fig. 5.1a shows two domains separated by a 109° DW with in-plane polarizations pointing top left and bottom left for the domains to the left and right, respectively. The polarized unit cell consists of a displacement of the Fe cation relative to the B-site-centered BFO unit cell as well as a 10-14° tilt of the oxygen octahedron. It stands to reason that because there is a structural change of the Fe and O octahedron, there should be a change in the vibrational properties as well. Studying the nature of these changes in the vibrational structure is imperative in order to investigate thermal properties of operating devices that utilize the polarizability of this material system.

In order to eliminate long-range polaritonic signals and isolate local phonon structure, we employ a DF VibEELS beam-detector geometry[53] as shown in Fig. 5.1b. We also use a 10mrad wide probe to allow for a greater portion of elastic scattering and limit EELS aberrations. This allows us to minimize the post-specimen tilt thereby maximizing the energy resolution and the quality of our acquired data.

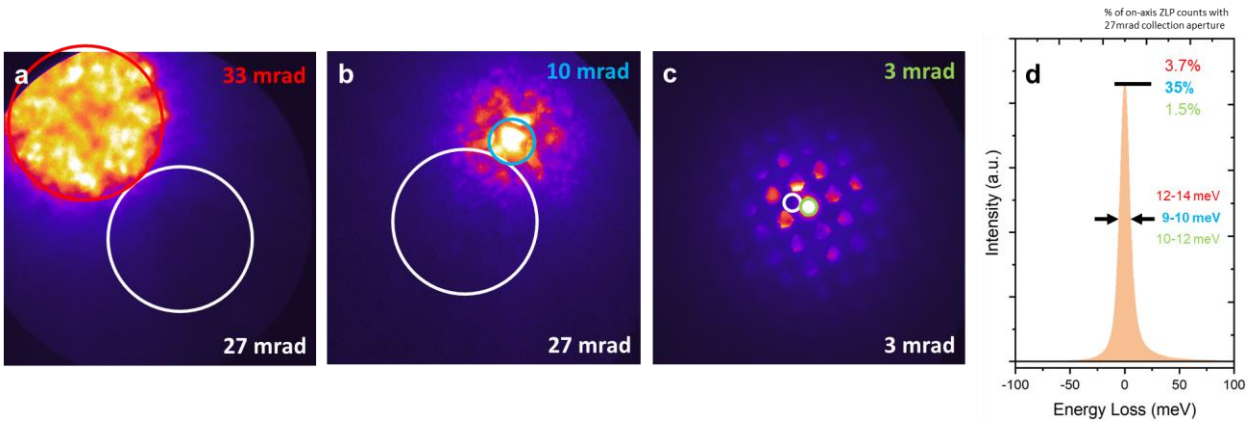

Fig. 5.2 DF VibEELS ZLP intensity and energy resolution at various convergence semi-angles. a-c, Diffraction patterns in BFO at various convergence angles. The diffraction image is overlaid with the sizes and locations of the on-axis brightfield disk and EELS collection aperture. d, ZLP shown with intensities and energy resolutions relative to the 33 mrad on-axis condition.

Fig. 5.2 overviews the specific strategy employed in this work. Normally, for spatially resolved experiments, it is sensible to utilize a large convergence semi-angle to obtain the smallest probe size. This is coupled with a similarly sized collection aperture for capturing a large number of scattered electrons (Fig. 5.2a). This experimental setup provides atomic resolution contrast, assuming aberrations and other factors are under control. Although atomic resolution capability is the hallmark of the STEM, it is not always desirable. For example, if one is trying to study phenomena on the order of nanometers, atomic resolution contrast may convolve and interfere with the nanometer-level feature. Even in dark field EELS, where the collection aperture is displaced such that none of the direct beam electrons enter the spectrometer, atomic resolution is still maintained.

At the other extreme, we could broaden the probe such that it is a few nanometers wide. This is equivalent to lowering the convergence semi-angle below 6 mrad, at least in our Nion system. We can similarly decrease the collection semi-angle to be on par with the probe size (Fig. 5.2c). If we do this, we can recover momentum resolution, as discussed in chapter 3. A

consequence of this is that the amount of electrons that enter the EELS spectrometer is drastically reduced by a factor of 1/81 when compared to using a 27 mrad collection semi-angle (Fig. 5.2d). This means that the vibEELS data will be much closer to the noise floor making data analysis an even greater challenge. A remedy to this solution is to use a large probe but large collection aperture. This way your probe size is still on the order of nanometers, a similar size to the feature of interest, while still acquiring an appreciable number of electrons. This is a good strategy for avoiding atomic contrast large-scale features. However, most features of interest lie on the order of a few unit cells. In this system, DWs and the BFO-TSO interface are roughly 1 unit cell in size. Exploring these features excludes the possibility of using such a large probe size.

But what if momentum resolution is not needed and you need a smaller probe size? The solution is then to use a probe size that is nearly the size of one unit cell. Accounting for the worsening of spatial resolution due to aberrations and other factors, this is about 10 mrad for the BFO-TSO system (Fig. 5.2b). This experimental setup has several advantages over the other two discussed earlier. The first is that this should ideally eliminate atomic contrast for phonon spectra as the scattering is average over entire unit cells. Second, using the 27mrad, since we don't require momentum resolution here, has the added benefit of much higher counts relative to the other two conditions (Fig. 5.2d). As a result, we have chosen this experimental condition to study the BFO-TSO system.

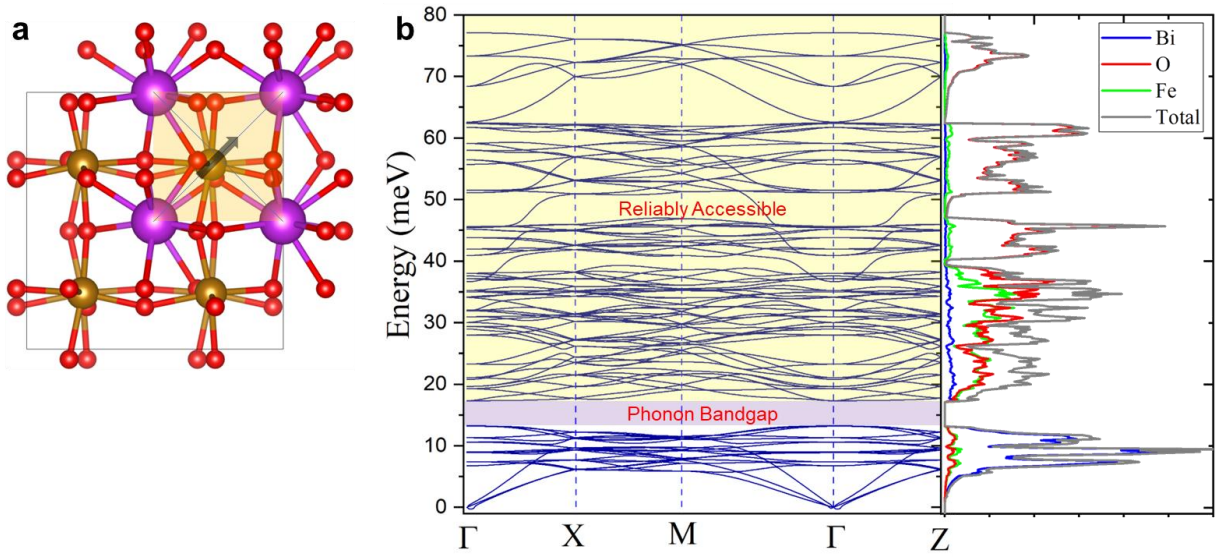

Figure 5.3 BFO phonon dispersion and DOS. a, 76-atom simulated BFO structure relaxed by DFT. This structure has polarization along the top-right in the plane of the page. b, phonon dispersion and DOS of bulk BFO in (a). Acoustic phonon modes lie below 10 meV, while optical modes lie in the 10-80 meV range. Due to the mass discrepancy between Bi and Fe, a phonon bandgap exists in the 13-17 meV range. Due to the energy resolution of the DF VibEELS technique in our system, only modes above 15 meV can be reliably accessed with current background subtraction techniques.

The interpretability of vibEELS data is quite difficult for perovskite oxides. This is because unlike Si, BN, SiC, and Grapehene, the BFO-TSO system consists of 5-basis unit cells (Fig. 5.3a) comprised of a complex perovskite structure with heavy elements such as Bi and Fe. This has two major consequences: heavier atoms means lower energy phonons and several atoms per unit cell translates to a diverse and complex phonon dispersion and DOS (Fig. 5.3b). The former can be thought about intuitively first. Likening phonons to a ball and spring model, as the mass of the ball increases, the spring cannot vibrate as rapidly due to the inertia of the heavy atom which translates to the spring constant decreasing. Mathematically, the eigen frequencies of a modes involving heavy masses will be reduced since the masses are in the denominator of the dynamical matrix. The latter has to do with the 3N degrees of freedom and thus, 3N phonon bands, available to the system where N is the number of atoms in the

unit cell. As a result, perovskite-oxide systems have a complex and diverse phonon band structure.

If the mode energies are too low, the energy resolution of the ZLP will become a significant issue that can limit the accurate isolation of the phonon signal. One may be forced to ignore the set of low energy modes that are not resolvable either due to them being buried in the ZLP or them being too close to the ZLP center. A diverse band structure means that individual modes become almost impossible to separate. In the previous chapter, modes could be easily separated since the phonon structure of Si and SiGe was not as complicated. In BFO and TSO however, it is unwise to label specific modes in the phonon signal. However, despite these problems there are a few simplifying strategies we can employ that will convert this complex problem into a manageable one.

The first step is to separate the contributions of individual elements to the total phonon DOS. The phonon DOS in Fig. 5.3b and Fig. 5.3a illustrates that phonons where Bi atomic motions are dominant mostly lie below about 15 meV. Fe contributing phonons are generally dominant between 12 meV and 40 meV. Oxygen contributing phonons are dominant from 12 meV to about 75 meV with only oxygen atoms contributing to phonons above 40 meV. This categorization makes it much simpler to understand phonons in BFO.

Fig. 5.1c shows background subtracted spectra from the two BFO domains depicted in Fig. 5.1a and the substrate, TSO. While the spectral differences between BFO and TSO are distinct, the polarization-induced changes are more nuanced. The energy range above 12 meV (3 THz) is dominated by contributions from Fe and O to the total phonon density of states (PDOS)[83] with the spectra of the two domains have the strongest departure in the 15-40 meV

energy range corresponding to strong Fe and O contributions to the total phonon signal (Fig. 5.3). This distinction suggests that these modes are strongly coupled with the ferroelectric polarization in BFO. Since we want to focus on Fe-O vibrations that relate strongly to ferroelectric polarization, we can treat Bi based phonons background and subtract them out. This is a similar strategy to the one employed by Hoglund et al.[82].

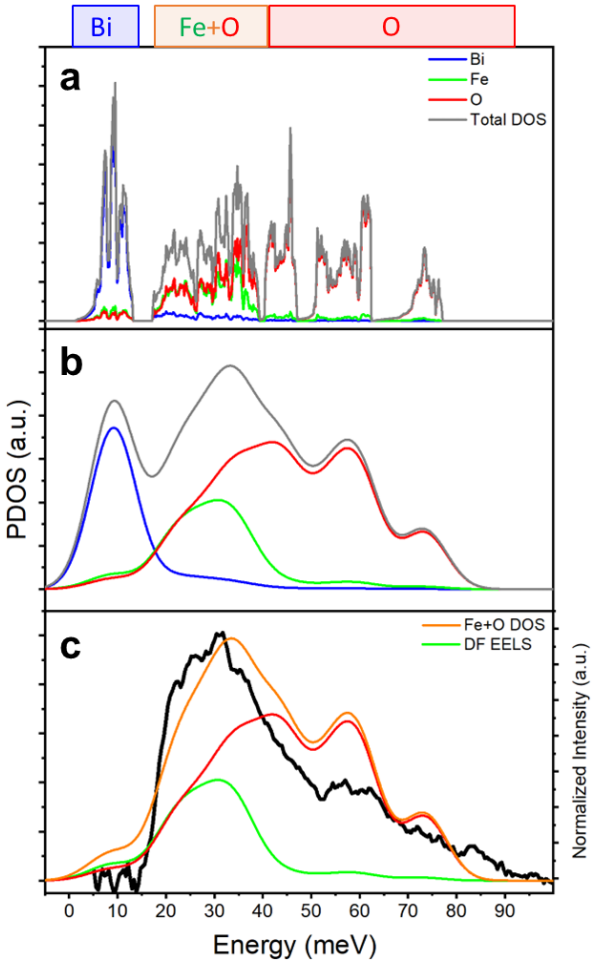

Figure 5.4 Phonon DOS comparison with DF VibEELS. a, Phonon DOS of bulk BFO with elemental contributions. Phonon DOS can be separated into dominant Bi, Fe+O, and O phonons. Phonons consisting of mainly vibrating Bi atoms lie in the 0-14 meV range. Phonons consisting of mostly Fe and O atoms vibrating together lie in the 15-40 meV range, while mainly O vibrations lie in the 40-80 meV range. b, Phonon DOS in (a) convolved with a 10 meV gaussian. c, Phonon DOS of the Fe and O contributions compared with experimental DF VibEELS data.

To directly compare the vibEELS result to theory, we employ DFT to accurately simulate the phonon DOS. To match the experimental energy resolution, the phonon DOS in Fig. 5.4a is convolved with a 10 meV gaussian to obtain Fig. 5.4b. Since Bi based phonons are too low in energy, we consider only Fe and O based phonons. Fig. 5.4b shows that the tail from the Bi contribution has a smooth decrease which we can use as the background for isolating the higher energy modes. Fig 5.4c illustrates that the energy ranges and overall shape of the vibrational signal is consistent with the broadened Fe and O contributing phonon DOS. The discrepancy in the relative intensity of the features such as the peak at 60 meV likely arises from the way EELS scales the individual modes based on the effective charge density and phonon polarization (Eq. 3.19) as mathematically described in section 1 of chapter 3. It is clear that phonons in the 15-40 meV range have a strong Fe and O contribution while phonons higher than 40 meV purely consist of vibrating O atoms.

Categorizing phonons as such simplifies the interpretability of vibEELS signals in the presence of structural changes and other real-space features in general. The next few sections examine strain fields and interfaces and how they impact phonons on the local scale. Additionally, phonon behavior in the ferroelectric domains themselves is explored.

5.3 Strain-induced anisotropic phonons

When BFO is grown on TSO, the lattice mismatch between the two materials induces a strain in BFO. The crystal structure of BFO has a slightly larger lattice parameter than TSO, which means that when BFO is grown on TSO, there is a mismatch in the lattice spacing between the two materials. This lattice mismatch can lead to a strain in BFO, as it tries to

accommodate the different lattice spacing of TSO. The strain induced in BFO can be either compressive or tensile, depending on the relative lattice parameters of the two materials. In the case of BFO grown on TSO, the lattice parameter of TSO is slightly smaller than BFO, so the strain in BFO is typically compressive. This compressive strain can cause a distortion in the crystal structure of BFO, which can affect its electronic and magnetic properties. For example, the distortion can result in a change in the direction of the spontaneous polarization of BFO, which can affect its ferroelectric properties. The strain induced in BFO can also be influenced by the thickness of the BFO film and the orientation of the crystal axes of BFO and TSO. By controlling these parameters, it is possible to tailor the strain in BFO and tune its properties for specific applications.

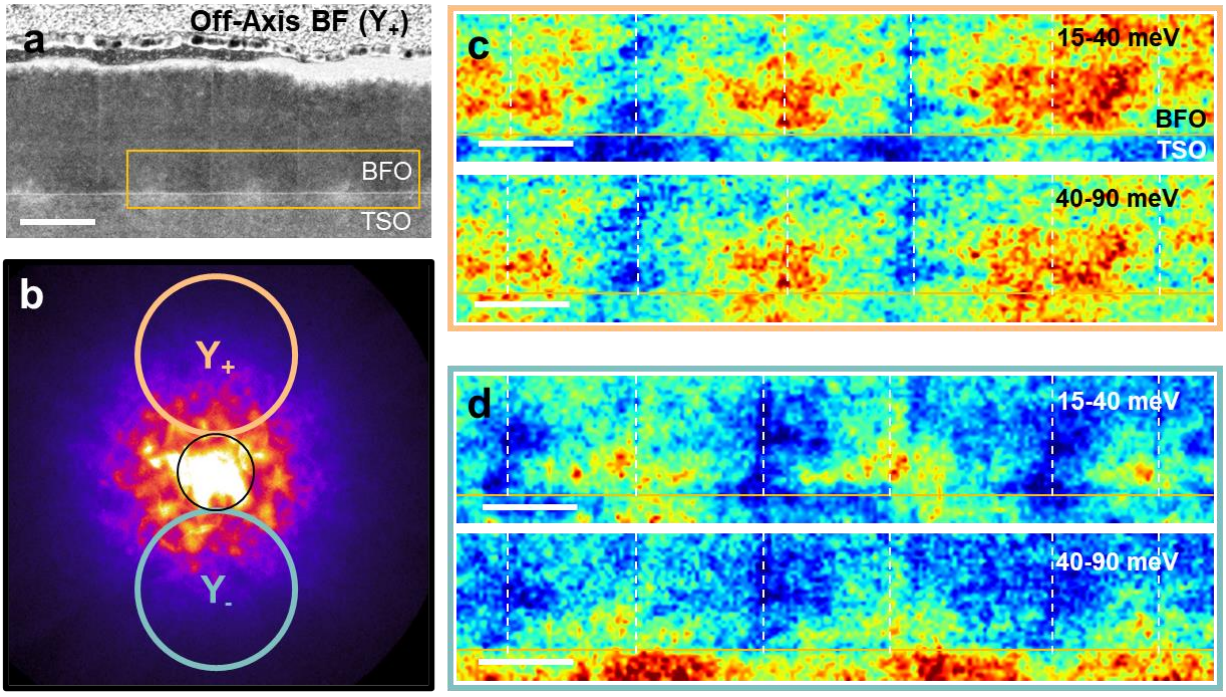

Figure 5.5 Strain-induced anisotropic phonons probed by oriented DF VibEELS a, Off-axis BF image. The central BF disk is deflected so that the BF detector collects electrons scattered in the +Y direction relative to the sample. Under this beam-detector geometry, every other domain wall shows a bright contrast and alternating bright and dark contrast is seen at the BFO-TSO interface. Scale bar denotes 50 nm. b, 10 mrad convergence semi-angle electron diffraction in BFO. Phonon maps are acquired with the EELS collection aperture placed in

the annotated Y_+ and Y_- directions. c-d, DF VibEELS phonon mapping with detector locations outlined in (b). Color coding of the annotated locations is matched with the outline of (c) and (d). Mappings show inverted features for both the 15-40 meV and 40-90 meV ranges. This indicates that phonon intensities are not symmetric in reciprocal space. Scale bars denote 20 nm.

Fig. 5.5a shows an off-axis BF image in the experimental condition where the BF detector is placed at the Y_+ location in Fig. 5.5b. The feature of importance here lie near the BFO-TSO interface where alternate bright and dark spots are seen. This alternating contrast are due to the substrate induced strain on the BFO film. The alternating polarization between domains generates tensile and compressive strain that alternates from DW to DW. This strain breaks the two fold symmetry and stretches or compresses the unit cell. This strain has profound implications for the phonon structure and, consequently, thermal transport in the BFO film.

Strain can alter the phonon dispersion relations in a material, leading to changes in the phonon density of states and anisotropy. Strain can create an intensity asymmetry in the inelastic background of electron diffraction patterns of a material. As a result, the inelastic background in electron diffraction patterns can become anisotropic and exhibit intensity asymmetries. When a material is strained, the phonon dispersion relations along different crystallographic directions become asymmetric, leading to changes in the angle-resolved phonon density of states[84–86]. The changes in the phonon density of states can then lead to intensity asymmetries in the inelastic background in electron diffraction patterns. Specifically, if the strain induces a higher density of states for phonons along one crystallographic direction, the inelastic background in electron diffraction will be more intense in that direction, leading to an intensity asymmetry in the diffraction pattern.

Using the DPM technique (Fig. 5.5b) developed by us in Gadre et al.[28], we are able to quantify the intensity asymmetry. The maps in Fig.5.5c,d are taken with the EELS collection aperture placed in the Y_+ and Y_- locations as shown in Fig. 5.5b. Fig.5.5c shows high phonon intensities at DWs 1, 3, and 5 while Fig.5.5d shows high phonon intensities at DWs 2, 4, and 6. Although phonon anisotropies have been imaged in the reciprocal space using electron diffract and X-ray diffraction, they have not been imaged at the nanoscale in real space. This demonstration marks a significant advancement in probing phonon anisotropies for studying nanoscale thermal transport.

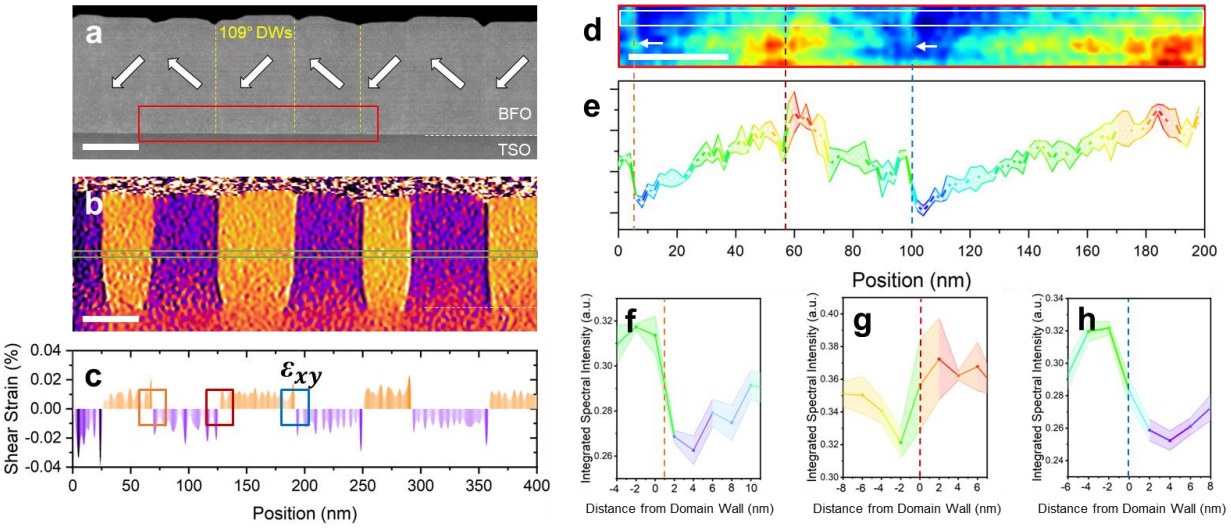

Figure 5.6 Polarization-Induced Shear Strain probed by DF VibEELS. a, Large field of view HAADF containing several ferroelectric domains with the phonon mapping region outlined in red. b, Geometric Phase Analysis (GPA) shear strain ε_{xy}. The scale bars in (a) and (b) denote 50 nm. c, Line profile of (b) from the region outlined in green. Shear strains can be seen reaching their local maximums at the DW. d, Integrated spectral intensity map in the energy range 15-40 meV. The scale bar denotes 50 nm. e, Vertically averaged line profile from the region in the white box in (d). The filled regions in the plot indicate the error range. f-h, Zoomed in regions around the 109° DWs of the line profile in (e) denoted by orange, red, and blue dashed lines.

A similar phenomenon appears even for shear strains. Essentially, any breaking of crystal symmetry will generate anisotropies in reciprocal space. We can probe these anisotropies differentially using the DPM technique to quantify the size of the asymmetry. However, we can still glean important information by only probing one side of the diffraction pattern. Fig. 5.6 showcases the results for shear strain based effects on the phonon signal. The trend in Fig. 5.6c matches well with that of Fig. 5.6e showing that the GPA mapping, which quantifies lattice distortions in real space, correlates with the intensity of phonon modes. If the other side of the diffraction pattern was to be probed, the trend is expected to flip, as demonstrated for tensile and compressive strain in Fig. 5.5. This further bolsters the capabilities of this technique to probe how phonons are modulated by nanometer level lattice strain and can be used to directly inform nanoscale thermal transport.

Imaging phonons at individual DWs has profound implications for cross-DW thermal transport. For example, it has been shown that the density and type of DW strongly affect thermal conductivity in ferroelectric thin films[81]. The source is ascribed to the structural mismatch and polarization gradient found between two domains. This is consistent with the result in this work as the polarization gradient induces a shear strain which strongly modifies the phonon DOS of the DW. Additionally, domain wall-localized phonons have been theoretically predicted which hold promise for tailored nanodevices and signal transmission[79]. Vibrational EELS is poised to uncover the fundamental physics at domain walls and inform the targetted design of devices that take advantage of these exotic phenomena.

5.4 Ferroelectricity-induced anisotropic phonons

Since ferroelectric polarization in perovskite oxides consists of a structural displacement of the b-site atom with respect to the oxygen octahedra, we can expect the phonon DOS to reflect the polarization in some way. For the case of imaging phonons in strain fields, the EELS aperture was deflected perpendicular to the BFO-TSO interface. However, the ferroelectric polarization induces an asymmetry along the 110 diffraction patterns. Therefore, in order to study polarization effects on phonons, we deflect the aperture along the bright $10\bar{1}$ spot.

The ferroelectric polarization affects the intensity of the diffraction spots in the pattern. This is because the polarization can induce changes in the electronic structure of the material, which can affect the scattering of the electrons off the atoms in the crystal lattice. The changes in intensity can depend on the direction of the polarization and the electron beam, as well as the specific crystallographic planes that give rise to the diffraction spots. In BFO, the bragg spots that lie on the axis perpendicular to the polarization direction have an intensity asymmetry.

This can also be understood in terms of dynamical diffraction effects. In BFO, the asymmetry in the diffraction pattern arises due to dynamical diffraction effects caused by the presence of the ferroelectric polarization. Due to dynamical diffraction effects, the ferroelectric polarization in BiFeO3 causes an uneven distribution of charges, resulting in an asymmetry of intensity between Friedel pairs of Bragg reflections. Specifically, the ferroelectric polarization can induce a modulation of the crystal lattice spacing along the direction of the polarization. This modulation can give rise to a spatially varying phase shift in the scattered

electrons which can interfere with the incident and other scattered electrons and modify the diffraction pattern. The resulting asymmetry in the diffraction pattern can depend on the orientation of the crystal lattice, the direction and energy of the incident electrons, and the magnitude and direction of the ferroelectric polarization[87].

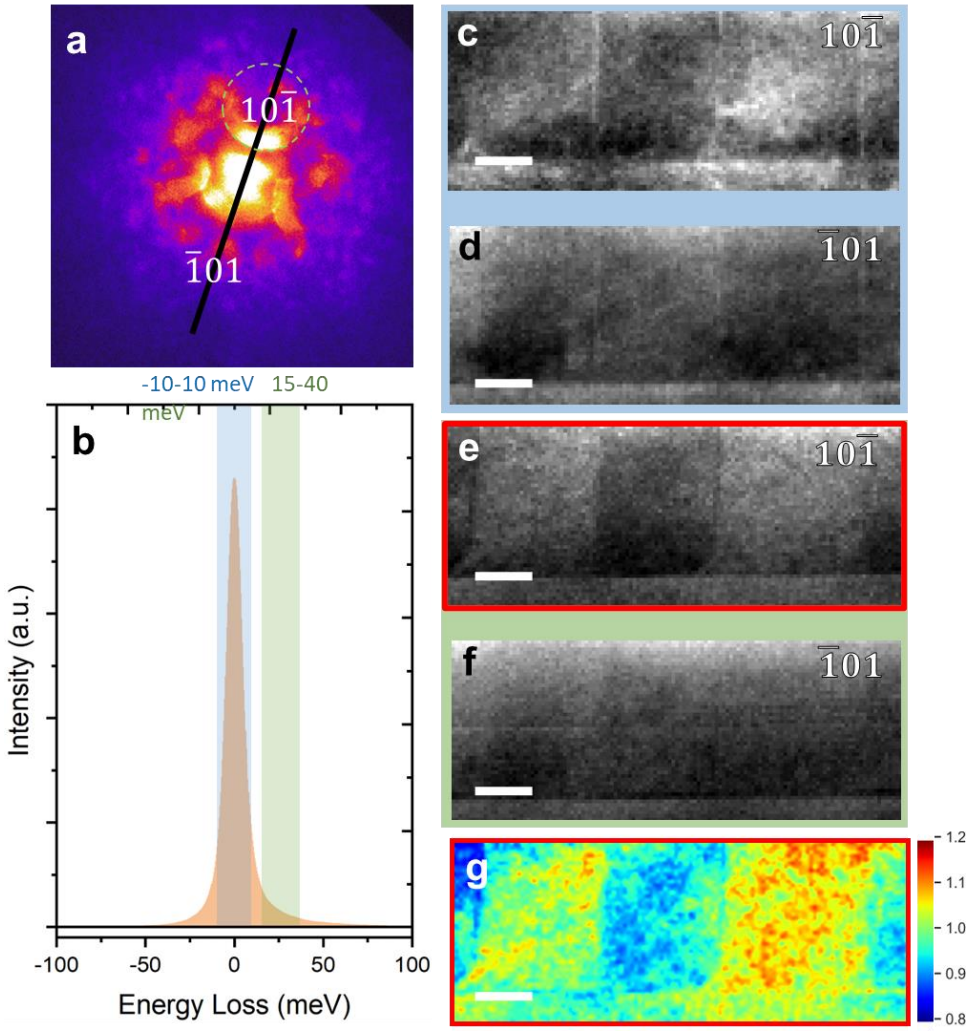

Figure 5.7 DF VibEELS along Friedel pairs showing domain contrast in phonon map. a, 10 mrad convergence semi-angle electron diffraction in BFO. The $10\bar{1}$ diffraction is brighter than the $\bar{1}01$ one indicating the breaking of Friedel symmetry due to the ferroelectric polarization. b, DF VibEELS spectrum in the low-meV range. Color regions indicate intensity integration along annotated energy ranges. c-f, Integrated intensity mappings in the energy range outlined (b) for diffraction spots labeled in (a). g, Unnormalized, background subtracted phonon map of (e). Scale bars denote 25 nm.

Experimentally we can image domain and DW contrast by considering the elastic (ZLP) and inelastic (phonon) scattering by fast electrons. With the aperture placed on either $10\bar{1}$ or $\bar{1}01$ diffraction spots (Fig. 5.7a), the off-axis elastic intensity (Fig. 5.7c,d) shows little domain contrast. Majority of the contrast likely comes from diffraction contrast due to shear and tensile strains in the material as shown in the previous section. It is interesting to see the contrast highlighting the domain walls when the aperture is placed on the $10\bar{1}$ spot. One possible explanation of this is that the diffraction contrast from strain dominates the contrast from the Friedel-pair symmetry breaking. On the other hand with the aperture place along the broken symmetry axis, the phonon map reveals domain contrast. One possible explanation for this comes from the fact that bragg intensity symmetry is broken as well as that of the inelastic background where phonon scattering is found. It is still unclear domain contrast is much stronger for phonon losses than elastic losses. Tauchert et al.[88] investigated a similar intensity anisotropy in the diffraction pattern, attributing it to phonon anisotropy.

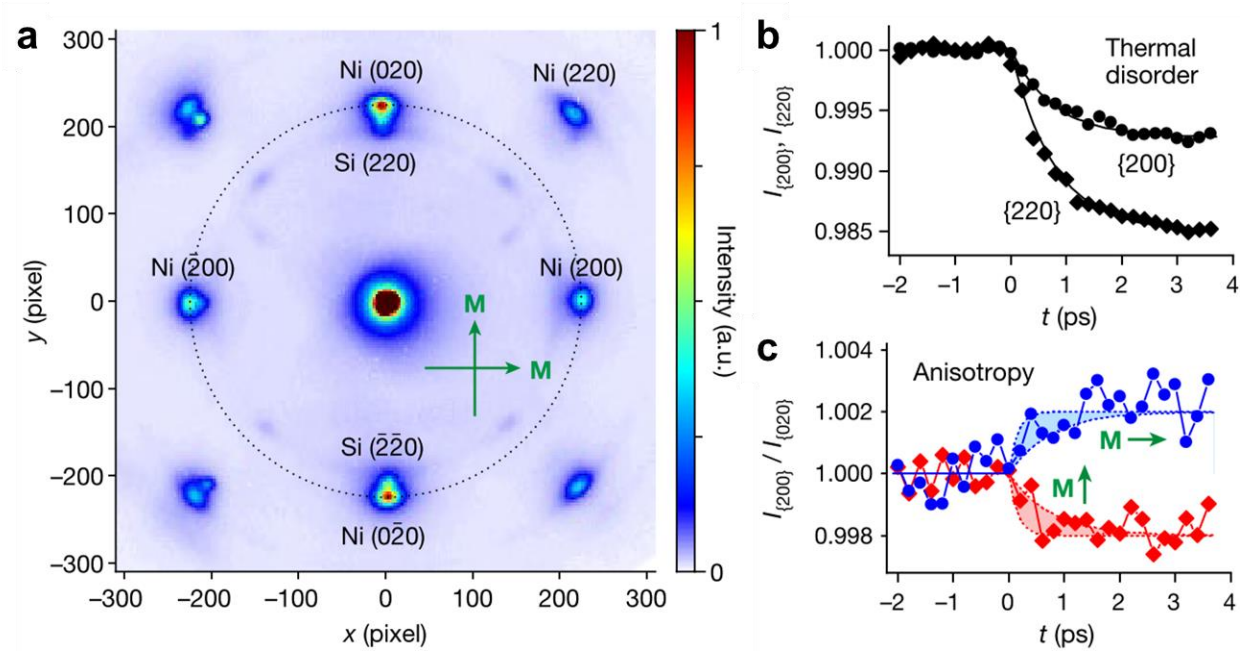

Figure 5.8 Electron diffraction measurements of atomic motions during ultrafast demagnetization. a, Diffraction pattern before laser excitation. The green arrows denote different magnetic field directions that are probed. b, Bragg spot intensities for two different diffraction orders as a function of time. The solid lines denote a decay time of 770 fs. Origin of this observation is thermal disorder. c, Anisotropy between crystallographically equivalent Bragg spots of different orientation with respect to the initial magnetic field. $I_{\{200\}} = \frac{1}{2}(I_{200} + I_{\bar{2}00})$ and $I_{\{200\}} = \frac{1}{2}(I_{020} + I_{0\bar{2}0})$. The green arrows denote an initial magnetization along) Ni[100] (blue data) or Ni[010] (red data). The measured levels after saturation (1 ps < t < 4 ps) are 0.9981 ± 0.0005 (red data) and 1.0019 ± 0.0007 (blue data) under the constraint of an antisymmetric effect. This figure is adapted from Tauchert, Sonja R., et al. Nature 602.7895 (2022): 73-77 with permission.

The authors used femtosecond electron diffraction to observe the dynamics of a nickel crystal subjected to a femtosecond laser pulse. They demagnetized the nickel crystal with a laser pulse and subsequently observed the electron diffraction pattern evolve with femtosecond resolution. They observe with time that the Bragg peak intensity adopt a peculiar anisotropy. Specifically, the intensities of the 020 and 200 Bragg spots depart from their equilibrium value. As the demagnetization progresses, the intensity values diverge from one another producing an anisotropic diffraction pattern. Through their calculations

they determine that the cause of this is the transfer of angular momentum from the magnetic moments to the angular momentum of the phonons. Eventually the phonons decay and the sample physically rotates a slight amount. This study discovers how the missing angular momentum from the magnetic ordering is then transferred to thermal carriers or phonons.

This presents an interesting case in the context of the BFO-TSO system as well. Instead of a transient process where the symmetry of the crystal is broken like in the nickel case, BFO has Friedel symmetry breaking at equilibrium. We can hypothesize that just as the electron diffraction anisotropy was contained in the phonon momentum in the demagnetized nickel, the breaking of the Friedel symmetry could also be attributed to an anisotropy in the phonon momentum. Additionally, any structure symmetry breaking is translated to the anisotropy of phonons in momentum space. This is why for tensile and sheard strain as well, there was a phonon momentum selectivity producing the spatial distribution seen in Figs.5.5 and 5.6. In general, this warrants a detailed simulation investigation of this phenomenon. Since probing phonons at these scales was impossible until recently, this phenomenon has not been explored.

5.5 Phonon anisotropy at ferroelectric-insulator interfaces

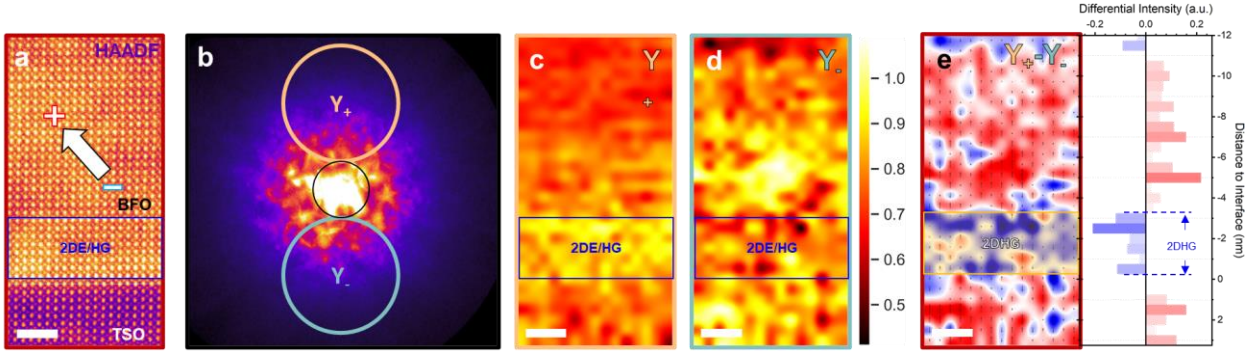

Figure 5.9 Anisotropic Phonons at a BFO-TSO interface. a, HAADF containing BFO and TSO with the 2DE/HG region marked in blue. This map region corresponds to the red box in Fig. 5.1a. b, Convergent beam electron diffraction pattern using a 10mrad probe. The regions labeled Y_+ and Y_- correspond to locations of the EELS entrance aperture where the DF VibEEL spectra were acquired. c-d, DF VibEELS vibrational maps showing distinct anisotropy. The 2DE/HG region is slightly larger than reported previously, likely due to the poorer spatial resolution of the 10 mrad probe. e, A Differential Phonon Momentum (DPM) Map showing phonon reflection from the BFO-TSO and bulk-2DHG interfaces along with its horizontally averaged line profile. The 2DE/HG region is slightly larger than reported previously, likely due to the poorer spatial resolution of the 10 mrad probe. Scale bars denote 2 nm.

In Ref.[28] we have developed a technique that maps the direction of phonon momentum in real space. We have achieved this by obtaining a differential map of data acquired along diametrically opposed regions in momentum space (Fig. 5.9b). Applying this technique at a ferroelectric-insulator interface reveals something quite striking. Unexpectedly, the specific Fe displacement along a particular direction generates anisotropy in momentum space i.e., there is preferential phonon scattering. The existence of 2DE/HG also imposes further anisotropy that warrants detailed exploration. It is reasonable to expect phonon momentum reflection at an interface between two materials of differing composition, however the phonon vectors also flip at the interface between the 2DHG and bulk BFO.

The vibrational mapping in Fig. 5.9c reveals anisotropic phonons wherein their amplitudes depend on their location in momentum space showing an opposite trend at the 2DE/HG. This is more clearly represented in the line plot in Fig. 5.9e. This suggests that the free charge carriers flip the anisotropy of the phonons in this region and can be extended to conclude that there is phonon reflection from charged interfaces. The likely cause of this is the symmetry breaking at each interface: ferroelectric-insulator interface and 2DE/HG-bulk interface.

This technique can be applied to charged and charge-neutral DWs so study phonon reflection. Atomistic characterization of DWs in this way is crucial in understand thermal management and more specifically cross-DW thermal conductivity in operating electronics based on oxide ferroelectrics. The case of the charged interface presents different physics than was at play in the case of strain and polarization. In the charged interface, structural symmetry is essentially the same as the bulk but phonon anisotropy is still present. This suggests that the physics at play here is not directly related to structure. This is also an open question as to how phonons interact with free charge especially when that charge is confined to a lower dimension. Again, intensive simulation is necessary to properly evaluate the physics at charge interfaces in ferroelectrics and their effect on phonons.

Chapter 6

ML-driven EELS data analysis framework for high-throughput data processing

6.1 Motivation

Electron energy loss spectroscopy (EELS) is a powerful tool for studying the vibrational properties of materials at the nanoscale. EELS data is rich in information because it provides detailed information about the energy levels of the electrons in a material and the vibrational modes of the material's atoms and molecules. The versatility of EELS is also imbedded in the complexity of its data. Unique scattering physics that originates from fast electron interaction with materials produces specific challenges in isolating the target information. For example, phonon signals are greatly affected by a slowly decaying ZLP tail that sometimes even obscures acoustic signals completely despite the advancements in monochromation [3meV Nion MM abstract]. This extended tail also modifies the onset of bandgap excitations[89] and sometimes even obscures them entirely.

Aside from the scattering-related challenges, instrument performance also has a significant impact on data analysis. Worsening of the scope alignment and detector factors like the point spread function, background noise, and varied pixel response, all influence the data to decrease its quality. Although, correcting for all these factors is often possible, a stable

microscope alignment and a detector with high dynamic range and single-electron response[33] is ideal for optimal energy resolution and data quality. Despite these solutions and advancements, an EELS spectroscopist may still encounter situations where these factors cannot be controlled and become a serious detriment to data quality. Therefore, various data acquisition and analysis techniques become necessary for transforming raw data into insight. Figure 6.1 describes the basic data acquisition and analysis process.

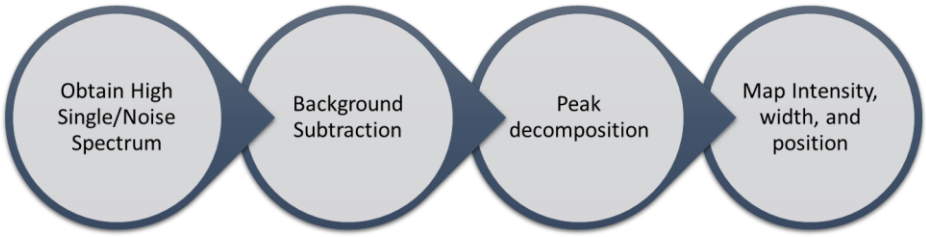

Figure 6.1. Basic vibrational EELS data acquisition and analysis workflow. First, high SNR spectra are acquired. Then, data is background subtracted to isolate vibrational signal. If the phonon band structure is not too diverse, the vibrational signal can be decomposed into individual modes or peaks. Finally peak properties such as intensity, width, and position can be mapped spatially.

Although one must be prudent to not overinterpret data beyond its means, extensive and thorough analysis is needed to extract subtler features. This requires data analysis tools for processing raw data accurately, transparently, and repeatably to obtain trustable, and meaningful results. Often this requires programming knowledge to write functions that are not part of commercial software. Unfortunately, the barrier to entry for developing custom functions seems to be high, at least from my experience. A microscopist may often find themselves to be in a position where they may be responsible for developing tools for a wide

range of use-cases, even ones not related to his thesis topic. Although custom solutions are being written and used for a wide variety of applications already, they lack modularity and transparency. Therefore, the goal of this section of the dissertation is to put forth the beginnings of a framework that makes gleaning insights from a bunch of numbers, flexible, transparent, and less intimidating to those that do not fashion themselves experts of data analysis.

6.2 Structure of EELS data

EELS data is typically presented as a spectrum, with the energy loss on the x-axis and the intensity of the signal on the y-axis. Most EELS detectors have approximately 2000 pixels which places a limit on energy loss range that is viewable in any given spectrum. An EEL spectrum appears as a 2D image on the detector where it is then integrated vertically to form a 1D spectrum (Fig. 6.2). Although there are techniques which make it possible to acquire multi-range EELS, the basic structure of the single spectrum remains the same. The energy axis is directly linked to the dispersion and energy offset of the EEL spectrometer. The dispersion fundamentally refers to the strength of the magnetic field in the EEL spectrometer; the higher the dispersion, the greater the energy spread of the electrons and smaller the single-pixel energy width. For low-loss and especially vibrational EELS data, dispersions range on the order of 0.5-10 meV while typical high-loss regimes have dispersions on the order of 50-100 meV. while the dispersion determines the width of the energy range of the spectrum, the energy off set sets the start of the spectrum. Together, only these 2 values are needed to determine the energy axis of the spectrum.

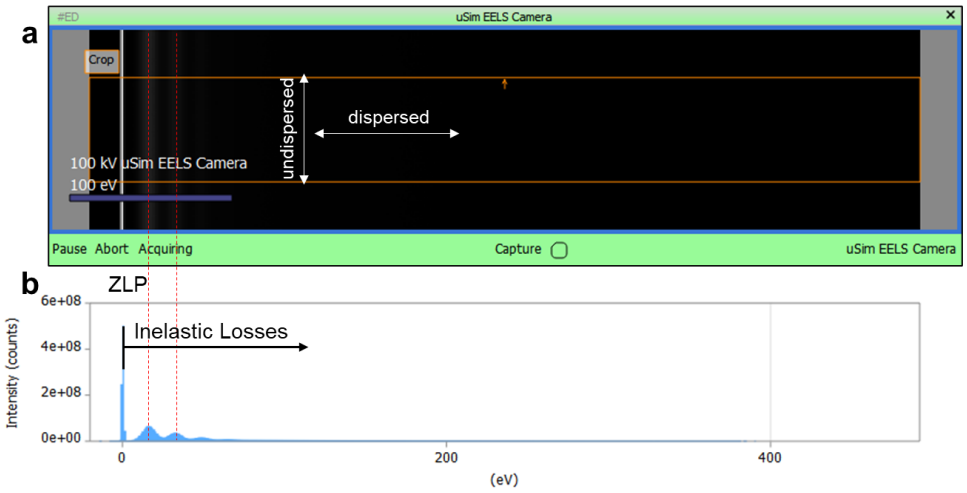

Figure 6.2 2D EELS image and vertically integrated EEL spectrum. a, 2D EELS image formed by fast electrons dispersed by magnetic prism in the EEL spectrometer. The vertical direction is undispersed while the horizontal direction is energetically dispersed by the magnetic prism. b, 1D spectrum formed by vertically integrating (a). The ZLP is usually the most intense peak representing electrons that have lost no energy to the material. Intensities to the right of the ZLP come from electrons that have lost energy to the material and are known as inelastic losses.

The intensity of a spectrum is given in counts which are mostly arbitrary numbers dependent on the gain of the pixels and are susceptible to background noise. Direct electron detectors, however, have single electron counting precision and often have very low noise floors. The actual scaling of the intensities of various excitations depends deeply on the physics of the scattering process, which is to say, the EELS scattering cross section. For example, the intensities of vibrational signals are proportional to the density of states (DOS) of the vibrational modes at a given energy loss while the exciton bandgap signal is a function of the transition problem of an electron to be excited from the valence band to the conduction band. Regardless of the detailed physics, the structure of the EEL spectrum is the same. In total, only 2048 pixels (# of horizontal pixels of the detector) and dispersion and offset values to define the energy axis. For spectrum images (SI) that consist of spectra acquired over a 2D region in real space, the data is organized as a 3D data cube (Fig. 6.3).

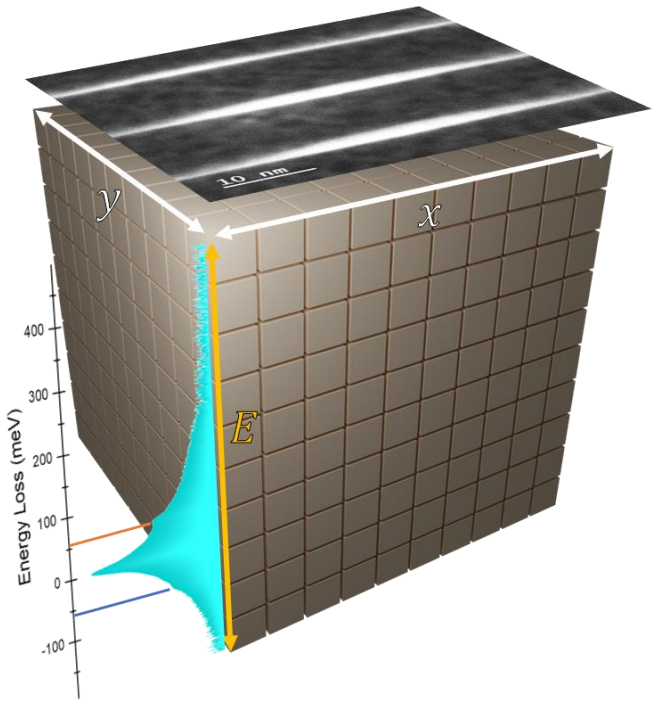

Figure 6.3 EELS data cube. EEL spectrum images consist of 2 spatial dimensions and one energy loss dimension. Log-scaled EEL spectrum is taken on Si and shows a clear optical mode in both energy loss (orange line) and energy gain (blue line) sides.

Beyond the organization of the data, detailed understanding of whats being presented in the spectrum is necessary to proceed with analysis. Depending on the specific scattering physics, features may manifest themselves as peaks, edges, or changes in the slowly varying background. Excitonic modes arising from electronic transitions from occupied to unoccupied orbitals appear as edges with extended features. In high-loss data, the shape of the features depends on the intra-core transitions. Vibrational modes in contrast, can be observed as peaks or features at specific energy losses. The position and shape of these peaks or features can provide information about the nature and strength of the vibrational modes in the material. The width of the peaks can also provide information about the lifetime of the vibrational modes and the coupling between different vibrational modes. This wealth of information warrants the proper acquisition of data to ensure high signal-to-noise (SNR)

and sharp linewidths. Due to the low-count nature of vibration EELS data, specific acquisition schemes must be employed. Some of these will be discussed in the next section.

6.3 Acquisition of vibrational EELS data

Normally, the user is at the mercy of the software and its functions for what they are able to do with the microscopy data. For implementation of specific acquisition schemes, software with proper hardware interfacing API is necessary. The industry standard for acquiring EELS data is called Digital Micrograph and is integrated into most TEM's. This software facilitates the viewing of data as well as its acquisition but lacks methods to easily control the instrument. This is also inhibited by the fact that DM-powered systems are usually systems with several parts mostly made by different manufacturers. This makes total instrument control almost impossible, or at the very least, a very unappealing task. However, Nion Hermes systems are such where nearly every component is designed and integrated by Nion. Additionally, the system is operated by an open-source software called Nion Swift is used. This software is far more flexible and allows for greater freedom in instrument control and has strong python integration with an easy-to-implement API. With this API, I was able to implement control and acquisition schemes (Fig. 6.4).

a

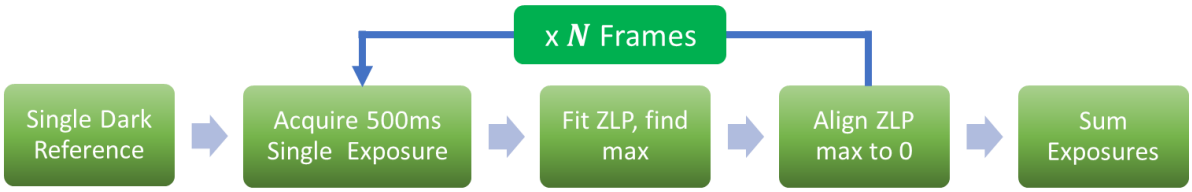

b

```
eels = api.get_hardware_source_by_id("eels_tuning_camera", "1.0")

exptime = interactive.get_integer("exposure time_ms", 1000)
fp_low_loss = {'binning' : 1, 'exposure_ms' : exptime}

data_list = eels.grab_next_to_start(fp_low_loss)
data_list = eels.grab_next_to_finish()
```

Figure 6.4. Multi-frame acquisition scheme and python code. a, Acquisition scheme for acquiring multiple spectra, aligning their ZLPs, and finally summing them to create a single high SNR spectrum. b, python code using nion swift API to control nion UltraSTEM hardware parameters and acquire spectra. This code may not be current by the time this thesis is published.

The objective of developing specific acquisition schemes for vibrational EELS data is to optimize SNR and to ensure the energy resolution remains optimal. To solve the first problem, the most straightforward solution is to collect a large amount of signal. However, this is limited by the saturation limit of the EELS detector. For acquiring spectra in vacuum, I found the limit to be around 300-500 ms after which the detector will saturate and the ZLP shape will become blunt (Fig. 6.5). Of course, this is highly related to emission current and response of the specific detector but generally, the method of simple acquiring more counts is not ideal. Although far more stable than in other systems, the ZLP at this dispersion has a non-negligible drift that results in a broader ZLP and worsening of the energy resolution during long acquisitions. Therefore, simply increasing the exposure time is not ideal. Instead, it is necessary to acquire several individual acquisitions and then sum them up. Before summing up, the ZLP's in each acquisition must be aligned. This way of acquiring high SNR

ensures that the ZLP does not saturate the detector, and then the drift of the ZLP is also correct (Fig. 6.6). Typically, the exposure time of these acquisitions or frames are set so that the ZLP is just weak enough to not saturate the detector. As the scaling of SNR is root(counts), it is advantageous to maximize counts. This point spectrum acquisition scheme is outlined in Fig. 6.4.

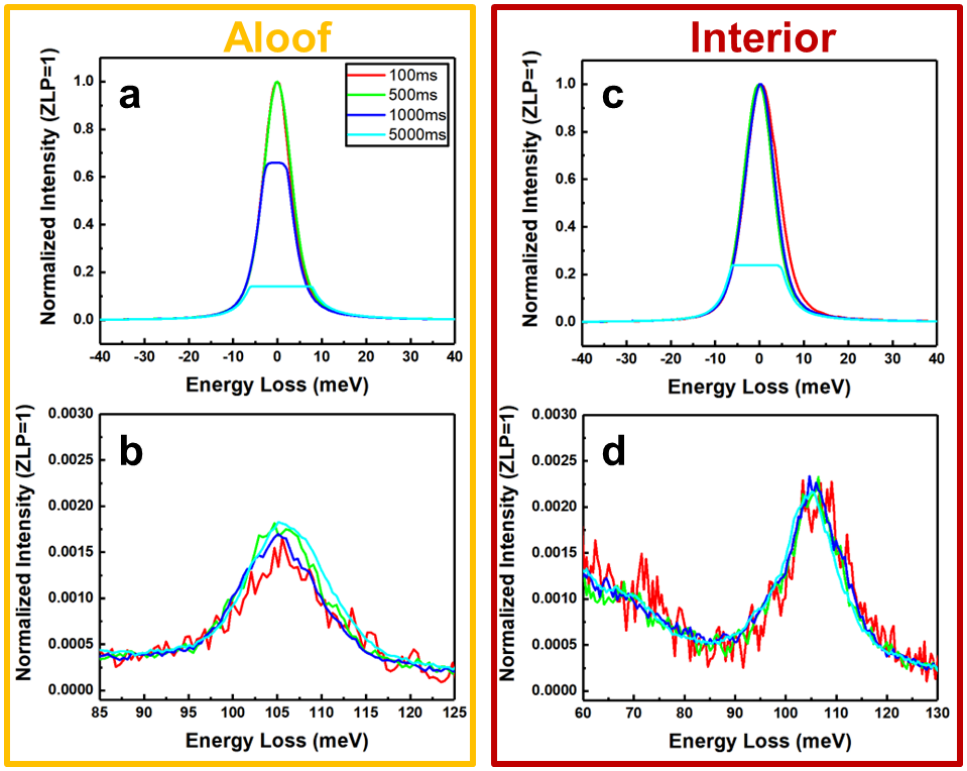

Figure 6.5 Effects of increasing exposure time. a, ZLP shapes under aloof configuration at various exposure times. EELS camera saturates at under 1000ms giving the ZLP its rounded shape. This makes determining the center impossible and may also damage the camera. b, SiC-3C SPhP under aloof configuration at various exposure times. SNR improves with increasing exposure time. c, ZLP shapes when probe is placed on the sample at exposure times. Here the EELS camera does not saturate at 1000ms due to less electrons making it to the detector after interacting with the sample. d, SiC-3C bulk and surface phonon signals at various exposure times. Here SNR also improves with increasing exposure time.

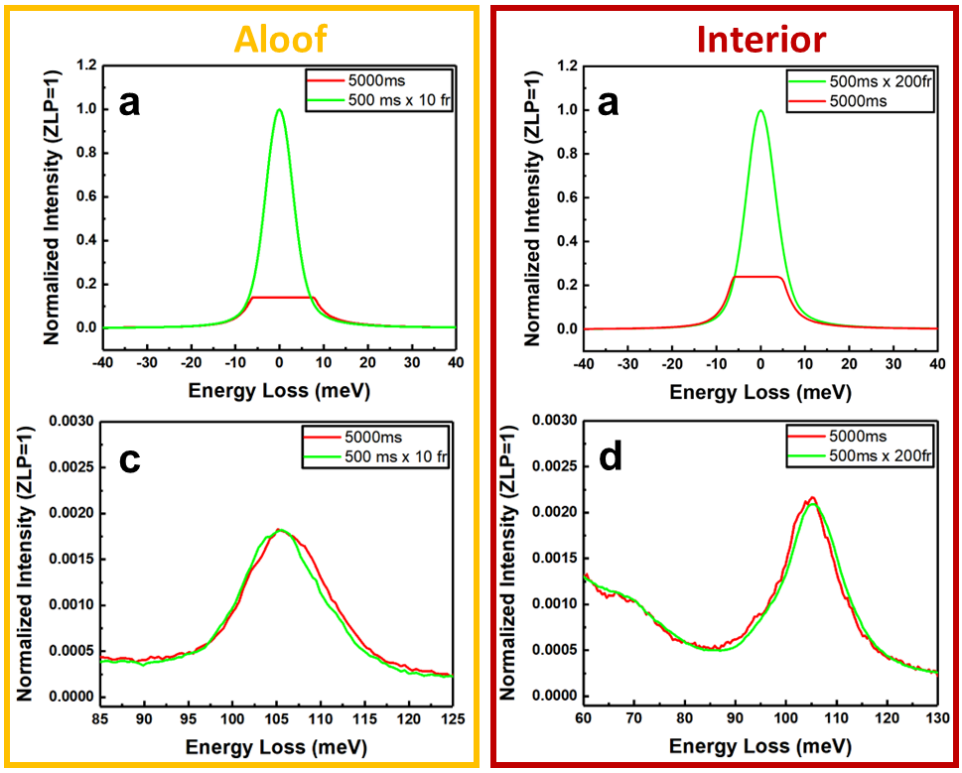

Figure 6.6. High exposure vs multi-frame acquisition. a, Aloof beam ZLP saturates for 5s exposure while multi-frame acquisition with the same total exposure time does not. b, SiC-3C SPhP under aloof configuration showing similar SNR for both single high-exposure and multi-frame acquisitions. c, ZLP saturates for 5s exposure while multi-frame acquisition can be scaled to an indefinite number of frames without saturation. d, Multi-frame acquisition with total time of 100s shows much higher SNR when compared to the single exposure 5s one.

The true capability of vibrational EELS in the STEM is unleashed when phonons are mapped spatially at previously inaccessible scales. However, as discussed earlier, phonon signals are quite weak and so multi-frame acquisition schemes become necessary. Combining multi-frame acquisition with spatial mapping, however, can lead to acquisitions that last multiple hours. On this time scale, microscope conditions can worsen, and beam current can fall presenting impediments to acquiring high quality maps. As a result, microscope control to correct for these factors needs to be implemented. The dominant factors behind worsening

of EELS conditions include broadening of the ZLP due to spectrometer aberrations and decreasing of the emission current. A correction and acquisition scheme is illustrated in Fig. 6.7. To combat the broadening of the ZLP that occurs over time as well as due to large FOV probe movements, 1st order EELS aberrations are corrected automatically. If the ZLP intensity is lower than a certain user defined threshold, the acquisition is paused, and the tip is flashed. Then the user can adjust other parameters before resuming the acquisition.

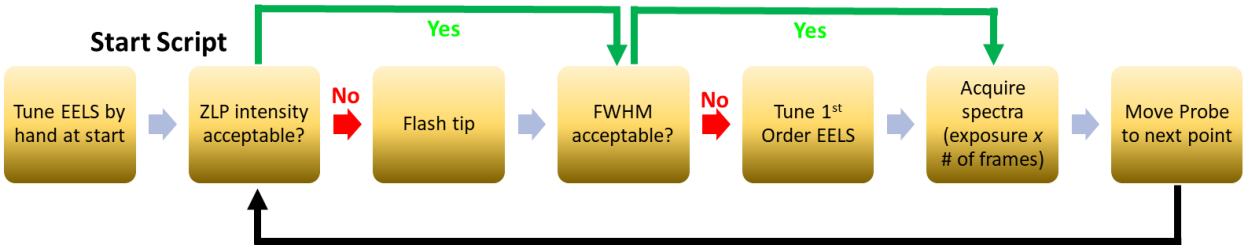

Figure 6.7 Correction and acquisition scheme for spatially mapping phonons. Script pauses acquisition if ZLP intensity is too low and flashes the tip. 1st order EELS aberrations are corrected if ZLP FWM is too wide, indicating a worsening of the energy resolution. Correcting for these factors allows high quality acquisitions on the order of hours.

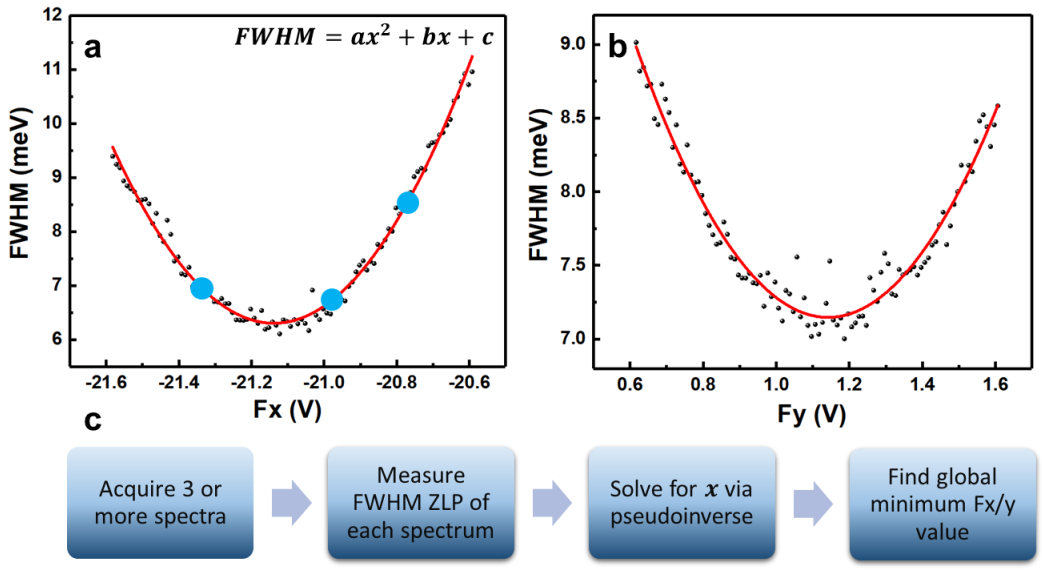

Figure 6.8 Correction of 1st order EELS aberrations. a-b, Fx/y quadratic relationship on ZLP FWHM. A minimum of 3 measurements of the ZLP FWHM are needed to define the global minimum. However, in practice it is best to acquire at least 5 to account for statistical error. c, Process for correcting 1st order aberrations.

I found that mainly 1st order EELS aberrations, Fx, and Fy, change over the course of an hour while higher order aberrations are more or less stable. This means that we need only correct for the 1st order in order to maintain optimal energy resolution. To uncover the relationship between the Fx/y EELS drives and the ZLP FWHM, several values are explored (Fig. 6.9). Once the unique quadratic relationship is determined with at least 5 ZLP FWHM measurements, Fx/y drives can be set to the global minimum value. This process takes approximately 1-5 seconds depending on how many measurements are taken. During the acquisition of 2D data using the process illustrated in Fig. 6.7, 1st order EELS aberration correction is typically only conducted once every 2-5 minutes depending on the stability of the microscope.

6.4 Unsupervised machine learning approaches for EELS data

Unsupervised machine learning involves training a model on a dataset without providing it with labeled or target outputs. Without guidance, the model is left to identify patterns and features in the data that may not be immediately apparent. There are several ways in which spectral data can be analyzed using unsupervised machine learning techniques. One common application of unsupervised machine learning in spectral data analysis is clustering, which involves grouping together data points that are similar to one another based on

certain features or characteristics. This can be useful for identifying patterns in the data that may not be immediately apparent, and for classifying diverse types of spectral data into distinct groups. Another common use is dimensionality reduction, which involves reducing the number of features or dimensions in the data in order to make it easier to analyze. Unsupervised machine learning can also be used to extract key features from spectral data, such as spectra peaks or wavelengths. These features can then be used to classify distinct types of spectral data, or to identify patterns and relationships in the data. Overall, unsupervised machine learning methods are valuable tools for gaining a deeper understanding of the data.

Before the data undergoes processing, it is often not only instructive but prudent to explore the data for correlative relationships. This is because data processing such as background subtraction can often bias the data if the model is too rigid. Additionally, understanding the correlations before the data has been processed already gives you a good idea of how many distinct features exist and how they are distributed. The parameter space of raw 3D data is the product of the spatial dimensions with the energy dimension. For a typical spectrum image of about 100x100 pixels in the spatial dimensions and about 2000 in the energy dimension results in 20 million parameters. It is very difficult to navigate such a large parameter space and find meaningful correlations. As a result, it is a widespread practice to reduce the size of the input domain by mapping it to a space with fewer, more manageable number of parameters. This can be achieved by either linear or non-linear transformations. After which correlations in the data are more easily seen and can be grouped via unsupervised clustering algorithms.

6.4.1 Matrix factorizations

Linear transformations are more straightforward to carry out and are often less computationally intensive relative to non-linear ones. Popular matrix transformations include principal component analysis (PCA) and non-negative matrix factorization (NMF). PCA has the advantage of being a unique factorization whereby the data is transformed into its eigen basis. NMF is a special case of PCA that has the constraint that components must be positive. This is commonly used for processing physical data as negative, non-physical decompositions are forbidden. Both algorithms involve a transformation that rotates the hyperdimensional coordinate system in order to maximize the variance of its components. This means that the first component of these decompositions contains the greatest amount of information while the last component contains the least. An extremely useful consequence of transforming the data in this way is that the notable features of the data occupy only the first few components while the rest are mainly noise (Fig. 6.9). As a result, denoising the data simply involves excluding higher order components. This effectively compressed the data to a lower dimensional latent space and is far more manageable and useful for further analysis. A brief description of the processes behind Principal component analysis (PCA) and Non-negative matrix factorization (NMF) is given in subsequent paragraphs.

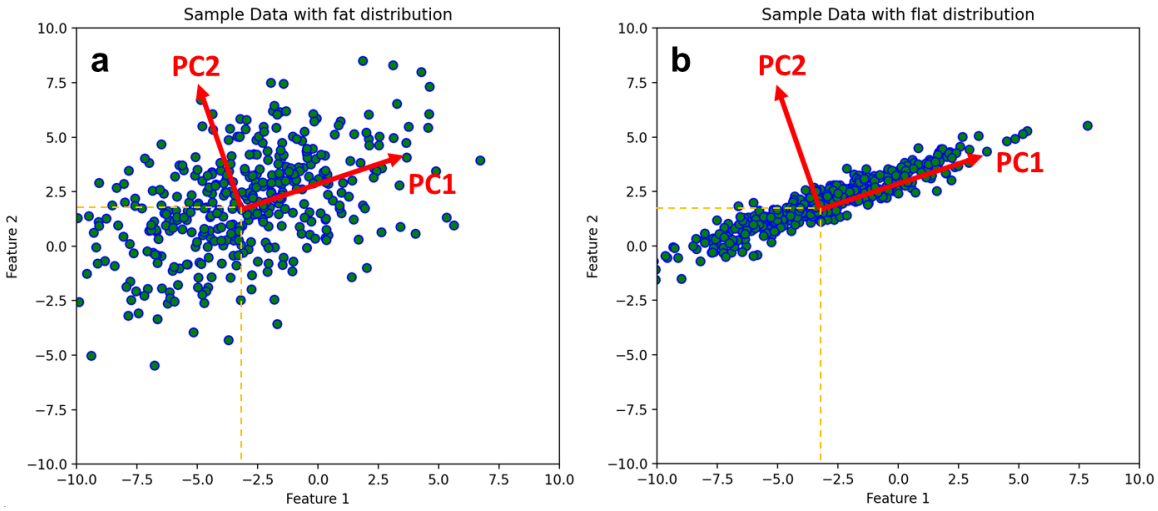

Figure 6.9 Examples of feature distributions in data and their PCA decompositions. a, Sample data with a "fat" distribution. b, sample data with a "flat" distribution. Mean of (a-b) is (-3, 2). PCA decomposition is identical in both cases, however in (b), PC2 can be excluded as the spread along that component is minimal. Although, if PC2 captures mostly "noise" in the data, it can also be ignored in order to "denoise" the data without impacting the "real" features in the data.

PCA, like other matrix factorization techniques, is a statistical technique used to analyze the patterns in data and reduce the dimensionality of the data, by identifying the directions in which the data varies the most. PCA works by finding a unique linear combination of the original features in the data that explains the most variance in the data. These linear combinations are called principal components where first principal component explains the most variance in the data. The second principal component is the one that explains the second most variance, and so on. PCA is often used to visualize high-dimensional data in a lower-dimensional space and can also be used to reduce the dimensionality of the data, by selecting only the most important principal components and discarding the rest. This can be useful in situations where the data has a lot of features, but only a few of them are relevant (Fig. 6.9).

To perform PCA, it is imperative to first standardize the data by subtracting the mean and dividing by the standard deviation for each feature so that each feature is given equal weight. Next, the covariance matrix of the data is calculated, which is a matrix that quantifies correlations between the various features. The covariance matrix is then diagonalized giving the eigenvectors, principal components, and the corresponding eigenvalues, explained variances of each component. The original data is decomposed into a product of samples in the PCA-space and principal components (Fig. 6.9a). The decomposition itself only rotates the data into a principal coordinate system and does not change the data. In this principal coordinate system, one can then select the number of principal components to keep, based on the amount of variance needed to explain the data or the number of dimensions the data needs to be reduced to. Mapping the data to a lower dimensional latent space is achieved by the omission of higher order components (Fig. 6.9b).

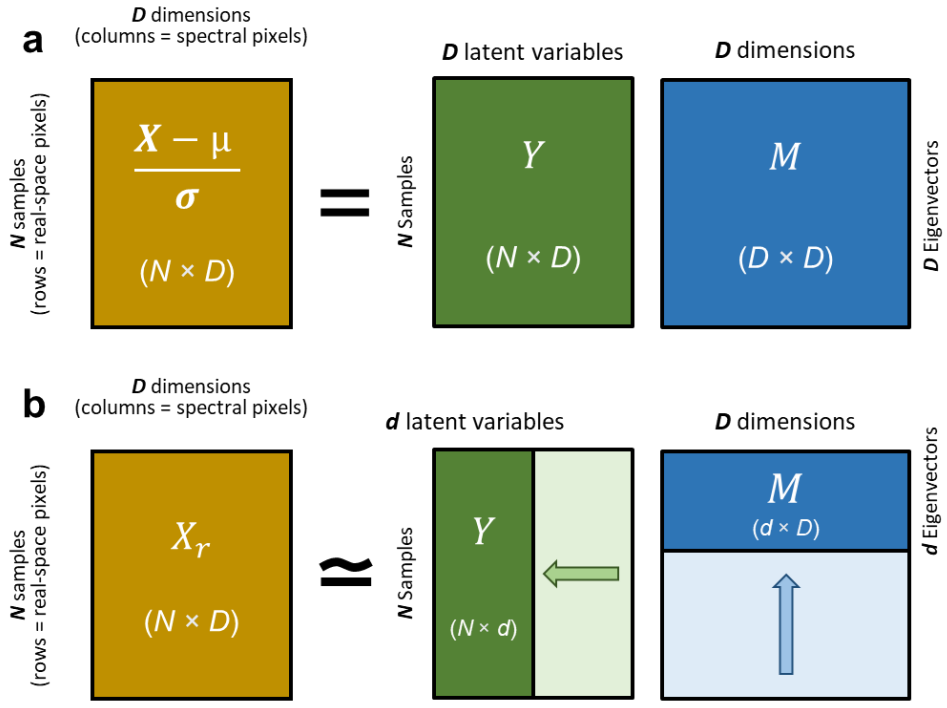

Figure 6.10 Illustration of PCA decomposition. a, Standardized data $\frac{X-\mu}{\sigma}$ is decomposed into samples Y in the principal coordinate system and principal components M. b, X_r is X in a reduced latent space and is formed by samples Y with d latent variables and first d principal components M.

Non-negative matrix factorization (NMF) on the other hand, is a technique for decomposing a matrix into the product of two other matrices, where all elements in the matrices are non-negative. It is a type of matrix factorization that is particularly useful for analyzing and interpreting data with non-negative values, such as counts or proportions making it especially suitable for use on EELS data. NMF decomposition begins with a non-negative matrix X that is decomposed into the product of two other matrices W and H, where W represents the weights of the features and H represents the activation of the features. The goal is to find the matrices W and H that minimize the reconstruction error, which is the difference between the original matrix X and the reconstructed matrix $W * H$. NMF can be solved using various optimization algorithms, such as multiplicative update or alternating least squares. It can also be extended to handle additional constraints, such as sparsity or smoothness, or to incorporate additional information, such as side information or missing data. NMF has several advantages over other matrix factorization techniques, such as PCA or SVD. It is more interpretable, as the elements in the matrices W and H are non-negative and can be interpreted as counts or proportions. It is also more robust to noise and missing data, as it can handle data with missing values and can impose additional constraints to regularize the solution.

For EELS datasets where each sample is one spectrum, dimensionality reduction is necessary both for denoising data and isolating correlations in the data. This allows for the parameters

space to be reduced from around 2000 to about 4-10 with the rest of the dimensions containing mostly noise. It should be noted that proper use of PCA on EELS data is highly dependent on the noise level. PCA on data with high noise level may bias the results and alter conclusions of the data[90]. However, with proper noise mitigation techniques at the acquisition level[91], PCA can be used as a reliable and powerful tool for denoising and reducing the dimensionality of EELS datasets.

Fig. 6.11 demonstrates a detailed analysis of applying PCA to a vibrational EELS dataset. Here, PCA is carried out using python's SciPy library which includes many other high-level functions for unsupervised machine learning. However, it is still necessary to customize and compile useful functions in a framework that is dedicated and optimized for EELS datasets. All panels in Fig. 6.11 are generated with only a single function call after the data is imported: EELSdata.PCAplots(plotlist) where plotlist is a list of plots to export for comparison between PCA filtered and raw data. These plots, with the desired arguments, generate descriptive panels that inform the user of the details of the decomposition making applying PCA to EELS datasets extremely simple and transparent. The backend code takes care of the preprocessing and postprocessing steps and finally generates easily interpretable graphs that are publication ready. The user also has the option to export CSV files of all the data shown in the panels for plotting with their software of choice. The same analysis can be accomplished for NMF and ICA decompositions as well.

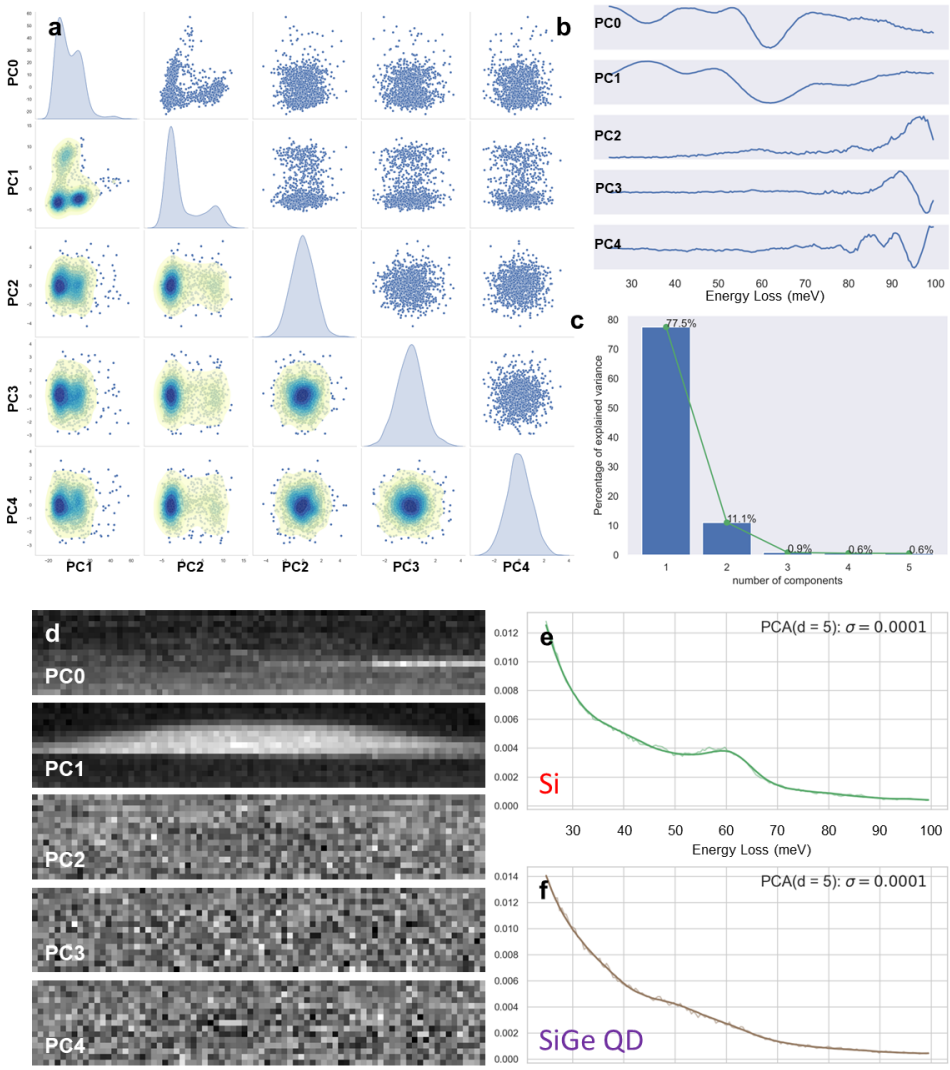

Figure 6.11 PCA of Vibrational EELS of a SiGe QD. a, Pair plots of 5 principal components (PC). In this lower dimensional latent space, correlations and agglomerations of expressive features are more easily seen. Colored contours are kernel density estimates that indicate how spectra are distributed in the latent space. Kernel density estimations (KDE) are overlayed: blue-green contrast indicate high density of points while yellow and transparent contrast indicate sparse distributions. b, scaled eigenvectors or PCs of the dataset. c, explained variance of the dataset. (d, Spatial map of first 5 PC loadings. PC0 map contains little contrast since it contains the underlying feature present in all spectra. PC1 begins to distinguish between vibrational signals in the Si and SiGe QD. (b-d) indicate that only the first two PCs contain crucial features of the dataset and account for nearly 90% of the data. In (b), PC2-4 only show variation past 80 meV where there are no vibrational signal. (b-d) indicate that PC2-4 only contain noise or other features that are not relevant to experiment. e-f, comparison between raw and 5 PC reconstruction of vibrational EEL spectra in Si and SiGe QD.

6.4.2 Clustering

Unsupervised clustering is a branch of machine learning that focuses on the identification of patterns within a dataset. The term "unsupervised" refers to the fact that these algorithms operate without prior knowledge or training data that has been classified or labeled. Instead, they seek to discover the inherent groupings within the data based on the data's own features. The primary mechanism by which unsupervised clustering operates is by measuring the distance or similarity between individual instances of data in feature space. The goal of these algorithms is to group together instances that are similar (minimizing intra-cluster distance) and separate instances that are dissimilar (maximizing inter-cluster distance).

There are several commonly used unsupervised clustering algorithms, each with its unique strengths and weaknesses. K-Means, for instance, is an algorithm that partitions the data into a specified number (K) of non-overlapping clusters. It begins by randomly initializing K centroids, then assigns each instance to the nearest centroid. The centroid is then updated by calculating the mean of all instances within the cluster. This process is repeated until the centroids stabilize and no longer change significantly. Hierarchical clustering, on the other hand, constructs a hierarchy of clusters either from a bottom-up (agglomerative) or top-down (divisive) approach. The result is a tree-like diagram known as a dendrogram, which allows the user to select the desired level of granularity for the clusters. Another notable algorithm is DBSCAN (Density-Based Spatial Clustering of Applications with Noise). This algorithm groups together instances that are densely packed, marking instances that lie alone in low-density regions as outliers.

However, unsupervised clustering is not without its challenges. Determining the optimal number of clusters can be difficult, especially for algorithms like K-Means that require the number of clusters to be specified in advance. Clustering algorithms can also be sensitive to initial conditions, such as the initial placement of centroids in K-Means. Furthermore, they may struggle with clusters of different shapes and sizes. Despite these challenges, unsupervised clustering remains a powerful tool for exploratory data analysis. It allows us to uncover hidden structures and patterns in data, but the interpretation of these clusters is subjective and depends on the domain knowledge of the data scientist or expert.

Unsupervised clustering can be a powerful tool for analyzing Electron Energy Loss Spectroscopy (EELS) data[92,93]. EELS generates a large amount of high-dimensional data, where each spectrum is a point in high-dimensional space. Each dimension corresponds to a different energy loss value, and the value in that dimension corresponds to the intensity at that energy loss. The high dimensionality of this data makes it difficult to glean notable information manually. Unsupervised clustering seeks to solve this problem by grouping distinct modes of the data.

Unsupervised clustering algorithms can be used to group similar spectra together based on their intensity profiles[92–94]. This can help to identify regions of the sample that have similar elemental composition or bonding environment. For example, if a sample is composed of distinct phases or contains inclusions or precipitates, these different regions will have different EELS spectra and can be identified by clustering.

The first step in applying these algorithms to EELS data is to preprocess the data. This typically involves noise reduction and normalization of the spectra. Noise reduction can be

achieved through methods such as Principal Component Analysis (PCA) or Singular Value Decomposition (SVD), which can help to remove random noise and retain the significant features of the spectra. Normalization ensures that all spectra are on the same scale, which is important for clustering algorithms that use distance measures. Although clustering can technically be accomplished without dimensionality reduction, the results are often uninterpretable due to the extremely high dimensional space that raw EELS data lives in. Therefore, dimensionality reduction preprocessing using matrix factorizations described in the previous section is necessary.

Once the data has been preprocessed, a clustering algorithm such as K-Means or hierarchical clustering can be applied. The choice of algorithm depends on the specific characteristics of the data and the goals of the analysis. For example, K-Means is a desirable choice if you expect the spectra to be grouped into distinct clusters, while hierarchical clustering might be more appropriate if you expect the spectra to be organized into nested groups. The output of the clustering algorithm is a set of labels, one for each spectrum, indicating which cluster the spectrum belongs to. These labels can be mapped back onto the spatial coordinates of the sample, creating an image that shows the spatial distribution of the different clusters. This image can provide valuable insights into the composition, structure, or vibrational features of the sample depending on which energy range is captured by the spectral data.

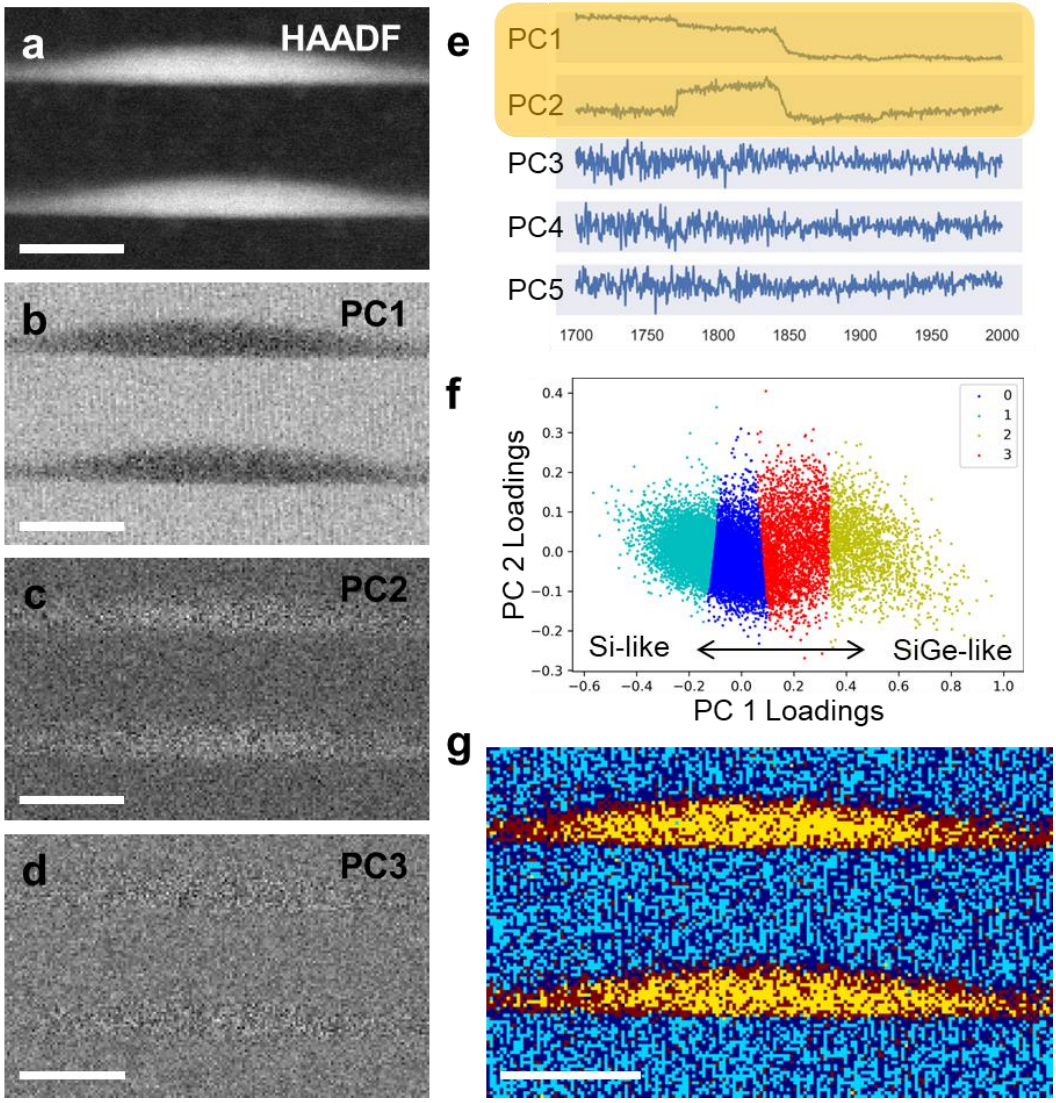

Figure 6.12 Matrix Factorization and Clustering of Composition mapping a, HAADF image of 2 QDs. b-d, loading maps of the first 3 principal components (PC) illustrating the spatial distribution of the factorized components. A strong spatial correlation of the first 2 PCs with the location of the QD is seen. e, Plot of the first 5 eigen vector signals. The first two PCs show distinct features recognizable from the EELS spectra in Ext. Data Fig. 2 highlighted by the yellow box. f, A k-means clustered scatter plot using the loadings of the first two PCs. The plot consists of a slightly higher density cluster to the left but in general, there are no distinct clusters. g, k-means clustering map displaying the spatial distribution of the clusters. From the mapping, it seems that a higher value of PC1 corresponds to a more SiGe-like EEL spectra. The mapping shows some evidence of Si overlapped regions around the QD but there is no clear separable cluster associated with such a signal; the transition is gradual. All scale bars denote 20nm.

We explored the possibility of separating the contribution from the QD and the interlayer Si in the beam direction (Fig 6.12). We employed PCA to factorize the hyperspectral core-loss EELS data to obtain the principal components of the data, essentially projecting it to a lower dimensional latent space. Since these are orthogonal by definition, any distinct variations in the signal are separated into their own eigenvectors. The loading maps for the first 3 PCs (Fig. 6.12b-d) do not immediately show any evidence of factorable signals along the edges of the QD. We then used the loadings of the PCA decomposition to perform K-means clustering to separate the signals into statistically significant groups. Fig. 6.12f suggests that PC1 is significant in determine if the core-loss character is Si-like or SiGe-like. The mapping Fig. 6.12g implies that the edge of the QD belong to a distinct group. This could suggest a degree of intermixing and could also be used to quanitify the smoothness of the interface.

K-means clustering and the export of plots in Fig. 6.12 are easily done in 1 line of code using the EELS framework by invoking EELSdata.cluster("K-means", $k = 4$). This abstraction assumes certain defaults and is a customized wrapper around sklearn's clustering class. Since we are dealing with EELS data, certain defaults in preprocessing as well as visualization can be assumed to make interfacing with high-level code simple and transparent.

Although there seems to be some separation of the signals at the borders of the QD, we were not able to confidently claim that we are able to separate the signals. This is possibly because of the QD being an imperfect alloy of Si and Ge i.e. not a perfect 1:1 mixture. With the existence of the pure Si OM even within the QD, there must be some random order of pure Si atoms that are not bonded with Ge. This means that the core-loss EELS signals from the interior are already a combination of Si-Si Si K-edges and Si-Ge Si K-edges resulting in the

fine structure of Si k-edge not being confidently separable. Additionally, the distribution of points in the PC1-PC2 latent space suggests that the modes of the data cannot be separated well by k-means clustering as their distribution seems gaussian-like

Gaussian Mixture Models (GMM) however, are adept at clustering gaussian distributions in latent space. GMMs are a type of probabilistic model used in machine learning for clustering, much like K-means. They are called "mixture models" because they model data as a mixture of several Gaussian distributions, each characterized by their mean and variance. The key idea is that each data point belongs to each Gaussian distribution to a certain degree, depending on the probability of the point being generated from that distribution. This is in contrast to K-means, which assigns each data point to the cluster with the nearest centroid, making a hard assignment. The main difference between GMMs and K-means is that GMMs take into account not just the mean of the data points in each cluster (like K-means) but also their variance. This allows GMMs to form elliptical clusters of different sizes, while K-means can only form spherical clusters of similar sizes. Furthermore, GMMs provide soft clustering, meaning each data point belongs to each cluster to a certain degree, while K-means provides hard clustering, meaning each data point belongs to exactly one cluster.

In the context of EELS data, each mode in the latent space can correspond to a different physical or chemical state of the sample. For example, different modes might correspond to different types of atoms, different chemical bonds, or different electronic states. These modes can overlap and interact in complex ways, making it challenging to separate them and analyze their properties. GMMs are particularly well suited to this task for several reasons including probabilistic modeling, flexibility, and soft clustering. GMMs provide a

probabilistic model of the data, which can capture the uncertainty and variability inherent in EELS measurements. This can help to quantify the confidence in the identified modes and their properties, and to account for measurement errors and noise. They can model a wide range of distributions, not just spherical clusters like K-means. By adjusting the means, variances, and covariances of the Gaussians, GMMs can capture elliptical and elongated modes, and modes with different sizes and orientations. This can provide a more accurate and detailed representation of the data. They also provide soft clustering, meaning that each data point belongs to each mode to a certain degree, depending on its probability under the corresponding Gaussian. This can capture the fact that the boundaries between different states in EELS data are often not clear-cut, but rather gradual or fuzzy.

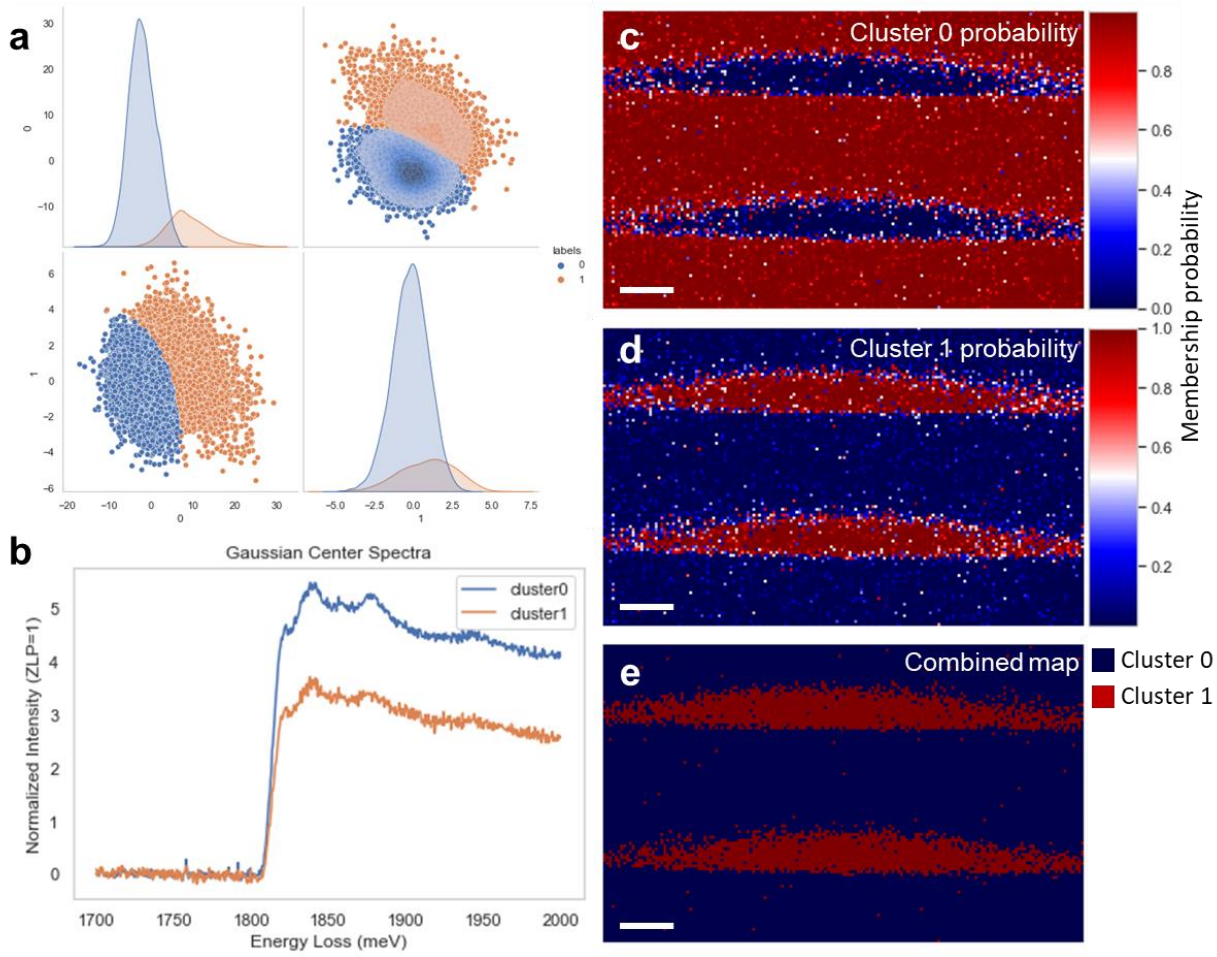

Figure 6.13 Gaussian Mixture Model decomposition a, Pair plots of 2 PC decomposition. Colors blue and orange indicate cluster assignments 0 and 1, respectively. The top right corner shows a pairplot overlaid with KDEs for the individual cluster assignments. b, Plot of the gaussian mean spectra. c-d, Cluster probability maps. e, Combined map of both clusters. Here, assignment is based on majority probability. All scale bars denote 10 nm.

Like K-means, GMM mode separation can be achieved simply by replacing the keyword to GMM: EELSdata.cluster("GMM", k = 2). The export of the function call presents the user with a complete description of the GMM decomposition including the cluster assignments in the pair plot (Fig. 6.13), plot of the mean spectra, and spatially resolved maps of the assignment. The mapping in Fig. 6.13c,d illustrates the flexibility of GMMs soft assignments. The variation of the Si K-edge is categorized into 2 groups with a non-negligible overlap between the two

at the QD-Si boundaries. Where K-means failed due to its spherical nature, GMMs allow for the fitting of elliptical data and data where there are steep correlations. The ability to soft-assign data points cannot be stressed more as EELS data often exists between a superposition of multiple sources.

6.5 Extracting Phonon modes from Data

Background subtraction and peak fitting are essential steps in the processing of vibrational EELS data. They allow us to remove unwanted signals, isolate the vibrational features of interest, and quantify their properties. This enables us to gain insights into the vibrational properties of materials, such as their phonon dispersion relations, bonding strength, and structural dynamics, among other things. Therefore, it's crucial to process the data through background subtraction and peak fitting.

6.5.1 Background Subtraction

The EELS spectrum usually contains a background signal that arises from inelastic scattering processes that do not involve vibrational excitations. This background can be due to multiple scattering, zero-loss peak, or the tail of the ionization edge, among other things. The background signal often has a smooth variation with energy loss, while the vibrational signals appear as sharp peaks superimposed on this background. Therefore, to accurately measure the intensity, position, and width of the vibrational peaks, it's necessary to subtract the background signal. Various methods can be used for background subtraction, such as

power-law fitting, exponential fitting, or fitting with a combination of different functions. The choice of method depends on the characteristics of the background signal and the specific requirements of the analysis.

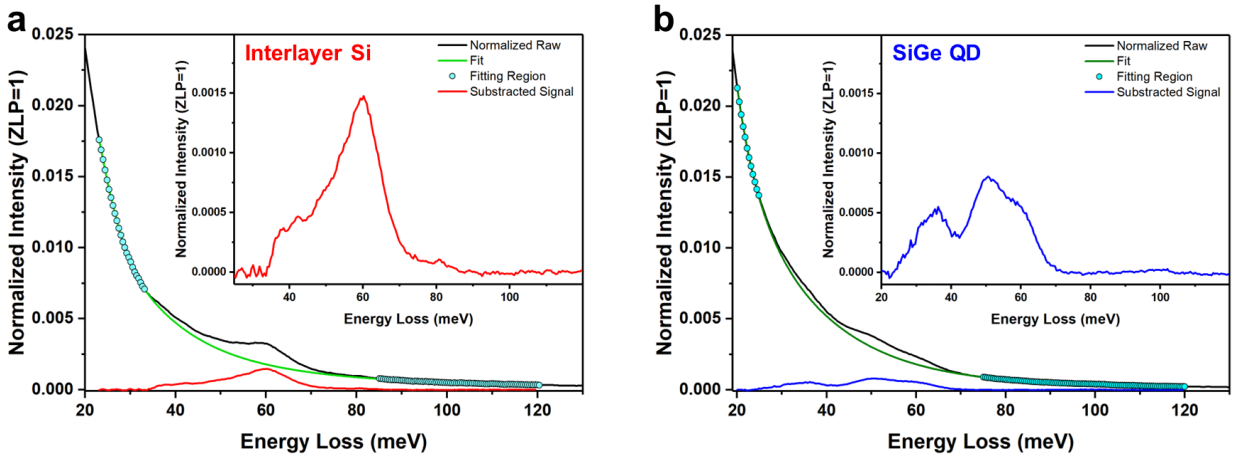

Figure 6.14 Background subtraction of vibEEL spectra. a-b, Typical background subtraction procedure of spectra acquired in interlayer Si and SiGe QD respectively. The green colored line represents the normalized as-acquired spectra in the corresponding regions. Blue dots represent the spectrum region used for fitting the background. The red curves in the main plot and in the inset represent the background subtracted signal.

The panels in Fig. 6.14 illustrate how the phonon signals of interest are a small fraction of the background from the ZLP. Before background removal, phonon intensity is obscured as the changes in the ZLP tail will overpower any changes in the phonon signal. To define the nature of the ZLP tail such that it can be removed requires the fitting of the tail using an analytical function.

The following describes a common process for background removal. Spectra are first normalized with respect to the ZLP maximum so that each vibrational intensity represents a fractional scattering probability. The model largely used in processing the data in this thesis

is composed of a Lorentzian centered on the ZLP and an exponential polynomial $e^{p(x)}$, where $p(x)$ is an even, 4^{th} order polynomial. The specific model described, produces a sharply decreasing left end and a slow and stable right tail that is efficient for accurately extracting the low energy phonon modes. In general, the model can be any analytical function that can estimate the background effectively. Next, the function curve_fit() in the scipy.optimize library is used to estimate the background but a least-squares optimization process. Finally, it is subtracted from the raw data to isolate the phonon signal. In some cases, parts of the signal must be excluded due to energy resolution limitations. For example, Fig. 6.14a,b do not include acoustic modes in the background subtracted phonon signal. Such inconsequential as they can be considered part of the background and subtracted out. The final output should still reflect the accurate intensities of the remaining signal.

6.5.2 Peak Decomposition

After background subtraction, the next step is to analyze the vibrational peaks in the spectrum. In one or two basis systems, the peaks in the signal can be separated into individual modes. In these cases. each vibrational peak corresponds to a different vibrational mode of the material, and the position, intensity, and width of the peak provide information about the energy, strength, and lifetime of the mode, respectively. To extract this information, it's necessary to fit the peaks with appropriate functions, such as Gaussian or Lorentzian functions. Peak fitting allows us to decompose the spectrum into its individual vibrational modes and to quantify their properties. It also helps to separate overlapping peaks that correspond to different vibrational modes.

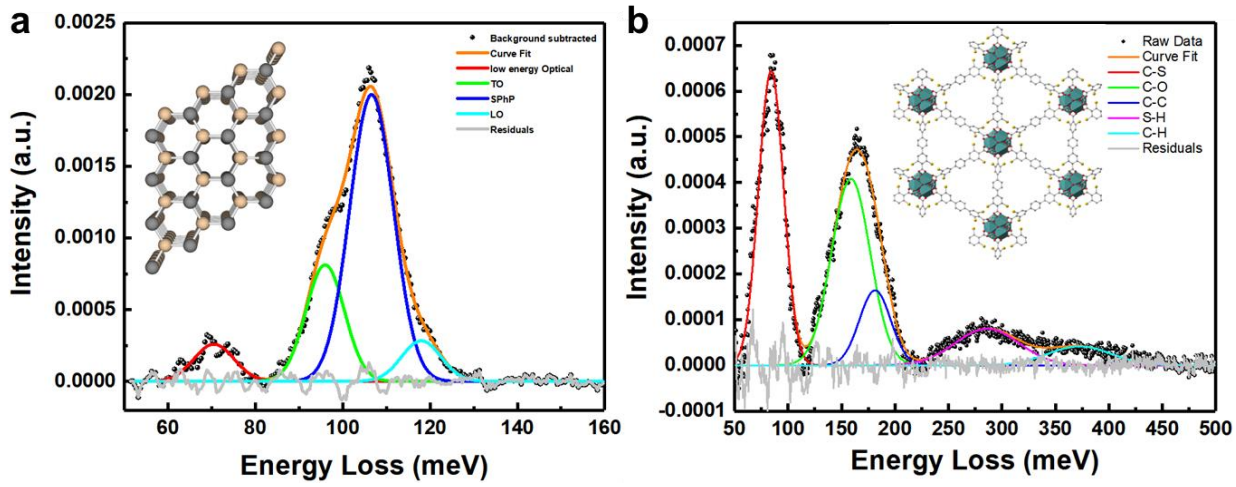

Figure 6.15 Phonon peak decomposition of SiC and a metal oxide framework (MOF). a, 3 interior modes: TO, LO, and a low energy optical mode is separated from the non-local SPhP mode. Structure model of SiC-3C is included in the top left corner. b, Vibrational signal of a complex MOF system with a diverse set of molecular bonds. Peak decomposition allows for identification of distinct molecular vibrations. The height, position, and width of these modes can be mapped for obtaining a nanoscale map of molecular bonding. Structure model of this MOF system is included in the top right corner.

By fitting the vibrational EELS signal with pseudo-Voight fits which are linear combinations of gaussians and lorentzians, we can gather information about a mode's excitation probability and its energy position given by the fitting intensity and peak position outputs. The peak decomposition in Fig. 4.2b,c allows for the mapping of position and intensity which each display crucial information about phonon properties in the SiGe QD structure. To fit the set of gaussians to the background subtracted signal, curve_fit() from scipy.optimize is utilized again. Fitting parameters of individual peaks and their corresponding errors are then extracted. The errors obtained from the covariance of the fit indicate the accuracy of the fit. These processes, as developed in the EELS framework allow for the mapping of peak properties and errors. More information will be discussed in the subsequent section.

6.6 Data Visualization

Data visualization plays a crucial role in the analysis of EELS data. It allows us to better understand and interpret complex data sets, revealing patterns, trends, and insights that might not be immediately apparent from raw data. Fitting Gaussian peaks to the background-subtracted signal can provide valuable information about the energy distribution of the vibrational modes. The height of the peak can indicate the state occupancy of a particular mode, the position can reveal its energy, and the width can provide information about the mode's dispersion or broadening. Mapping these parameters spatially across the sample can provide insights into the spatial variation of these properties, which can be linked to variations in the material's structure or composition. For example, changes in peak position might indicate changes in bond lengths or angles, while changes in peak width might suggest variations in crystallographic order. Furthermore, visualizing these maps can help identify regions of interest, such as defects, grain boundaries, or areas with particular elemental composition. This can guide further analysis or experimental work, making data visualization an indispensable tool for the effective use of EELS in materials science.

Apart from mapping phonon properties it is also necessary to visualize every step of the data analysis process. The previous figures showcased how PCA decomposition using the EELS data analysis framework clearly displaces the result and contributes to a more transparent data analysis process. Similarly, the quality of the background subtraction and peak decomposition can also be determined by plotting the fit. Fig. 6.16 illustrates background subtraction, peak decomposition, and mapping of peak properties spatially. Contour plots of

mapping data were created using matplotlib.pyplot, another python library which is wrapped by the EELS framework with customized defaults geared for the visualization of spatial EELS data.

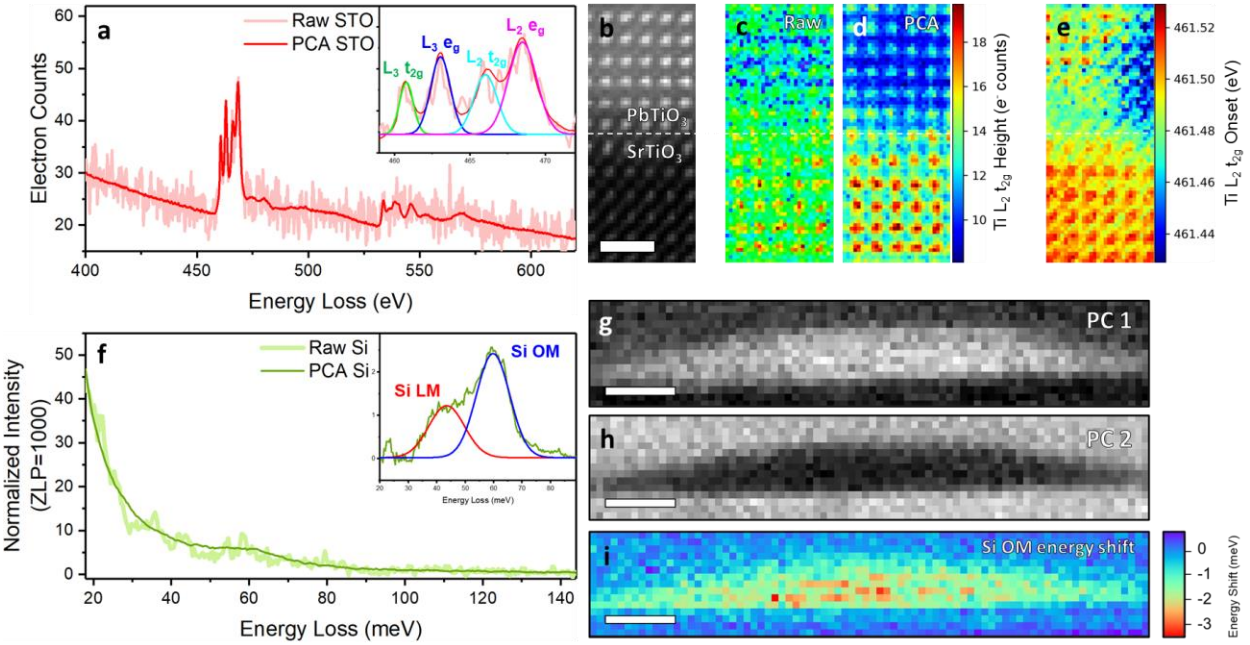

Figure 6.16 Post data processing high and low loss EELS mapping. a. PCA filtered single-pixel spectrum with inset of peak decomposition of Ti L_3 and L_2 edges. b. HAADF image containing a $PbTiO_3$-$SrTiO_3$ interface. c. Ti L_2 t_{2g} intensity mapping of untreated data d. Ti L_2 t_{2g} intensity mapping of PCA filtered data e. Ti L_2 t_{2g} onset mapping obtained from peak decomposition. Scale bars in (b-e) denote 1 nm. f. PCA filtered, single-pixel spectrum with inset of peak decomposition of Si vibrational modes. g-h. Map of loadings of first two principal components. i. Map of Si optical mode (OM) peak shift. Scale bars in (g-i) denote 10 nm.

Fig. 6.16 represents the culmination of the end-to-end EELS data processing. Starting with raw data and ending with a spatially correlated map of phonon properties. PCA is central in converting noisy data to high signal-to-noise spectra whose features can be reliably analyzed. In Fig 6.16d, there is a significant increase in the signal-to-noise ratio (S/N), enabling the decomposition of the Titanium (Ti) fine structure. It's important to note that without the application of PCA, peak decomposition would be unachievable as the fitting

would either fail or yield large errors. The PCA filtered maps in Fig. 6.16d,e present a clear improvement over the untreated data in Fig 6.16c.

By mapping the peak properties of the Ti L_2 t_{2g} peak, we can determine the Ti valence state. Just above the interface, the onset dips, suggesting a lower oxidation state and, therefore, the presence of a two-dimensional electron gas (2DEG). While previous EELS studies of free charge carriers have been limited to single point scans or line scans, for the first time, 2D mapping of oxidation state and charge carriers is achievable. Fig. 6.16f shows a similar improvement for vibrational spectra as Fig. 6.16a. One of the main utilities of PCA is its ability to separate high variance features. Fig. 6.16g and 6.16h demonstrate the distinctiveness of the Silicon-Germanium (SiGe) and Germanium (Ge) vibrations, respectively. Moreover, the ability to observe a compositional vibrational redshift is made possible by enhancing the quality of the data through PCA.

6.7 Accelerated data processing

EELS generates large volumes of data that can be challenging to process and analyze. Each EELS spectrum image contains a multitude of pixels, each of which represents a spectrum that needs to be processed. Without parallel processing, these pixels would need to be processed sequentially, which could be time-consuming and computationally intensive. As a result, parallel processing becomes essential. Parallel processing involves dividing a large task into smaller subtasks that can be executed simultaneously on multiple processors. This can significantly speed up the processing of large EELS datasets, as multiple spectra can be processed at the same time. However, implementing parallel processing can be complex,

requiring careful coordination of tasks and communication between processors. This is where tools like Dask come into play.

Dask is a flexible library for parallel computing in Python. It allows you to easily build and execute computation graphs that describe complex computations involving many tasks. Dask automatically handles the scheduling and execution of these tasks, allowing you to focus on your computation rather than the details of parallelization. Dask also integrates well with existing Python libraries like NumPy and Pandas, making it easy to parallelize existing code. It allows for the parallel processing of data, meaning that multiple spectra can be processed simultaneously, significantly accelerating the overall data processing time. This not only speeds up the analysis but also optimizes the use of computational resources.

Moreover, Dask also provides tools for handling larger-than-memory computations, which may occur when processing EELS data. It does this by breaking the computation into smaller tasks and executing them in an order that minimizes memory usage. This allows you to work with large datasets on a single machine or across a cluster of machines. Dask's ability to handle larger-than-memory computations means that it can efficiently process EELS datasets that are too large to fit into memory, making it a powerful tool for large-scale EELS data analysis. By accelerating EELS data processing, we can obtain insights from data more quickly, enhancing the productivity and efficiency

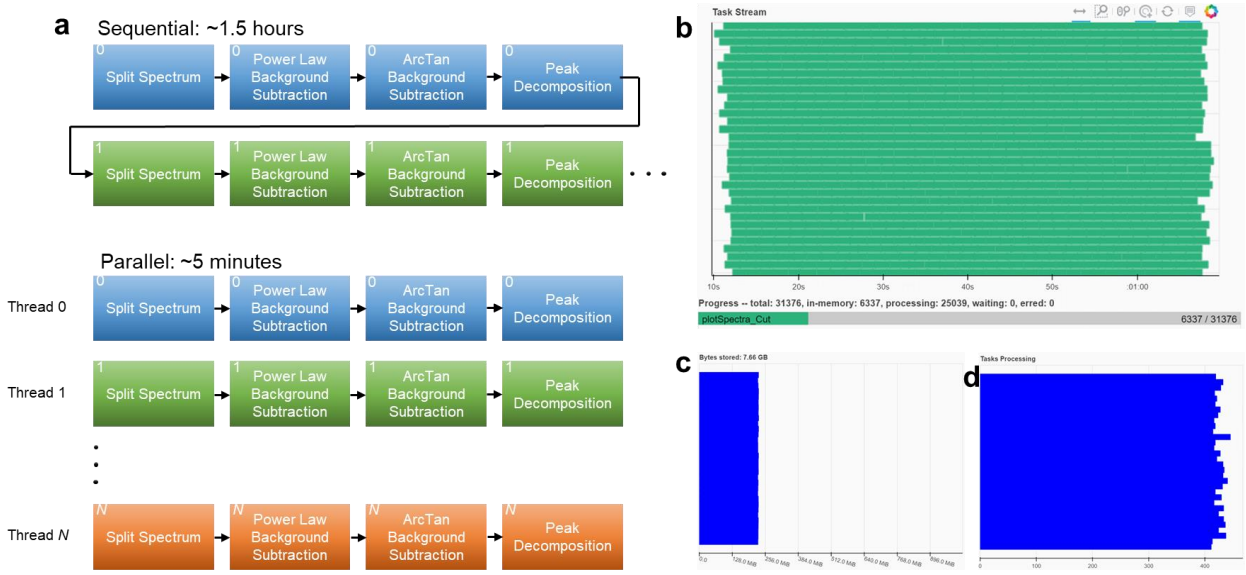

Figure 6.17: Task scheduling of core loss EELS data. a, Comparison of sequential and parallel processing schemes b, Task stream of local cluster displayed by Dask c, Memory allocation per thread d, Task scheduling per thread.

Fig. 6.17 presents an overview of Dask benefits and its scheduling. Processing the fine structure of core-loss EELS data, depending on the size of the mapping, can take upwards of 1.5 hours if done sequentially. With Dask scheduling, parallel processing of the same data takes about 5 mins indicating a 14x speedup. Figs. 6.17b,c show the distribution of tasks in the task stream and memory allocation, respectively. Dask allows the efficient use of high-end, multithreaded hardware for the accelerated processing of EELS data. For low-end systems, Dask also offers lazy loading and processing which allows for the analysis of large, complex datasets on lower-end hardware. As a result, the addition of Dask to any EELS data analysis pipeline is a must. The EELS data analysis framework developed as part of this Ph.D. includes Dask-accelerated functions where parallel processing is appropriate. Future plans to extend hardware acceleration capabilities target the efficient use of GPUs and scaling to computing clusters for even speedier results.

7. Summary and outlook

Our exploration of thermal properties in nanostructured materials, specifically within a SiGe quantum dot (QD) superlattice, has unveiled significant insights into nanoscale phonon physics. Utilizing vibrational spectroscopy in a transmission electron microscope, we have been able to map Si optical phonons in a single SiGe QD with an impressive 6 mev (~50 cm-1) energy resolution. Our findings reveal a composition-induced strain in the alloy matrix of the QD nanostructure, which results in a redshift in the phonon energy, perfectly aligning with the nonuniform composition distribution.

Perhaps most intriguingly, we have identified an accumulation of non-equilibrium phonons below the sharp interface. To delve deeper into this phenomenon, we pioneered a novel technique, differential momentum mapping (DPM), which has enabled us to map propagating phonon modes. This has led to the unprecedented discovery of a significantly larger reflection of phonons from the sharp interface than the gradual one, providing the first-ever imaging of dynamical thermal processes at the nanoscale.

These findings open up a new frontier in the study of thermal properties in nanostructured materials. The DPM technique, in particular, holds immense potential for further investigations into the dynamics of non-equilibrium phonons and other nanoscale thermal processes. Our research thus sets the stage for a deeper understanding of nanoscale phonon physics, which could have far-reaching implications for the development of high-temperature thermoelectrics and other applications.

Next, we applied vibrational EELS to the ferroelectric-insulator system, $BiFeO_3/TbScO_3$ (BFO/TSO), has led to significant discoveries in the field of nanoscale electron-phonon dynamics. Our primary objective was to discern the relationship between phonon structure and ferroelectricity in BFO, and our findings have exceeded expectations. We have identified that the shear strain localized at ferroelectric domain walls (DW), due to alternating polarization, results in anisotropic propagation of phonons. This was made possible by the innovative DPM technique developed in our previous work.

Moreover, we found that the free charge gases at the interface also disrupt phonon symmetry, but this is due to the accumulation of net charge rather than structural distortions. This research has provided a nanoscale angle-resolved image that explains the decrease in cross-DW and cross-interface thermal conductivity.

Our results have profound implications for the fabrication of ferroelectric-based materials and the design of ferroelectric memories. By uncovering these fundamental aspects of phonon dynamics, we are better equipped to inform the fabrication process and optimize the design of these materials and devices. Our future work will continue to explore these dynamics and their implications, with the aim of further advancing our understanding and application of ferroelectric materials.

On the more data-oriented side, the development of our data workflow stack for EELS data analysis has been a significant stride towards enhancing accuracy, efficiency, transparency, and usability in the field. The advent of advanced detectors and electron spectroscopy techniques has led to an escalating demand for intelligent, high throughput processing. However, the lack of programming and data analysis expertise has often been a barrier to

entry. Our developed modules address this challenge by leveraging low-level APIs that interface with data and provide scientific analysis tools, all wrapped in high-level modules designed for user-specific workflows.

We have demonstrated the effectiveness of this approach with a workflow for vibrational EELS, which includes steps from aligning the zero-loss peak (ZLP) to visualizing the data in the form of line plots or contour maps. The framework also includes tools for analyzing the fine structure of core-loss edges, bandgap measurements, and a general set of tools including deconvolution, clustering, and filtering.

We believe that this framework, which condenses entire blocks of the workflow into single lines of code, will empower non-coders to process their data using innovative data analysis techniques. We anticipate that this will not only democratize access to advanced data analysis but also spur further innovation in the field. Our future work will continue to refine and expand this framework, with the aim of further enhancing its utility and accessibility for researchers in the field.

References

1. Chen, J. & Meng, L. Effects of Different Phonon Scattering Factors on the Heat Transport Properties of Graphene Ribbons. *ACS Omega* 7, 20186–20194 (2022).

2. Chen, G. Thermal conductivity and ballistic-phonon transport in the cross-plane direction of superlattices. *Phys. Rev. B* 57, 958–973 (1998).

3. Cahill, D. G. *et al.* Nanoscale thermal transport. *J. Appl. Phys.* 93, 793–818 (2003).

4. Cahill, D. G. *et al.* Nanoscale thermal transport. II. 2003-2012. *Appl. Phys. Rev.* 1, (2014).

5. Biswas, K. *et al.* High-performance bulk thermoelectrics with all-scale hierarchical architectures. *Nature* 489, 414–418 (2012).

6. Pernot, G. *et al.* Precise control of thermal conductivity at the nanoscale through individual phonon-scattering barriers. *Nat. Mater.* 9, 491–495 (2010).

7. He, J. & Tritt, T. M. Advances in thermoelectric materials research: Looking back and moving forward. *Science* 357, eaak9997 (2017).

8. Poudel, B. *et al.* High-thermoelectric performance of nanostructured bismuth antimony telluride bulk alloys. *Science* 320, 634–638 (2008).

9. Hochbaum, A. I. *et al.* Enhanced thermoelectric performance of rough silicon nanowires. *Nature* 451, 163–167 (2008).

10. Pei, Y. *et al.* Convergence of electronic bands for high performance bulk

thermoelectrics. *Nature* 473, 66–69 (2011).

11. Kim, W. *et al.* Thermal conductivity reduction and thermoelectric figure of merit increase by embedding nanoparticles in crystalline semiconductors. *Phys. Rev. Lett.* 96, 045901 (2006).

12. Harman, T. C., Harman, T. C., Taylor, P. J., Walsh, M. P. & Laforge, B. E. Quantum Dot Superlattice Thermoelectric Materials and Devices. *Science* 2229, 2229–2232 (2008).

13. Rosi, F. D., Abeles, B. & Jensen, R. V. Materials for thermoelectric refrigeration. *J. Phys. Chem. Solids* 10, 191–200 (1959).

14. Liu, W. L., Borca-Tasciuc, T., Chen, G., Liu, J. L. & Wang, K. L. Anisotropic Thermal Conductivity of Ge Quantum-Dot and Symmetrically Strained Si/Ge Superlattices. *J. Nanosci. Nanotechnol.* 1, 39–42 (2001).

15. R. E. Cohen. Origin of ferroelectricity in perovskite oxides. *Nature* 359, 136–138 (1992).

16. Dawber, M., K, R. & J, S. Physics of thin-film ferroelectric oxides. *Rev. Mod. Phys.* 77, 1083–1130 (2005).

17. Scott, J. F. & Paz De Araujo, C. A. Ferroelectric memories. *Science* 246, 1400–1405 (1989).

18. Kaminow, I. Principles and applications of ferroelectrics and related materials. *Oxford University Press* (1977) doi:10.1109/jqe.1978.1069813.

19. Zhang, Y. *et al.* Anisotropic polarization-induced conductance at a ferroelectric–insulator interface. *Nat. Nanotechnol.* 13, 1132–1136 (2018).

20. Song, K. *et al.* Direct imaging of the electron liquid at oxide interfaces. *Nat. Nanotechnol.* 13, 198–203 (2018).

21. Okunishi, E. *et al.* Visualization of light elements at ultrahigh resolution by stem annular bright field microscopy. *Microsc. Microanal.* 15, 164–165 (2009).

22. Ishikawa, R. *et al.* Direct imaging of hydrogen-atom columns in a crystal by annular bright-field electron microscopy. *Nat. Mater.* 10, 278–281 (2011).

23. Egerton, R. F. *Electron Energy-Loss Spectroscopy in the Electron Microscope*. *Springer Science+Business Media* (2011). doi:10.1093/acprof:oso/9780198716525.003.0015.

24. Inokuti, M. Inelastic collisions of fast charged particles with atoms anInokuti, M. (1971). Inelastic collisions of fast charged particles with atoms and molecules-The bethe theory revisited. Reviews of Modern Physics, 43(3), 297–347. http://doi.org/10.1103/RevModPhy. *Rev. Mod. Phys.* 43, 297–347 (1971).

25. Atwater, H. A., Wong, S. S., Ahn, C. C., Nikzad, S. & Frase, H. N. Analysis of monolayer films during molecular beam epitaxy by reflection electron energy loss spectroscopy. *Surf. Sci.* 298, 273–283 (1993).

26. Krivaneka, O. L., Tanishiro, Y., K., T. & Yagi, K. Electron Energy Loss Spectroscopy in glancing reflection from bulk crystals. *Ultramicroscopy* 11, 215–222 (1983).

27. Crozier, P. A. Quantitative elemental mapping of materials by energy-filtered

imaging. *Ultramicroscopy* 58, 157–174 (1995).

28. Gadre, C. *et al.* Nanoscale Imaging of Phonon Dynamics by Electron Microscopy. *Nature* 606, 292–297 (2022).

29. Rez, P. *et al.* Damage-free vibrational spectroscopy of biological materials in the electron microscope. *Nat. Commun.* 7, 1–7 (2016).

30. Hachtel, J. A. *et al.* Identification of site-specific isotopic labels by vibrational spectroscopy in the electron microscope. *Science* 363, 525–528 (2019).

31. Rafferty, B. & Brown, L. Direct and indirect transitions in the region of the band gap using electron-energy-loss spectroscopy. *Phys. Rev. B* 58, 10326–10337 (1998).

32. Yan, X. *et al.* Anomalous Linear Layer-Dependent Blue Shift of Ultraviolet-Range Interband Transition in Two-Dimensional MoS2. *J. Phys. Chem. C* 124, 1609–1616 (2019).

33. Plotkin-Swing, B. *et al.* Hybrid pixel direct detector for electron energy loss spectroscopy. *Ultramicroscopy* 217, 113067 (2020).

34. Muller, D. A. *et al.* Atomic-scale chemical imaging of composition and bonding by aberration-corrected microscopy. *Science* 319, 1073–1076 (2008).

35. Crewe, A. V., Isaacson, M. & Johnson, D. A High Resolution Electron Spectrometer for Use in Transmission Scanning Electron Microscopy. *J. Sci. Instrum.* 42, 411–420 (1948).

36. Isaacson, M. & Scheinfein, M. A High Performance Electron Energy Loss Spectrometer

for Use With a Dedicated Stem. *J. Vac. Sci. Technol. B Microelectron. Nanom. Struct.* 1, 1338–1343 (1983).

37. Hachtel, J. A., Lupini, A. R. & Idrobo, J. C. Exploring the capabilities of monochromated electron energy loss spectroscopy in the infrared regime. *Sci. Rep.* 8, 1–10 (2018).

38. Fransen, M. J. Experimental evaluation of the extended Schottky model for ZrO/W electron emission. *J. Vac. Sci. Technol. B Microelectron. Nanom. Struct.* 16, 2063 (1998).

39. Kim, H. S., Yu, M. L., Thomson, M. G. R., Kratschmer, E. & Chang, T. H. P. Energy distributions of Zr/O/W Schottky electron emission. *J. Appl. Phys.* 81, 461–465 (1997).

40. Swanson, L. W. & Schwind, G. A. *A Review of the Cold-Field Electron Cathode*. *Advances in Imaging and Electron Physics* vol. 159 (Elsevier Inc., 2009).

41. Nelayah, J. *et al.* Mapping surface plasmons on a single metallic nanoparticle. *Nat. Phys.* 3, 348–353 (2007).

42. Kimoto, K., Kothleitner, G., Grogger, W., Matsui, Y. & Hofer, F. Advantages of a monochromator for bandgap measurements using electron energy-loss spectroscopy. *Micron* 36, 185–189 (2005).

43. Krivanek, O. L. *et al.* Vibrational spectroscopy in the electron microscope. *Nature* 514, 209–212 (2014).

44. Krivanek, O. L. *et al.* High-energy-resolution monochromator for aberration-corrected scanning transmission electron microscopy/electron energy-loss

spectroscopy. *Philos. Trans. R. Soc. A Math. Phys. Eng. Sci.* 367, 3683–3697 (2009).

45. Lovejoy, T. C., Corbin, G. C., Dellby, N., Hoffman, M. V. & Krivanek, O. L. Advances in Ultra-High Energy Resolution STEM-EELS. *Microsc. Microanal.* 24, 446–447 (2018).

46. Krivanek, O. L. *et al.* Progress in ultrahigh energy resolution EELS. *Ultramicroscopy* 203, 60–67 (2019).

47. Dellby, N. *et al.* Ultra-high Energy Resolution EELS. *Microsc. Microanal.* 26, 1804–1805 (2020).

48. Lagos, M. J., Trügler, A., Hohenester, U. & Batson, P. E. Mapping vibrational surface and bulk modes in a single nanocube. *Nature* 543, 529–532 (2017).

49. Yan, X. *et al.* Single-defect phonons imaged by electron microscopy. *Nature* 589, 65–69 (2021).

50. Hage, F. S. *et al.* Nanoscale momentum-resolved vibrational spectroscopy. *Science Advances* 4, eaar7495 (2018).

51. Senga, R. *et al.* Position and momentum mapping of vibrations in graphene nanostructures. *Nature* 573, 247–250 (2019).

52. Qi, R. *et al.* Measuring phonon dispersion at an interface. *Nature* 599, 399–403 (2021).

53. Hage, F. S., Kepaptsoglou, D. M., Ramasse, Q. M. & Allen, L. J. Phonon Spectroscopy at Atomic Resolution. *Phys. Rev. Lett.* 122, 16103 (2019).

54. Hage, F. S., Radtke, G., Kepaptsoglou, D. M., Lazzeri, M. & Ramasse, Q. M. Single-atom

vibrational spectroscopy in the scanning transmission electron microscope. *Science* 367, 1124–1127 (2020).

55. Sturm, K. Dynamic Structure Factor: An Introduction. *Zeitschrift fur Naturforsch. - Sect. A J. Phys. Sci.* 48, 233–242 (1993).

56. Van Hove, L. Correlations in space and time and born approximation scattering in systems of interacting particles. *Phys. Rev.* 95, 249–262 (1954).

57. Egerton, R. F. Vibrational-loss EELS and the avoidance of radiation damage. *Ultramicroscopy* 159, 95–100 (2015).

58. Zhou, W., Pennycook, S. J. & Idrobo, J. C. Localization of inelastic electron scattering in the low-loss energy regime. *Ultramicroscopy* 119, 51–56 (2012).

59. Venkatraman, K., Levin, B. D. A., March, K., Rez, P. & Crozier, P. A. Vibrational Spectroscopy at Atomic Resolution with Electron Impact Scattering. *Nat. Phys.* submitted, 1–5 (2019).

60. Dwyer, C. Prospects of spatial resolution in vibrational electron energy loss spectroscopy: Implications of dipolar scattering. *Phys. Rev. B* 96, 1–9 (2017).

61. Lee, S.-M., Cahill, D. G. & Venkatasubramianian, R. Thermal conductivity of Si and Ge. *Appl. Phys. Lett.* 77, 2957–2959 (1997).

62. Luckyanova, M. N. *et al.* Coherent Phonon Heat Conduction in Superlattices. *Science* 338, 936–939 (2012).

63. Ravichandran, J. *et al.* Crossover from incoherent to coherent phonon scattering in

epitaxial oxide superlattices. *Nat. Mater.* 13, 168–172 (2014).

64. Swartz, E. T. & Pohl, R. O. Thermal boundary resistance. *Rev. Mod. Phys.* 61, 605–668 (1989).

65. Liu, J. L. *et al.* Optical and acoustic phonon modes in self-organized Ge quantum dot superlattices. *Appl. Phys. Lett.* 76, 586–588 (2000).

66. Groenen, J. *et al.* Phonons as probes in self-organized SiGe islands. *Appl. Phys. Lett.* 71, 3856–3858 (1997).

67. Hu, Y., Zeng, L., Minnich, A. J., Dresselhaus, M. S. & Chen, G. Spectral mapping of thermal conductivity through nanoscale ballistic transport. *Nat. Nanotechnol.* 10, 701–706 (2015).

68. Idrobo, J. C. *et al.* Temperature Measurement by a Nanoscale Electron Probe Using Energy Gain and Loss Spectroscopy. *Phys. Rev. Lett.* 120, 95901 (2018).

69. Yan, X. *et al.* Unexpected Strong Thermally Induced Phonon Energy Shift for Mapping Local Temperature. *Nano Lett.* 19, 7494–7502 (2019).

70. Hage, F. S., Ramasse, Q. M. & Allen, L. J. Contrast reversal in atomic-scale phonon spectroscopic imaging. *Phys. Rev. B* 102, 214111 (2020).

71. Chang, H. T., Wang, S. Y. & Lee, S. W. Designer Ge/Si composite quantum dots with enhanced thermoelectric properties. *Nanoscale* 6, 3593–3598 (2014).

72. Mateeva, E., Sutter, P., Bean, J. C. & Lagally, M. G. Mechanism of organization of three-dimensional islands in SiGe / Si multilayers. *Appl. Phys. Lett.* 71, 3233–3235 (1997).

73. Schmidt, O. & Eberl, K. Multiple layers of self-asssembled Ge/Si islands: Photoluminescence, strain fields, material interdiffusion, and island formation. *Phys. Rev. B* 61, 13721–13729 (2000).

74. Alonso, M. I. & Winer, K. Raman spectra of c-Si1-xGex alloys. *Phys. Rev. B* 39, 10056–10062 (1989).

75. Tsang, J. C., Mooney, P. M., Dacol, F. & Chu, J. O. Measurements of alloy composition and strain in thin Ge $_x$ Si $_{1-x}$ layers. *J. Appl. Phys.* 75, 8098–8108 (1994).

76. Nakashima, S., Mitani, T., Ninomiya, M. & Matsumoto, K. Raman investigation of strain in Si/SiGe heterostructures: Precise determination of the strain-shift coefficient of Si bands. *J. Appl. Phys.* 99, 053512 (2006).

77. Lockwood, D. J. *et al.* Si/SiGe heterointerfaces in one-, two-, and three-dimensional nanostructures: Their impact on SiGe light emission. *Front. Mater.* 3, 12 (2016).

78. Liao, B. *et al.* Significant reduction of lattice thermal conductivity by the electron-phonon interaction in silicon with high carrier concentrations: A first-principles study. *Phys. Rev. Lett.* 114, 115901 (2015).

79. Chen, P., Ponet, L., Lai, K., Cingolani, R. & Artyukhin, S. Domain wall-localized phonons in BiFeO3: spectrum and selection rules. *npj Comput. Mater.* 6, (2020).

80. Zang, Y. *et al.* Giant Thermal Transport Tuning at a Metal/Ferroelectric Interface. *Adv. Mater.* 34, (2022).

81. Langenberg, E. *et al.* Ferroelectric Domain Walls in PbTiO3 Are Effective Regulators of Heat Flow at Room Temperature. *Nano Lett.* 19, 7901–7907 (2019).

82. Hoglund, E. R. *et al.* Emergent interface vibrational structure of oxide superlattices. *Nature* 601, 556–561 (2022).

83. Wang, Y. *et al.* First-principles lattice dynamics and heat capacity of BiFeO3. *Acta Mater.* 59, 4229–4234 (2011).

84. Zhu, T. & Ertekin, E. Resolving anomalous strain effects on two-dimensional phonon flows: The cases of graphene, boron nitride, and planar superlattices. *Phys. Rev. B* 91, 1–8 (2015).

85. Cai, Q. *et al.* Raman signature and phonon dispersion of atomically thin boron nitride. *Nanoscale* 9, 3059–3067 (2017).

86. Zhang, A. X., Liu, J. T., Guo, S. D. & Li, H. C. Strain effects on phonon transport in antimonene investigated using a first-principles study. *Phys. Chem. Chem. Phys.* 19, 14520–14526 (2017).

87. Caretta, L. *et al.* Nonvolatile Electric-Field Control of Inversion Symmetry. *Nat. Mater.* (2022) doi:10.1038/s41563-022-01412-0.

88. Tauchert, S. R. *et al.* Polarized phonons carry angular momentum in ultrafast demagnetization. *Nature* 602, 73–77 (2022).

89. Granerød, C. S., Zhan, W. & Prytz, Ø. Automated approaches for band gap mapping in STEM-EELS. *Ultramicroscopy* 184, 39–45 (2018).

90. Lichtert, S. & Verbeeck, J. Statistical consequences of applying a PCA noise filter on EELS spectrum images. *Ultramicroscopy* 125, 35–42 (2013).

91. Wang, Y. *et al.* Towards atomically resolved EELS elemental and fine structure mapping via multi-frame and energy-offset correction spectroscopy. *Ultramicroscopy* 184, 98–105 (2018).

92. Blanco-Portals, J., Peiró, F. & Estradé, S. Strategies for EELS Data Analysis. Introducing UMAP and HDBSCAN for Dimensionality Reduction and Clustering. *Microsc. Microanal.* 28, 109–122 (2022).

93. Baró, M. D. *et al.* Clustering analysis strategies for electron energy loss spectroscopy (EELS). *Ultramicroscopy* 185, 42–48 (2017).

94. Ryu, J. *et al.* Dimensionality reduction and unsupervised clustering for EELS-SI. *Ultramicroscopy* 231, 113314 (2021).

95. Lambin, P. & Vigneron, J. P. Computation of crystal Green's functions in the complex-energy plane with the use of the analytical tetrahedron method. *Phys. Rev. B* 29, 3430–3437 (1984).

96. Stillinger, F. H. & Weber, T. A. Computer simulation of local order in condensed phases of silicon. *Phys. Rev. B* 31, 5262–5271 (1985).

97. Blöchl, P. E. Projector augmented-wave method. *Phys. Rev. B* 50, 17953–17979 (1994).

98. Perdew, J. P., Burke, K. & Ernzerhof, M. Generalized gradient approximation made simple. *Phys. Rev. Lett.* 77, 3865–3868 (1996).

99. Giannozzi, P. *et al.* QUANTUM ESPRESSO: A modular and open-source software project for quantum simulations of materials. *J. Phys. Condens. Matter* 21, 395502

(2009).

100. Togo, A. & Tanaka, I. First principles phonon calculations in materials science. *Scr. Mater.* 108, 1–5 (2015).

101. Chen, G. Nanoscale energy transport and conversion: a parallel treatment of electrons, molecules, phonons, and photons. *Oxford Univ. Press* (2005) doi:10.5860/choice.43-2818.

102. Dingle, R. B. Electrical Conductivity of Thin Wires. *Proc. R. Soc. London* 12, 103–109 (1950).

103. Chen, G. Non-Fourier phonon heat conduction at the microscale and nanoscale. *Nat. Rev. Phys.* 3, 555–569 (2021).

104. Zhang, R. *et al.* Compositionally complex doping for zero-strain zero-cobalt layered cathodes. *Nature* 610, 67–73 (2022).

105. Wang, C. *et al.* Resolving complex intralayer transition motifs in high-Ni-content layered cathode materials for lithium-ion batteries. *Nat. Mater.* 22, (2023).

106. Lee, Y. G. *et al.* High-energy long-cycling all-solid-state lithium metal batteries enabled by silver–carbon composite anodes. *Nat. Energy* 5, 299–308 (2020).

107. Liu, X. *et al.* Local electronic structure variation resulting in Li 'filament' formation within solid electrolytes. *Nat. Mater.* 20, 1485–1490 (2021).

108. Lee, T. *et al.* Atomic-scale origin of the low grain-boundary resistance in perovskite solid electrolytes. *Nat. Commun.* (2023) doi:10.1038/s41467-023-37115-6.

109. Hoglund, E. R. *et al.* Direct Visualization of Localized Vibrations At Complex Grain-Boundaries. *arXiv* 1–43 (2022).

110. Haas, B. *et al.* Atomic-Resolution Mapping of Localized Phonon Modes at Grain Boundaries. *Nano Lett.* (2023) doi:10.1021/acs.nanolett.3c01089.

111. Cheng, Z. *et al.* Experimental observation of localized interfacial phonon modes. *Nat. Commun.* 12, 1–10 (2021).

112. Yu, L., Li, M., Wen, J., Amine, K. & Lu, J. (S)TEM-EELS as an advanced characterization technique for lithium-ion batteries. *Mater. Chem. Front.* 5, 5186–5193 (2021).

113. Saitoh, M. *et al.* Systematic analysis of electron energy-loss near-edge structures in Li-ion battery materials. *Phys. Chem. Chem. Phys.* 20, 25052–25061 (2018).

114. Gao, X. *et al.* Cation ordering in A-site-deficient Li-ion conducting perovskites La(1-x)/3LixNbO3. *J. Mater. Chem. A* 3, 3351–3359 (2015).

Appendix A

Calculations for beam-induced nanoscale phonon dynamics

This supplementary section is devoted to supporting theoretical calculations for chapter 4. This section has largely been adapted from the supplementary section of.[28]. On our quest to decipher the surprising phenomenon of the intensity enhancement at the bottom of the abrupt interface, a plethora of calculations in order to discern its source. Among the myriad calculations that were done, only the most pertinent will be included in this appendix. For brevity, the atomistic Green's function calculations will not be included. For a more thorough discussion please refer to the supplementary Ref.[28]. The calculations included here are the those of the spatially resolved phonon DOS of a Si-SiGe-Si systema and strain effects on the phonon DOS of Si. These calculations explore the structural and interfacial effects on the phonon DOS as a possible source for the intensity enhancement in Fig. 4.4.1a. Next, I show how the electron beam, when modeled as a phonon generator, can produce non-eq phonons that reflect from the abrupt interface. To this end, I demonstrate roughly how many phonons per electron on average are generated. Finally develop a Boltzmann transport equation (BTE) formalism for handling the spatial distribution of non-eq phonons as a result of the beam (Fig. 4.4.1c). Our BTE result combined with our estimated value for phonons per electron generated does an adequate job of explaining the intensity enhancement.

A.1 Local Phonon Density of States using lattice dynamics calculations

Since the vibrational EELS cross section is intimately related to the phonon DOS[28,51], we speculated that the cause of the usual increased intensity lay within the phonon DOS. Using a virtual crystal approximation (VCA), The QD system was modeled as a 3-layer heterostructure consisting of Si, SiGe, and Si. VCA models alloys in terms of average atomic mass rather than using discrete Si and Ge atoms to generate the alloy. This structure includes two interfaces: one with an abruptly changing average atomic mass, and another one with a gradually changing atomic mass. The density of states are then calculated for an abrupt and a gradual interface are calculated to see if local density of states of Si is modified by the presence of the Si/Ge QD.

The local density of states is obtained from the imaginary part of Green's function, defined by $D(\omega, \boldsymbol{R}_i) = \sum_{\boldsymbol{q}\nu} u^*_{\boldsymbol{q}\nu,\alpha}(\boldsymbol{R}_i) u_{\boldsymbol{q}\nu,\alpha}(\boldsymbol{R}_i) \delta(\omega - \omega_{\boldsymbol{q}\nu})$, where $u_{\boldsymbol{q}\nu,\alpha}$ is the phonon eigenvector along α direction and R_i is the position of i^{th} atom. Tetrahedron smearing was used to sample the states with certain frequency[95]. The force constant is calculated from Stillinger-Weber (SW) potential[96] with lattice constant chosen as 5.431 Å. A 20×20×18 k point mesh is used to calculate density of states. Our calculation shows that, the local density of states of Si are insensitive to the interface structure (Fig. A.1). With this, we can see that the local density of states does not contribute to the enhancement of EELS intensity.

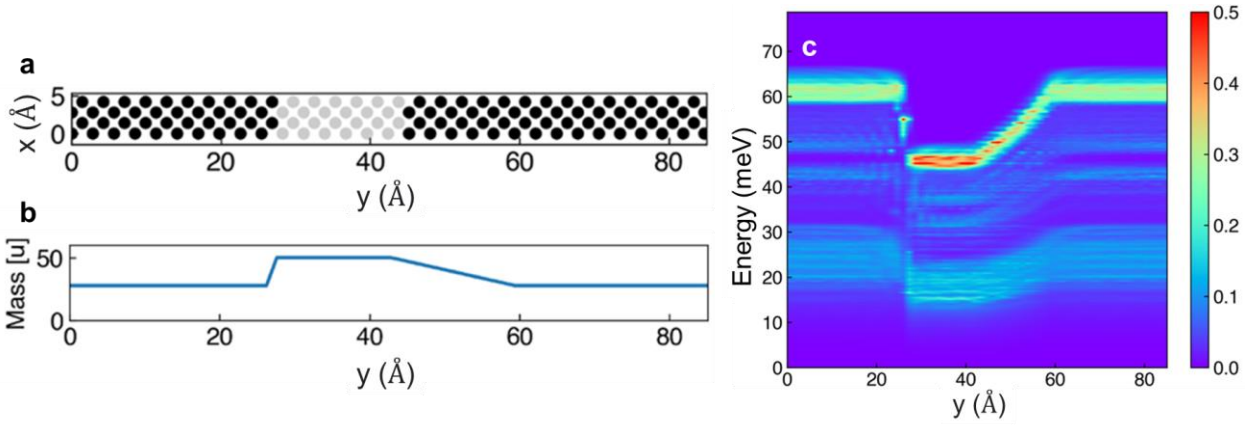

Fig. A.1 Local Phonon Density of States of a SiGe nanostructure. a, Superlattice supercell with SiGe alloy structure formed by atoms representing the average mass of Si and Ge with the gray color indicating an atomic mass of $Si_{0.5}Ge_{0.5}$. The 12 layers of atoms to the right of the gray colored ones have a mass gradient that transitions from $Si_{0.5}Ge_{0.5}$ to pure Si. b, Mass profile of (a) along the *y*-direction. Near the abrupt Si-QD interface, the mass abruptly changes. The gradual interface is modeled by continuously changing the mass profile as a function of position. c, The local density of phonons for vibrational modes along the *y*-direction in the superlattice depicted in (a).

A.2 Effect of Strain on the Si OM

Here, I discuss if strain-induced changes in the phonon DOS could lead to the observed enhancement in EELS. The functional type for the pseudopotential is the Projector Augmented Wave[97] with Perdew-Burke-Ernzerhof (PBE) exchange-correlation and nonlinear core correction[98]. The energy cutoff is 36 Ry and a 4×4×4 Monkhorst-Pack mesh is used. The lattice constant at equilibrium (zero strain) is found to be 5.4662 Å by minimizing the total energy. 2×2×2 supercells with 64 atoms are used for calculating the harmonic force constant. The DFT calculation is conducted using Quantum ESPRESSO package[99] and the phonon calculation is carried out using phonopy[100] package. Through DFT calculation of phonon band and density of states of Si with different strain, it is revealed that the strain effect always modifies the phonon density of states and shifts the frequency

simultaneously (Fig. A.2), whilst in experiment, we only observe intensity difference of EELS but not the phonon frequency in Si (Figs. 4.3.1b and 4.4.1a). This suggests strain effect cannot explain the experimental observation.

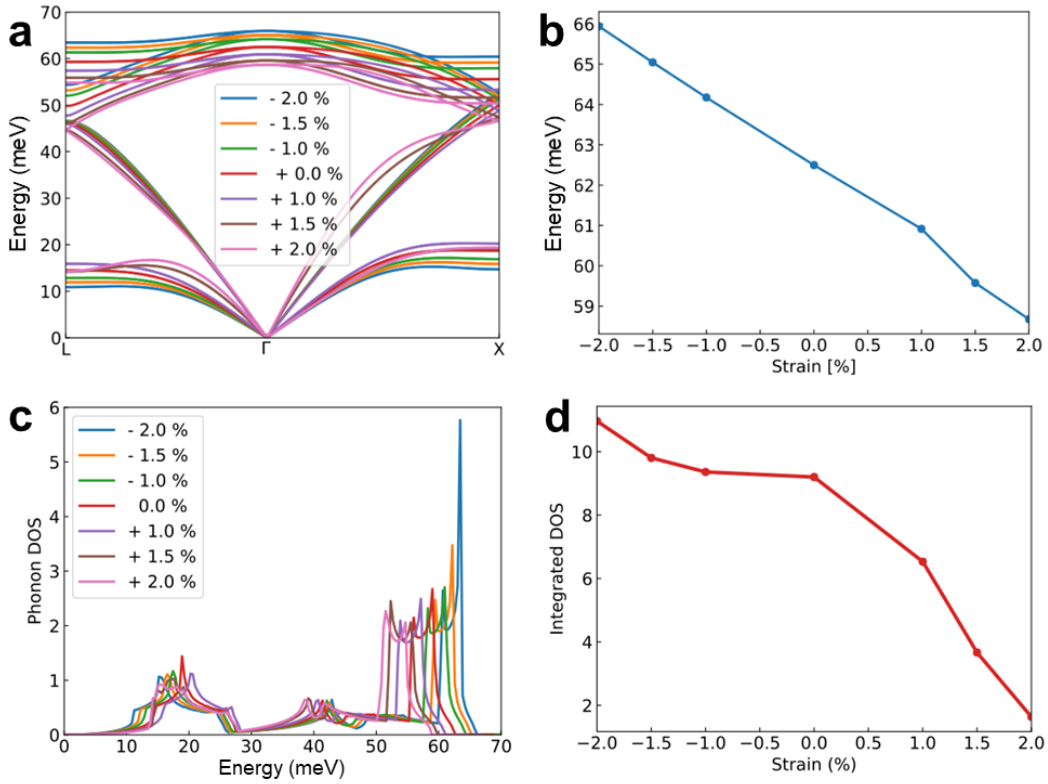

Fig. A.2 Strain effect on Phonon Dispersion and Density of States. a, Phonon dispersion for silicon under different strains. b, The energy of longitudinal phonon at Γ point as a function of strain. c, Phonon density states from DFT calculations for different strains. The percentage marks the relative change in lattice constant compared to equilibrium state. d, The integrated phonon density of states from 55 meV to 65 meV. As the lattice constant enlarges, the integrated DOS in the energy window from 55 meV to 65 meV decreases due to the red shift and spreading of optical phonons.

A.3 Estimations of beam-induced phonon generation and temperature rise

The phonon DOS calculations on the Si-SiGe-Si heterostructure and strain simulations on a Si supercell revealed that the intensity enhancement is not caused by changes in the phonon DOS as a result of proximity to an interface or strain effects. Here, beam effects are explored as a possible source of non-eq phonons. A schematic depicting the generation of phonons by the electron beam is given in Fig. A.3.

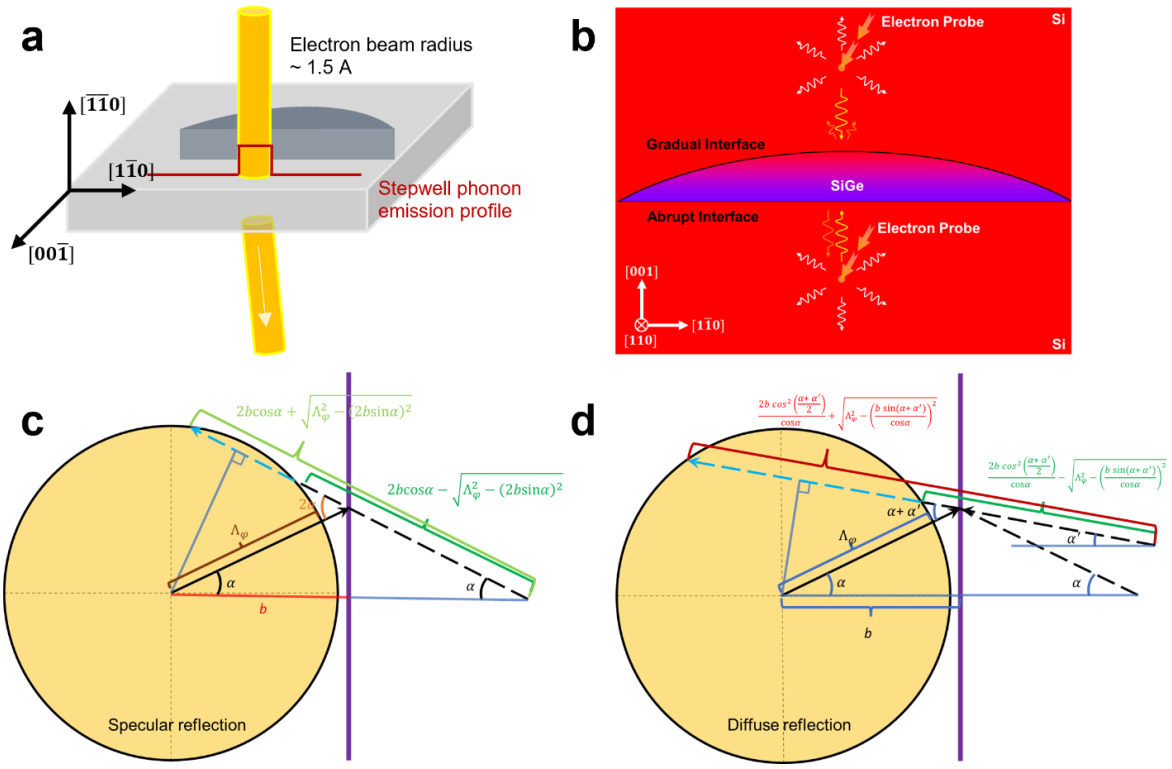

Fig. A.3 Phonon generation and reflection schematic. a, Schematic for the electron beam as a phonon emission source in EELS. The crystal directions are noted to the left. b, Two-dimensional geometry from top view with crystal directions included in the bottom left. The dark region indicates the quantum dot. The beam is indicated by the orange circle and its

area is exaggerated for visual convenience. The arc measured is found be about 36.5° with the radius around 138.8 nm. The mean free path of Si OM phonons is chosen as 10 nm with a group velocity of 1000 m/s. c-d, Specular and diffuse reflection geometries, respectively. The yellow circle denotes the area over which the electron beam can sense phonons. The vertical purple lines denote the interfaces. The cyan dashed arrows in both c and d denote the area over which the reflected phonons are measured by the electron beam. For specular reflection, the reflected angle is equal to the angle of incidence and for diffuse reflection, the reflected angles are spread over angles $-\pi/2 < \alpha' < \pi/2$. The same crystal directions as in b apply.

The EELS spectrum is a clear way to demonstrate what the average energy loss probability looks like for a single electron. It is instructive to think about an EELS spectrum as being built by an accumulation of several electrons. For example, each electron will undergo a specific energy loss that will land it somewhere on the energy axis. How much energy the fast electron loses is depending on its scattering cross-section which essentially describes the probability a fast electron will loss energy E and is a function of kinetic energy, angle of incidence, and material properties. The sampling of this beam and material dependent probability density function is equivalent to generating an EEL spectrum at high exposure ensuring that enough fast electrons have scattered and lost various amounts of energy. The result is the EELS spectrum in Fig. A.4. In other words, the building of the EEL spectrum by measuring the energy loss of nearly a billion electrons effectively samples this probability density. Given this, it becomes clear that Fig. A.4 represents the probability density of a single electron. Using this information, we can calculate the average energy loss per electron which represents the average amount of energy that the material system gains. With the

assumption that nonradiative losses are negligible in semiconductors, we assume that the average energy gained by the material eventually decays to phonons as they are lowest energy-carrying quasiparticles, at least in non-magnetic semiconductors.

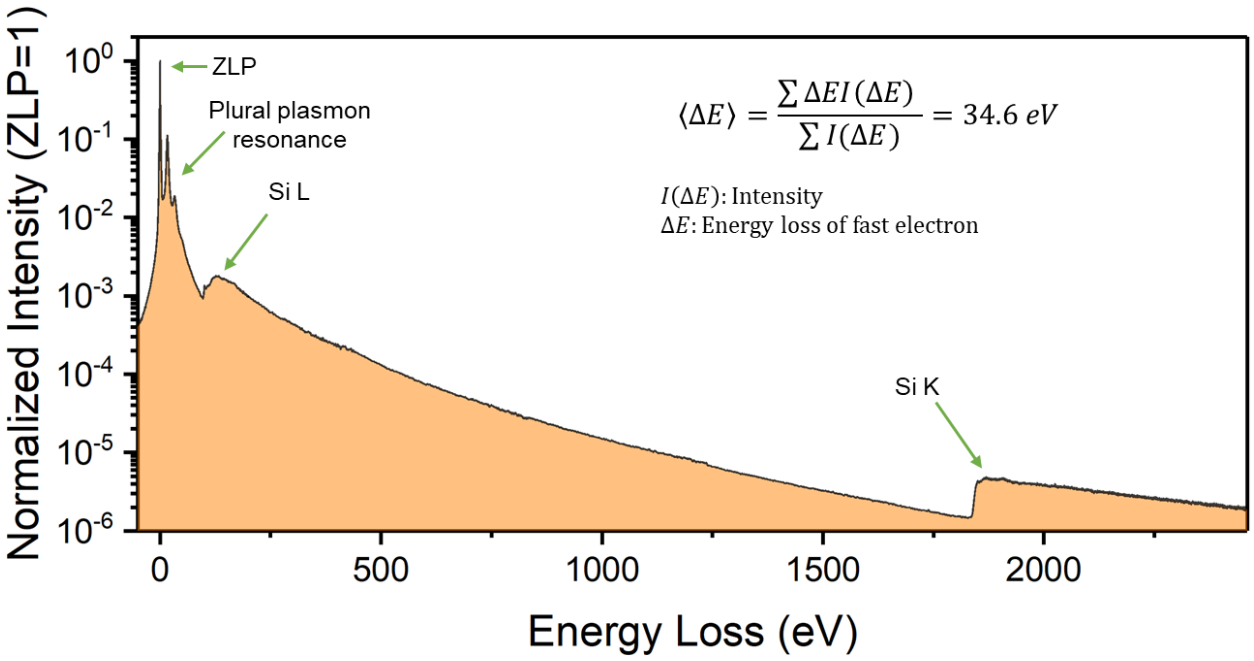

Fig. A.4 High-range EELS for average energy loss on interlayer Si. An EEL spectrum contains a probability-like distribution of the energy loss of single electron. This high-range spectrum shows plural plasmon resonance, Si *L* edge, and Si *K* edge that, assuming nonradiative losses in Si, eventually decay into phonons. Weighting by Si DOS, there are 291 Si OM phonons generated per fast electron.

In the following, estimations of how many phonons are generated by the electron beam per unit time is given. The electron beam current through the sample is measured to be 3 pA meaning that there are 0.019 electrons travelling through sampler per ns. If we consider the beam as a stream of consecutive single electrons, the average time interval between electrons transmitting through sample is 53 ns. By examining the EELS intensity, $I(\Delta E)$, the average energy loss per electron: $\langle \Delta E \rangle = \int (\Delta E) I(\Delta E) \mathrm{d}\Delta E / \int I(\Delta E) \mathrm{d}\Delta E = 34.6$ eV, where ΔE denotes the energy loss of the fast electron (Fig. A.4). Although the energy loss is in various

forms, for example plasmons, eventually the energy loss all become heat energy to excite phonons with various decay times. From the density of states computed using first-principles calculations, we find the average phonon energy $<E_{ph}>=\int \hbar\omega D(\omega)\mathrm{d}\omega/\int D(\omega)\mathrm{d}\omega$ = 40.4 meV. Then, the number of Si OM phonons per electron is given by $\frac{\langle \Delta E\rangle}{\langle E_{ph}\rangle}\int_{\omega_1}^{\omega_2} D(\omega)\mathrm{d}\omega/\int D(\omega)\mathrm{d}\omega = 291$ where $\hbar\omega_1$=55 meV to $\hbar\omega_2$=65 meV. This calculation represents the upper limit for the number of phonons that survive until the next electron arrives. With 291 Si OM phonons per electron, we can calculate the beam-induced non-equilibrium phonon generation rate $\dot{n} = 5.43\times10^9$ s^{-1} for Si OM phonons. In addition, from the first-principles calculation, we find that the volume-specific heat capacity for optical phonons is $C_{\mathrm{p,OM}} = 4.53\times10^5$ J/m^3/K. If further assuming the energy of those optical phonons are uniformly confined within the range of mean free path, *i.e.,* with the volume of a cylinder of $\pi\times(10\text{ nm})^2\times50$ nm where 50 nm is the thickness of the slab, the effective temperature rise due to optical phonons is estimated to be 0.36 K, which is negligible compared to room temperature 300 K. Thus, the equilibrium part of the phonon occupation number is well described by the Bose-Einstein distribution at 300 K.

A.4 Phonon population from Boltzmann transport equation

Armed with the calculations in section A.3, we can begin out semi-classical treatment of phonon dynamics. To properly describe the nonequilibrium phonon population near an interface, the phonon Boltzmann transport equation (BTE) with source within the relaxation time approximation writes[101],

$$\frac{\partial f_{\boldsymbol{q}\nu}}{\partial t} + v_{\boldsymbol{q}\nu} \cdot \nabla f_{\boldsymbol{q}\nu} = -\frac{f_{\boldsymbol{q}\nu} - f_{\boldsymbol{q}\nu,0}}{\tau_{\boldsymbol{q}\nu}} + \dot{n}_A, \tag{A.1}$$

where $f_{\boldsymbol{q}\nu}$ is the phonon distribution function, $v_{\boldsymbol{q}\nu}$ is the group velocity, $f_{\boldsymbol{q}\nu,0}$ is the equilibrium phonon population i.e., the Bose-Einstein distribution, $\tau_{\boldsymbol{q}\nu}$ is the phonon lifetime and $\dot{n}_A$ is the phonon generation rate per unit time per unit area due to the energy transferred from electron beam to sample. $\dot{n}_A = \dot{n} \,/\, A_e$ with A_e as the area of electron beam (πa^2), where a is the radius of electron beam ($a = 0.075$ nm for 33 mrad convergence semi-angle condition). Define $g_{q\nu}$ as the nonequilibrium part of the phonon population as: $g_{\boldsymbol{q}\nu} = f_{\boldsymbol{q}\nu} - f_{\boldsymbol{q}\nu,0}$.

As discussed in above section, the temperature rise is negligible thus $f_{q\nu,0}$ is approximated to be a constant for all modes. Additionally, since the electrons constantly hit the sample slab, we treat this process as quasi-steady state. Thus, the time-derivative of the phonon population ($\partial f_{q\nu}/\partial t$) is dropped. As a result, Eq. A.1 becomes,

$$\boldsymbol{v}_{\boldsymbol{q}\nu} \cdot \boldsymbol{\nabla} g_{\boldsymbol{q}\nu} = -\frac{g_{\boldsymbol{q}\nu}}{\tau_{\boldsymbol{q}\nu}} + \dot{n}_A. \tag{A.2}$$

We chose cylindrical coordinate for mathematical convenience because of the cylindrical nature of the electron beam transmitting through the slab with the z axis along the beam axis labeled as $[\bar{1}\bar{1}0]$ (Fig. A.3). We set the origin to be the center of the beam and we then solve the Boltzmann transport equation (BTE) by Eq. A.2.

$$\left(v_r \hat{\boldsymbol{r}} + v_\theta \widehat{\boldsymbol{\theta}}\right) \cdot \boldsymbol{\nabla} g(\boldsymbol{r}, \boldsymbol{\theta}, v_r, v_\theta) = -\frac{g(\boldsymbol{r}, \boldsymbol{\theta}, v_r, v_\theta)}{\tau} + \dot{n}_A(\boldsymbol{r}, \boldsymbol{\theta}), \tag{A.3}$$

where we drop the superscript and subscript for clarity. In relation to the QD structure in Fig. 4.2.2a, a denotes the diameter of the electron beam and r denotes the distance from the beam. In the derivation, θ represents the angular spread of the phonons generated by the

electron beam. The phonon source is represented by a step function, $\dot{n}(r,\theta) = \Theta(-r)$. The radial and tangential component of velocity are $v_r = v_y \sin\theta + v_x \cos\theta$ and the $v_\theta = v_y \cos\theta - v_x \sin\theta$. When the phonon source is located far from the interface, the boundary conditions of phonon BTE are $g(0,\theta,|v_r|,v_\theta) = g(0,\theta,-|v_r|,v_\theta)$, g is continuous at $r = a$, and $g(v\tau,\theta,-|v_r|,v_\theta) = 0$, where $v = \sqrt{v_x^2 + v_y^2}$. Thus, the solution[102] is,

$$g(\boldsymbol{r}) = \begin{cases} \dot{n}_A \tau \left(1 - e^{-\frac{v_r r - \sqrt{a^2 v^2 - r^2 v_\theta^2}}{v^2 \tau}}\right), r < a \\ 2\dot{n}_A \tau e^{-\frac{v_r r}{v^2 \tau}} \sinh\left(\frac{\sqrt{a^2 v^2 - v_\theta^2 r^2}}{v^2 \tau}\right), r \geq a \end{cases}, \tag{A.4}$$

Eq. A.4 describes a quasi-1D trajectory along (v_r, v_θ) as depicted in Fig. A.5.

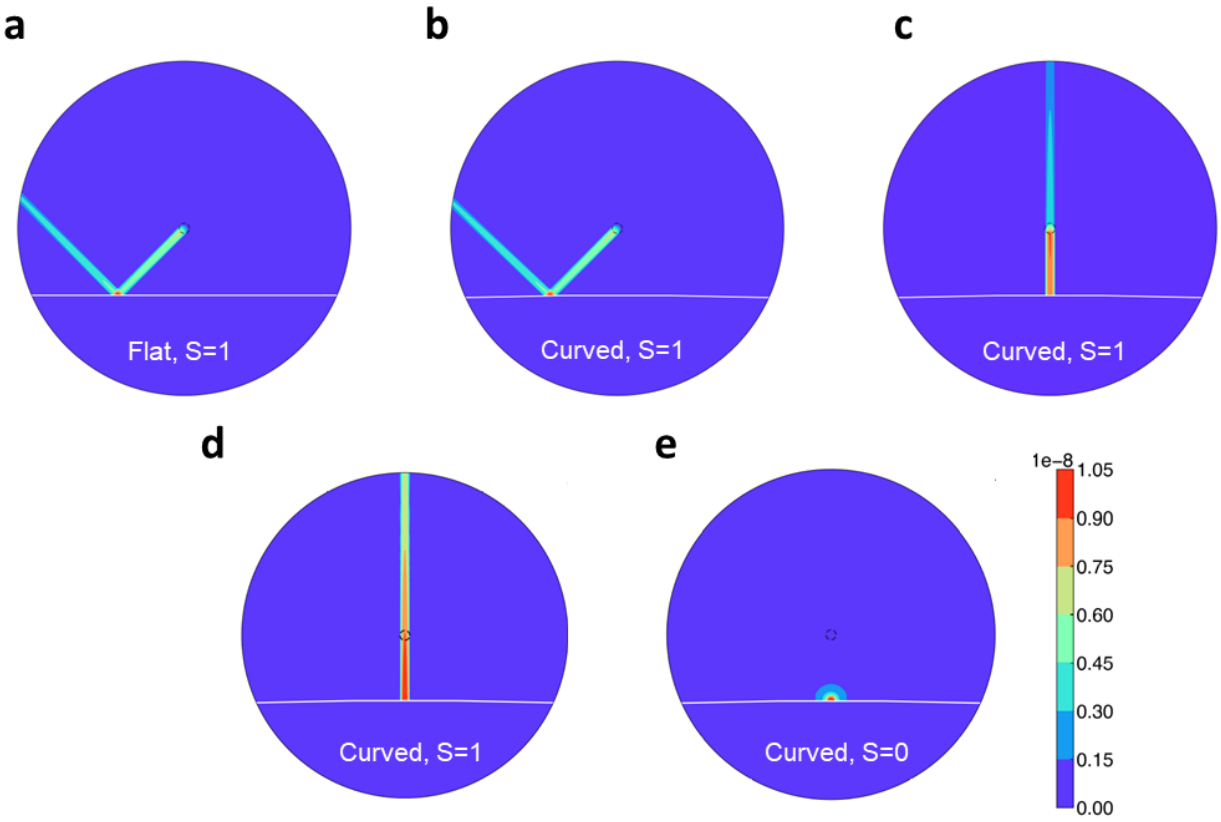

Fig. A.5 Effect of interface geometry and specularity on phonon reflection. a-c, The non-equilibrium phonon distribution function g for a phonon mode along certain polar angle that consists of the incoming and corresponding fully specularly reflected phonons (S=1, R=1) near a flat a and curved b, interface with source phonon moving with along θ = -135° and a curved interface c, with source phonon moving along θ = -90°, respectively. We find that only normal incident phonons have significant enhancement in the nonequilibrium phonon population. d, e, The fully specularly reflected (S=1, R=1) and diffusively scattered (S=0, R=1) nonequilibrium phonon distribution $g'(r', v_r', v_\theta')$ and $g''(r)$ respectively, when the incoming phonon at normal to the interface. Only reflected phonon population are plotted for d and e. From e, we find the diffusively scattered part is highly localized near the interface such that we can neglect the enhancement of phonon population from the contribution of diffusively scattered phonons. The small, dashed circles in the center of a-e indicate the location of the phonon emission source. The color bar represents the phonon population with arbitrary units.

To obtain a 2D distributed population, we begin with a polar integration of Eq. A.4 while also integrating over the angular distribution α of the quasi-1D trajectory:

$$g(\boldsymbol{r}) = \frac{1}{2\pi}\int_{\alpha_1}^{\alpha_2} \dot{n}_A d\alpha \int_{r_1}^{r_2} r dr \int_0^{2\pi} d\theta \, g(\boldsymbol{r}, \boldsymbol{\theta}, v_r, v_\theta). \tag{A.5}$$

For $r > a$, we can approximate $g(r, \theta, v_r, v_\theta)$ and simplify the integral:

$$g(\boldsymbol{r}) = \frac{1}{2\pi}\int_{\alpha_1}^{\alpha_2} \dot{n}_A d\alpha \int_{r_1}^{r_2} r dr \int_{-\frac{a}{r}}^{\frac{a}{r}} d\theta \, 2\tau e^{-\frac{r}{\Lambda}\frac{a}{\Lambda}}. \tag{A.6}$$

The general result without inclusion of specific reflection geometries is:

$$g(\boldsymbol{r}) = \frac{2}{\pi^2}\dot{n}\tau\frac{1}{\Lambda}\int_{\alpha_1}^{\alpha_2}\left(e^{-\frac{r_1}{\Lambda}} - e^{-\frac{r_2}{\Lambda}}\right)d\alpha. \tag{A.7}$$

Here, r_1 and r_2 are the bounds within which the population distribution is sensed by the electron beam, indicated by blue dashed arrows in Fig. A.3. This radius of this area is known as the phonon coherence length Λ_φ. We argue that the although the electron beam is extremely small in radius, the phonons generated are populated in a larger area due to the planewave nature of phonons. The phonons that are excited by the fast electron and keep

their memory of origin, shall be within the phonon coherence length[103] from the beam center. For inelastic scattering dominated phonons, the coherence length is proportional to the inelastic phonon mean free path, $\Lambda_\varphi = \Lambda_{in}/\sqrt{3}$, where Λ_{in} is the phonon mean free path. In the Si side, the dominate scattering mechanisms are inelastic phonon-phonon interactions such that $\Lambda = \Lambda_{in}$. Thus, we have the cutoff radius $\Lambda_\varphi = \Lambda/\sqrt{3}$. Since the beam radius is typically much smaller than the phonon mean free path Λ, we can obtain an approximated form of Eq. A.7.

The expressions for beam generated, specularly reflected, and diffusely reflected phonons, respectively, are given below. For brevity, only solutions where $b > \Lambda_\varphi$ are given.

$$g_0 = \frac{4}{\pi}\dot{n}\tau\left(1 - e^{-\frac{\Lambda_\varphi}{\Lambda}}\right), \tag{A.8}$$

$$g' = \frac{8}{\pi^2}\dot{n}\tau\int_0^{\sin^{-1}\left(\frac{\Lambda_\varphi}{2b}\right)} e^{-\frac{2b\cos\alpha}{\Lambda}}\sinh\frac{\sqrt{\Lambda_\varphi^2-(2b\sin\alpha)^2}}{\Lambda}\,d\alpha, \tag{A.9}$$

and

$$g'' = \frac{4}{\pi^3}\dot{n}\tau\int_0^{\frac{\pi}{2}} d\alpha\int_{-\sin^{-1}\left(\frac{\Lambda_\varphi\cos\alpha}{b}\right)-\alpha}^{\sin^{-1}\left(\frac{\Lambda_\varphi\cos\alpha}{b}\right)-\alpha} e^{-\frac{2b\cos^2\left(\frac{\alpha+\alpha'}{2}\right)}{\Lambda\cos\alpha}}\sinh\frac{\sqrt{\Lambda_\varphi^2-\left(\frac{b\sin(\alpha+\alpha')}{\cos\alpha}\right)^2}}{\Lambda}\,d\alpha'. \tag{A.10}$$

Near an interface, the total phonon population is:

$$f = f_0 + g_0 + S\,R_s\,g' + (1-S)R_d\,g'', \tag{A.11}$$

where g_0 is nonequilibrium phonon population directly generated by incident electron beam, g' is the specular reflection of nonequilibrium phonon from the interface, and g'' is the diffuse reflection of nonequilibrium phonon from the interface. Here S is the specularity parameter

at the interface ($0 \leq S \leq 1$), R_s and R_d are the specular and diffuse reflectance of the interface ($0 \leq R \leq 1$), respectively.

We first consider specular reflection with oblique and normal incidence and find only normal incidence towards interface causes enhancement in the nonequilibrium phonon population, shown in Figs. A.5a–c. Then, we consider the case of reflected nonequilibrium phonon population from diffuse reflection, $g'' = \int g_d(\alpha)\, \mathrm{d}\alpha / 2\pi$, where $g_d(\alpha)$ is the diffusely reflected phonon population with α being the angle for diffusely reflected phonons. As shown in Figs. A.5d,e, we find the diffuse reflection does not contribute to the phonon population enhancement except extremely close to interface on the order of beam size, which is unresolvable in our experiment due to the larger step size. In conclusion, only specular reflection of normal incident phonons causes enhancement in nonequilibrium phonon population. In Fig. 4.4.3, we have shown the nonequilibrium phonon population only considering normal incidence.

The expressions for specular and diffuse reflection at normal incidence are:

$$g' = 16\dot{n}\tau a^2 e^{-\frac{2b}{\Lambda}} \sinh\frac{\Lambda_\varphi}{\Lambda}, \tag{A.12}$$

and

$$g'' = \frac{4}{\pi^3}\dot{n}\tau \int_{-\sin^{-1}\left(\frac{\Lambda_\varphi}{b}\right)}^{\sin^{-1}\left(\frac{\Lambda_\varphi}{b}\right)} e^{-\frac{2b\cos^2\left(\frac{\alpha'}{2}\right)}{\Lambda}} \sinh\frac{\sqrt{\Lambda_\varphi^2 - (b\sin(\alpha'))^2}}{\Lambda} d\alpha'. \tag{A.13}$$

To compare the enhancement ratio (Δ_{sd}) with experiment, we use the emission probability $f + 1$:

$$\Delta_{\mathrm{sd}} = \frac{1+f_0+g_0+S_a R_s g' + (1-S_a) R_d g''}{1+f_0+g_0+S_g R_s g' + (1-S_g) R_d g''} - 1. \quad \text{(A.14)}$$

Here, S_a and S_g are the specularity parameters of the abrupt and gradual interfaces, respectively. We also assume maximum secularity S_a=1, R_s=1 for the abrupt interface and we set S_g=0, $R_d = 0$ for the gradual interface to obtain a maximum upper bound the estimate:

$$\Delta_{\mathrm{sd}} = \frac{1+f_0+g_0+g'}{1+f_0+g_0} - 1. \quad \text{(A.15)}$$

Under these conditions and the values discussed in the section Estimations of beam-induced phonon generation and temperature rise, we estimate the enhancement ratio to be 17.5% This estimation is within an order of magnitude with our experimental result of 15.9% and we note that the total phonon occupation is only a part of the full scattering cross section expression and that other terms likely also influence the true quantitative value. The total phonon occupation, however, is the dominant factor in the EELS intensity enhancement.

Considering the exponential decay feature of expression in Eq. A.12 from an interface with distance b, the reflected phonon population can be fit by,

$$f + 1 = A\, e^{-\frac{2b}{\Lambda}} + C. \quad \text{(A.16)}$$

This result is used to estimate the MFP of Si OM (Fig. 4.4.4). We want to emphasize that although we assume the same mean free path for all optical phonons as well as same lifetime while those properties are actually momentum-dependent, our model based on BTE qualitatively rather than quantitively captures the physics of interface scattering. BTE simulation was performed by our custom python code.

Appendix B

Vibrational EELS for mapping atomic-scale Li distributions in solid electrolytes

All-solid-state batteries (ASSBs) hold the promise to significantly transform the energy storage sector due to their superior energy density, enhanced safety, and extended cycle life compared to conventional lithium-ion batteries. However, several obstacles, including low ionic conductivity and issues related to structural and thermal performance during charge/discharge cycles, need to be overcome for their widespread adoption. It's crucial to investigate structural changes and lithium distributions in anode and cathode materials during lithiation and delithiation processes to unlock the potential of high energy density and long-lasting ASSBs[104–106]. Understanding ionic conduction mechanisms in solid electrolytes is also vital, as low ionic conductivity at grain boundaries (GB) can hinder overall battery performance[107,108].

Scanning transmission electron microscopy (STEM) combined with electron energy loss spectroscopy (EELS) is a potent tool for characterizing atomic-scale structure and composition, and it has significantly advanced our understanding of lithiation mechanisms and performance[104–108]. However, traditional STEM techniques lack the ability to directly study the interaction between lattice vibrations and Li transport, which is key to

characterizing structural transitions and thermal performance. Furthermore, in some oxide solid electrolytes like $Li_{0.375}Sr_{0.4375}Ta_{0.75}Zr_{0.25}O_3$ (LSTZ0.75), mapping Li distributions using conventional STEM-EELS techniques may be challenging due to the presence of heavy element edges near the Li-K edge[108].

Vibrational EELS addresses this problem by mapping Li-O vibrations, which are typically much higher in energy than heavy-element vibrations. Besides its ability to map Li distributions at the atomic scale, vibrational EELS (VibEELS) has shown the potential to map single defects[49], grain boundaries[108–110], and interfaces[28,82,111], making it an ideal tool for investigating structural and thermal properties in ASSBs. Portions of this appendix are taken from Ref.[108].

B.1 Challenges in determining Li distribution in LSTZ0.75 by low-energy core-loss EELS

We attempted to study the distribution of Lithium (Li) at the grain boundaries (GBs) by using electron energy loss spectroscopy (EELS) in the low energy loss range. Due to a lack of existing literature on the EELS of Strontium (Sr), Tantalum (Ta), and Zirconium (Zr), we conducted our own EELS measurements on $SrZrO_3$ and Ta_2O_5 to help identify the two peaks in the LSTZ0.75 spectrum. The EELS spectrum for $SrZrO_3$ showed a single peak at 42.5 eV, which was identified as the Sr-N_1 edge while the spectrum for Ta_2O_5 showed a single peak at 52.5 eV, which was attributed to the Ta-$O_{2,3}$ edge (Fig. B.1). Based on these results, the peaks at 42.5 eV and 52.5 eV in the LSTZ0.75 spectrum arise from the Sr-N_1 and Ta-$O_{2,3}$ edges, respectively. However, these peaks are at too low an energy loss to be identified as the Li-K

edge, which usually appears at 55-65 eV[112,113]. Additionally, the Ta-$O_{2,3}$ edge, due to its broad shape and closeness to the Li-K edge, dominates over the Li-K edge. This is expected, but unfortunate, as the composition $Li_{0.375}Sr_{0.4375}Ta_{0.75}Zr_{0.25}O_3$ has twice as much Ta as Li. Therefore, it is not possible to map the Li distribution in the grains and GBs of LSTZ0.75 using the Li-K edge, as well as in systems with a high Ta:Li ratio. Previous studies have also found it challenging to identify the Li-K edges in perovskite-type solid electrolytes[113,114], as they generally have lower volume densities of Li atoms compared to other types of solid electrolytes.

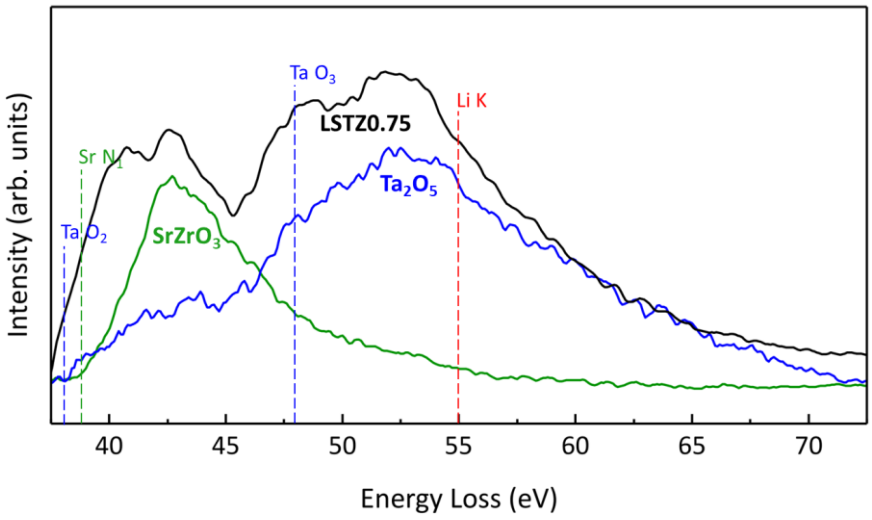

Figure B.1 Distinct Li-K edge of LSTZ0.75 is not observed due to its close proximity to the Ta-$O_{2,3}$ edge. Integrated EEL spectra collected at the low energy loss regime. Edge corresponding to each peak is assigned. Low-energy loss EEL spectra from the 3 material systems are labeled as LSTZ0.75 (black curve), $SrZrO_3$ (green curve), and Ta_2O_5 (blue curve). Low-energy loss elemental edges are marked according to their edge energies.

We attempted to use the low-energy core-loss features to glean information on the Li distribution. We mapped the variations in the Ta $O_{2,3}$ peak in an effort to isolate the Li distribution. However, due to the low Li content in LSTZ0.75, the weak scattering power of

Li (with an atomic number of 3), and the overlap with the Ta-$O_{2,3}$ edge, this investigation proved to be difficult as discussed previously. The representative spectra in Fig. B.2a barely show distinguishable features for the Li-K edge, as is overshadowed by the Ta-$O_{2,3}$ edges due to the larger quantities of Ta. Therefore, the variation in the average peak height shown in Fig. B.2b is a combination of signals from the Ta-$O_{2,3}$ and Li-K edges. The line profile and contour plots (Fig. B.2b,d) display two small bumps in the left grain due to the superlattice (SL) and a dip at the GB. This could suggest the presence of vacancies of either Ta or Li, but it's unclear which element is primarily responsible for the decrease in signal. Consequently, it's not feasible to map the Li distribution in the grains and GBs of LSTZ0.75 using the Li-K edge, especially in systems with a high Ta:Li ratio.

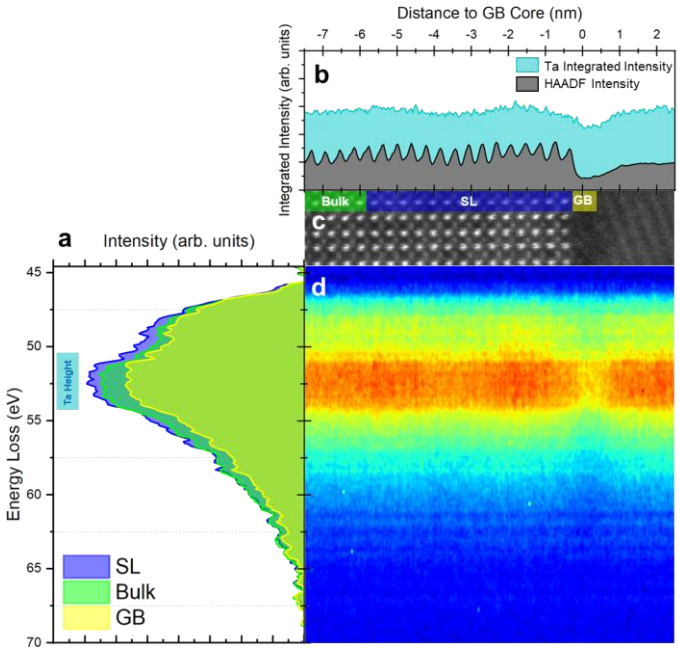

Figure B.2 Low-Loss EELS of (010) faceted GB. a, Representative spectra of Ta-$O_{2,3}$ edge at the SL, bulk, and GB regions. Average Ta-$O_{2,3}$ peak height is higher at the SL region than both the bulk and GB. The cyan-colored label above the peak denotes the energy range over which the Ta-$O_{2,3}$ peak height was averaged. b, Line profile of the averaged Ta-$O_{2,3}$ peak height overlaid with vertically integrated HAADF line profile. c, HAADF image of the region corresponding to the region low energy core-loss EELS was acquired. d, Contour plot of spectral slices stacked horizontally. The

vertical axis denotes energy loss while the horizontal axis denotes the horizontal real-space position corresponding to the HAADF in (c).

B.2 Vibrational EELS set-up

To overcome the challenge of mapping Li distributions using conventional methods, we decided to probe the vibrations of Li-O. We used vibrational electron energy loss spectroscopy (EELS), which is enhanced by high energy resolution monochromation. We used a specific beam-detector setup known as dark field vibrational EELS (DF VibEELS) (Fig. B.3c) to ensure that only high spatial resolution signals were collected[53,54]. This allows us to map the vibrational structure at grain boundaries with atomic precision.

Fig. B.2a,b shows atomic resolution images of a 100-facetted GB and a general GB, respectively. The 100-facetted GB also shows evidence of a compositional SL while the general GB does not. To exclude the contributions the phonon polaritons to the total vibrational signal, a DF vibEELS beam-detector geometry was employed. As discussed in other chapters of this thesis, this is achieved by using post-specimen lenses to deflect the direct beam away from the EELS entrance aperture. Because the polaritonic signatures exist at low scattering angles, moving the direct-beam disk away from the EELS entrance aperture ensures these non-local signals are excluded and that atomic resolution information can be unambiguously obtained. Fib. B.3d shows an example vibrational EEL spectrum revealing vibrational signatures from 10-150 meV.

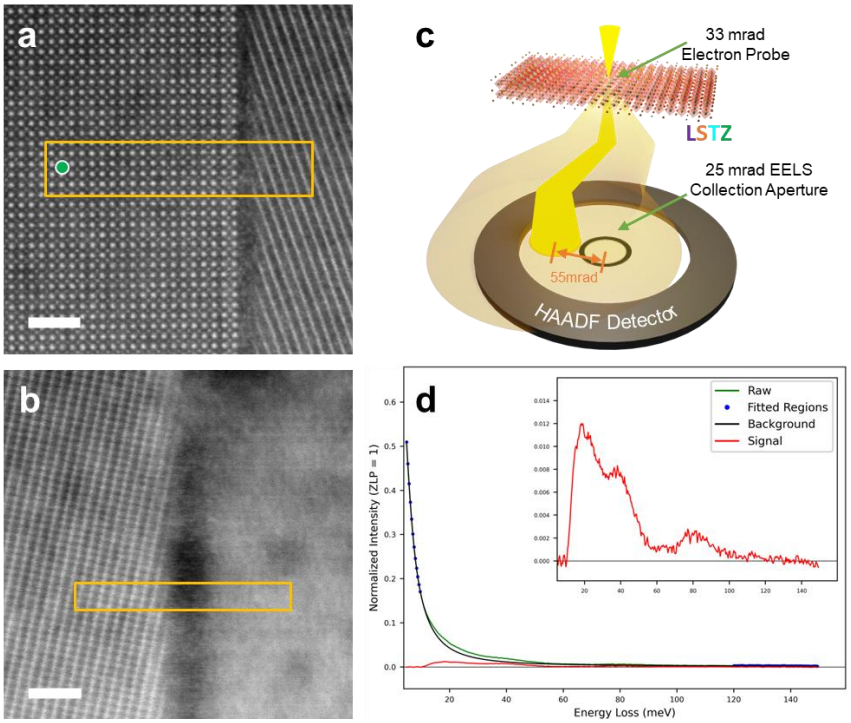

Figure B.3 DF VibEELS Beam-Detector Geometry and Spectra. a, HAADF image where mapping data Fig. B.5a-d was obtained. b, HAADF image where mapping data Figs. B.5e-h was obtained. The regions outlined in orange in a and b correspond to the vibrational map sizes. Scale bars denote 2 nm. c, DF VibEELS beam-detector geometry illustrating a deflected post-specimen scattering beam and the collection of off-axis scattered electrons producing a purely local vibrational signal. The direct beam is deflected by 55 mrad from the collection aperture center. d, Background subtraction of DF VibEEL spectra obtained from the region denoted by the green circle in a. The green colored line represents the normalized as-acquired spectra in the corresponding regions. Blue dots represent the spectrum region used for fitting the background. The red curves in the main plot and in the inset represent the background subtracted signal.

B.3 Utilizing Vibrational EELS for mapping elemental distributions

Vibrational Electron Energy Loss Spectroscopy (EELS) is a powerful tool for studying the vibrational properties of complex materials but is not without its own set of challenges. One of the main hurdles is its relatively poor energy resolution, especially when compared to other vibrational spectroscopy techniques such as Raman or FTIR spectroscopies. This can make it difficult to distinguish between closely spaced vibrational modes, a common occurrence in complex materials such as perovskite

oxides. The question then becomes, how do take advantage of the high spatial resolution of vibEELS to map variations in the vibrational structure due to vacancies, defects, or grain boundaries while also interpreting the complex vibrational signal. To circumvent these obstacles, we employed a robust strategy that allowed us to glean useful information from the complex vibrational signal.

The study of complex materials using vibEELS involves a multi-step process that begins with the simulation of the phonon density of states (DOS) of the material. This simulation, which can be performed using computational methods such as Density Functional Theory (DFT) or Molecular Dynamics (MD), provides a theoretical prediction of the vibrational properties of the material, including the contributions from each element. Once the phonon DOS is simulated, it can be decomposed into the contributions from each element, yielding the vibrational spectrum of each element in the material. This element-projected DOS serves as a reference for interpreting the vibrational EELS data.

The final step in the process is the analysis of the EELS data. This involves comparing the EELS data with the simulated phonon DOS and identifying the contributions from different elements by looking at specific energy ranges in the EELS spectrum. Such analysis can help determine the nature of the vacancies or defects in the material. For instance, a vacancy might lead to a decrease in the contribution from a particular element, while a defect might cause a shift in the energy of the vibrational modes.

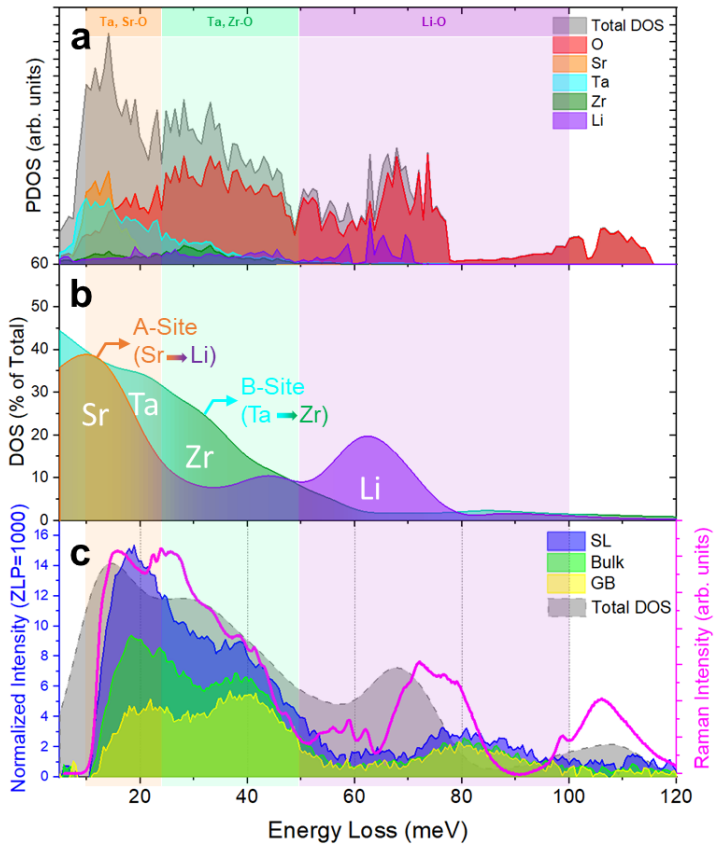

Figure B.4 Elemental Contributions to Total Phonon Density of States and Vibrational EELS. a, Phonon Density of States (PDOS) along with individual elemental contributions. Labels at the top indicate energy ranges where the labeled vibrations are most dominant. b, A, B-site contributions normalized by total PDOS convolved with a 9 meV gaussian to match experimental DF VibEELS energy resolution. A-site and B-site curves are the sum of Li and Sr, and Ta and Zr projected PDOS elemental contributions, respectively. The orange and purple, and cyan and green colors represent varying percentage of Sr and Li, and Ta and Zr, respectively, as indicated by the labels. c, Plots of convolved PDOS, Raman spectra of the LSTZ pellet, and DF VibEEL spectra in the SL, Bulk, and GB regions.

Fig. B.4 shows the phonon DOS for our LSTZ0.75 system. Due to the complexity of the structure, we employed an active learning machine learning strategy to obtain DFT-accurate potentials for large structures. This is necessary since utilizing DFT to converge large structures, such as the vacancy-engineered LSTZ0.75, is computationally infeasible. The process behind using a machine-learned potential is to first converge several small but similar structures using DFT. This forms the initial training set that trains the momentum

tensor potential (MTP). The MTP is further trained via active learning using Monte Carlo Molecular Dynamics (MC/MD). More details can be found in the supplementary information of ref.[108]. This process produces a DFT-accurate MTP that is valid for large structures. Force constants were then obtained from the MTP using finite displacement method. Finally, the phonon DOS was obtained by plugging in the force constants into the dynamical matrix under the harmonic approximation as discussed in the first section of chapter 1.

To discern the contributions of individual elements to the phonon states, the phonon DOS is first projected onto each atom. Subsequently, the phonon DOS projections of atoms belonging to the same element are summed together. This process yields the element-projected phonon DOS and is shown in Fig. B.4a. The low energy range, about 10-25 meV, is dominated by Sr and Ta atoms vibrating with oxygen. The 25-50meV range sees strong oxygen as well as Ta-related vibrations. The highest energy range, 50, 100 meV, contains vibrations predominantly of oxygen as well as Li-related vibrations. Fig. B.4b is employed in an effort to categorize these phonon modes further by labeling them by the site their contributing elements occupy in the perovskite oxide matrix. The lower energy is roughly dominated by A-site vibrations, mainly Sr-O species. B-site vibrations such as Ta-O phonons also dominate in that energy range but are more easily isolated in the 25-50 meV energy range. The highest energy range have O-O vibrations as well as Li-O vibrations. This energy range is dominated by the vibrations of the oxygen octahedral as well as the A-site Li.

By breaking down the phonon DOS in terms of its elemental and site contributions, we now have a solid foundation upon which to analyze the complex vibrational EELS signal (Fig. B.4c). Representative spectra in the bulk, SL, and the GB are shown in shaded colors. These

spectra are supplemented with the total phonon DOS and Raman spectrum to illustrate consistency across simulation and different spectroscopic techniques.

B.4 Mapping Vacancies, GB defects, and Li distributions using Vibrational EELS

Several notable features are evident in the contour plot (Fig. B.5d), including a significant variation in intensity in the SL region and a sharp decrease in intensity at the GB in the low energy region of the phonon signal. The orange curve in Fig. B.5b, which primarily consists of Sr, Ta vibrations with O (Fig. B.4b), exhibits strong intensity modulation in the SL region due to the increased concentration of Sr. The dip at the GB suggests a deficiency in Sr, Ta vibrational species.

Considering that the concentration of O remains constant throughout this region (Fig. B.6), the DF VibEELS mapping (Fig. B.5b) indicates the presence of Sr and Ta vacancies, aligning with Fig. B.6. The green curve represents the spatial trend of vibrations that are largely dominated by Ta-, Zr-O. The dip at the GB here is less pronounced due to slight vacancies in Ta and Zr, which can be more clearly seen in Fig. B.5d. A similar contrast for Ta-, Zr-O vibrations in the SL region is seen in Fig. B.5b and, to a much lesser degree, in the intensity profiles in Fig. B.6, suggesting that DF VibEELS is highly sensitive to local elemental modulation and can be extended to map minute variations in composition. This is not unlike VibEELS ability to measure structural changes that manifest as defect modes[49]. The purple curve, which primarily contains Li-O vibrations, also shows strong intensity modulation in the SL region, produced by an alternating Sr-rich and Li-rich SL. Unlike the other curves, Li-O shows no decrease in integrated intensity at the GB, indicating that there are no Li

vacancies at the GB. This can also be seen in the representative spectra in Fig. B.5a where the intensities in the 50–100meV region hardly change between the bulk and the GB. Given the presence of Sr, Ta, and Zr vacancies, the relative atomic % of Li is higher at the GB, which aligns with findings in ref.[108]. Coupled with the phonon DOS, DF VibEELS mapping allows us to map the distribution of not only Li but also Sr, Ta, and Zr at the atomic scale.

DF VibEELS was also conducted on the general GB and similar trends in vibrational intensity can be observed (Fig. B.5e–h). Like the (010) faceted GB, the general GB also exhibited Sr, Ta, and Zr vacancies as evidenced by Fig. B.5f. The intensity of low energy vibrations in the 10–25meV and 25–50 meV range corresponding to Sr-, Ta-O and Ta-, Zr-O vibrations decreases at GB and is consistent with the corresponding elemental mapping in ref.[108]. However, the vibrational intensity in the 50–100meV corresponding to Li-O vibrations remains constant, suggesting that, similar to the (010) faceted GB, general GBs also do not contain Li+ vacancies. The slight variation in spectral shapes between (010) faceted GB and general GB spectra are a result of the changes to the in-plane vibrations due to the differing zone axes, demonstrating that this technique is highly sensitive to crystal orientation.

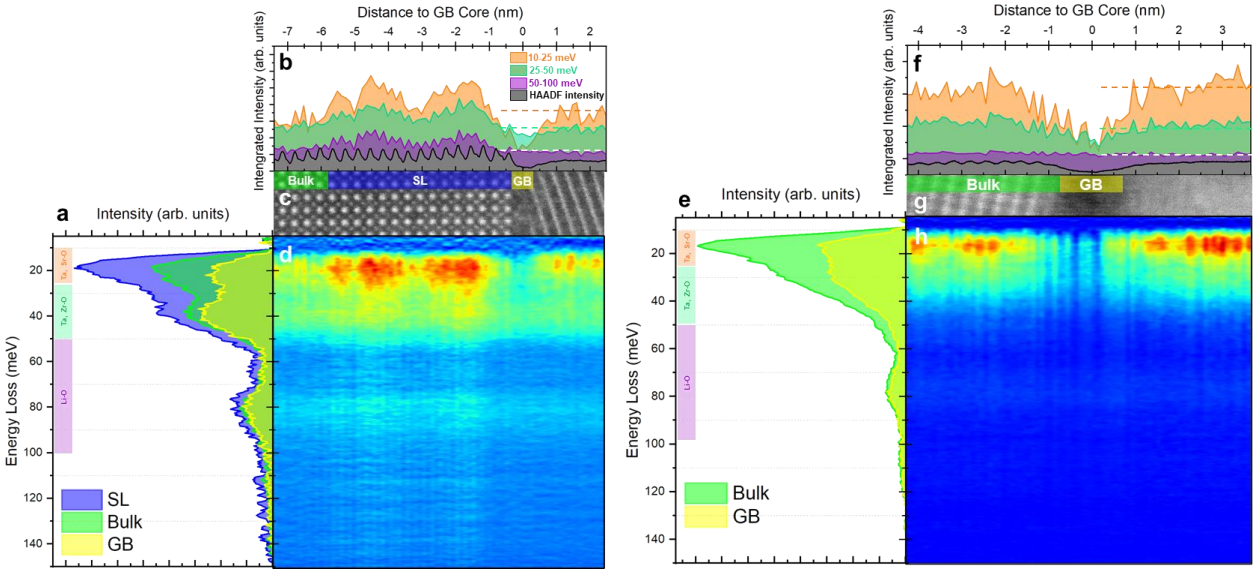

Figure B.5 Vibrational EELS of (010) facetted and General GBs. a, Representative vibrational spectra at the SL, bulk, and GB regions of a (010)-facetted GB. Averaged vibrational spectral intensities are higher at the SL region than in the bulk and GB. The colored labeling to the left of the peak denotes the energy ranges over which the signal was averaged and corresponds to specific elemental vibrations with oxygen. b, Line profiles of the averaged intensities denoted in (a) overlaid with a vertically integrated HAADF line profile. While all intensity-averaged curves show modulations in the SL region, only the intensity of the Ta, Sr-O vibrations shows a large dip at the GB. The B-site vibrational intensity (Ta, Zr-O) shows a smaller dip while the vibrational EELS signal corresponding to Li-O vibrations shows no change from bulk at the GB c, HAADF image corresponding to the region the (010) facetted GB spectra were acquired. d, Contour plot of vertically-integrated spectral slices stacked horizontally. The vertical axis denotes energy loss while the horizontal axis denotes the horizontal real-space position labeled in the horizontal axis of (b). e, Representative vibrational spectra at the bulk, and GB regions of a general GB. f, Line profiles of the averaged intensities denoted in (e) overlaid with a vertically integrated HAADF line profile. The intensity of the Ta, Sr-O vibrations show a large dip at the GB, the B-site vibrational intensity (Ta, Zr-O) shows a smaller dip, while the vibrational EELS signal corresponding to Li-O vibrations shows no change from bulk at the GB. Plot labels are the same as in (b) g, HAADF image corresponding to the region the general GB spectra were acquired. h, Contour plot of vertically-integrated spectral slices stacked horizontally. The streaks in Figs. 5d,h indicate atomic resolution vibrational mapping[53].

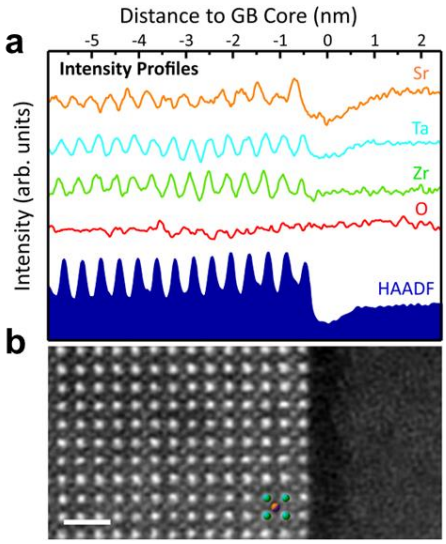

Figure B.6 Elemental mapping (010) faceted GB. a, composition line profiles from core-loss EELS. b, atomic resolution HAADF image of a (010) faceted GB.

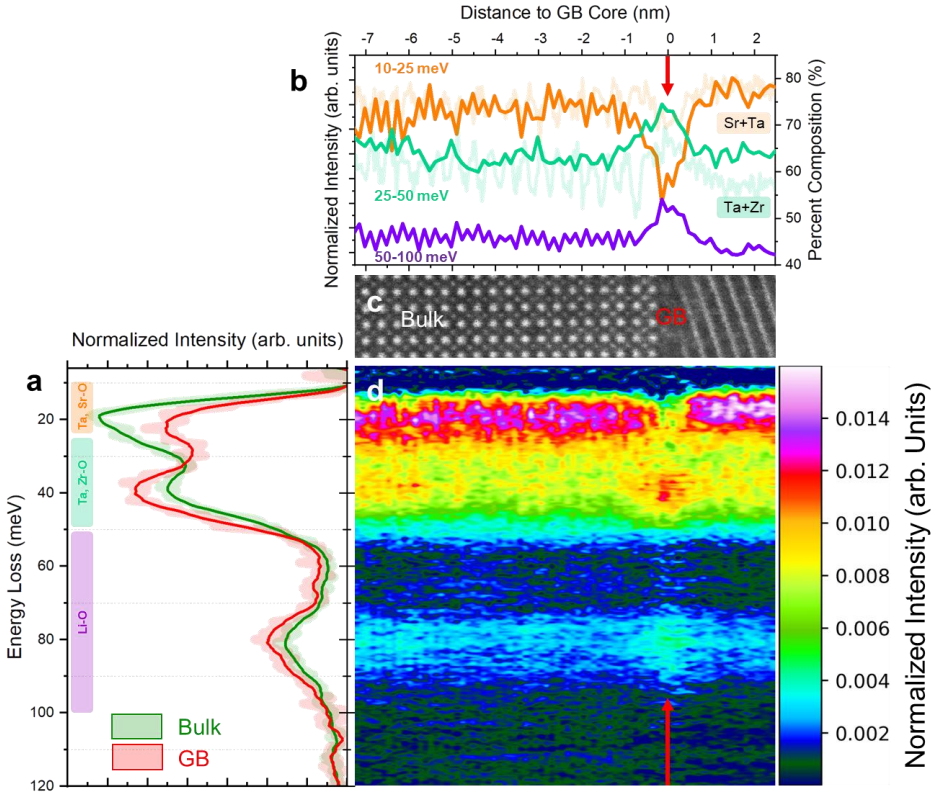

Figure B.7 Vibrational EELS of (010) facetted and General GBs. a, Representative vibrational spectra at the bulk and GB regions of a (010)-facetted GB. The colored labeling to the left of the peak denotes the energy ranges over which the signal was averaged and corresponds to specific elemental vibrations with oxygen. b, Line profiles of the integrated intensities

denoted in (a) and normalized to the sum of the entire phonon signal. The normalized intensity of the Ta, Sr-O vibrations shows a large dip at the GB while that of Ta, Zr-O and Li-O show a peak. This is fully consistent with the percent composition line profiles (in light colors) of Sr+Ta and Ta+Zr, respectively. c, HAADF image corresponding to the region the (010) facetted GB spectra were acquired. d, Contour plot of vertically-averaged spectral slices stacked horizontally. The vertical axis denotes energy loss while the horizontal axis denotes the horizontal real-space position labeled in (b).

In exhaustive detail, Fig. B.7 illustrates a robust comparison between core-loss elemental mapping and vibEELS. The technique of mapping sum-normalized vibrational signals enables the examination of relative contributions at the grain boundaries (GB), unaffected by global variations in the vibrational structure. Figure B.7a compares the signal-normalized vibrational spectra of the bulk material with that of the GB, highlighting a decrease in the lowest energy peak and an increase in the adjacent peak relative to the total vibrational signal. The spatial pattern of the integrated vibrational signals, as shown in Figure B.7b, indicates a strong correlation between the percent compositions of Sr+Ta and Ta+Zr and their corresponding vibrational modes, thereby establishing VibEELS as a highly sensitive tool for mapping chemical vacancies. Crucially, this technique can map the distribution of Li, revealing a higher atomic percentage of Li at the GB. Figure B.7d provides a spectrally and spatially resolved contour plot that demonstrates how the relative elemental composition independently impacts A-site and B-site vibrations.

This technique proves to be crucial for solid electrolytes with compositions that have high Ta:Li ratios. This is because the Ta-$O_{2,3}$ edge tends to overshadow and dominate the Li-K edge, making it impossible to map Li distributions using conventional core-loss EELS. As a result, the Dark Field (DF) VibEELS technique emerges as a uniquely powerful method capable of characterizing LSTZ and its derivatives (such as $Li_{0.375}Sr_{0.4375}Hf_{0.25}Ta_{0.75}O_3$ and

$Li_{0.38}Sr_{0.44}Ta_{0.7}Hf_{0.3}O_{2.95}F_{0.05}$) at the atomic scale. More broadly, we showcase vibrational EELS as an extremely effective tool for characterizing atomic scale structural and compositional variations. VibEELS can be powerfully employed to map Li content, defects, strain fields, phase changes, and thermodynamics in general. Beyond mapping vibrations at grain boundaries in solid electrolytes, VibEELS can serve as a highly sensitive probe for lattice irregularities in cathode and anode materials, potentially predicting expected Li pathways and failure mechanisms. Therefore, VibEELS is a versatile technique that can either complement or replace traditional compositional mapping and other Scanning Transmission Electron Microscopy (STEM) techniques.